# The Prediction of Swirling Recirculating Flow and the Fluid Flow and Mixing in Stirred Tanks

by

**Yousef Jassim Easa Al-wazzan**

**Thesis submitted for the degree of**

**Doctor of Philosophy**

**in the Faculty of Engineering**

**University of London**

**and**

**for the Diploma of Membership of Imperial College**

**Imperial College of Science, Technology and Medicine**

**Department of Mechanical Engineering**

**May 1997**

BIC
LONDIN.
UNIV

# Abstract

This study is concerned with the application of computational fluid dynamics to the calculation of swirling recirculating flows and the fluid flow and mixing in stirred tanks with emphasis placed on the use of accurate differencing schemes and second order turbulence closures.

The Hybrid, Linear Upwind and TVD differencing schemes are compared using two simple two-dimensional convection-diffusion problems. Comparisons show that the second order TVD and Linear Upwind differencing schemes are in good agreement with the analytic solution, although the latter exhibited boundedness problems. The TVD scheme and Reynolds Stress turbulence model are used to model the sudden expansion of swirling coaxial water jets. Grid independent results are compared with experimental data and predictions made with the usual Hybrid differencing and $\kappa$ - $\varepsilon$ turbulence model. The comparisons show that the TVD scheme has greatly improved the numerical accuracy of the computations and the Reynolds Stress closure has improved the physical behaviour of the predictions.

The above methods are coupled with three impeller models (Simple, Drag and Dynamic) and applied to the prediction of the fluid flow in a vessel stirred by single and double Rushton impellers and the results are compared with experimental data. The flow generated by the single impeller is influenced chiefly by the choice of impeller model (Dynamic model was best), whereas the flow generated by the double impeller also depends on the turbulence model and differencing scheme (Reynolds Stress turbulence model and TVD scheme were best) because the impingement of the two impeller jets streams generates high circumferential velocities and turbulence levels.

The three-dimensional calculation of the mixing in a vessel stirred by a single Rushton impeller was compared against experimental data. There is no clear "best" combination of impeller model, differencing scheme and turbulence model, although, the predictions obtained using the Simple impeller model with TVD scheme and Reynolds Stress/Scalar Flux turbulence model and those of the Dynamic impeller model with TVD scheme and $\kappa$ - $\varepsilon$ turbulence model were closest to the experimental data.

# Acknowledgements

First of all I would like to express my sincere thanks to my supervisor Dr. A. J. Marquis for his guidance and encouragement throughout the course of the work.

I am grateful to Kuwait Institute For Scientific Research (KISR) for providing the scholarship and the study leave without which this work would not have been possible.

My appreciation is also extended to my colleagues at the Water Resources Division (KISR) Dr. Jawad Alsulami, Sadiq Ibrahim, Dr. Mahmoud Abdul Jawad, Sameer Abo Hamad, Mohammed Suffer, Ahmed Alsaffar and Ahmed Alhaji for their support and understanding throughout my period of study.

Deepest and dearest thanks are extended to my wife Bibi and my lovely children Yagoub and Noor for their support and encouragement during the course of the work.

In addition, special thanks are extended to my father Jassim, my mother Sophia and my brothers and sisters Hameed, Fatema, Bader, Mohammed, Nadia and Lila for their moral support throughout my period of study.

I would like to acknowledge the moral support I have received from Ms. Nusaiba Ibrahim Ben-Shaibah and my Aunt Bugum Ben-Shaibah.

Finally, my appreciation is also extended to my friends Said Abbas, Ghaleb Darwish, Saleh Habeeb, Adel Fakhral-Deen, Dr. Abdulkareem Alsaffar and Hassan Mosa for their help and support throughout my period of study.

# Table of Contents

**Abstract**.....i

**Acknowledgement**.....ii

**Contents**.....iii-vi

**Nomenclature**.....vii-ix

**Lists of Figures**.....x-xviii

**Lists of Tables**.....xix-xx

## Chapter 1

1. INTRODUCTION.....1

1.1 Introductory Remarks.....1

1.2 Objectives.....4

1.3 Details of Present Work.....4

1.4 Thesis Outline.....5

## Chapter 2

2. DISCRETISATION SCHEMES.....8

2.1 Introduction.....8

2.2 Governing Equations.....8

2.3 Finite Difference Approximations.....10

2.4 Discretisation Technique.....13

2.5 Scalar Transport Equation.....14

2.6 Formulation of Discretisation Schemes.....18

2.6.1 Central Differencing (CD).....18

2.6.2 Upwind Differencing (UD).....20

2.6.3 Hybrid Differencing .....22
2.6.4 Linear Upwind Differencing (LUD) .....22
2.6.5 Total Variation Diminishing (TVD).....26
2.7 Summary.....29

## Chapter 3

3. TURBULENCE AND TURBULENCE MODELLING.....30
3.1 Introduction.....30
3.2 Turbulence Modelling.....32
3.3 Eddy Viscosity Models.....35
3.3.1 Mixing Length Models.....36
3.3.2 One-Equation Model.....36
3.3.3 Two- Equation Models.....37
3.3.4 Drawbacks of Eddy Viscosity Models.....40
3.4 Reynolds Stress and Scalar Flux Models.....42
3.4.1 Reynolds Stress Model.....42
3.4.2 Scalar Flux Model.....45

## Chapter 4

4. TWO DIMENSIONAL FLOW CALCULATIONS.....50
4.1 Flow Inclined at 45°.....50
4.1.1 Problem Specification.....50
4.1.2 Results and Discussion.....50
4.2 Flow Moving Through 180° (IAHR Problem).....51
4.2.1 Problem Specification.....51
4.2.2 Results and Discussion.....52
4.3 The Sudden Expansion of Swirling Coaxial Water Jets.....52

4.3 The Sudden Expansion of Swirling Coaxial Water Jets.....52
4.3.1 Flow Configuration.....52
4.3.2 Boundary Conditions.....53
4.3.3 Results and Discussion.....56
4.3.3a Grid Independent Solution.....56
4.3.3b Hybrid and TVD Schemes and the $\kappa$ - $\varepsilon$ Turbulence Model.....57
4.3.3c Hybrid and TVD Schemes and the Reynolds Stress Turbulence Model...63
4.4 Computational Effort.....68
4.5 Conclusions.....70

## Chapter 5

5. FLUID FLOW IN STIRRED TANKS.....93
5.1 Introduction.....93
5.2 Flow Configuration.....97
5.3 Boundary Conditions.....97
5.3.1 Symmetry.....98
5.3.2 Wall.....98
5.3.3 Baffles and Impeller Disk.....100
5.4 Impeller Models.....101
5.4.1 Simple Model.....101
5.4.2 Drag Force Model.....101
5.4.3 Dynamic Model.....104
5.5 Single Rushton Turbine.....106
5.5.1 Results and Discussion.....106
5.6 Double Rushton Turbine.....121
5.6.1 Results and Discussion.....121
5.7 Influence of Grid Refinement on the Computations.....137
5.7.1 Results and Discussion.....137
5.8 Computational Effort.....139

5.9 Circumferential Effect of the Impeller Models.....142
5.10 Conclusions.....144

## Chapter 6

6. MIXING IN STIRRED TANK.....171
6.1 Introduction.....171
6.2 Flow Configuration.....174
6.3 Boundary Conditions.....174
6.4 Results and Discussion.....175
6.4.1 Experimental Data.....175
6.4.2 Results of Calculations.....176
6.5 Computational Effort.....184
6.6 Summary.....186

## Chapter 7

7. MAIN FINDINGS AND FUTURE WORK.....203
7.1 Summary and Conclusions.....203
7.2 Suggestions for Future Work.....207

References.....209

# Nomenclature

| | |
|---|---|
| $A$ | Cross sectional area of a control volume |
| $A_B$ | Area of impeller blade |
| $A_f$ | Time averaged blade area |
| $a_{ij}$ | Anisotropy of the Reynolds Stress $\overline{u_i u_j}$ |
| $B_\Phi$, $Q_\Phi$ | Linearised source terms |
| $C_D$ | Drag coefficient |
| $C'_D$ | Mean drag coefficient |
| $C_s$, $C'_s$ | Diffusional term constants |
| $C_1$, $C_2$, $C_3$, $C_4$ | Constants in the Reynolds Stress model |
| $C_{\varepsilon 1}$, $C_{\varepsilon 2}$ | Constants in the $\varepsilon$ equation |
| $C_\phi$, $C_{\phi 1}$, $C_{\phi 2}$ | Constants in the Scalar Flux equation |
| $d$ | Diameter in a pipe |
| $\frac{d}{dt}$ | Substantial derivative |
| $F_x$, $F_y$, $F_z$ | Body forces terms |
| $F_D$ | Drag force |
| $F_{DT}$ | Total drag force |
| $F'_D$ | Drag force acting on each impeller control volume |
| $F'_{DT}$ | Total drag force over all the cells contained within the impeller swept volume |
| $\kappa$ | Turbulent kinetic energy $\overline{u_i u_i}/2$ |
| $K$ | Von Karman's constant |
| $\ell$ | Length scale |
| $\ell_m$ | Mixing length |
| $N$ | Number of impeller blades |
| $P$ | Pressure |
| $P_e$ | Peclet number |

| | |
|---|---|
| r | Radius |
| $r_T$ | Mean impeller radius |
| $R_e$ | Reynolds number |
| S | Source term |
| T | Time |
| $U_i$ | Mean velocity tensor $U_1 = U$, $U_2 = V$, $U_3 = W$ |
| U, V, W | Mean velocities in x, y, z directions |
| $u_i$ | Fluctuating component of velocity $U_i$ |
| $\overline{u_i u_j}$ | Reynolds Stress tensor |
| $\overline{u_i \phi}$ | Scalar Flux tensor |
| $x_i$ | Cartesian tensor |
| x, y, z | Cartesian co-ordinates |
| x, r | Cylindrical polar co-ordinates (2D) |

*Greek*

| | |
|---|---|
| $\Delta x, \Delta y, \Delta z$ | Finite difference mesh dimensions |
| $\delta_{ij}$ | Kronecker delta |
| $\varepsilon$ | Dissipation rate |
| $\Gamma$ | Transport diffusion coefficient |
| $\mu$ | Molecular viscosity |
| $\nu$ | Kinematic viscosity |
| $\nu_t$ | Turbulent kinematic viscosity |
| $\rho$ | Density |
| $\sigma$ | Laminar Prandtl/Schmidt number |
| $\sigma_t$ | Turbulent Prandtl/Schmidt number |
| $\sigma_\kappa$ | Turbulent kinetic energy Prandtl number |
| $\omega$ | Rotational speed |
| $\Phi$ | Mean scalar |

| | |
|---|---|
| $\overline{\phi^2}$ | Mean scalar variance |
| $\Psi$ | Flux limiter |
| $\delta$ P | Pressure correction |
| $\Delta$V | Volume of the control volume |
| $\delta_r \delta_\theta \delta_x$ | Radial, tangential and axial sizes of the control volume |

*Subscripts*

| | |
|---|---|
| i, j | Co-ordinates indices |
| $\kappa, \varepsilon, \Phi$ | Constant relating to $\kappa$, $\varepsilon$ or $\Phi$ |
| N, S, E, W, P, | Nodal positions |
| NN, SS, EE, WW | |
| n, s, e, w | Mid-points positions |

*Superscripts*

| | |
|---|---|
| T | Maximum time level |
| n | Time level |

# List of Figures

## Chapter 2

2.1- Velocity values are stored midway between pressure nodes.....14

2.2- A typical control volume.....15

2.3- West boundary control volume.....16

2.4- East boundary control volume.....16

## Chapter 4

4.1- Uniform flow inclined at 45°.....72

4.2a- Profiles for uniform flow inclined at 45°
(mesh size used is 9x9).....72

4.2b- Profiles for uniform flow inclined at 45°
(mesh size used is 19x19).....73

4.2c- Profiles for uniform flow inclined at 45°
(mesh size used is 39x39).....73

4.3- Uniform flow for the IAHR problem.....74

4.4a- Profiles for uniform flow for the IAHR problem
(mesh size is 19x9).....74

4.4b- Profiles for uniform flow for the IAHR problem
(mesh size is 39x19).....75

4.4c- Profiles for uniform flow for the IAHR problem
(mesh size is 79x39).....75

4.5- Flow geometry of the sudden expansion of swirling coaxial
water jets.....76

4.6- Shear regions with the sudden expanding of swirling coaxial
water jets.....76

4.7a- Prediction of the U axial velocity using $\kappa - \varepsilon$ turbulence model
and Hybrid scheme.....77

4.7b- Prediction of the U axial velocity using $\kappa$ - $\varepsilon$ turbulence model and TVD scheme.....77

4.7c- Prediction of the U axial velocity using Reynolds Stress turbulence model and Hybrid scheme.....78

4.7d- Prediction of the U axial velocity using Reynolds Stress turbulence model and TVD scheme.....78

4.8a- Prediction of the V radial velocity using $\kappa$ - $\varepsilon$ turbulence model and Hybrid scheme.....79

4.8b- Prediction of the V radial velocity using $\kappa$ - $\varepsilon$ turbulence model and TVD scheme.....79

4.8c- Prediction of the V radial velocity using Reynolds Stress turbulence model and Hybrid scheme.....80

4.8d- Prediction of the V radial velocity using Reynolds Stress turbulence model and TVD scheme.....80

4.9a- Prediction of the W angular velocity using $\kappa$ - $\varepsilon$ turbulence model and Hybrid scheme.....81

4.9b- Prediction of the W angular velocity using $\kappa$ - $\varepsilon$ turbulence model and TVD scheme.....81

4.9c- Prediction of the W angular velocity using Reynolds Stress turbulence model and Hybrid scheme.....82

4.9d- Prediction of the W angular velocity using Reynolds Stress turbulence model and TVD scheme.....82

4.10a- Prediction of the $\bar{u}\left(\bar{u} = \sqrt{\overline{uu}}\right)$ normal stress using $\kappa$ - $\varepsilon$ turbulence model and Hybrid scheme.....83

4.10b- Prediction of the $\bar{u}\left(\bar{u} = \sqrt{\overline{uu}}\right)$ normal stress using $\kappa$ - $\varepsilon$ turbulence model and TVD scheme.....83

4.10c- Prediction of the $\bar{u}\left(\bar{u} = \sqrt{\overline{uu}}\right)$ normal stress using Reynolds Stress turbulence model and Hybrid scheme.....84

4.10d- Prediction of the $\overline{u}\left(\overline{u}=\sqrt{\overline{uu}}\right)$ normal stress using Reynolds Stress turbulence model and TVD scheme.....84

4.11a- Prediction of the $\overline{v}\left(\overline{v}=\sqrt{\overline{vv}}\right)$ normal stress using $\kappa$ - $\varepsilon$ turbulence model and Hybrid scheme.....85

4.11b- Prediction of the $\overline{v}\left(\overline{v}=\sqrt{\overline{vv}}\right)$ normal stress using $\kappa$ - $\varepsilon$ turbulence model and TVD scheme.....85

4.11c- Prediction of the $\overline{v}\left(\overline{v}=\sqrt{\overline{vv}}\right)$ normal stress using Reynolds Stress turbulence model and Hybrid scheme.....86

4.11d- Prediction of the $\overline{v}\left(\overline{v}=\sqrt{\overline{vv}}\right)$ normal stress using Reynolds Stress turbulence model and TVD scheme.....86

4.12a- Prediction of the $\overline{w}\left(\overline{w}=\sqrt{\overline{ww}}\right)$ normal stress using $\kappa$ - $\varepsilon$ turbulence model and Hybrid scheme.....87

4.12b- Prediction of the $\overline{w}\left(\overline{w}=\sqrt{\overline{ww}}\right)$ normal stress using $\kappa$ - $\varepsilon$ turbulence model and TVD scheme.....87

4.12c- Prediction of the $\overline{w}\left(\overline{w}=\sqrt{\overline{ww}}\right)$ normal stress using Reynolds Stress turbulence model and Hybrid scheme.....88

4.12d- Prediction of the $\overline{w}\left(\overline{w}=\sqrt{\overline{ww}}\right)$ normal stress using Reynolds Stress turbulence model and TVD scheme.....88

4.13a- Prediction of the $\overline{uv}$ shear stress using $\kappa$ - $\varepsilon$ turbulence model and Hybrid scheme.....89

4.13b- Prediction of the $\overline{uv}$ shear stress using $\kappa$ - $\varepsilon$ turbulence model and TVD scheme.....89

4.13c- Prediction of the uv shear stress using Reynolds Stress turbulence model and Hybrid scheme.....90

4.13d- Prediction of the $\overline{uv}$ shear stress using Reynolds Stress turbulence model and TVD scheme.....90
4.14a- Prediction of the $\overline{uw}$ shear stress using $\kappa$ - $\varepsilon$ turbulence model and Hybrid scheme.....91
4.14b- Prediction of the $\overline{uw}$ shear stress using $\kappa$ - $\varepsilon$ turbulence model and TVD scheme.....91
4.14c- Prediction of the $\overline{uw}$ shear stress using Reynolds Stress turbulence model and Hybrid scheme.....92
4.14d- Prediction of the $\overline{uw}$ shear stress using Reynolds Stress turbulence model and TVD scheme.....92

## Chapter 5

5.1- Cylindrical tank with single Rushton turbine impeller.....148
5.2- Cylindrical tank with double Rushton turbine impeller.....148
5.3a- Mean velocity vectors for a single Rushton turbine in the $\theta$ = 0° plane.....149
5.3b- Mean velocity vectors for a single Rushton turbine in the x = 33.5mm plane.....149
5.3c- Node distribution for a single Rushton turbine in the axial-radial plane.....150
5.3d- Node distribution for a single Rushton turbine in the radial-tangential plane.....150
5.4a- Mean velocity vectors for a double Rushton turbine in the $\theta$ = 0° plane.....151
5.4b- Mean velocity vectors for a double Rushton turbine in the x = 33.1mm plane....151
5.4c- Node distribution for a double Rushton turbine in the axial-radial plane.....152
5.4d- Node distribution for a double Rushton turbine in the radial-tangential plane.....152

*Single Rushton Turbine*

5.5a,b- Prediction of the mean axial velocity using the Simple impeller model with Hybrid and TVD differencing schemes respectively in the plane $\theta$ = 0°.....153
5.6a,b- Prediction of the mean axial velocity using the Drag impeller model with Hybrid differencing and the Dynamic impeller model with TVD scheme respectively in the plane $\theta$ = 0°.....153
5.7a,b- Prediction of the mean radial velocity using the Simple impeller model with Hybrid and TVD differencing schemes respectively in the plane $\theta$ = 0°.....154

4.13d- Prediction of the $\overline{uv}$ shear stress using Reynolds Stress turbulence model and TVD scheme.....90
4.14a- Prediction of the $\overline{uw}$ shear stress using $\kappa$ - $\varepsilon$ turbulence model and Hybrid scheme.....91
4.14b- Prediction of the $\overline{uw}$ shear stress using $\kappa$ - $\varepsilon$ turbulence model and TVD scheme.....91
4.14c- Prediction of the $\overline{uw}$ shear stress using Reynolds Stress turbulence model and Hybrid scheme.....92
4.14d- Prediction of the $\overline{uw}$ shear stress using Reynolds Stress turbulence model and TVD scheme.....92

## Chapter 5

5.1- Cylindrical tank with single Rushton turbine impeller.....148
5.2- Cylindrical tank with double Rushton turbine impeller.....148
5.3a- Mean velocity vectors for a single Rushton turbine in the $\theta$ = 0° plane.....149
5.3b- Mean velocity vectors for a single Rushton turbine in the x = 33.5mm plane.....149
5.3c- Node distribution for a single Rushton turbine in the axial-radial plane.....150
5.3d- Node distribution for a single Rushton turbine in the radial-tangential plane.....150
5.4a- Mean velocity vectors for a double Rushton turbine in the $\theta$ = 0° plane.....151
5.4b- Mean velocity vectors for a double Rushton turbine in the x = 33.1mm plane....151
5.4c- Node distribution for a double Rushton turbine in the axial-radial plane.....152
5.4d- Node distribution for a double Rushton turbine in the radial-tangential plane.....152

*Single Rushton Turbine*

5.5a,b- Prediction of the mean axial velocity using the Simple impeller model with Hybrid and TVD differencing schemes respectively in the plane $\theta$ = 0°.....153
5.6a,b- Prediction of the mean axial velocity using the Drag impeller model with Hybrid differencing and the Dynamic impeller model with TVD scheme respectively in the plane $\theta$ = 0°.....153
5.7a,b- Prediction of the mean radial velocity using the Simple impeller model with Hybrid and TVD differencing schemes respectively in the plane $\theta$ = 0°.....154

5.8a,b- Prediction of the mean radial velocity using the Drag impeller model with Hybrid differencing and the Dynamic impeller model with TVD scheme respectively in the plane $\theta = 0°$.....154
5.9a,b- Prediction of the mean tangential velocity using the Simple impeller model with Hybrid and TVD differencing schemes respectively in the plane $\theta = 0°$.....155
5.10a,b-Prediction of the mean tangential velocity using the Drag impeller model with Hybrid differencing and the Dynamic impeller model with TVD scheme respectively in the plane $\theta = 0°$.....155
5.11a,b-Prediction of the mean axial velocity using the Simple impeller model with Hybrid and TVD differencing schemes respectively in the plane $\theta = 45°$.....156
5.12a,b-Prediction of the mean axial velocity using the Drag impeller model with Hybrid differencing and the Dynamic impeller model with TVD scheme respectively in the plane $\theta = 45°$.....156
5.13a,b-Prediction of the mean radial velocity using the Simple impeller model with Hybrid and TVD differencing schemes respectively in the plane $\theta = 45°$.....157
5.14a,b-Prediction of the mean radial velocity using the Drag impeller model with TVD differencing and the Dynamic impeller model with Hybrid scheme respectively in the plane $\theta = 45°$.....157
5.15a,b-Prediction of the mean tangential velocity using the Simple impeller model with Hybrid and TVD differencing schemes respectively in the plane $\theta = 45°$.....158
5.16a,b-Prediction of the mean tangential velocity using the Drag impeller model with Hybrid differencing and the Dynamic impeller model with TVD scheme respectively in the plane $\theta = 45°$.....158
5.17a,b-Prediction of the tangential fluctuating velocity using the Simple impeller model with Hybrid and TVD differencing schemes respectively in the plane $\theta = 0°$...159
5.18a,b-Prediction of the tangential fluctuating velocity using the Drag impeller model with Hybrid differencing and the Dynamic impeller model with TVD scheme respectively in the plane $\theta = 0°$.....159

5.19a,b-Prediction of the tangential fluctuating velocity using the Simple impeller model with Hybrid and TVD differencing schemes respectively in the plane $\theta = 45°$. 160

5.20a,b-Prediction of the tangential fluctuating velocity using the Drag impeller model with Hybrid differencing and the Dynamic impeller model with TVD scheme respectively in the plane $\theta = 45°$ ..... 160

*Double Rushton Turbine*

5.21a,b-Prediction of the mean axial velocity using the Simple impeller model with Hybrid and TVD differencing schemes respectively in the plane $\theta = 0°$ ..... 161

5.22a,b-Prediction of the mean axial velocity using the Drag impeller model with Hybrid differencing and the Dynamic impeller model with TVD scheme respectively in the plane $\theta = 0°$ ..... 161

5.23a,b-Prediction of the mean radial velocity using the Simple impeller model with Hybrid and TVD differencing schemes respectively in the plane $\theta = 0°$ ..... 162

5.24a,b-Prediction of the mean radial velocity using the Drag impeller model with Hybrid differencing and the Dynamic impeller model with TVD scheme respectively in the plane $\theta = 0°$ ..... 162

5.25a,b-Prediction of the mean tangential velocity using the Simple impeller model with Hybrid and TVD differencing schemes respectively in the plane $\theta = 0°$ ..... 163

5.26a,b-Prediction of the mean tangential velocity using the Drag impeller model with Hybrid differencing and the Dynamic impeller model with TVD scheme respectively in the plane $\theta = 0°$ ..... 163

5.27a,b-Prediction of the mean axial velocity using the Simple impeller model with Hybrid and TVD differencing schemes respectively in the plane $\theta = 45°$ ..... 164

5.28a,b-Prediction of the mean axial velocity using the Drag impeller model with Hybrid differencing and the Dynamic impeller model with TVD scheme respectively in the plane $\theta = 45°$ ..... 164

5.29a,b-Prediction of the mean radial velocity using the Simple impeller model with Hybrid and TVD differencing schemes respectively in the plane $\theta = 45°$ ..... 165

5.30a,b-Prediction of the mean radial velocity using the Drag impeller model with Hybrid differencing and the Dynamic impeller model with TVD scheme respectively in the plane $\theta = 45°$.....165
5.31a,b-Prediction of the mean tangential velocity using the Simple impeller model with Hybrid and TVD differencing schemes respectively in the plane $\theta = 45°$.....166
5.32a,b-Prediction of the mean tangential velocity using the Drag impeller model with Hybrid differencing and the Dynamic impeller model with TVD scheme respectively in the plane $\theta = 45°$.....166
5.33a,b-Prediction of the tangential fluctuating velocity using the Simple impeller model with Hybrid and TVD differencing schemes respectively in the plane $\theta = 0°$...167
5.34a,b-Prediction of the tangential fluctuating velocity using the Drag impeller model with Hybrid differencing and the Dynamic impeller model with TVD scheme respectively in the plane $\theta = 0°$.....167
5.35a,b-Prediction of the tangential fluctuating velocity using the Simple impeller model with Hybrid and TVD differencing schemes respectively in the plane $\theta = 45°$.168
5.36a,b-Prediction of the tangential fluctuating velocity using the Drag impeller model with Hybrid differencing and the Dynamic impeller model with TVD scheme respectively in the plane $\theta = 45°$.....168

*Grid Refinement*

5.37a,b-Prediction of the mean radial velocity using the Dynamic impeller model with TVD scheme in the planes $\theta = 0°$ and $\theta = 45°$ respectively.....169
5.38- Prediction of the tangential fluctuating velocity using the Dynamic impeller model with Hybrid differencing in the plane $\theta = 0°$.....169

*Circumferential Effect of the Impeller Models*

5.39a- Circumferential mean velocity profile obtained experimentally by Lee(1995)....170
5.39b,c-Circumferential mean velocity profiles obtained using the Hybrid differencing and $\kappa$ - $\varepsilon$ turbulence model with the Drag and Dynamic impeller models respectively.....170
5.39d- A profile obtained using the impeller function, $F_{DS}$.....170

## Chapter 6


6.1- Cylindrical tank with single Rushton turbine impeller and injection system.....189

6.2- Top view of cylindrical tank with injection system.....189

6.3- Mixing time measurement locations.....190

6.4- Experimental data for the Rushton turbine for locations above the impeller.....191

6.5- Experimental data for the Rushton turbine for locations below the impeller.....192

6.6- Predictions for the Rushton turbine for locations above the impeller obtained using the Drag impeller model with Hybrid differencing and $\kappa$ - $\varepsilon$ turbulence model.....193

6.7- Predictions for the Rushton turbine for locations below the impeller obtained using the Drag impeller model with Hybrid differencing and $\kappa$ - $\varepsilon$ turbulence model.....194

6.8- Predictions for the Rushton turbine for locations above the impeller obtained using the Drag impeller model with TVD scheme and $\kappa$ - $\varepsilon$ turbulence model....195

6.9- Predictions for the Rushton turbine for locations below the impeller obtained using the Drag impeller model with TVD scheme and $\kappa$ - $\varepsilon$ turbulence model....196

6.10- Predictions for the Rushton turbine for locations above the impeller obtained using the Dynamic impeller model with TVD scheme and $\kappa$ - $\varepsilon$ turbulence model.....197

6.11- Predictions for the Rushton turbine for locations below the impeller obtained using the Dynamic impeller model with TVD scheme and $\kappa$ - $\varepsilon$ turbulence model.....198

6.12- Predictions for the Rushton turbine for locations above the impeller obtained using the Drag impeller model with Hybrid differencing and Reynolds Stress/Scalar Flux turbulence model.....199

6.13- Predictions for the Rushton turbine for locations below the impeller obtained using the Drag impeller model with Hybrid differencing and Reynolds Stress/Scalar Flux turbulence model.....200

6.14- Predictions for the Rushton turbine for locations above the impeller obtained using the Simple impeller model with TVD scheme and Reynolds Stress/Scalar Flux turbulence model.....201
6.15- Predictions for the Rushton turbine for locations below the impeller obtained using the Simple impeller model with TVD scheme and Reynolds Stress/Scalar Flux turbulence model.....202

# List of Tables


## Chapter 2

2.1- Coefficient quantities.....17

## Chapter 3

3.1- Proposals to determine the length scale.....39

## Chapter 4

4.1- Chamber dimensions.....53

4.2- A summery of the inlet boundary conditions for the jets.....54

4.3- A list of computational meshes used in the calculations.....55

4.4- Flow field CPU time required to complete one iteration.....69

4.5- Velocity variables for which transport equations are solved.....69

## Chapter 5

5.1- A summary of the different impeller model, differencing scheme, turbulence model combinations presented in figures 5.5-5.20.....107

5.2- A summary of the different impeller model, differencing scheme, turbulence model combinations presented in figures 5.22-5.36.....123

5.3- Flow field CPU time required to complete one iteration for the single Rushton impeller calculations.....140

5.4- Flow field CPU time required to complete one iteration for the double Rushton impeller calculations.....140

5.5- Velocity variables for which transport equations are solved for either the single or double impellers.....141

## Chapter 6

6.1- Dimensions of stirred tank used by Middleton et al(1986) and Ziman(1990).....173

6.2- A summary of the different impeller model, differencing scheme and turbulence model combinations presented in figures 6.6-6.15.....177

6.3- Predicted and experimental concentration first arrival time (seconds) at measurement points above and below the impeller.....178

6.4- Predicted concentration first arrival time (seconds) at measurement points above and below the impeller.....180
6.5- Predicted concentration first arrival time (seconds) at measurement points above and below the impeller.....181
6.6- Predicted concentration first arrival time (seconds) at measurement points above and below the impeller.....182
6.7- Predicted concentration first arrival time (seconds) at measurement points above and below the impeller.....183
6.8- Scalar CPU time required to complete one iteration.....184
6.9- Scalar transport equations solved.....184

# Chapter 1

# Introduction

## 1.1 Introductory Remarks

Fluid dynamics is very important in many branches of engineering and considered to be the heart of the process industry. During the 1960s, advances in fluid dynamics were made with the combination of experimental and basic theoretical analysis. The theoretical studies are capable of producing data in a mathematical form avoiding the use of scaling relationships. Such studies are sometimes useful when used to obtain a preliminary design since reasonable results and answers can be reached in a minimum amount of time. The design of systems and components used in the industry such as pumps, chemical reactors, turbines, impellers, combustion chambers and many others relies upon detailed experimental programs in order to identify the key parameters and design variables. Experimental studies are capable of being more realistic compared to theoretical studies, however, the information that can be gathered from these studies is often limited, due to the time and expense of executing an experimental program, difficulty with working with process fluids due to toxicity or flammability and difficulty of extrapolating from

laboratory scales and pilot scale apparatus to full size plants. The need to overcome these problems and the gradual advancement in the speed of computers and the increase in memory size has led to the emergence of Computational Fluid Dynamics (CFD). Since the 1970s CFD has not only been considered as an engineering tool but as another branch of fluid dynamics which does not replace but complements experimental and theoretical fluid dynamics by providing an alternative cost effective means of investigating real flows. In addition to cost CFD may also have the potential of reducing the amount of time during the design and development process, simulating flow conditions which are not reproducible in experimental model tests and providing detailed and comprehensive information.

The starting point of numerical simulations using CFD is the mathematical formulation of the equations governing the transport of mass, momentum and energy. Several techniques have been developed to solve transport equations and now are commonly used to obtain a numerical simulations for many different types of CFD problem. For example, the finite element approach is used for stress calculations while the finite difference technique is used for solving fluid flow and heat transfer problems. In both cases the process of numerical simulations can be divided into the following two steps, the numerical approximation and solution of the governing equations and the modelling of physical processes taking place within the region of interest, e.g. turbulence.

In this work, attention is focused on obtaining numerical simulations of swirling recirculating flow and fluid flow and mixing in stirred tanks and the method selected is the finite difference technique and the basic governing equations are the Navier-Stokes equations. In the finite difference method, the domain over which a solution of the flow equations is sought is discretised so that the dependent variables are considered to exist at discrete points and is known as discretisation. Derivatives are expressed in terms of other values at the surrounding nodes resulting in an algebraic representation of the governing partial differential equations. After writing the governing equations in a finite difference form, then all that is required in principle to obtain a numerical solution of the fluid flow is a set of boundary conditions and an algorithm to solve the set of algebraic equations.

Many workers simulating recirculating flow and fluid flow in stirred tanks during the last few years have used the well known Hybrid differencing scheme to discretise the convection term in the conservation equations governing the flow of interest and the $\kappa$ - $\varepsilon$ turbulence model to represent the turbulent transport during the calculations. The Hybrid differencing scheme, however, is known to introduce a diffusional flux normal to the flow direction which effects some features of the flow such as lowering peak values where-ever the Peclet number is greater than two.

The $\kappa$ - $\varepsilon$ turbulence model uses the mean velocity field distribution and the turbulent kinetic energy of the turbulent motions and its dissipation rate in order to determine the turbulent stress distribution throughout the solution domain. This turbulence model is well known and used in many applications because it is simple, able to produce feasible stress distributions with minimum input and computationally efficient. In spite of these advantages, the $\kappa$ - $\varepsilon$ turbulence model does have some disadvantages. Many theoretical studies have shown that the $\kappa$ - $\varepsilon$ turbulence model can not reflect the sensitivity of the shear stress and the anisotropy between normal stresses to curvature effects (Bradshaw, 1976), the assumption that the axes of stress and strain are coincident, which is hardly correct in any shear flow though it often has little serious consequences in thin shear layers and underestimates the effects of swirl and body forces.

Many workers have shown that using the Hybrid differencing scheme together with $\kappa$ - $\varepsilon$ turbulence model during the numerical computations of a stirred tank have produced a reasonably accurate results compared with experimental data, however, a large mesh size is required to obtain a grid independent solution and as computer time dramatically increases as mesh size increases the cost of the numerical calculations is considerable.

## 1.2 Objectives

The ultimate aim of this work was to predict the flow and mixing in a stirred tank and to this end the following objectives were set:

1) Identify, using simple two-dimensional convection-diffusion problems, an accurate, stable and conservative scheme for the discretisation of the convection terms.
2) To demonstrate the suitability of the selected discretisation scheme in two-dimensional turbulent flow calculation with a second order turbulence closure.
3) To calculate the flow in a stirred tank using the selected discretisation scheme with a second order turbulence closure.
4) To calculate the scalar mixing in a batch operated tank.

## 1.3 Details of Present Work

This study is divided into four parts. The first part deals with the application of three discretisation schemes, Hybrid, Linear Upwind Differencing (LUD) and Total Variation Diminishing (TVD), to the solution of the scalar transport equation using the finite difference method. The three schemes were tested for their accuracy and boundedness using two dimensional simple convection-diffusion problems; i.e. flow inclined at 45° and the flow moving through 180°, often known as the IAHR (International Association of Hydraulic Research) problem.

In the second part of this study, the finite difference solution of the time averaged conservation equations is used to model the sudden expansion of swirling coaxial water jets studied experimentally by Roback et al(1983). The experiment was a continuation of the work carried out by Johnson and Bennett(1981), who performed this study on the same geometry but for the non-swirling case. Predictions of the latter using the $\kappa$ - $\varepsilon$ and

Reynolds Stress/Scalar Flux turbulence models have already been performed by Marquis(1986). The predictions in this work of the swirling coaxial water jets were obtained using the Hybrid and TVD differencing schemes with the $\kappa$ - $\varepsilon$ and Reynolds Stress turbulence models and are compared with the experimental data of Roback et al.

In the third part, the three-dimensional finite difference solution of the time averaged conservation equations is used to model the fully baffled cylindrical tank stirred by one and two Rushton impeller turbines studied experimentally by Lee(1995). The system investigated consisted of a cylindrical vessel with four vertical baffles equally spaced around the perimeter. The shaft of the impeller was concentric with the axis of the tank and the impeller is located one third and two thirds of the tank height from the base for the single and double impeller respectively. In this section, three impeller models called the Simple, Drag and Dynamic are described for the modelling of the velocity field in a fully baffled cylindrical tank stirred by one and two Rushton impellers. The predictions of the velocity field in the vessel were obtained using the three impeller models, the Hybrid and TVD differencing schemes and the $\kappa$ - $\varepsilon$ and Reynolds stress turbulence models and compared with the experimental data of Lee(1995).

Finally, the three-dimensional calculation of the mixing in a fully baffled cylindrical tank stirred by single Rushton impeller studied experimentally by Distelhoff et al(1996) was carried out using the $\kappa$ - $\varepsilon$ and Reynolds stress/Scalar Flux turbulence models. The velocity fields used in the mixing calculations were obtained using a similar methods as described in part three with the Simple, Drag and Dynamic impeller models. The predictions obtained are then discussed and compared with the experimental data of Distelhoff et al(1996).

## 1.4 Thesis Outline

Chapter 2 starts with a description of the general principles behind finite difference approximations and then focuses attention on the formulation of different discretisation

schemes. The discretisation schemes presented along with a discussion of their stability and suitability for use in computer codes are the Central , Upwind, Hybrid, Linear Upwind and TVD differencing schemes.

Chapter 3 is concerned with the nature of turbulence and necessity of turbulence modelling and a description of the widely used $\kappa$ - $\varepsilon$ and Reynolds Stress/Scalar Flux turbulence models is given.

Chapter 4 is divided into two parts, the first part is concerned with scalar transport equation tests of Hybrid, Linear Upwind and TVD differencing schemes in two simple two-dimensional convection-diffusion problems which are used to test the above discretisation schemes for their boundedness and accuracy. The second part is concerned with modelling the sudden expansion of swirling coaxial water jets studied experimentally by Roback et al(1983). Predictions using the Hybrid and TVD differencing schemes with the $\kappa$ - $\varepsilon$ and Reynolds Stress/Scalar Flux turbulence models are investigated for grid independence and their comparison with the experimental data of Roback et al is presented and discussed.

Chapter 5 opens with a literature survey showing the importance of modelling the impeller region to stirred tank computations and the effect of the different impeller models used by several workers on the accuracy of the calculations compared with experimental data are presented and discussed. Three impeller models which are represented as a quadratic source for the tangential momentum equation are described. These impeller models with the $\kappa$ - $\varepsilon$ and Reynolds Stress/Scalar Flux turbulence models along with the Hybrid and TVD differencing schemes are applied to the modelling of the fluid flow in a fully baffled cylindrical tank stirred by one and two Rushton impellers and the numerical results obtained are compared with the experimental data of Lee(1995).

Chapter 6 start with a discussion of the scalar mixing time in a vessel stirred by a Rushton impeller obtained numerically by Middleton et al(1986) and Ziman(1990). Then three-

dimensional calculations of mixing in a fully baffled cylindrical tank stirred by single Rushton impeller studied experimentally by Distelhoff et al(1996) were carried out using the $\kappa$ - $\varepsilon$ and Reynolds stress/Scalar Flux turbulence models. The velocity fields used in the mixing calculations were obtained using the methods as described in chapter 5. A comparison between the numerical predictions obtained and the experimental data obtained by Distelhoff et al is presented and discussed.

Finally, a brief overview of the work carried out is given in chapter 7, where the findings of the investigation are summarised and recommendations for future work are identified.

# Chapter 2

# Discretisation Schemes

## 2.1 Introduction

The starting point for any flow analysis is always a statement of the conservation equations and boundary conditions governing the process of the interest. The term 'conservation equations' refers to the equations expressing conservation of mass, momentum and energy. This chapter describes a method of solving flows with recirculation, 'elliptic flows', using the finite difference technique. The method can be applied to both laminar and turbulent flow, although for turbulent flow, a turbulence model is required and two possible turbulence models are discussed in a later chapter.

## 2.2 Governing Equations

Considering the steady, three dimensional flow of a Newtonian fluid, in a Cartesian (x,y,z) co-ordinate frame in which the corresponding velocity components of velocity vector $\underline{u}$ are (U, V, W), the non-linear coupled governing equations of motion are

**(a) Conservation of Mass**

$$\frac{\partial(\rho U)}{\partial x} + \frac{\partial(\rho V)}{\partial y} + \frac{\partial(\rho W)}{\partial z} = 0 \qquad (2.1)$$

**(b) Conservation of Momentum**

**X-direction( u - equation)**

$$\frac{\partial(\rho U U)}{\partial x} + \frac{\partial(\rho V U)}{\partial y} + \frac{\partial(\rho W U)}{\partial z} =$$

$$2\frac{\partial}{\partial x}\left(\mu\frac{\partial U}{\partial x}\right) + \frac{\partial}{\partial y}\left[\mu\left(\frac{\partial U}{\partial y} + \frac{\partial V}{\partial x}\right)\right] + \frac{\partial}{\partial z}\left[\mu\left(\frac{\partial U}{\partial z} + \frac{\partial W}{\partial x}\right)\right] - \frac{\partial P}{\partial x} + F_x \qquad (2.2)$$

**Y-direction( v - equation)**

$$\frac{\partial(\rho U V)}{\partial x} + \frac{\partial(\rho V V)}{\partial y} + \frac{\partial(\rho W V)}{\partial z} =$$

$$\frac{\partial}{\partial x}\left[\mu\left(\frac{\partial U}{\partial y} + \frac{\partial V}{\partial x}\right)\right] + 2\frac{\partial}{\partial y}\mu\left(\frac{\partial V}{\partial y}\right) + \frac{\partial}{\partial z}\left[\mu\left(\frac{\partial W}{\partial y} + \frac{\partial V}{\partial z}\right)\right] - \frac{\partial P}{\partial y} + F_y \qquad (2.3)$$

**Z-direction( w - equation)**

$$\frac{\partial(\rho U W)}{\partial x} + \frac{\partial(\rho V W)}{\partial y} + \frac{\partial(\rho W W)}{\partial z} =$$

$$\frac{\partial}{\partial x}\left[\mu\left(\frac{\partial U}{\partial z} + \frac{\partial W}{\partial x}\right)\right] + \frac{\partial}{\partial y}\left[\mu\left(\frac{\partial V}{\partial z} + \frac{\partial W}{\partial y}\right)\right] + 2\frac{\partial}{\partial z}\left[\mu\left(\frac{\partial W}{\partial z}\right)\right] - \frac{\partial P}{\partial z} + F_z \qquad (2.4)$$

where $\rho$, $\mu$ and P are the fluid density, viscosity and static pressure respectively and $F_x$, $F_y$ and $F_z$ are body forces terms.

**(C) Conservation of Energy/Chemical Species ('Scalars')**

$$\frac{\partial}{\partial x}(\rho U \Phi) + \frac{\partial}{\partial y}(\rho V \Phi) + \frac{\partial}{\partial z}(\rho W \Phi) =$$

$$\frac{\partial}{\partial x}\left(\Gamma \frac{\partial \Phi}{\partial x}\right) + \frac{\partial}{\partial y}\left(\Gamma \frac{\partial \Phi}{\partial y}\right) + \frac{\partial}{\partial z}\left(\Gamma \frac{\partial \Phi}{\partial z}\right) + B_\Phi - Q_\Phi \Phi \qquad (2.5)$$

where $\Gamma = \mu / \sigma$ is the transport diffusion coefficient for $\Phi$ and $\sigma$ is the appropriate Prandtl/Schmidt number and $B_\Phi$ and $Q_\Phi$ are source terms. $\Phi$ can stand for any scalar quantity which is transported, i,e. convected or diffused such as chemical-species mass fraction and turbulence energy.

## 2.3 Finite Difference Approximations

An analytical solution to the above equations cannot in general be found because of the non-linear coupled nature of the set of partial differential equations and so numerical solution procedures offer the only practical method of obtaining solutions to these equations. In this work, the numerical approximations to the governing set of partial differential equations are generated by the method of finite differences, where the domain over which a solution of the flow equations is sought is discretised so that the dependent variables are considered to exist at discrete points. The discretisation techniques which are discussed later in this chapter will replace the set of non-linear partial differential equations with a set of non-linear algebraic equations which can be solved. There are a number of methods of devising finite difference approximations, for example, Taylor series

expansion, Polynomial fitting and the Macro-integral/control volume techniques. of which the later is used in this work. Conservation, consistency, accuracy and boundedness are important factors for finite difference approximation and these are discussed below.

*Conservation*

The scalar transport equation (2.5) is a conservation law for the quantity Φ. This means that the rate at which Φ enters an arbitrary volume by convection and diffusion is equal to the rate of accumulation of Φ and the source of Φ in that volume. The solution of a discretised scheme should therefore be conservative over the finite volume. However, it is necessary to know that the conservation principle does not simply require that Φ be conserved in a single finite volume, but that Φ is conserved 'between' adjoining volumes to ensure that the solution is globally conservative. Therefore the flux leaving one cell through any face must be identical to that entering the next cell through the same face.

*Consistency*

Consistency requires that the solution of the discrete equations should be the solution of the governing equations. If a discretisation technique does not have this important property then it is not really solving the problem posed but some other problem. Consistency should be verified by examining the solution scheme or procedure to ensure that it is consistent with the original equations.

A Taylor series is usually used for the purpose of examining consistency, which means that discrete terms are related to their continuous counterparts and the governing equations are reconstructed.

*Accuracy*

If the finite difference form of the partial derivatives given above are derived using the Taylor series expansions a truncation error of magnitude $\delta$, $\delta^2$, $\delta^3$ etc. is developed. If

the scheme has a truncation error of magnitude $\delta$ , then the scheme is known as a first order accurate scheme. If the truncation error is of magnitude $\delta^2$, then the scheme is of a second order accuracy and so on. The Taylor series does not give definitive estimates of errors on finite meshes and it does not enable one to derive usable schemes of arbitrary accuracy.

The matter of what degree of accuracy is desirable depends on the type of problem being solved, for example, in some cases a higher accuracy may require more grid points, resulting in more computer time required for each spatial step, however, in other cases a higher accuracy may require a smaller number of total grid points in a flow solution to obtain comparable overall accuracy Anderson(1995).

***Boundedness***

It is known that when a simple convection-diffusion problem is being solved, the maximum and minimum values occur on the boundary of the solution domain. When the algebraic equations of the differencing scheme being used reflect this property, the differencing scheme is referred to as being bounded. Lack of boundedness is an important issue, an unbounded scheme usually manifests itself as wiggles in the solution with successive nodes being alternately high and low. This problem might be acceptable in some circumstances, when the oscillation magnitude is very small. However, there are serious consequences of lack of boundedness, for example, a physical property such as concentration is required to be unconditionally positive to be physically realistic; an unbounded scheme may produce negative values. Convergence difficulties may also arise with a lack of boundedness.

## 2.4 Discretisation Technique

This section is concerned with the steps followed to derive the finite difference approximation which can be summarised as follows:

i) A computational grid and control volume are constructed.
ii) The volume integration of the governing equations of motion over a typical control volume is performed.
iii) The integrals of step two are expressed in terms of the surrounding nodel values.

The location of the dependent variables on the computational mesh adopts are of two arrangements colocated or staggered. In the colocated arrangement, all variables are stored at the same set of grid points and the same control volumes for all variables are used. This approach tends to minimize the coefficient storage and simplify the programming particularly in complex solution domains. This type of arrangement was not used for a long time for incompressible flow computation due to the difficulties with pressure-velocity coupling and the occurrence of oscillations in the pressure (Harlow and Welsh, 1965). However, the development of improved pressure-velocity coupling algorithms in the 1980's has led to the increased use of the colocated arrangements.

The staggered grid arrangement made popular by Harlow and Welsh(1965) offers several advantages over the colocated arrangement and is used in this study. The staggered grid arrangement shown in figure 2.1, where the values of velocity U and V are stored at locations midway between the nodes is used. Many terms that require interpolation with the colocated arrangement, can be calculated using the staggered grid arrangement to a second-order approximation without interpolation. The pressure and diffusion terms are naturally approximated by central differences approximations without interpolation, since the pressure nodes lie at the control face centres and the velocity derivatives needed for the diffusive terms are readily calculated at the control volume faces

as shown in figure 2.2. The main advantage of this type of grid arrangement is the strong coupling between the velocities and the pressure, which helps to avoid some types of convergence problems and oscillations in the pressure and velocity fields.

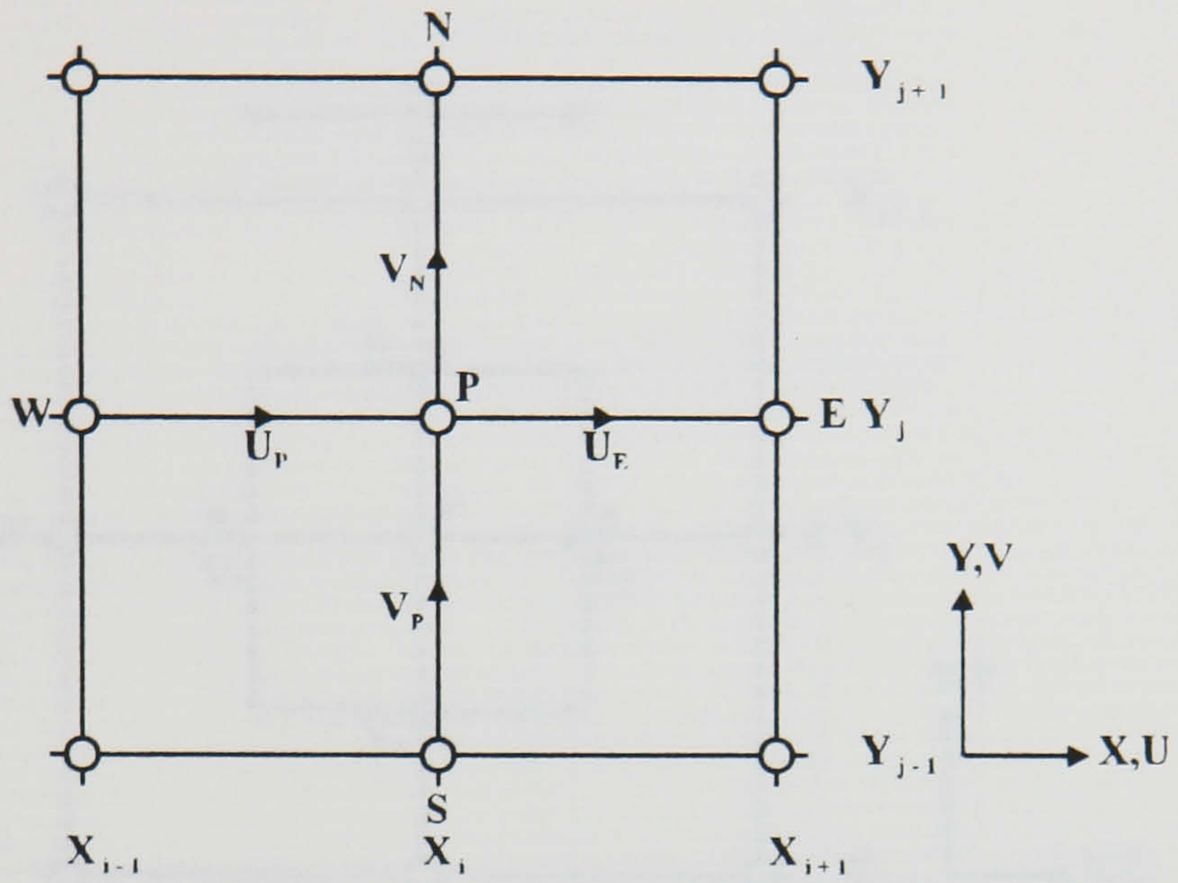



Figure.2.1. Velocity values are stored midway between pressure nodes.

However, the use of a staggered grid arrangement requires the construction of several control volumes (one control volume for each equation to be numerically solved). For example, four control volumes are needed for U, V, W and Φ, if three dimensions are being considered and three control volumes for U, V and Φ if two dimensions are constructed.

## 2.5 Scalar Transport Equation

This section is concerned with the discretisation of the scalar transport equation, the Momentum and Continuity equations can be treated in a similar manner, equation 2.5, in 2-D flows can be written in the following general form

$$\frac{\partial \rho U\Phi}{\partial x}+\frac{\partial \rho V\Phi}{\partial y}-\Phi\left[\frac{\partial \rho U}{\partial x}+\frac{\partial \rho V}{\partial y}\right]=\frac{\partial}{\partial x}\left(\Gamma\frac{\partial \Phi}{\partial x}\right)+\frac{\partial}{\partial y}\left(\Gamma\frac{\partial \Phi}{\partial y}\right)+B_{\Phi}-Q_{\Phi}\Phi \qquad (2.6)$$

This equation is discretised by integrating over the control volume shown in figure 2.2, whose surfaces lie mid way between the mesh lines.

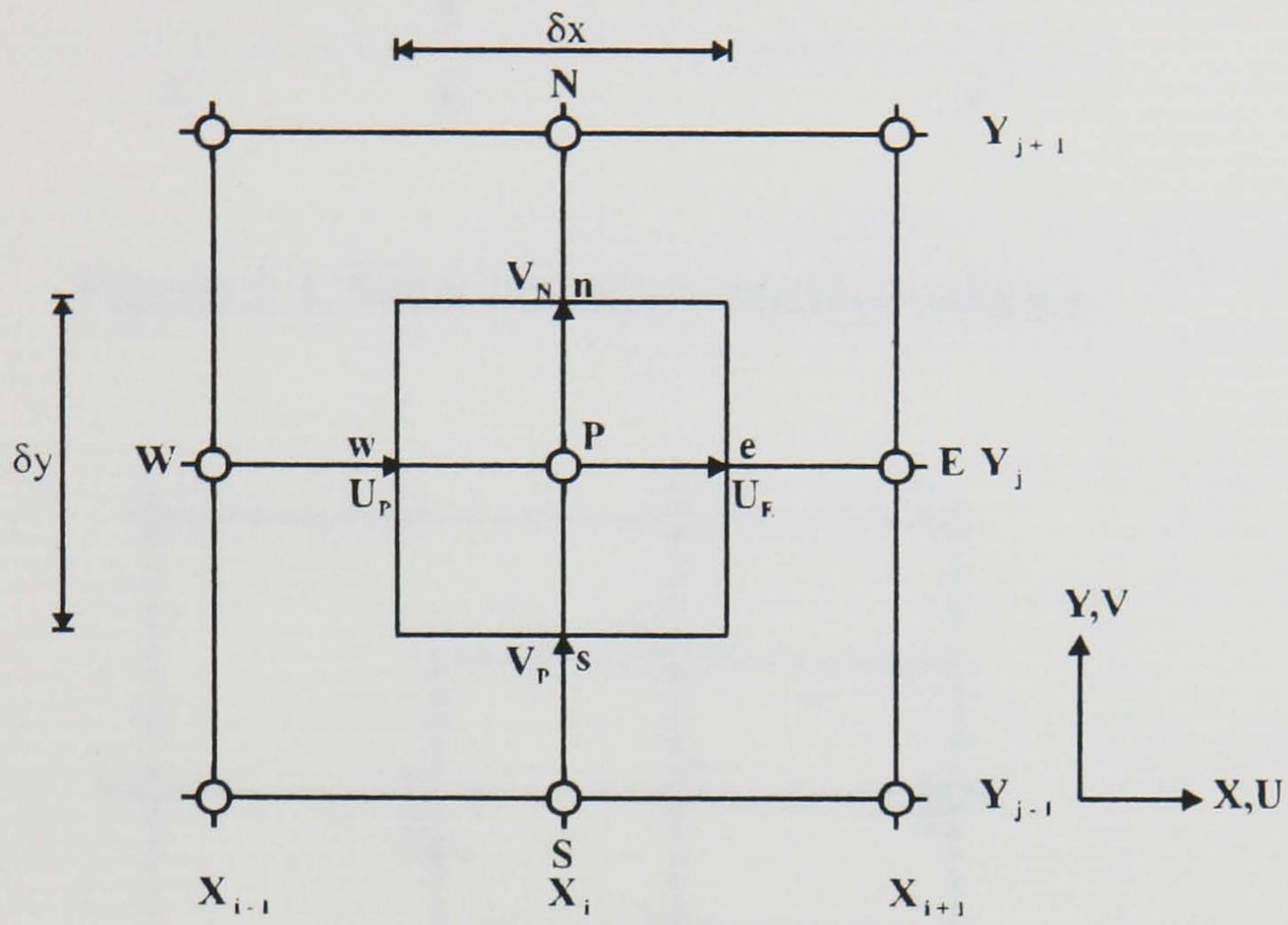



Figure.2.2. A typical control volume.

The node within the cell is labeled P and its neighbours are given the labels N, S, W and E. Cell surfaces are denoted by lower case versions of the adjacent node labels, i.e., n, s, e and w. The mesh arrangements for the east and west boundaries are shown in figures 2.3 and 2.4 respectively. The control volume is extended to the boundaries and values of U, $\rho$, $\Gamma$ and $\Phi$ are all stored on the boundary mesh line. East and west cells will be considered through the rest of this study, north and south boundary cells can be treated by analogy. Since, east and west boundaries are considered here, then modifications only needed on the terms involving the x-derivatives.

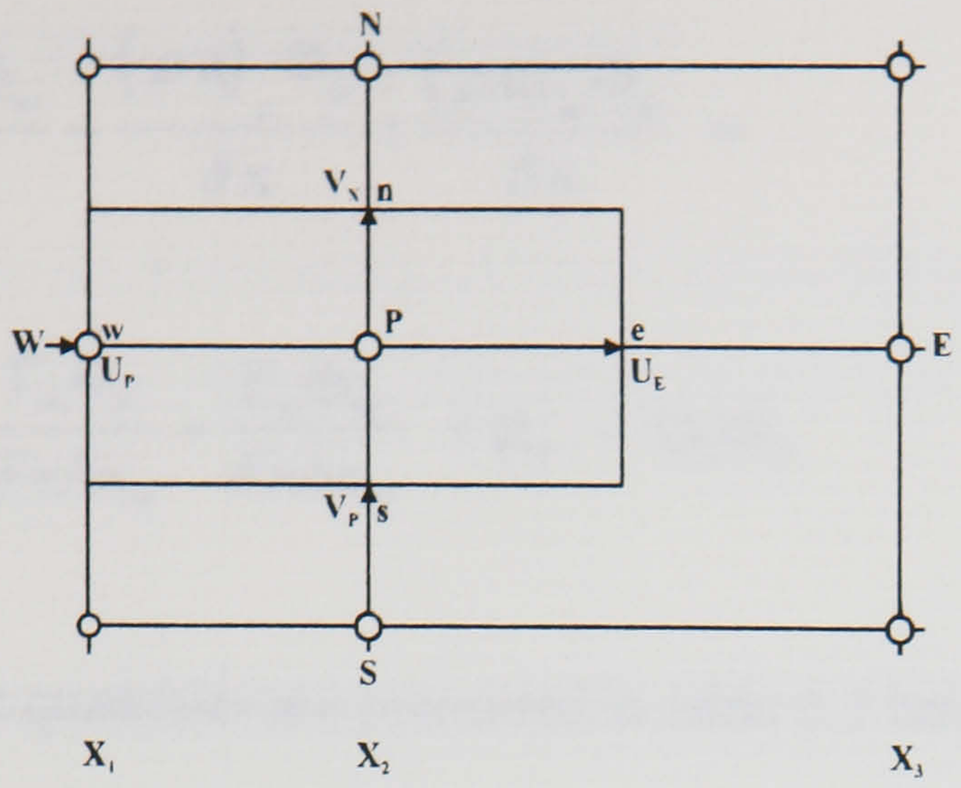



Figure.2.3. West boundary control volume.

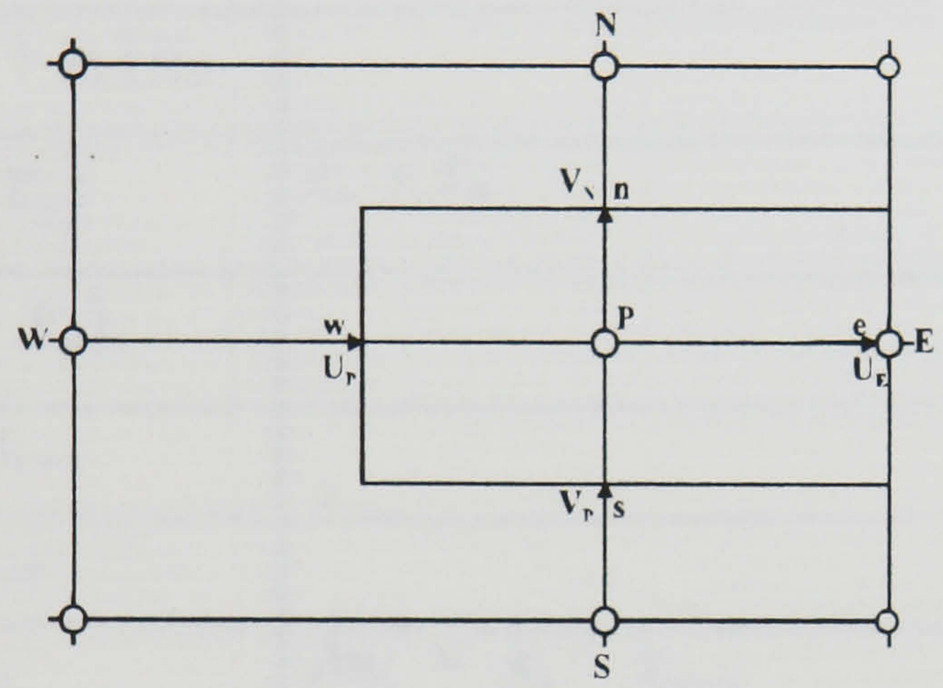



Figure.2.4. East boundary control volume.

On integrating the scalar equation the following are assumed:

i) The sources terms B and Q are assumed constant over the control volume.
ii) The dependent variables, such as velocity, are assumed to vary linearly between node points, but to be constant over each surface of the control volume.

After integration the scalar equation for the east and west directions is rewritten in the following form

$$\frac{(\rho u)_e \Phi_e - (\rho u)_w \Phi_w}{\delta x} - \frac{(\rho u)_e \Phi_p}{\delta x} + \frac{(\rho u)_w \Phi_p}{\delta x} =$$

$$\frac{\Gamma_e \Phi_E}{\delta x \Delta x_e} - \frac{\Gamma_e \Phi_p}{\delta x \Delta x_e} - \frac{\Gamma_w \Phi_p}{\delta x \Delta x_p} + \frac{\Gamma_w \Phi_W}{\delta x \Delta x_p} + B_P - Q_P \Phi_P \qquad (2.7)$$

where the coefficient quantities are presented in table 2.1 below.

| **Midnode Cell** | **East Boundary Cell** | **West Boundary Cell** |
|---|---|---|
| $(\rho u)_e = 0.5(\rho_E + \rho_P) U_E$ | $(\rho u)_e = \rho_E U_E$ | |
| $(\rho u)_w = 0.5(\rho_W + \rho_P) U_P$ | | $(\rho u)_w = \rho_W U_P$ |
| $\Gamma_e = 0.5(\Gamma_E + \Gamma_P)$ | $\Gamma_e = \Gamma_E$ | |
| $\Gamma_w = 0.5(\Gamma_W + \Gamma_P)$ | | $\Gamma_w = \Gamma_W$ |
| $\Delta x_{ee} = x_{i+2} - x_{i+1}$ | | |
| $\Delta x_w = x_{i-1} - x_{i-2}$ | | |
| $\Delta x_e = x_{i+1} - x_{i-1}$ | $\Delta x_e = x_n - x_{n-1}$ | |
| $\Delta x_p = x_i - x_{i-1}$ | $\Delta x_p = x_{n-1} - x_{n-2}$ | $\Delta x_p = x_2 - x_1$ |
| $\delta x = \frac{x_{i+1} - x_{i-1}}{2}$ | $\delta x = x_n - \left(\frac{x_{n-1} + x_{n-2}}{2}\right)$ | $\delta x = \left(\frac{x_3 + x_2}{2}\right) - x_1$ |

Table 2.1. Coefficient quantities.

The use of Central differencing for the diffusion terms results in schemes that are both consistent and stable, however, if Central differencing is used for convection terms stability problems may arise. In the following section a number of alternative differencing procedures are presented and discussed.

## 2.6 Formulation of Discretisation Schemes

This section presents the formulation of the Central differencing, Upwind differencing. Hybrid differencing, Linear Upwind differencing and Total Variation Diminishing (TVD) discretisation schemes.

### 2.6.1 Central Differencing (CD)

Central differencing scheme(Thom, 1933) is second order accurate and corresponds to linear interpolation between the nodes within the cell labeled P and its neighbors N, S, W and E shown in figure 2.2. In this scheme, the diffusion discretisation coefficients fails to provide an over all diagonal dominance and boundedness and stability problems arise, if the Peclet number ( $\rho |u| \delta x / \Gamma$ or $\rho |v| \delta y / \Gamma$) is greater than 2 and has been observed by Timin and Esmail(1983), Shyy and Correa(1985) and Patel and Markatos(1986).

**Midnode Cell Formulation**

$$\Phi_e = \frac{\Phi_E + \Phi_p}{2}; \qquad \Phi_w = \frac{\Phi_p + \Phi_w}{2}$$

After substituting the expression $\Phi_e$ and $\Phi_w$ into equation (2.7) and with some arrangement the final equation is of the form

$$A_P \Phi_P = A_E \Phi_E + A_W \Phi_W + B_P \qquad (2.8)$$

where

$$A_E = \frac{1}{\delta x}\left(\frac{\Gamma_e}{\Delta x_e} - \frac{(\rho u)_e}{2}\right); \qquad A_W = \frac{1}{\delta x}\left(\frac{\Gamma_w}{\Delta x_p} + \frac{(\rho u)_w}{2}\right)$$

$$A_p = \sum_{\alpha = E,W} A_\alpha + Q_P$$

## Boundary Cell Formulation

### West Boundary

$$\Phi_e = \frac{\Phi_E + \Phi_p}{2} \; ; \qquad \Phi_w = \Phi_W$$

Substituting $\Phi_e$ and $\Phi_w$ into equation (2.7). Then the coefficient at the west boundary $A_w$ is expressed as

$$A_w = \frac{1}{\delta x}\left(\frac{\Gamma_w}{\Delta x_p} + (\rho u)_w\right)$$

For the node points adjacent to the boundary at x = w, it is only the coefficient $A_w$ which will differ from its interior node form.

### East Boundary

$$\Phi_e = \Phi_E \; ; \qquad \Phi_w = \frac{\Phi_p + \Phi_E}{2}$$

Substituting $\Phi_e$ and $\Phi_w$ into equation (2.7) and with some arrangement the east boundary coefficient $A_E$ can be expressed as

$$A_E = \frac{1}{\delta x}\left(\frac{\Gamma_e}{\Delta x_e} - (\rho u)_e\right)$$

For the node points adjacent to the boundary at x = e, $A_E$ is the only coefficient which will differ from its interior node form.

### 2.6.2 Upwind Differencing (UD)

This differencing scheme overcomes the loss of diagonal dominance by approximating the mid point values using the node immediately adjacent to and upstream of the mid point. This scheme is always stable and bounded and solutions are readily achievable in practice. However, in multidimensional high Peclet number problems where the flow is not aligned with the mesh, then Upwind differencing exhibits a phenomenonknown as numerical diffusion which seriously degrades the accuracy of the solution. This behavior is observed by Atias et al(1977), Leschziner(1980), Smith and Hutton(1982) and Hassan and Kim (1985a).

The impact of numerical diffusion on the accuracy obtained in practice varies depending on the problem being solved and the computational mesh being used. The numerical diffusion will effect the accuracy of the computations when the convection terms are dominant in the computation.

**Midnode Cell Formulation**

$$\Phi_e = \Phi_P \qquad U > 0.0$$

$$\Phi_w = \Phi_W$$

$$\Phi_e = \Phi_E \qquad U < 0.0$$

$$\Phi_w = \Phi_P$$

After substituting $\Phi_e$ and $\Phi_w$ values into equation number (2.7), the coefficient $A_E$ and $A_W$ are

$$A_E = \frac{\Gamma_e}{\delta x \, \Delta x_e} \qquad U > 0.0$$

$$A_W = \frac{1}{\delta x}\left(\frac{\Gamma_w}{\Delta x_p} + (\rho u)_w\right)$$

$$A_E = \frac{1}{\delta x}\left(\frac{\Gamma_e}{\Delta x_e} - (\rho u)_e\right)$$

$$A_W = \frac{\Gamma_w}{\delta x \, \Delta x_p}$$

**Boundary Cell Formulation**

**West Boundary**

$\Phi_e = \Phi_P$ $\quad U > 0.0$

$\Phi_w = \Phi_W$

$\Phi_e = \Phi_E$ $\quad U < 0.0$

$\Phi_w = \Phi_W$

After substituting the above values into equation (2.7), $A_W$ can be written as

$$A_W = \frac{1}{\delta x}\left(\frac{\Gamma_w}{\Delta x_p} + (\rho u)_w\right)$$

**East Boundary**

$\Phi_e = \Phi_E$ $\quad U > 0.0$

$\Phi_w = \Phi_W$

$\Phi_e = \Phi_E$ $\quad U < 0.0$

$\Phi_w = \Phi_P$

After substituting the above values into equation (2.7), $A_E$ can be written as

$$A_E = \frac{1}{\delta x}\left(\frac{\Gamma_e}{\Delta x_e} - (\rho u)_e\right)$$

### 2.6.3 Hybrid Differencing

This technique simply results in a switching from central to upwind differencing of the convection term plus neglecting the diffusion term in the direction considered, where-ever the Peclet number is greater than two (Spalding , 1972). The solution utilized in this work is to add a numerical contribution to the physical transport coefficient, $\Gamma$, which is sufficient enough to preserve the positive nature of the coefficients $A_E$ and $A_w$ and is written in the following general form

$$\Gamma = \text{Max}\left\{\frac{|\rho u|}{2}, \Gamma\right\}$$

The resulting scheme is more accurate than Upwind differencing when the Peclet number is less than two and is always bounded. However, the above has the effect of switching to the lower order scheme for the convection terms just as the convection terms are becoming dominant and so at high Peclet numbers numerical diffusion dominates and smearing of features takes place (particularly in regions of skewed flow). The Hybrid scheme has been tested and compared against other schemes by many authors including Roache(1972), Hah(1983), Shyy and Correa(1985), Claus et al(1985) and Joseph(1983).

### 2.6.4 Linear Upwind Differencing (LUD)

Linear Upwind differencing is a second order accurate scheme, which was originally introduced in a finite difference context by Price et al(1966) and uses the additional nodes EE, WW, NN and SS. The scheme corresponds to the extrapolation of $\Phi_e$ or $\Phi_w$ from the two nodes immediately upstream as shown below. In one dimension Linear Upwind differencing is unconditionally bounded, but it is not bounded for unsteady problems

(Shyy, 1984) or multidimensional problems. Atias et al(1977) indicated that it is more accurate than Upwind differencing and frequently nearly as accurate as Central differencing. Atias et al also noted that Linear Upwind differencing was least accurate on coarse meshes at high Reynolds numbers.

Shyy(1983, 1984), Shyy and Correa(1985) and Castro and Jones(1987) performed several scalar transport and laminar flow tests with Linear Upwind differencing and other popular schemes. They found that Linear Upwind differencing was generally the best scheme even though boundedness problems were reported. Wilkes and Thompson(1983) concluded that Linear Upwind differencing is more accurate but required about 60% more computer time than Upwind differencing.

**Midnode Cell Formulation**

$$\Phi_e = \frac{\Delta x_e}{\Delta x_p}\left(\frac{\Phi_P - \Phi_W}{2}\right) + \Phi_P \qquad U > 0.0$$

$$\Phi_w = \frac{\Delta x_p}{\Delta x_w}\left(\frac{\Phi_W - \Phi_{WW}}{2}\right) + \Phi_W$$

$$\Phi_e = \Phi_E - \frac{\Delta x_e}{\Delta x_{ee}}\left(\frac{\Phi_{EE} - \Phi_E}{2}\right) \qquad U < 0.0$$

$$\Phi_w = \Phi_P - \frac{\Delta x_p}{\Delta x_e}\left(\frac{\Phi_E - \Phi_P}{2}\right)$$

By substituting into equation (2.7) $A_E$, $A_W$, $A_{EE}$ and $A_{WW}$ coefficients are written in the following form

$$A_E = \frac{\Gamma_e}{\delta x \, \Delta x_e}$$

$$U > 0.0$$

$$A_{WW} = -\frac{1}{2}\left(\frac{(\rho u)_w \, \Delta x_p}{\delta x \, \Delta x_w}\right)$$

$$A_W = \frac{1}{\delta x}\left(\frac{\Gamma_w}{\Delta x_p} + \frac{(\rho u)_e \, \Delta x_e}{2 \, \Delta x_p} + \frac{(\rho u)_w \, \Delta x_p}{2 \, \Delta x_w} + (\rho u)_w\right)$$

$$A_W = \frac{\Gamma_w}{\delta x \, \Delta x_p}$$

$$U < 0.0$$

$$A_{EE} = \frac{(\rho u)_e \, \Delta x_e}{2 \, \delta x \, \Delta x_{ee}}$$

$$A_E = \frac{1}{\delta x}\left(\frac{\Gamma_e}{\Delta x_e} - \frac{(\rho u)_e \, \Delta x_e}{2 \, \Delta x_{ee}} - \frac{(\rho u)_w \, \Delta x_p}{2 \, \Delta x_e} - (\rho u)_e\right)$$

then equation (2.8) will be rewritten as

$$A_P \, \Phi_P = A_W \, \Phi_W + A_{WW} \, \Phi_{WW} + A_E \, \Phi_E + A_{EE} \, \Phi_{EE} + B_P$$

where

$$A_P = Q_P + \sum_{\alpha = W,E,WW,EE} A_\alpha$$

## Boundary Cell Formulation

## West Boundary

$$\Phi_e = \frac{\Delta x_e}{\Delta x_p}\left(\frac{\Phi_P - \Phi_W}{2}\right) + \Phi_P$$

$$U > 0.0$$

$$\Phi_w = \Phi_W$$

$$\Phi_e = \Phi_E - \frac{\Delta x_e}{\Delta x_{ee}}\left(\frac{\Phi_{EE} - \Phi_E}{2}\right)$$

$U < 0.0$

$$\Phi_w = \Phi_W$$

After substituting the above values into equation (2.7), $A_W$ and $A_{WW}$ are the only coefficients which will differ from their interior node form and are written as

$$A_W = \frac{1}{\delta x}\left(\frac{\Gamma_w}{\Delta x_p} + \frac{(\rho u)_e \Delta x_e}{2\,\Delta x_p} + (\rho u)_w\right)$$

$U > 0.0$

$$A_{WW} = 0.0$$

$$A_W = \frac{\Gamma_w}{\delta x\,\Delta x_p}$$

$U < 0.0$

$$A_{WW} = 0.0$$

**East Boundary**

$$\Phi_e = \Phi_E$$

$U > 0.0$

$$\Phi_w = \frac{\Delta x_p}{\Delta x_w}\left(\frac{\Phi_W - \Phi_{WW}}{2}\right) + \Phi_W$$

$$\Phi_e = \Phi_E$$

$U < 0.0$

$$\Phi_w = \Phi_p - \frac{\Delta x_p}{\Delta x_e}\left(\frac{\Phi_E - \Phi_P}{2}\right)$$

After substituting the above values into equation (2.7), $A_E$ and $A_{EE}$ are the only coefficients which will differ from their interior node form and are expressed as

$$A_E = \frac{\Gamma_e}{\delta x \, \Delta x_e}$$

$U > 0.0$

$A_{EE} = 0.0$

$$A_E = \frac{1}{\delta x}\left(\frac{\Gamma_e}{\Delta x_e} - \frac{(\rho u)_w \, \Delta x_p}{2 \, \Delta x_e} - (\rho u)_e\right)$$

$U < 0.0$

$A_{EE} = 0.0$

### 2.6.5 Total Variation Diminishing (TVD)

Total variation diminishing schemes have been devised for Gas Dynamics problems and employ flux limiters for the purpose of producing a high resolution schemes without the spurious oscillations associated with the more classical second order schemes. Flux limiters are nonlinear functions used to limit gradients by modifying the flux terms in the difference equations (Anderson, 1995). A wide range of TVD schemes are available in the literature, but that of Van Leer(1974) is presented here. The TVD scheme has been demonstrated to yield low-diffusive and accurate solutions and applied successfully to the calculations of two and three-dimensional turbulent flows, e.g. Fairweather et al(1988) and Alvarez(1994).

## Midnode Cell Formulation

$$\Phi_e = \Phi_P + \Psi_e\left(\frac{\Phi_E - \Phi_P}{2}\right)$$

$$\Phi_w = \Phi_W + \Psi_w\left(\frac{\Phi_P - \Phi_W}{2}\right)$$

$$U > 0.0$$

$$R_e = \frac{\left(\Phi_P - \Phi_W\right)\left(x_{i+1} - x_i\right)}{\left(\Phi_E - \Phi_P\right)\left(x_i - x_{i-1}\right)}$$

$$R_w = \frac{\left(\Phi_W - \Phi_{WW}\right)\left(x_i - x_{i-1}\right)}{\left(\Phi_P - \Phi_W\right)\left(x_{i-1} - x_{i-2}\right)}$$

$$\Phi_e = \Phi_E + \Psi_e\left(\frac{\Phi_P - \Phi_E}{2}\right)$$

$$\Phi_w = \Phi_P + \Psi_w\left(\frac{\Phi_W - \Phi_P}{2}\right)$$

$$U < 0.0$$

$$R_e = \frac{\left(\Phi_E - \Phi_{EE}\right)\left(x_{i+1} - x_i\right)}{\left(\Phi_P - \Phi_E\right)\left(x_{i+2} - x_{i+1}\right)}$$

$$R_w = \frac{\left(\Phi_P - \Phi_E\right)\left(x_i - x_{i-1}\right)}{\left(\Phi_W - \Phi_P\right)\left(x_{i+1} - x_i\right)}$$

where the limiter ,$\Psi$, is given in the following general form

$$\Psi_\alpha = \frac{R_\alpha + \left|R_\alpha\right|}{1 + \left|R_\alpha\right|}$$

where $\alpha$ = e, w, n and s. By substituting the above values into equation (2.7), then $A_E$ and $A_W$ coefficients are written in the following form

$$A_E = \frac{1}{\delta x}\left(\frac{\Gamma_e}{\Delta x_e} - \frac{(\rho u)_e \Psi_e}{2}\right) \qquad U > 0.0$$

$$A_W = \frac{1}{\delta x}\left(\frac{\Gamma_w}{\Delta x_p} - \frac{(\rho u)_w \Psi_w}{2} + (\rho u)_w\right)$$

$$A_E = \frac{1}{\delta x}\left(\frac{\Gamma_e}{\Delta x_e} + \frac{(\rho u)_e \Psi_e}{2} - (\rho u)_e\right) \qquad U < 0.0$$

$$A_W = \frac{1}{\delta x}\left(\frac{\Gamma_w}{\Delta x_p} + \frac{(\rho u)_w \Psi_w}{2}\right)$$

**West Boundary**

$$\Phi_e = \Phi_P + \Psi_e\left(\frac{\Phi_E - \Phi_P}{2}\right) \qquad U > 0.0$$

$$\Phi_w = \Phi_W$$

$$\Phi_e = \Phi_E + \Psi_e\left(\frac{\Phi_P - \Phi_E}{2}\right) \qquad U < 0.0$$

$$\Phi_w = \Phi_W$$

By substituting the above values into equation (2.7), where $A_W$ is the only coefficient which will differ from its interior node form and is expressed as

$$A_W = \frac{1}{\delta x}\left(\frac{\Gamma_w}{\Delta x_p} + (\rho u)_w\right)$$

**East Boundary**

$$\Phi_e = \Phi_E$$

$$\Phi_w = \Phi_W + \Psi_w \left( \frac{\Phi_P - \Phi_W}{2} \right) \qquad U > 0.0$$

$$\Phi_e = \Phi_E$$

$$\Phi_w = \Phi_P + \Psi_w \left( \frac{\Phi_W - \Phi_P}{2} \right) \qquad U < 0.0$$

By substituting the above values into equation (2.7), where $A_E$ is the only coefficient which differ from its interior node form and it is expressed as

$$A_E = \frac{1}{\delta x} \left( \frac{\Gamma_w}{\Delta x_e} + (\rho u)_e \right)$$

## 2.7 Summary

In this chapter, the general principle behind finite difference approximation along with some important factors such as conservation, consistency, accuracy and boundedness were briefly described. The rest of this chapter was focused on the formulation of Central, Upwind, Hybrid, Linear Upwind and TVD differencing schemes along with a discussion of their suitability for use in computer codes. Accuracy and boundedness tests of the latter three discretisation schemes are discussed in sections 4.1 and 4.2.

# Chapter 3

# Turbulence and Turbulence Modelling

## 3.1 Introduction

Most flows encountered in nature and in engineering practice are turbulent. The water currents below the surface of the oceans are turbulent, the flow of water in rivers and canals is turbulent, the flow of natural gas and oil in pipelines is turbulent, combustion processes depend on turbulence, chemical engineers use turbulence to mix and homogenise fluid mixtures and to accelerate chemical reaction rates in liquids or gases. Turbulence is a fact of life.

Many people have tried to give a definition for turbulence, Taylor(1937) and Von Karman(1930) have introduced turbulence as an irregular motion which in general makes its appearance in fluids, gaseous or liquids, when they flow past solid surfaces or even when neighbouring streams of the same fluid flow over one another. Hinze(1959) defined turbulence as an irregular condition of flow in which the various quantities show a random variation with time and space co-ordinates. Tennekes and Lumley(1992) indicated that it is

very difficult to give a precise definition of turbulence and all one can do is list some of the characteristics of turbulent flows. One main characteristic of turbulence is irregularity or randomness. Another important feature of turbulent flows is diffusivity, which causes rapid mixing and increases the rates of momentum, heat and mass transfer. Reynolds(1883) demonstrated that an important nondimensional parameter that determines the kind of flow that can be sustained is

$$R_e = U\, d\, /\, \nu$$

where U is the ( bulk ) velocity, d the diameter in a pipe and $\nu$ the kinematic viscosity. He found that turbulent flow could be sustained only for $R_e$ greater than about 2300, a value known as the critical Reynolds number. Turbulent flows are dissipative in nature, viscous shear stresses perform deformation work, which increases the internal energy and so turbulence needs a continuous supply of energy to make up for these viscous losses. If no energy is supplied, turbulence decays rapidly. Turbulence is also known to be a feature of fluid flow but not of fluids, for example, if the Reynolds number of turbulence is large enough, the major characteristics of turbulent flows are not controlled by the molecular properties of the fluid in which turbulence occurs.

The equations of motion given in the previous chapter are, in principle, capable of describing the motion of a fluid in both laminar and turbulent flow. In laminar flows the resolution of the smallest motions can be attained with a reasonable number of discretisation points, however, this is not possible for turbulent flows, because the smallest length and time scales are much smaller than in the laminar case. To circumvent the problem of having to resolve the smallest length and time scales of turbulent motion a statistical approach is adopted. This statistical approach makes use of mean properties whose length and time scales are an order of magnitude greater than those of the turbulence. However, the statistical approach, originated by Reynolds(1894), produces a set of averaged equations in which there are more unknown terms than there are

equations. The main objective of turbulence modelling is to close the equation set by expressing these new unknowns in terms of known variables.

## 3.2 Turbulence Modelling

### Equations of Motion

The instantaneous conservation equations of motion for an incompressible Newtonian fluid with constant density and viscosity in tensor notation are

### Continuity

$$\frac{\partial U_i}{\partial x_i} = 0 \qquad (3.1)$$

### Momentum

$$\frac{\partial \rho U_i}{\partial t} + \frac{\partial \rho U_i U_\iota}{\partial x_\iota} = \frac{\partial}{\partial x_\iota}\left\{\mu \frac{\partial U_i}{\partial x_\iota}\right\} - \frac{\partial P}{\partial x_i} + F_i \qquad (3.2)$$

### Scalar Conservation

$$\frac{\partial \rho \Phi}{\partial t} + \frac{\partial \rho \Phi U_\iota}{\partial x_\iota} = \frac{\partial}{\partial x_\iota}\left\{\frac{\mu}{\sigma}\frac{\partial \Phi}{\partial x_\iota}\right\} + S_\Phi \qquad (3.3)$$

The commonly adopted approach to the solution of the turbulence field is to decompose the instantaneous quantities U, P and Φ into their time averaged and fluctuating components which can be written as

$$U_i = \overline{U_i} + u_i \quad , \quad P = \overline{P} + p \quad , \quad \Phi = \overline{\Phi} + \phi$$

where an overbar denotes the time averaged quantity and the lower case letters denote the fluctuating component. The time average is defined by

$$\overline{U_i} = \lim_{T \to \infty} \frac{1}{T} \int_t^{t+T} U_i dt \tag{3.4}$$

where the time T represents the interval over which the averaging is to be carried out, which is large compared with turbulent time scale. The average of the fluctuating quantity itself is zero by definition

$$\overline{u_i} = \lim_{T \to \infty} \frac{1}{T} \int_t^{t+T} u_i dt = 0 \tag{3.5}$$

Using the above definitions, the averages of products and summations of correlated variables are computed in the following way

$$\overline{U_i + U_j} = \overline{U_i} + \overline{U_j}$$

$$\overline{U_i U_j} = \left(\overline{U_i + u_i}\right)\left(\overline{U_j + u_j}\right) = \overline{U_i}\,\overline{U_j} + \overline{U_i u_j} + \overline{u_i U_j} + \overline{u_i u_j} = \overline{U_i}\,\overline{U_j} + \overline{u_i u_j}$$

The terms consisting of a product of a mean and fluctuation disappears when averaged and the average of any individual fluctuating quantity is zero.

By substituting the above definitions into the instantaneous conservation equations of motion, the time averaged conservation equations of motion can be written as

**Continuity**

$$\frac{\partial \overline{U_i}}{\partial x_i} = 0 \qquad (3.6)$$

**Momentum**

$$\frac{\partial \rho \overline{U_i}}{\partial t} + \frac{\partial \rho \overline{U_i}\,\overline{U_\iota}}{\partial x_\iota} = \frac{\partial}{\partial x_\iota}\left\{\mu \frac{\partial \overline{U_i}}{\partial x_\iota}\right\} - \frac{\partial \bar{P}}{\partial x_i} - \frac{\partial \rho \overline{u_i u_\iota}}{\partial x_\iota} + \rho F_i \qquad (3.7)$$

**Scalar Conservation**

$$\frac{\partial \rho \bar{\Phi}}{\partial t} + \frac{\partial \rho \bar{\Phi}\,\overline{U_\iota}}{\partial x_\iota} = \frac{\partial}{\partial x_\iota}\left\{\frac{\mu}{\sigma}\frac{\partial \bar{\Phi}}{\partial x_\iota}\right\} - \frac{\partial \rho \overline{u_\iota \phi}}{\partial x_\iota} + \overline{S_\Phi} \qquad (3.8)$$

Comparing the equations of motion (3.1, 3.2 and 3.3) to the set of averaged equations (3.6, 3.7 and 3.8), a number of similarities are observed, however, unknown terms, $\rho \overline{u_i u_\iota}$ and $\rho \overline{u_\iota \phi}$, have appeared due to the averaging process; these terms are known as the Reynolds Stresses and the Scalar Fluxes respectively.

The appearance of the unknowns Reynolds Stresses and Scalar Fluxes terms has increased the number of unknowns beyond the number of equations in the original set of equations; the specification of these unknowns is the basis of turbulence modelling. These unknowns may be specified algebraically, this is the basis of eddy viscosity models, or may be determined by the solution of a transport equation, this is the basis of Reynolds Stress and Scalar Flux models.

**In order to facilitate the description of each type of model below the over bars on capital letters will be dropped.**

## 3.3 Eddy Viscosity Models

Boussinesq(1877) suggested that the stress-strain relationship for the time averaged turbulent momentum equations may be written in a similar way to that used in the laminar momentum equations (Newtonian fluid). The only change made is to replace the laminar viscosity $\nu$ with a turbulent viscosity $\nu_t$, where $\nu_t$ is a property of the flow and not the fluid.

For the general case of incompressible turbulent flow, the Reynolds Stresses using tensor notation, are written as

$$-\overline{u_i u_j} = \nu_t \left[ \frac{\partial U_i}{\partial x_j} + \frac{\partial U_j}{\partial x_i} \right] - \frac{2}{3} \delta_{ij} \kappa \qquad (3.9)$$

where $\overline{u_i u_j}$ is the Reynolds turbulent stress, $\kappa$ is the turbulent Kinetic Energy and $\delta_{ij}$ is the Kronecker Delta ($\delta_{ij} = 1$ when i = j and $\delta_{ij} = 0$ when i ≠ j ). There are nine Reynolds Stresses and they are

$$\overline{u_i u_j} = \begin{matrix} \overline{u_1 u_1} & \overline{u_1 u_2} & \overline{u_1 u_3} \\ \overline{u_2 u_1} & \overline{u_2 u_2} & \overline{u_2 u_3} \\ \overline{u_3 u_1} & \overline{u_3 u_2} & \overline{u_3 u_3} \end{matrix}$$

where $\overline{u_1 u_1}$, $\overline{u_2 u_2}$ and $\overline{u_3 u_3}$ are the normal stresses and the other six are the shear stresses. Similarly the Scalar Fluxes can be written as

$$-\overline{u_i \phi} = \frac{\nu_t}{\sigma_t} \frac{\partial \Phi}{\partial x_i} \qquad (3.10)$$

where $\sigma_t$ is the turbulent Prandtl/Schmidt number which is also a property of the flow. Equations 3.9 and 3.10 are written in a form, where variables are expressed in terms of velocity/scalar gradients. The only unknown term is the turbulent viscosity $\nu_t$, which needs to be modelled. Dimensionally $\nu_t$ can be regarded as the product of a length scale and a velocity scale and the specifications of these scales form the basis of the Mixing length. One equation and Two equation models described briefly below.

### 3.3.1 Mixing Length Models

Prandtl(1925) suggested that $\nu_t$ is related to the mean flow and a mixing length, $\ell_m$, by the following expression

$$\nu_t = \ell_m^2 \left|\frac{\partial U}{\partial y}\right|$$

The only unknown in this type of model is the mixing length and its specification is required to close the turbulence model. In simple flows such as plane wake and jet, the mixing length is assumed to be proportional to the local layer width and in near wall flows the mixing length is assumed to vary linearly with the distance from the wall. However, the mixing length, $\ell_m$, becomes difficult to specify for flows which are more complex than a simple shear layer.

### 3.3.2 One-Equation Model

The next level of complexity in describing the Reynolds Stresses are the One-Equation Models. Prandtl(1945) and Kolmogorov(1942) have proposed that the most physically meaningful velocity scale is $\sqrt{\kappa}$, where $\kappa$ is the time-averaged turbulent kinetic energy defined by

$$\kappa = \frac{1}{2}\left(\overline{u_i u_i}\right)$$

from which the turbulent $\nu_t$ can be calculated from

$$\nu_t = C_1 \ell \sqrt{\kappa} \text{ and } C_1 = 0.09 \qquad (3.11)$$

The turbulent kinetic energy itself must be derived from an additional partial differential equation. This model is used only in certain classes of turbulent flows such as thin shear layers and whilst offering an improvement in these flows suffers in complex flows because , $\ell$, is again difficult to specify.

### 3.3.3 Two-Equation Models

Two equation turbulence models solve a conservation equation model for both the velocity scale, usually $\kappa$, and the length scale.

***The Turbulent Kinetic Energy Transport Equation***

An equation for $\kappa = \overline{u_i u_i}/2$ is derived from the equation of motion, 3.2, by multiplying the equation for $\left(U_i + u_i\right)$ by $u_i$ and averaging. At high Reynolds numbers the $\kappa$-equation can be written as

$$U_i \frac{\partial \kappa}{\partial x_i} = - \frac{\partial}{\partial x_j}\left(\frac{1}{2}\overline{u_j u_i u_i} + \frac{\overline{p u_j}}{\rho}\right) - \overline{u_i u_j}\frac{\partial U_i}{\partial x_j} - \nu \frac{\overline{\partial u_i}}{\partial x_j}\frac{\overline{\partial u_i}}{\partial x_j} \qquad (3.12)$$

(a) (b)

(1) (2) (3) (4)

where the above terms are identified as (1) mean - flow convection, (2) diffusion, consisting of (a) turbulent, (b) pressure, (3) mean shear production and (4) viscous dissipation, $\varepsilon$. All terms on the right hand side of equation 3.12 are unknown, except the production term. Therefore, models are needed for the remaining two terms before equation 3.12 can be used to model the transport of turbulent kinetic energy. The turbulent diffusion is represented by

$$\frac{1}{2}\overline{u_j u_i u_i} = -\frac{\nu_t}{\sigma_\kappa}\frac{\partial \kappa}{\partial x_j}$$

where $\sigma_\kappa$ is the turbulent Prandtl number for the turbulent kinetic energy and it is given the value of 1.0. Pressure diffusion has long been assumed to be negligibly small or to be incorporated in the above expression for $\overline{u_j u_i u_i}$. The dissipation rate $\varepsilon$ is represented by

$$\varepsilon = \nu \overline{\frac{\partial u_i}{\partial x_j}\frac{\partial u_i}{\partial x_j}} = C_D \frac{\kappa^{3/2}}{\ell}$$

where $C_D$ is an empirical constant and , $\ell$, is again a length scale. By substituting the above models into equation 3.12, the turbulent kinetic equation can be written as

$$U_i \frac{\partial \kappa}{\partial x_i} = \frac{\partial}{\partial x_j}\left[\frac{\nu_t}{\sigma_\kappa}\frac{\partial \kappa}{\partial x_j}\right] - \overline{u_i u_j}\frac{\partial U_i}{\partial x_j} - \varepsilon \qquad (3.13)$$

***The Length Scale Equation***

Previously it was seen that, the use of a prescribed length scale is seldom satisfactory because it lacks generality. Numerous workers have proposed that the conservation equation of a further variable be used to determine the length scale and table 3.1 lists

several proposals for the dependent variable. The most common second variable in use is the dissipation rate, $\varepsilon \equiv \frac{\kappa^{3/2}}{\ell}$, giving rise to the well known $\kappa$ - $\varepsilon$ two equation turbulence model from which the turbulent viscosity $\nu_t$ is determined using

$$\nu_t = C_\mu \frac{\kappa^2}{\varepsilon} \quad \text{where } C_\mu = 0.09.$$

| Workers Name | Length Scale Proposals |
|---|---|
| Kolmogorov(1942) | $\frac{\kappa^{1/2}}{\ell}$ |
| Chou(1945), Davidov(1961), Harlow & Nakayama(1967) and Jones & Launder(1972) | $\frac{\kappa^{3/2}}{\ell}$ |
| Rotta(1968) | $\kappa\ \ell$ |
| Spalding(1971), Saffman(1970) | $\frac{\kappa}{\ell^2}$ |
| Abid & al(1991) | $\frac{\ell}{\sqrt{\kappa}}$ |

Table 3.1. Proposals to determine the length scale.

The dissipation rate transport equation for high Reynolds number, Jones(1971), can be written as

$$U_j \frac{\partial \varepsilon}{\partial x_j} = \frac{\partial}{\partial x_j}\left[\frac{\nu_t}{\sigma_\varepsilon} \frac{\partial \varepsilon}{\partial x_j}\right] + C_{\varepsilon 1} \frac{\varepsilon}{\kappa} \overline{u_i u_j} \frac{\partial U_i}{\partial x_j} - C_{\varepsilon 2} \frac{\varepsilon^2}{\kappa} \qquad (3.14)$$

where $C_{\varepsilon 2} = 1.9$ , $C_{\varepsilon 1} = 1.38$ and $\sigma_\varepsilon = 1.3$.

The formulation of $\kappa$ - $\varepsilon$ turbulence model is completed by equations (3.13) and (3.14). By using the algebraic relationships (3.9), (3.10) and (3.11) along with the $\kappa$ and $\varepsilon$ transport equations, the turbulence properties can be computed and used in the time averaged conservation equations (3.7) and (3.8).

### 3.3.4 Drawbacks of Eddy Viscosity Models

In the eddy viscosity approach, the Mixing Length models are simple to implement and gives realistic predictions of the velocity and shear stress distributions and the general behaviour of boundary layer flows. However, the Mixing Length models are difficult to use for flows other than thin shear layers and attached boundary layers because it is difficult to specify, $\ell_m$, in separated or recirculating flows and takes no account of the convection or diffusion of turbulence. The results obtained from the one-equation models are not much different and at the same time share the failures as well as the successes of the Mixing Length models, Spalding and Launder(1972).

The two-equations models, of which the $\kappa$ - $\varepsilon$ turbulence model is the most widely used due to its simplicity in both theory and implementation and are qualitatively realistic for a minimal amount of input data from the user. However, this model and other two-equation models underestimate the effects of swirl, longitudinal streamline curvature and body forces. The model also underpredicts the decrease in skin friction in decelerated boundary layers.

There are two assumptions behind the two-equation models which imply that the models will become less accurate as the flow becomes more complex. The first assumption, that the Reynolds Stresses can be determined as a linear function of the mean rate of strain, in general, this can be illustrated by considering the nearly homogeneous flow of Champagne et al(1970) where the only non-zero velocity gradient was $\partial U/\partial y$ and the measured values of the anisotropy tensor is defined by

$$a_{ij} = \frac{\overline{u_i u_j}}{\kappa} - \frac{2}{3}\delta_{ij}$$

where

$$a_{11} = 0.3 \qquad a_{22} = -0.18 \qquad a_{33} = -0.12 \qquad a_{12} = 0.33$$

The anisotropy tensor as predicted by the two-equations models is however,

$$a_{11} = a_{22} = a_{33} = 0 \qquad a_{12} = 0.33$$

Therefore the mechanism that causes an inequality of the normal stresses can not be predicted using a two-equation type of model . The second assumption of coincident principle axes of stress and strain makes the eddy viscosity turbulence model always predict the position of zero shear stress as being coincident with the maxima and minima of the velocity field. This can be illustrated by writing equation 3.9 for the shear stress $\overline{uv}$ in a situation where $\partial U/\partial y$ is again the only zero velocity gradient which leads to

$$\overline{u_1 u_2} = -\nu_t \frac{\partial U_1}{\partial x_2}$$

Therefore, the two-equation models can not predict accurately the shear stresses in simple flow such as a flow around a pipe bend or in a square duct.

In addition, the Scalar Flux equation (3.10) has the disadvantage of not being able to produce what is known as counter-gradient diffusion (Marquis, 1986).

## 3.4 Reynolds Stress and Scalar Flux Models

Models employing the eddy viscosity principle deduce the Reynolds stresses and Scalar Fluxes from the eddy viscosity and mean velocity or mean scalar gradients. Reynolds Stress and Scalar Flux models involve the derivation and solution of transport equations for each component of the Reynolds Stress, $\overline{u_i u_j}$ and Scalar Flux, $\overline{u_j \phi}$. Sections 3.4.1 and 3.4.2 describes the derivations of the Reynolds stress and Scalar Flux models.

### 3.4.1 Reynolds Stress Model

Chou(1945) was the first to derive an exact conservation equation for the Reynolds Stress, $\overline{u_i u_j}$, from the equations of motion, even though Keller and Friedmann(1924) were the first to suggest the determination of the Reynolds Stresses from their differential equations. The exact form of Reynolds Stress equation can be derived as follows

i) Subtract equation 3.7 from equation 3.2.

ii) Multiply the resulting equation by the fluctuating velocity $u_j$.

iii) Repeat processes i), and ii), using the momentum equation for $U_j$ and the fluctuating velocity $u_i$.

iv) Add the two resulting equations and then average with respect to time to obtain the Reynolds Stress transport equation.

Following Bradshaw(1976) and Jones(1980), the conservation equation without buoyancy effects for the Reynolds Stress $\overline{u_i u_j}$ can be written as

$$\frac{d\overline{u_i u_j}}{dt} = -\overline{u_i u_\ell}\frac{\partial U_j}{\partial x_\ell} - \overline{u_j u_\ell}\frac{\partial U_i}{\partial x_\ell} \qquad \text{Production}$$

$$-\frac{1}{\rho}\left[\overline{u_i \frac{\partial p}{\partial x_j}} + \overline{u_j \frac{\partial p}{\partial x_i}} - \frac{2}{3}\delta_{ij}\overline{u_\ell \frac{\partial p}{\partial x_\ell}}\right] \qquad \text{Redistribution}$$

$$-2\nu\,\overline{\frac{\partial u_i}{\partial x_\ell}}\,\overline{\frac{\partial u_j}{\partial x_\ell}} \qquad \text{Dissipation}$$

$$-\frac{\partial}{\partial x_\ell}\left[\overline{u_i u_j u_\ell} + \frac{2}{3}\delta_{ij}\overline{\frac{u_\ell p}{\rho}}\right] \qquad \text{Diffusion}$$

(3.15)

Equation (3.15) in its present form is not immediately employable as a model of turbulent motion, because the right-hand side of the equation contains unknown correlations of turbulence quantities, for example $\overline{u_i u_j u_\ell}$, which must be prescribed to re-close the set of equations.

The first term on the right-hand side of equation (3.15), which does not require modelling is a production term representing the interaction between the mean velocity field and turbulence properties. The second term is the pressure-strain correlation and is commonly referred to as a 'redistribution' term. This redistribution term involves most of the modelling effort in most Reynolds Stress models. Chou(1945) showed that during the interaction process between the pressure-strain and turbulence, pressure fluctuations tend to make the turbulence more isotropic by increasing the weaker normal stresses at the expense of the stronger and reducing the magnitude of shear stresses. Such reasoning led Rotta(1951), Launder, Reece and Rodi(1975), Lumely and Khajeh-Nouri(1974) and Daly and Harlow(1970) to divide the pressure-strain into two parts. The first involves the term generated from a mutual interaction between turbulence components, while the second

involves the mean rate of pressure-strain and its interaction with turbulence. The pressure-strain model used here is that of Musonge(1983) who suggested that the return to isotropy is a product of the Reynolds Stresses and mean velocity field. The pressure-strain equation of Musonge(1983) for constant density flow may be expressed as

$$- C_1 \frac{\varepsilon}{\kappa}\left[\overline{u_i u_j} - \frac{2}{3}\delta_{ij}\kappa\right] + C_2\delta_{ij}\overline{u_\ell u_m}\frac{\partial U_\ell}{\partial x_m} + C_3\left[\overline{u_j u_\ell}\frac{\partial U_i}{\partial x_\ell} + \overline{u_i u_\ell}\frac{\partial U_j}{\partial x_\ell}\right]$$

$$+ C_4\kappa\left[\frac{\partial U_i}{\partial x_j} + \frac{\partial U_j}{\partial x_i}\right] - \left(\frac{3}{2}C_2 + C_3\right)\left[\overline{u_j u_\ell}\frac{\partial U_\ell}{\partial x_i} + \overline{u_i u_\ell}\frac{\partial U_\ell}{\partial x_j}\right]$$

Where the constants $C_1 = 1.8$ , $C_2 = -0.51$ , $C_3 = 0.63$ and $C_4 = -0.41$ were obtained from the experimental data of Tavoularis and Corrison(1981a,b).

The third term in equation (3.15) is the dissipation rate. The dissipation rate was determined by assuming the dissipative motion to be isotropic, so equation (3.14) is again used here. The last term in equation (3.15) is the diffusion term and represents diffusion by pressure and velocity fluctuations. Many models have been used for the diffusion transport term, such as the simple gradient model by Daly and Harlow(1970) or the more complex models by Hanjalic and Launder(1972). The model used here is the simple model of Launder and Dekeyser(1983) and Dekeyser(1985), which may be written as

$$\overline{u_i u_j u_\ell} + \frac{2}{3}\delta_{ij}\frac{\overline{u_\ell p}}{\rho} = - C_s\frac{\kappa}{\varepsilon}\overline{u_\ell u_m}\frac{\partial\overline{u_i u_j}}{\partial x_m}$$

where $C_s = 0.22$.

The models above for the pressure-strain term, dissipation term and diffusion term can now be substituted in equation (3.15) resulting in the final form of the Reynolds Stress transport equation for high Reynolds number constant density flows, equation (3.16).

$$\frac{d\overline{u_i u_j}}{dt} = -\left[\overline{u_i u_\ell}\frac{\partial U_j}{\partial x_\ell} + \overline{u_j u_\ell}\frac{\partial U_i}{\partial x_\ell}\right] - \frac{2}{3}\delta_{ij}\varepsilon + \frac{\partial}{\partial x_\ell}C_s\left[\frac{\kappa}{\varepsilon}\overline{u_\ell u_m}\frac{\partial\overline{u_i u_j}}{\partial x_m}\right]$$

$$- C_1\frac{\varepsilon}{\kappa}\left[\overline{u_i u_j} - \frac{2}{3}\delta_{ij}\kappa\right] + C_2\delta_{ij}\overline{u_\ell u_m}\frac{\partial U_\ell}{\partial x_m}$$

$$-\left(\frac{3}{2}C_2 + C_3\right)\left[\overline{u_j u_\ell}\frac{\partial U_\ell}{\partial x_i} + \overline{u_i u_\ell}\frac{\partial U_\ell}{\partial x_j}\right]$$

$$+ C_3\left[\overline{u_j u_\ell}\frac{\partial U_i}{\partial x_\ell} + \overline{u_i u_\ell}\frac{\partial U_j}{\partial x_\ell}\right] + C_4\kappa\left[\frac{\partial U_i}{\partial x_j} + \frac{\partial U_j}{\partial x_i}\right] \qquad (3.16)$$

The Reynolds Stress turbulence model does not suffer from the limitations of the $\kappa$ - $\varepsilon$ turbulence model and is considered to be a more universal model because it does not have to be modified to suit the type of flow being studied. But, this model contains many highly coupled partial differential equations which increases the amount of computational time compared to the $\kappa$ - $\varepsilon$ turbulence model.

### 3.4.2 Scalar Flux Model

The Scalar Flux transport equation can be derived following a similar path to that adopted for the derivation of the Reynolds Stress transport equation. At high turbulence Reynolds numbers the exact form of the Scalar Flux, $\overline{u_i \phi}$ and the Scalar Fluctuations, $\overline{\phi}^2$ may be written without buoyancy, Jones(1980), in the following form

$$\frac{d\,\overline{u_i\phi}}{dt} = -\overline{u_\iota\phi}\,\frac{\partial U_i}{\partial x_\iota} - \overline{u_i u_\iota}\,\frac{\partial \Phi}{\partial x_\iota}$$ Production

$$-\frac{\partial}{\partial x_\iota}\left(\overline{u_i u_\iota \phi}\right)$$ Diffusion

$$-\frac{\overline{\phi\,\partial p}}{\rho\,\partial x_i}$$ Pressure Scrambling

(3.17)

$$\frac{d\,\overline{\phi^2}}{dt} = -2\,\overline{u_\iota\phi}\,\frac{\partial \Phi}{\partial x_\iota}$$ Production

$$-\frac{\partial}{\partial x_\iota}\left(\overline{u_\iota\phi^2}\right)$$ Diffusion

$$-2\,\frac{\nu}{\sigma}\,\overline{\frac{\partial \phi}{\partial x_\iota}}\,\overline{\frac{\partial \phi}{\partial x_\iota}}$$ Dissipation

(3.18)

The derivation of the above equations introduces two unknown terms in each equation (3.17) and (3.18) respectively, for which models need to be specified. In equation (3.17) the two unknowns, which needs to be modelled are the diffusion term and pressure scrambling term. The model used for the diffusion term is that of Launder(1978) and is written as

$$\overline{u_i u_\iota \phi} = -C_\phi\,\frac{\kappa}{\varepsilon}\left[\overline{u_i u_\iota}\,\frac{\partial \overline{u_j\phi}}{\partial x_\iota} + \overline{u_j u_\iota}\,\frac{\partial \overline{u_i\phi}}{\partial x_\iota}\right]$$

where $C_\phi = 0.11$ and $\kappa/\varepsilon$ is the characteristic time scale of the turbulence motion.

The pressure scrambling term is modelled following Samaraweera(1978) and can be written as

$$-\frac{\overline{\phi}}{\rho}\frac{\overline{\partial p}}{\partial x_i} = -C_{\phi 1}\frac{\varepsilon}{\kappa}\overline{u_i\phi} + C_{\phi 2}\overline{u_\iota\phi}\frac{\partial U_i}{\partial x_\iota}$$

where $C_{\phi 1} = 3.0$ and $C_{\phi 2} = 0.5$. Substituting the above two models into equation (3.17) to obtain the final form of the Scalar Flux transport equation given below

$$\frac{d\overline{u_i\phi}}{dt} = -\overline{u_\iota\phi}\frac{\partial U_i}{\partial x_\iota} - \overline{u_iu_\iota}\frac{\partial \Phi}{\partial x_\iota}$$

$$+ \frac{\partial}{\partial x_\iota}\left[C_\phi\frac{\kappa}{\varepsilon}\left[\overline{u_\iota u_m}\frac{\partial\overline{u_i\phi}}{\partial x_m} + \overline{u_iu_m}\frac{\partial\overline{u_\iota\phi}}{\partial x_m}\right]\right]$$

$$- C_{\phi 1}\frac{\varepsilon}{\kappa}\overline{u_i\phi} + C_{\phi 2}\overline{u_\iota\phi}\frac{\partial U_i}{\partial x_\iota} \qquad (3.19)$$

The Scalar Fluctuations equation (3.18) contains two unknowns, which again require modelling. The first is the diffusion term and is modelled by using the following simple gradient diffusion model

$$\overline{u_\iota\phi^2} = -C_s'\frac{\kappa}{\varepsilon}\overline{u_\iota u_m}\frac{\partial\overline{\phi^2}}{\partial x_m}$$

where $C_s' = 0.22$. The second term of equation (3.18) represents the dissipation rate and the following model is used

$$\frac{\nu}{\sigma}\frac{\overline{\partial\phi}}{\partial x_\iota}\frac{\overline{\partial\phi}}{\partial x_\iota} = C_D\overline{\phi^2}\frac{\varepsilon}{\kappa}$$

where $C_D = 2.0$. Substituting the above two models into equation (3.18), the Scalar Fluctuations transport equation may be written in the following final form

$$\frac{d\,\overline{\phi^2}}{dt} = -2\,\overline{u_i\phi}\,\frac{\partial\,\Phi}{\partial\,x_i} + \frac{\partial}{\partial x_i}\left[\,C_s'\,\frac{\kappa}{\varepsilon}\,\overline{u_i u_m}\,\frac{\partial\overline{\phi^2}}{\partial x_m}\,\right] - C_D\,\overline{\phi^2}\,\frac{\varepsilon}{\kappa} \qquad (3.20)$$

# Chapter 4

# Two Dimensional Flow Calculations

This chapter is concerned with discussing and evaluating the results obtained from three test configurations: flow inclined at 45°, flow moving through 180° known as the IAHR (International Association of Hydraulic Research) problem and the sudden expansion of swirling coaxial water jets.

The aim of the first two studies was to evaluate the performance of three discretisation schemes, Hybrid, Linear Upwind and TVD, in terms of their accuracy and boundedness using the scalar transport equation. The aim of the third study is to evaluate and compare the performance of the following combinations of differencing scheme and turbulence model

i) Hybrid scheme and $\kappa$ - $\varepsilon$ turbulence model,
ii) Hybrid scheme and Reynolds Stress turbulence model,
iii) TVD scheme and $\kappa$ - $\varepsilon$ turbulence model,
iv) TVD scheme and Reynolds Stress turbulence model,

in terms of their accuracy compared with experimental data and numerical performance. The results are compared with the experimental data obtained by Roback et al(1983) for the sudden expansion of swirling coaxial water jets and was a continuation of the work conducted by Johnson and Bennett(1981). Predictions of the latter using the $\kappa$ - $\varepsilon$ and Reynolds Stress/Scalar Flux turbulence models have already been performed by Marquis(1986).

## 4.1 Flow Inclined at 45°

### 4.1.1 Problem Specification

This problem is a two dimensional uniform flow inclined at 45° to the mesh and is shown in figure 4.1 with the appropriate boundary conditions. The two dimensional scalar convection diffusion equation was solved using the three differencing schemes, Hybrid, Linear Upwind and TVD on 9x9, 19x19 and 39x39 regular spaced meshes for a diffusion coefficient , $\Gamma = 10^{-6}$ which essentially represents pure convection.

### 4.1.2 Results and Discussion

Figures 4.2a, b and c show the predicted scalar $\Phi$ profiles for the Hybrid, Linear Upwind and TVD discretisation schemes on the different meshes. Figure 4.2a shows the predicted scalar $\Phi$ profile using the Hybrid, Linear Upwind and TVD discretisation schemes together with the exact solution on regular mesh of 9x9. The three profiles show a reasonable accuracy when compared to the exact solution, however, the profiles predicted using the Linear Upwind and TVD schemes agree more with the exact solution than the Hybrid scheme. As the mesh size increases, the accuracy of the scalar $\Phi$ profile using the different discretisation schemes also increases as shown in figures 4.2b and 4.2c and indicates that the results of the above schemes are still mesh size dependent. As the mesh size increases the accuracy of the scheme also increases, however, this accuracy is at a

cost because as the mesh size increases the computing time also increases. It was noted that the solution on the 19x19 mesh using the Linear Upwind and TVD schemes shown in figure 4.2b is as accurate as the solution using the Hybrid differencing scheme on the 39x39 mesh shown in figure 4.2c. Figures 4.2a, b and c show that the Linear Upwind and TVD scheme predictions are coincident with each other except that some of the Linear Upwind predicted values exceed the upper and lower bounds of $\Phi$ (1 and 0), i.e. the Linear Upwind scheme is unbounded whereas the TVD scheme is not.

## 4.2 Flow Moving Through 180° (IAHR Problem)

### 4.2.1 Problem Specification

This problem was used at the working group for the refined modelling of turbulent flows, held by the IAHR in 1980 for testing the accuracy of finite difference computer programs in a well defined linear test problem. The problem considered is a two dimensional flow moving through 180° as shown in figure 4.3 which also shows the boundary conditions. The flow field in this problem is described algebraically as

$$U = 2y\,(1 - x^2)$$

$$V = -\,2x\,(1 - y^2)$$

The two dimensional scalar convection diffusion equation was again solved using the three differencing schemes, Hybrid, Linear Upwind and TVD on 19x9, 39x19 and 79x39 regular grids for a diffusion coefficient, $\Gamma = 10^{-6}$ which again represents pure convection.

### 4.2.2 Results and Discussion

Figures 4.4a, b and c show the outlet profiles of the scalar Φ using regular meshes of 19x9, 39x19 and 79x39 respectively. Each figure shows the profiles predicted using the Hybrid, Linear Upwind and TVD schemes and for comparison the 'exact' solution is also shown. Figure 4.4a shows that the profiles obtained using the Linear Upwind and TVD schemes were closer to the exact solution than the profile predicted using the Hybrid scheme and this is due to their higher order accuracy. In this problem it was again noted that as the mesh size increases, the accuracy of the scalar profile using the different discretisation schemes also increases as shown in figures 4.4b and c respectively, which indicates that the accuracy of the predictions are mesh size dependent. The solution on the 39x19 using the Linear Upwind and TVD schemes is as accurate as the solution obtained using the Hybrid differencing scheme on the 79x39 mesh. Again the predicted profiles using the Linear Upwind and TVD schemes are largely coincident with each other and again some of the predicted values of the Linear Upwind scheme again exceed the upper and lower bounds Φ (1 and 0), i.e. the Linear Upwind scheme is again unbounded.

## 4.3 The Sudden Expansion of Swirling Coaxial Water Jets

### 4.3.1 Flow Configuration

The flow computed is the sudden expansion of swirling coaxial water jets studied by Roback et al(1983) and is shown in figure 4.5. The coaxial jets discharge into a chamber of circular cross-section, the ratios of the annular jet and the outer wall diameter to the inner jet diameter are two and four respectively. The inner jet enters the chamber without swirl, while the annular jet enters the chamber with swirl angle of 30°. The dimensions of the chamber are given in table 4.1.

| DIMENSIONS | $R_1$ | $R_{1out}=R_{2in}$ | $R_{2out}$ | Ro | L |
|---|---|---|---|---|---|
| Length (mm) | 12.5 | 15.3 | 29.5 | 61.0 | 1016 |
| Radius ratio r/Ro | 0.205 | 0.251 | 0.484 | 1.0 | ------ |

Table 4.1. Chamber dimensions.

The flow downstream of the discharge, shown in figure 4.6, may be divided up into three major shear regions: a recirculation region, a reattachment region and a shear region between the inner and annular jets. The inner jet contains dye as a trace element and the results described by Roback et al(1983) include detailed LDA and LIF measurements of mean and fluctuating velocity and dye concentrations throughout the flow.

### 4.3.2 Boundary Conditions

The boundary conditions used in the calculations were derived from the mean axial velocities of both the inner and outer jets. The angular velocity for the annular jet was computed from the mean axial velocity U and the mean swirl angle and an assumed turbulent intensity of $u/U \approx 0.1$ was used to calculate the inner and annular turbulent kinetic energies using

$$\kappa = \frac{3}{2}\left(0.1 \text{ x } \overline{U}\right)^2$$

For both jets, the fluctuating components of the axial, radial and angular velocities were assumed to be equal and calculated using

$$\overline{u}^2 = \overline{v}^2 = \overline{w}^2 = \frac{2}{3}\kappa$$

The dissipation rates, $\varepsilon$, was estimated for both the inner and annular jets using

$$\varepsilon = \frac{\kappa^{3/2}}{\ell}$$

where the length scale $\ell$ is

For the inner jet $\ell = R_{1out}$

For the annular jet $$\ell = \frac{R_{2out} - R_{2in}}{2}$$

| | Inner Jet | Annular Jet |
|---|---|---|
| U (m/s) | 0.52 | 1.66 |
| V (m/s) | 0 | 0 |
| W (m/s) | 0 | 0.9584 |
| $\kappa$ ($m^2/s^2$) | $4.056 \times 10^{-3}$ | 0.055 |
| $\varepsilon$ ($m^2/s^3$) | 0.02 | 1.822 |
| $\overline{u^2} = \overline{v^2} = \overline{w^2}$ ($m^2/s^2$) | $2.704 \times 10^{-3}$ | $3.667 \times 10^{-2}$ |
| $\overline{uv} = \overline{uw} = \overline{vw}$ ($m^2/s^2$) | 0 | 0 |

Table 4.2. A summary of the inlet boundary conditions for the jets.

Table 4.2 summarises the boundary conditions used at the jet inlets. At the solid walls the fully turbulent equilibrium wall-law profiles were assumed to prevail at the boundary conditions applied at the remaining domain boundaries were as follows

Symmetry $\quad r = 0 \quad \overline{uv} = \overline{uw} = 0$

$$V = W = 0$$

$$\frac{\partial}{\partial r} = 0 \qquad \text{otherwise}$$

Outflow $\quad \frac{x}{Ro} = 16.7 \quad \frac{\partial}{\partial x} = 0$

In addition, the outflow total mean flow rate was corrected to ensure overall mass conservation. The computed results using the Hybrid and TVD schemes with the $\kappa$ - $\varepsilon$ and Reynolds Stress turbulence models were obtained using the computational meshes listed in table 4.3

| Differencing schemes | $\kappa$ - $\varepsilon$ turbulence model | Reynolds Stress turbulence model |
|---|---|---|
| Hybrid | 40x80 | 40x80 |
| | 80x160 | 80x160 |
| | 80x320 | 80x320 |
| | 80x480 | 80x480 |
| | --------- | 80x640 |
| TVD | 40x80 | 40x80 |
| | 80x160 | 80x160 |
| | 80x320 | 80x320 |
| | --------- | 80x480 |

Table 4.3. A list of computational meshes used in the calculations.

where the first and second numbers represent the number of nodes in the radial and axial directions respectively. The meshes are equally spaced in the radial direction and in the axial direction an increasing mesh spacing with a constant mesh spacing ratio of 1.1 was between $0 \leq x / Ro \leq 5.0$ and then equally spaced mesh for x/Ro > 5.0.

### 4.3.3 Results and Discussion

In the results to be compared and described below, the radial and axial location's have been normalised with respect to the outer radius Ro and all velocities have been nondimensionalised with the average mean velocity in the duct, Uo = 0.29 m/s.

Figures 4.7-4.14 present radial profiles for the axial, radial and angular mean and fluctuating velocities and shear stresses. Each figure contains three sets of profiles taken at the axial locations of x/Ro = 0.83, 2.5 and 5.0 and each axial location contains three to five predicted profiles and the experimental data. Predictions obtained using the $\kappa$ - $\varepsilon$ turbulence model and Hybrid differencing scheme are shown in figures 4.7a-4.14a, $\kappa$ - $\varepsilon$ turbulence model and TVD scheme are shown in figures 4.7b-4.14b, Reynolds Stress turbulence model and Hybrid differencing scheme are shown in figures 4.7c-4.14c and predictions obtained using Reynolds Stress turbulence model and TVD scheme are shown in figures 4.7d-4.14d.

The numerical accuracy of the differencing schemes and turbulence models will be discussed in section 4.3.3a and the physical accuracy of the differencing schemes and turbulence models will be discussed in sections 4.3.3b and 4.3.3c.

#### 4.3.3a Grid Independent Solution

Figures 4.7-4.14 which are discussed in more details in sections 4.3.3b and 4.3.3c show that the predicted profiles vary as the mesh size changes until a point is reached after which no further change takes place as the mesh size is increased, i.e. a grid independent solution is reached. For example, it was noted that the predictions obtained using the Hybrid differencing scheme and the $\kappa$ - $\varepsilon$ turbulence model with mesh sizes of 80x320 and 80x480 presented in figures 4.7a-4.14a were similar as were the predictions obtained using the TVD scheme and the $\kappa$ - $\varepsilon$ turbulence model, figures 4.7b-4.14b, but with mesh sizes of 80x160 and 80x320. This indicates that using the TVD scheme has reached

a grid independent solution using a smaller mesh, 80x160, than the Hybrid differencing scheme, 80x320. The grid independent solutions reached using either differencing scheme with the $\kappa$ - $\varepsilon$ turbulence model are the same and this is expected.

The predictions presented in figures 4.7c-4.14c and 4.7d-4.14d show that the profiles predicted using the Reynolds Stress turbulence model with Hybrid differencing and TVD schemes have reached a grid independent solution using mesh sizes of 80x480 and 80x320 respectively. The TVD scheme has again reached a grid independent solution using a smaller mesh size compared with the Hybrid differencing scheme. The meshes used to reach a grid independent solutions using the Reynolds Stress turbulence model are larger than those used with the $\kappa$ - $\varepsilon$ turbulence model and is expected because the turbulence source terms in the Reynolds Stress turbulence model are more dependent on velocity gradients than those in the $\kappa$ - $\varepsilon$ turbulence model. However, the grid independent solutions reached using the two differencing schemes and the Reynolds Stress turbulence model are not the same and this was not expected. This behaviour is not caused by an error in implementing the differencing schemes or the Reynolds Stress turbulence model. It may be possible that a grid independent solution was not actually reached. Although this possibility was not investigated further.

### 4.3.3b Hybrid and TVD Schemes and the $\kappa$ - $\varepsilon$ Turbulence Model

The previous section indicates that the predictions obtained using the two differencing schemes and the $\kappa$ - $\varepsilon$ turbulence model on the 80x320 mesh were grid independent and similar and will be used for comparison against the experimental data throughout the rest of this section.

## Mean Velocities

*Mean Axial Velocity*

According to the experimental data of Roback et al(1983) for this swirling flow, the velocity along the centreline decreased rapidly, passed through zero at x/Ro = 0.65, remained negative until approximately x/Ro = 2.73 and then gradually increased to the average value for fully developed duct flow. Negative axial velocities near the peripheral wall were also observed for the axial locations between x/Ro = 0.83 and 1.7 indicating a recirculation region near the outer wall. Finally the experimental results indicated that once reattachment of the annular jet occurred, the axial velocity profile tended to flatten with momentum transport from the outside (near the solid wall) inward (towards the centreline).

Figures 4.7a and 4.7b present the mean axial velocity predicted at the axial locations of x/Ro = 0.83, 2.5 and 5.0 using the Hybrid and TVD differencing schemes respectively. The predictions obtained using either scheme show at x/Ro = 0.83 negative velocities on the centreline and at x/Ro = 5.0 the predictions and experimental data show an almost uniform profile. At x/Ro = 0.83, the peaks of the predicted profiles using either differencing scheme were located at r/Ro = 0.73 and their peak velocity underpredicted the experimental data by 11 percent. At x/Ro = 2.5, the predicted velocities again have underpredicted the peak in the experimental data by 12.5 percent.

*Mean Radial Velocity*

In general, the Roback et al(1983) experimental data shows that at x/Ro = 0.83 the radial velocity is about 75 percent of the axial velocity indicating that the flow was moving outward at an angle of approximately 35 degrees. Between x/Ro = 0.83 and 1.7, the flow attaches to the wall and was directed radially inward as the flow was deflected by the

wall. The radial velocity profile flattened out and approached zero as the duct flow became fully developed for x/Ro > 5.0.

Figures 4.8a and 4.8b present the mean radial velocity profiles predicted at the axial locations of x/Ro = 0.83, 2.5 and 5.0 using the Hybrid and TVD differencing schemes respectively. The predicted profiles obtained using either scheme at x/Ro = 0.83 tend to follow a similar trend as the experimental data but overpredicted the peak value by 10 percent. At x/Ro = 2.5, the predictions using either scheme fall within the experimental data which shows considerable scatter between the maximum and minimum of the radial velocity V/Uo of 0.4 and -1.2. The predicted profiles at x/Ro = 5.0 are uniform and coincident between r/Ro = 0 and 1.0 where the radial velocity is zero, however, the experimental radial velocity only approached zero for r/Ro > 0.5.

*Mean Angular Velocity*

According to the experimental data of Roback et al(1983), at x/Ro = 0.83, the mean angular velocity increased up to r/Ro = 0.6 then decreased as it approaches the wall. At x/Ro = 2.5, the mean angular velocity has linearly increased up to r/Ro = 0.4 then again decreased as it approaches the wall and at x/Ro = 5.0 a similar behaviour was followed.

Figures 4.9a and 4.9b present the radial profiles of the mean angular velocity predicted at the axial locations of x/Ro = 0.83, 2.5 and 5.0 using the Hybrid and TVD schemes respectively. The predicted profiles at x/Ro = 0.83 using either scheme overpredict the experimental data at r/Ro > 0.74 by few percent and at x/Ro = 2.5 the predictions agreed well with the experimental data. At x/Ro = 5.0 the predictions correspond to solid body rotation, while the experimental data is very different. The peaks of these predictions located at r/Ro = 0.4 were underpredicted by 20 percent.

## Fluctuating Velocities

The experimental profiles for the fluctuating velocities indicate that the intensities of the fluctuations increase and decrease with the development of the shear layers between the inner and annular jets, between the annular jet and the recirculation zone, near the outside wall and in the reattachment region. The largest fluctuations occurred within the first 51mm (x/Ro = 0.83) of the duct and dampened relatively rapidly between x/Ro = 0.83 and 1.7 which might be attributed to the stabilising effect of the uniform angular velocity profile. The fluctuating radial and angular velocity profiles showed trends similar to the axial fluctuating velocity profiles, however, the intensity of the axial velocity fluctuation was generally greater. At x/Ro = 2.5, the ratios of radial and angular fluctuations tended towards 1, as the local shear rate decreased. But for the axial locations where the fluctuations were more intense, the axial fluctuations were 1.5 to 2 times greater than either the radial or angular fluctuations indicating anisotropic turbulence.

The predicted fluctuating velocity profiles which are discussed in more detail further below agree with the experimental data in that they show that the greatest fluctuations occur at x/Ro = 0.83 and decays further downstream and the axial fluctuations are greater than either the radial or angular fluctuations which indicates anisotropic turbulence.

Figures 4.10a and 4.10b present radial profiles of the axial fluctuating velocity at the axial locations of x/Ro = 0.83, 2.5 and 5.0 using the Hybrid and TVD differencing schemes respectively. The predictions obtained using either scheme at x/Ro = 0.83 follow a similar trend as the experimental data, however, the peaks located at r/Ro = 0.6, 0.8 and 0.92 were underpredicted by 19, 40 and 27 percent respectively. At x/Ro = 2.5, the predictions closely follow the experimental data except at outer wall were the predictions have underpredicted the experimental data by approximately 55 percent. The predicted profiles at x/Ro = 5.0 have underpredicted the experimental data by approximately 30 percent on the centreline and about the same on the outer wall.

Figures 4.11a and 4.11b present radial profiles of the radial fluctuating velocity at the axial locations of x/Ro = 0.83, 2.5 and 5.0 using the Hybrid and TVD differencing scheme respectively. At x/Ro = 0.83, the predicted fluctuating velocity using either scheme have underpredicted the experimental data at r/Ro = 0.71 by 38 percent, whereas, the predicted profile using either scheme at x/Ro = 2.5 have underpredicted the experimental data by 25 percent between r/Ro = 0.0 and 0.6 and at x/Ro = 5.0 the centreline, r/Ro = 0.0. the predicted profile was underpredicted by 50 percent.

Figures 4.12a and 4.12b present radial profiles of the angular fluctuating velocity at the axial locations of x/Ro = 0.83, 2.5 and 5.0 using the Hybrid and TVD differencing schemes respectively. At x/Ro = 0.83 the peaks of the predicted profiles obtained using either scheme located at r/Ro = 0.6, 0.72 and 0.94 underpredicted the experimental data by approximately 13, 27 and 2 percent respectively. The only significant difference between the predicted profiles obtained using either scheme compared with the experimental data at x/Ro = 2.5 and 5.0 occurred between r/Ro = 0.0 and 0.2. At x/Ro = 2.5 and 5.0 the centreline, r/Ro = 0.0, values were underpredicted by 27 and 58 percent respectively.

**Momentum Transport**

*Turbulent Transport* $\overline{uv}$ *(Shear Stress) in the Radial - Axial Plane*

The experimental data of Roback et al(1983) indicated that a recirculation zone existed near the centreline for axial locations x/Ro = 0.65 < x/Ro < 2.74. The experimental results also indicated that there is little momentum transport near the centreline, r/Ro < 0.4, for axial locations, x/Ro = 0.83 and 1.67, the upstream end of the centreline recirculation cell. There was a weak negative momentum flux for r/Ro < 0.4 at x/Ro = 2.5 which is close to the downstream edge of the centreline recirculation zone. The momentum turbulent transport rate near the outside wall, r/Ro > 0.8 was still positive at x/Ro = 0.83 but became zero at x/Ro = 1.67 indicating that the end of the recirculation

zone near the outside wall is located between x/Ro = 0.83 and 1.67. At axial locations. 0.83< x/Ro < 3.3, the momentum turbulent transport rate was negative and was essentially zero for x/Ro ≥ 5.0.

Figures 4.13a and 4.13b present the $\overline{uv}$ shear stress predicted at the axial locations of x/Ro = 0.83, 2.5 and 5.0 using the Hybrid and TVD differencing schemes respectively. The greatest values again occurs at x/Ro = 0.83 and decay towards the duct outlet where the velocities approached zero at x/Ro ≥ 5.0 as indicated by the experimental data. At x/Ro = 0.83, the profiles predicted using either scheme overpredict the experimental data by 43 percent at r/Ro = 0.5. The predictions at x/Ro = 2.5 followed a similar trend as the experimental data and at x/Ro = 5.0 the predicted profiles are coincident with the experimental data.

*Turbulent Transport* $\overline{uw}$ *(Shear Stress) in the Axial - Angular Plane*

The momentum turbulent transport rate was positive for x/Ro < 1.67 especially in the annular jet region, 0.25 < r/Ro < 0.60. For 1.67 < r/Ro < 3.3, the momentum transport rate was positive for r/Ro < 0.4 and negative near the outside wall, r/Ro > 0.6. The momentum turbulent transport rate in the $\overline{uw}$ measurement plane became essentially zero for x/Ro > 5.0 and r/Ro > 0.2. The momentum transport rate was positive at x/Ro = 0.83 except at 0.72 < r/Ro < 0.86.

Figures 4.14a and 4.14b presents the $\overline{uw}$ shear stress predicted at the axial locations of x/Ro = 0.83, 2.5 and 5.0 using the Hybrid and TVD differencing schemes respectively. At x/Ro = 0.83 and 2.5, the predictions obtained using either scheme are in general poor compared with the experimental data. The predictions at x/Ro = 5.0 are coincident with the experimental data at r/Ro > 0.3, indicating that the predictions are unable to reproduce the peak of the experimental data near the centreline.

### 4.3.3c Hybrid and TVD Schemes and the Reynolds Stress Turbulence Model

Section 4.3.3a indicates that the predictions obtained using either differencing scheme with the Reynolds Stress turbulence model and mesh, 80x480, show a grid independent solution but these predictions are different. The predictions obtained using the 80x480 mesh will be used through out the rest of this section to show the difference between the predictions obtained using the Hybrid and TVD differencing schemes and for comparison with the experimental data. The predictions in this section will also be compared with the predictions obtained using the $\kappa$ - $\varepsilon$ turbulence model discussed in the previous section.

**Mean Velocities**

*Mean Axial Velocity*

Figures 4.7c and 4.7d present radial profiles of the mean axial velocity predicted at the axial locations of x/Ro = 0.83, 2.5 and 5.0 using the Hybrid and TVD differencing schemes respectively. At x/Ro = 0.83, the predicted peak velocity obtained using the TVD scheme has increased from 3.3 using the Hybrid differencing to 4.0, however, it underpredicts the experimental data by 17 percent. The predicted profile obtained using the TVD scheme at x/Ro = 2.5 underpredicted the experimental data between r/Ro = 0.0 and 0.6 compared with those obtained using the Hybrid differencing.

The predictions at x/Ro = 0.83 obtained using the Hybrid differencing and $\kappa$ - $\varepsilon$ turbulence model better represent the peak value compared with the Hybrid differencing and Reynolds Stress turbulence model predictions shown in figure 4.7c. At x/Ro = 2.5, the predictions obtained using Hybrid differencing and Reynolds Stress turbulence model agree more with the experimental data at the peak compared with the profiles predicted using the $\kappa$ - $\varepsilon$ turbulence model. However, the predicted profiles obtained using the $\kappa$ - $\varepsilon$ turbulence model at x/Ro = 5.0 are closer to the experimental data than the

predictions obtained using the Reynolds Stress turbulence model with either scheme near the centreline.

*Mean Radial Velocity*

Figures 4.8c and 4.8d present radial profiles of the mean radial velocity predicted at the axial locations of x/Ro = 0.83, 2.5 and 5.0 using the Hybrid and TVD differencing schemes respectively. The predicted velocity peak value at x/Ro = 0.83 using the Reynolds Stress turbulence model with TVD scheme has overpredicted the experimental data by 7 percent compared with 3.4 percent, for the Hybrid differencing with Reynolds Stress turbulence model, and 12.5 percent, for the $\kappa$ - $\varepsilon$ turbulence model with either differencing scheme. There were no significant improvement for x/Ro > 0.83 between the predictions obtained using either scheme and turbulence model. At x/Ro = 0.83, the Reynolds Stress turbulence model with Hybrid differencing have decreased the predicted profile peak velocity by few percent bringing a closer agreement with the experimental data compared with the predictions obtained using the $\kappa$ - $\varepsilon$ turbulence model.

*Mean Angular Velocity*

Figures 4.9c and 4.9d present radial profiles of the mean angular velocity predicted at the axial locations of x/Ro = 0.83, 2.5 and 5.0 using the Hybrid and TVD differencing schemes respectively. At x/Ro = 0.83, the predicted angular velocity profile obtained using the Hybrid differencing overpredicts the experimental data by a few percent between r/Ro = 0.68 and the outer wall and agrees well with the experimental data for r/Ro < 0.68. The predictions at x/Ro = 5.0 obtained using the Hybrid differencing agree more with the experimental data between r/Ro = 0.2 and 0.5 compared with the predictions obtained using the TVD scheme.

At x/Ro = 2.5, the predictions obtained using the $\kappa$ - $\varepsilon$ turbulence model and the Reynolds Stress turbulence model with Hybrid differencing agree well with the

experimental data but with small differences between r/R = 0.0 and 0.4. At x/Ro = 0.83 and 2.5, the predictions obtained using the $\kappa$ - $\varepsilon$ turbulence model are in general closer with the experimental data than the predictions obtained using the TVD scheme and Reynolds Stress turbulence model. The predictions obtained using the $\kappa$ - $\varepsilon$ turbulence model at x/Ro = 5.0 correspond to solid body rotation and those of the Reynolds Stress turbulence model follow the experimental data more closely.

**Fluctuating Velocities**

The predicted fluctuating velocity profiles obtained using the Reynolds Stress turbulence model with either differencing scheme show that the greatest fluctuations occur at x/Ro = 0.83 and decay towards the exit as indicated by the experimental data. The axial fluctuations are again greater than either the radial or angular fluctuations which indicates anisotropic turbulence.

Figures 4.10c and 4.10d present radial profiles of the axial fluctuating velocity predicted at the axial locations of x/Ro = 0.83, 2.5 and 5.0 using the Hybrid and TVD differencing schemes respectively. At x/Ro = 0.83 and 2.5 the predicted axial fluctuating velocity obtained using the TVD scheme at r/Ro = 0.85 and 0.75 have moved closer to the experimental data by 16 and 17 percent respectively compared to that obtained using the Hybrid differencing.

At x/Ro = 0.83, the predictions on the centreline obtained using the $\kappa$ - $\varepsilon$ turbulence model agree well with the experimental data, whereas the predictions obtained using either differencing scheme with the Reynolds Stress turbulence model have underpredicted the experimental data by approximately 18 percent. The predicted profile obtained at r/Ro = 0.75 using the TVD scheme with Reynolds Stress turbulence model have improved the agreement with the experimental data by 13 percent compared with the predictions obtained using the $\kappa$ - $\varepsilon$ turbulence model. At x/Ro = 2.5, the profiles predicted using the Reynolds Stress turbulence model has improved the agreement with the experimental

data compared with the predictions obtained using the $\kappa$ - $\varepsilon$ turbulence model. At x/Ro = 5.0 no significant changes were noted between the predictions obtained using either scheme and turbulence model.

Figures 4.11c and 4.11d present radial profiles of the radial fluctuating velocity predicted at the axial locations of x/Ro = 0.83, 2.5 and 5.0 using the Hybrid and TVD differencing schemes respectively. The TVD scheme has moved the maximum peak of the profile predicted at x/Ro = 0.83 inwards bringing a closer agreement with the experimental data compared to that predicted using Hybrid differencing. At the same axial location, the predictions obtained using the $\kappa$ - $\varepsilon$ turbulence model agrees more with the experimental data than those obtained using the Reynolds Stress turbulence model with either differencing scheme. Further downstream at x/Ro = 2.5 and 5.0, no significant changes were noted between the predictions obtained using either scheme and turbulence model.

Figures 4.12c and 4.12d present radial profiles of the angular fluctuating velocity predicted at the axial locations of x/Ro = 0.83, 2.5 and 5.0 using the Hybrid and TVD differencing schemes respectively. At x/Ro = 0.83 the peaks of the predicted profile obtained using the TVD scheme at r/Ro = 0.6 and 0.9 have increased by 1.5 and 15 percent respectively. At x/Ro = 2.5, the profile predicted using the TVD scheme agrees more with the experimental data at r/Ro > 0.25 compared with the predicted profile obtained using Hybrid differencing. However, no significant differences were noted when compared with the predictions obtained using the $\kappa$ - $\varepsilon$ turbulence model. At x/Ro = 0.83 and 2.5 the predictions obtained using the $\kappa$ - $\varepsilon$ turbulence model agree more with the experimental data than the predictions obtained using the Reynolds Stress turbulence model with Hybrid differencing. At x/Ro = 5.0, the differences between the predictions obtained using either scheme and turbulence model were small, however, they underpredict the experimental data on the centreline by approximately 60 percent.

## Momentum Transport

*Turbulent Transport* $\overline{uv}$ *Shear Stress in the Radial - Axial Plane*

Figures 4.13c and 4.13d present radial profiles of the $\overline{uv}$ shear stress at the axial locations of x/Ro = 0.83, 2.5 and 5.0 using the Hybrid and TVD differencing schemes respectively. At x/Ro = 0.83, the agreement between the predictions obtained using either scheme with the Reynolds Stress turbulence model is poor compared with the experimental data. At x/Ro = 2.5, no significant differences were noted between the predicted profiles obtained using either scheme and the Reynolds Stress turbulence model, however, the predicted profiles agree more with the experimental data than the predicted profiles obtained using the $\kappa$ - $\varepsilon$ turbulence model. At x/Ro = 5.0, the predicted profiles approached zero as do the experimental data.

*Turbulent Transport* $\overline{uw}$ *(Shear Stress) in the Axial - Angular Plane*

Figures 4.14c and 4.14d present radial profiles of the $\overline{uw}$ shear stress at the axial locations of x/Ro = 0.83, 2.5 and 5.0 using the Hybrid and TVD differencing schemes respectively. At x/Ro = 0.83, the profiles predicted using the TVD scheme and Hybrid differencing schemes have underpredicted the experimental peak by 24 and 40 percent respectively.

The predictions obtained at x/Ro = 0.83 using either differencing scheme with Reynolds Stress turbulence model are better predicted than the predictions obtained using the $\kappa$ - $\varepsilon$ turbulence model. The agreement between the experimental data and the predictions obtained using either scheme and turbulence model is generally poor at x/Ro = 2.5. At x/Ro = 5.0, the predictions obtained using either scheme and turbulence model followed a similar trend as the experimental data in the outer part of the duct r/Ro > 0.3. At the same location the experimental data near the centreline showed negative values whereas the predictions do not.

## 4.4 Computational Effort

The calculations carried out for the different combinations shown in table 4.3 and discussed in the previous section were computed on a DEC Alpha workstation. Table 4.4 presents the flow field CPU time, in seconds, required to complete one iteration for the meshes which show a grid independency as described in the previous section. This table shows that as mesh size increases, the CPU time also increases. For example, using the meshes, 80x320 and 80x480, with the $\kappa$ - $\varepsilon$ turbulence model and Hybrid differencing took 3.1 and 4.7 seconds of CPU time respectively. This increase in CPU time is consistent with the mesh size increase ratio of 1.5.

Table 4.4 shows that the TVD scheme used 11 percent more CPU time per iteration than the Hybrid differencing using mesh, 80x320 and $\kappa$ - $\varepsilon$ turbulence model. The TVD scheme again used 11 percent more CPU time to complete one iteration than Hybrid differencing using mesh, 80x480 and Reynolds Stress turbulence model.

Table 4.4 also shows that using mesh, 80x480, with the Hybrid differencing and Reynolds Stress turbulence model took 19.2 seconds of CPU time, however, it only took 4.7 seconds of CPU time when using the same mesh size and differencing scheme but with the $\kappa$ - $\varepsilon$ turbulence model. It was also noted that mesh, 80x320, with the TVD scheme and Reynolds Stress turbulence model have taken 10.8 seconds more CPU time than the same mesh size and differencing scheme but again with the $\kappa$ - $\varepsilon$ turbulence model. The CPU time increase in both cases described above are consistent with an increase ratio of 4.1.

| Turbulence model | Differencing scheme | Mesh size | CPU time/iteration (seconds) |
|---|---|---|---|
| $\kappa$ - $\varepsilon$ | Hybrid | 80x320 | 3.1 |
| | | 80x480 | 4.7 |
| | TVD | 80x160 | 1.73 |
| | | 80x320 | 3.5 |
| Reynolds Stress | Hybrid | 80x480 | 19.2 |
| | | 80x640 | 25.6 |
| | TVD | 80x320 | 14.3 |
| | | 80x480 | 21.5 |

Table 4.4. Flow field CPU time required to complete one iteration[1].

| Turbulence models | $\kappa$ - $\varepsilon$ | RS/SF |
|---|---|---|
| Velocity variables | U, V, W, $\delta$P , $\kappa$, $\varepsilon$ | U, V, W, $\delta$P, $\varepsilon$, $\overline{uu}$, $\overline{vv}$, $\overline{ww}$, $\overline{uv}$, $\overline{uw}$, $\overline{vw}$ |
| Number of transport equations | 6 | 11 |

Table 4.5. Velocity variables for which transport equations are solved.

Table 4.4 indicates that the CPU time required to complete one iteration was affected by the mesh size, differencing schemes and turbulence models used during the calculations. In the first case, an increase in mesh size will lead to an increase in the number of nodes involved in the computations and therefore an increase in the CPU time is expected. The TVD scheme in the second case takes more CPU time to complete one iteration than the Hybrid differencing because additional contributions to the convection terms containing flux limiters were added to the source term. Finally, the Reynolds Stress turbulence model takes longer CPU time to complete one iteration than the $\kappa$ - $\varepsilon$ turbulence model because the number of equations used by the Reynolds Stress turbulence model is greater than that used by the $\kappa$ - $\varepsilon$ turbulence model as indicated by table 4.5 which shows that the number

[1] The determination of the actual CPU time is more difficult to specify because a particular calculation was often restarted from a previous calculation to speed up convergence or to avoid numerical problems associated with inappropriate initial conditions.

of equations used by the Reynolds Stress turbulence model are 11. whereas only 6 equations are used by the $\kappa$ - $\varepsilon$ turbulence model. The ratio of CPU time between the Reynolds Stress and $\kappa$ - $\varepsilon$ turbulence models is constant at 4.085 and is consistent with the increase in the number of equations and the increase complexity of the Reynolds Stress transport equations.

## 4.5 Conclusions

Figures 4.7-4.14 discussed above show that the predictions obtained using the Hybrid and TVD differencing schemes with $\kappa$ - $\varepsilon$ turbulence model have reached a grid independent solution for mesh size of 80x320 and 80x160 respectively. The mesh used to reach a grid independent solution using the Reynolds Stress turbulence model is significantly larger, i.e. 80x480 and 80x320 for the Hybrid and TVD differencing schemes respectively. In both cases the TVD scheme is able to reach a grid independent solution using a smaller mesh size and therefore less computer time compared with the Hybrid differencing scheme and this reflects the greater numerical accuracy of the TVD scheme. The grid independent solutions obtained using either differencing scheme and the $\kappa$ - $\varepsilon$ turbulence model are the same, which is expected, whereas the grid independent solutions obtained with the two differencing schemes and the Reynolds Stress turbulence model are not and this is unexpected. One possible explanation for such behaviour is that a grid independent solution was not reached even though the predictions indicated that it was.

The results also show that at x/Ro = 5.0 the mean angular velocity predicted using the Reynolds Stress turbulence model agrees more closely with the experimental data than that obtained using the $\kappa$ - $\varepsilon$ turbulence model which correspond more to solid body rotation.

In addition, the predicted axial fluctuating velocities obtained using either scheme and turbulence model are greater than either the radial or angular fluctuating velocities indicating anisotropic turbulence which agrees with the experimental data. The predicted

radial and angular fluctuating velocities, x/Ro = 0.83, obtained using the $\kappa$ - $\varepsilon$ turbulence model agree more closely with the experimental data than those obtained using either differencing scheme and Reynolds Stress turbulence model. At the same axial location, the predicted axial fluctuating velocity obtained using the TVD scheme and Reynolds Stress turbulence model is the closest to the experimental data.

Finally it can be concluded that the implementation of high order convection approximation, TVD, has greatly improved the numerical accuracy of the computations by reaching a grid independent solution using a smaller mesh size. The use of more advanced Reynolds Stress turbulence model has improved the physical behaviour of the predictions as seen in the predictions of the mean angular velocity near the exit of the duct. In addition, this study showed that the anisotropic turbulence can be predicted using either turbulence model.

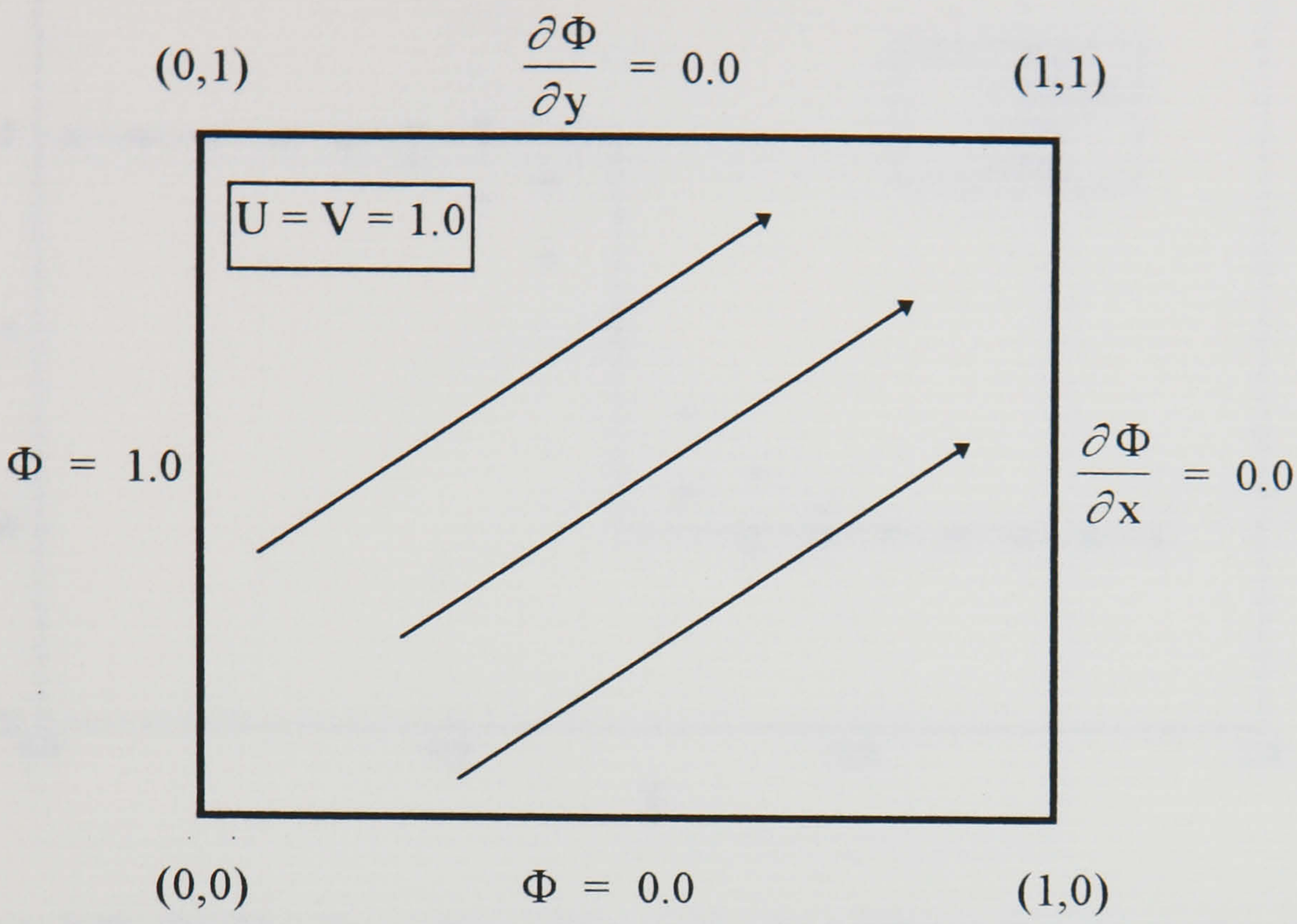



Figure.4.1. Uniform flow inclined at 45°.

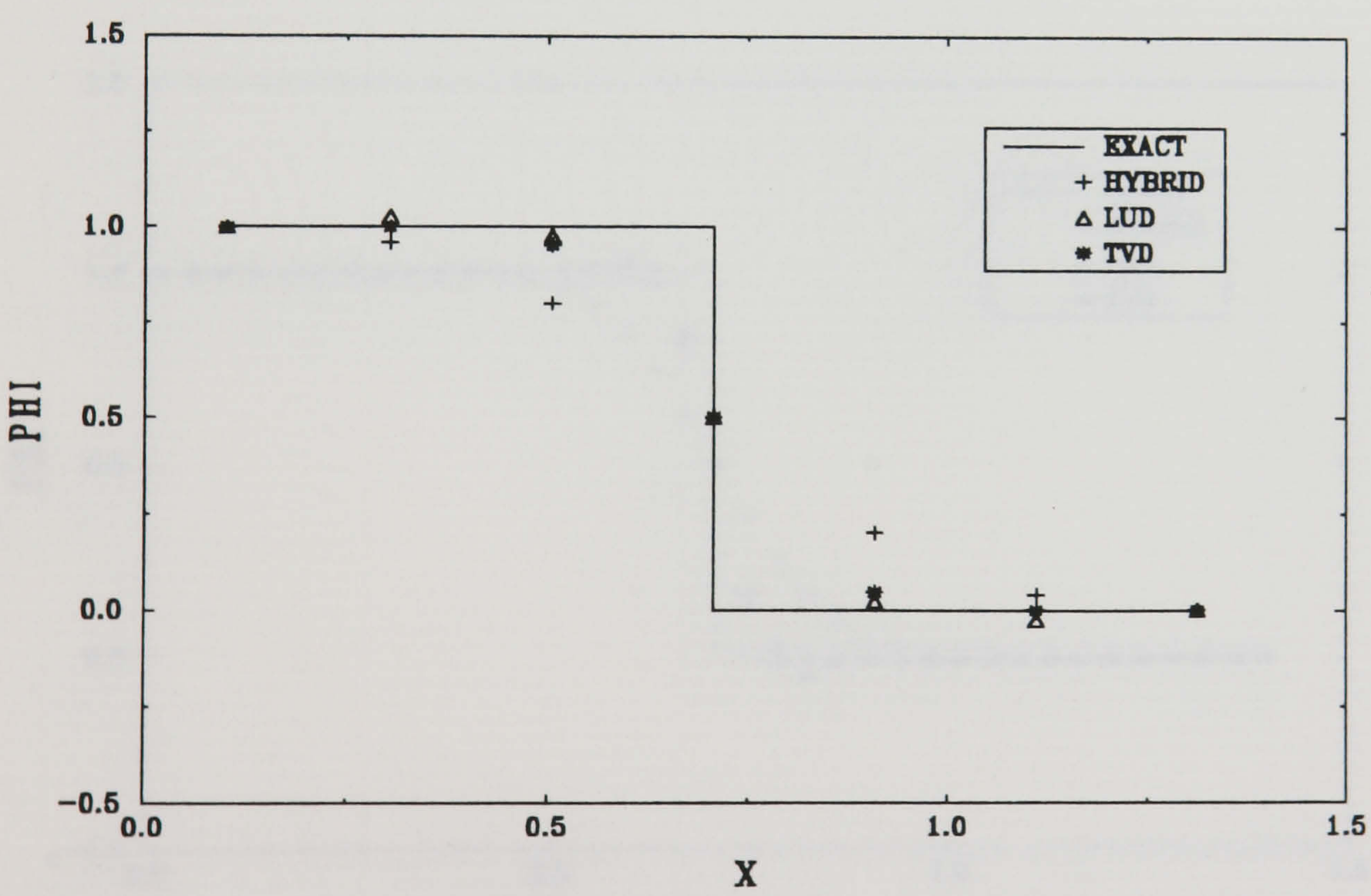



Figure.4.2a. Profiles for uniform flow inclined at 45° (mesh size used is 9x9).

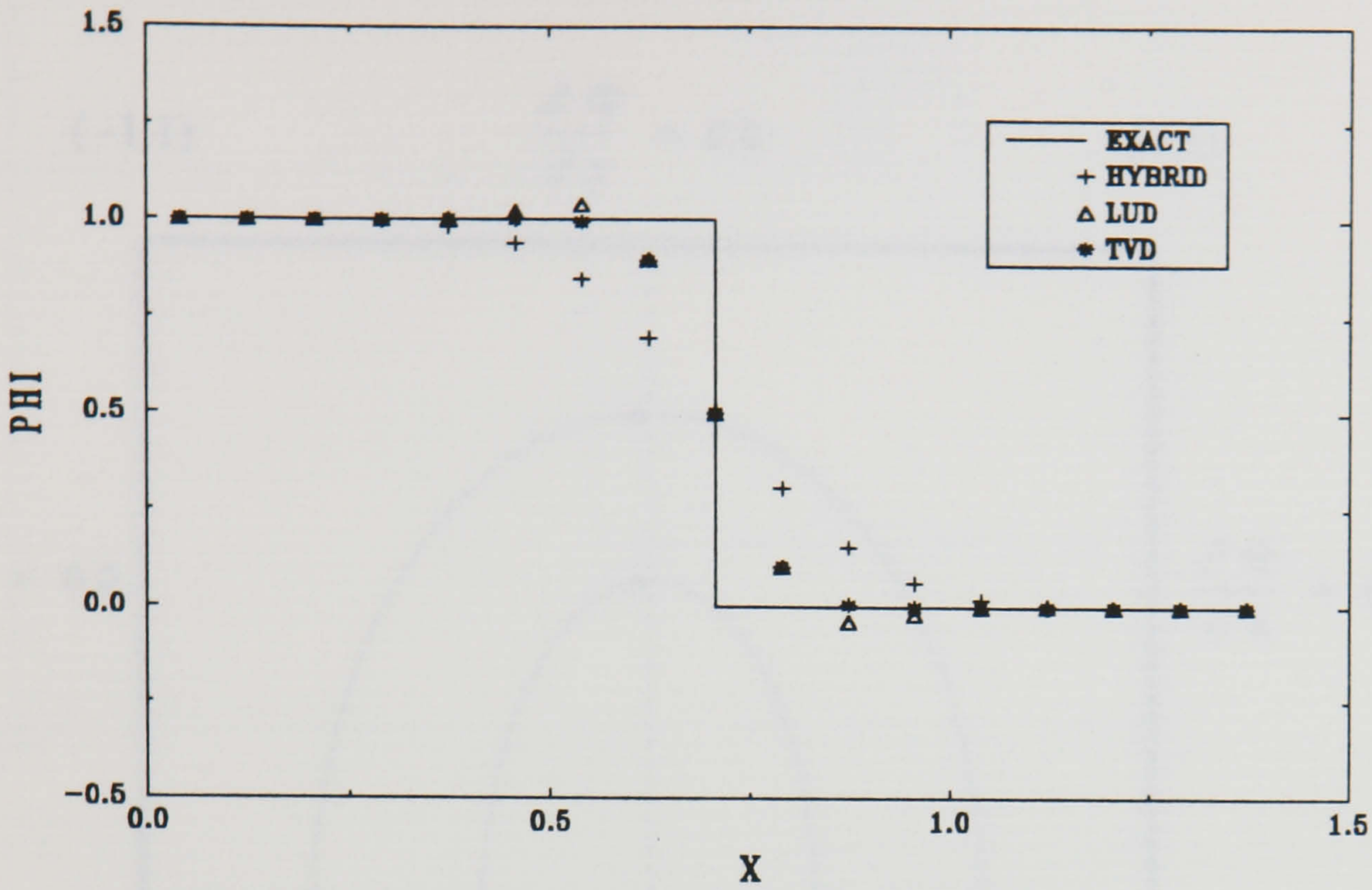



Figure.4.2b. Profiles for uniform flow inclined at 45° (mesh size used is 19x19).

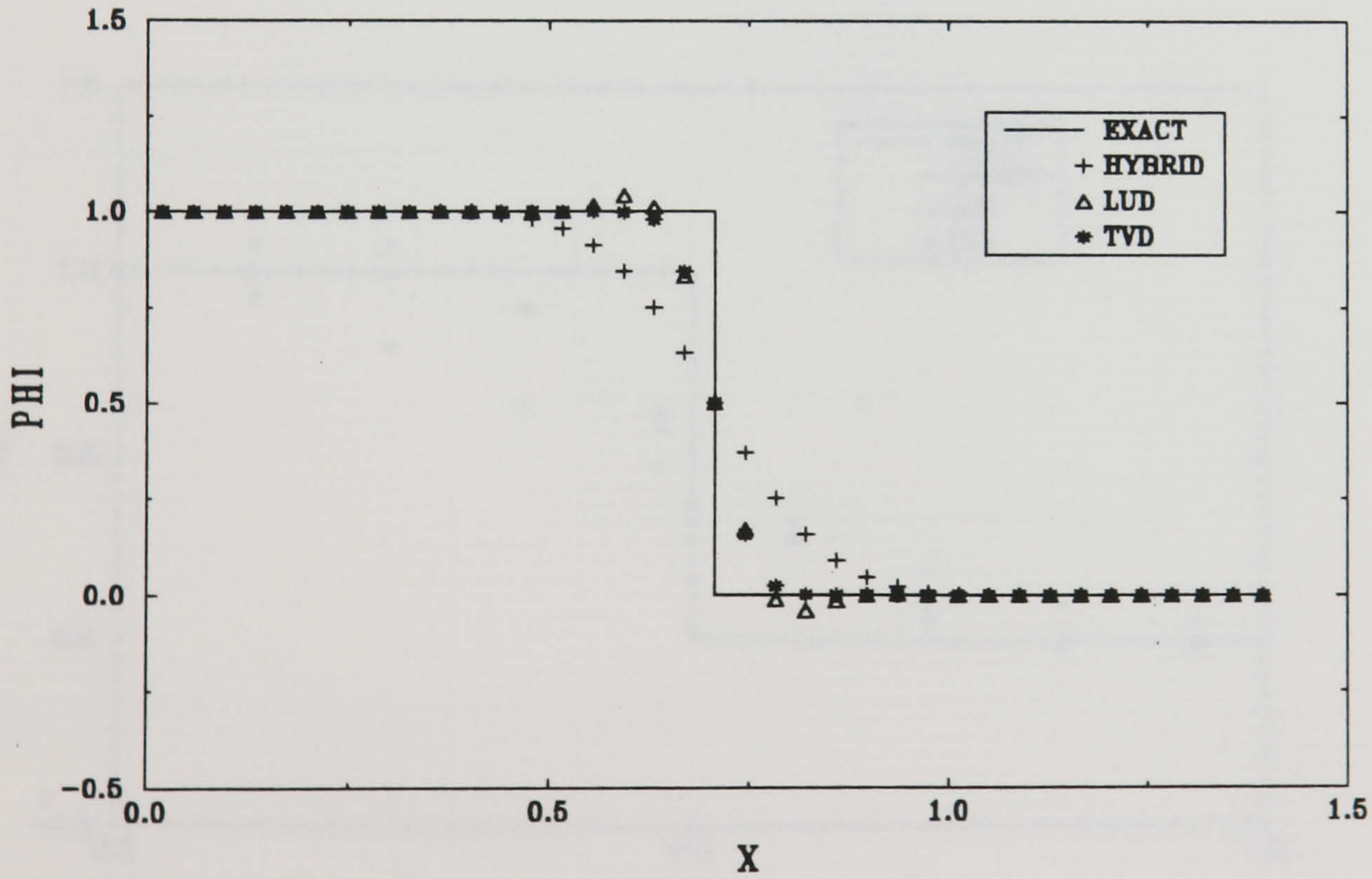



Figure.4.2c. Profiles for uniform flow inclined at 45° (mesh size used is 39x39).

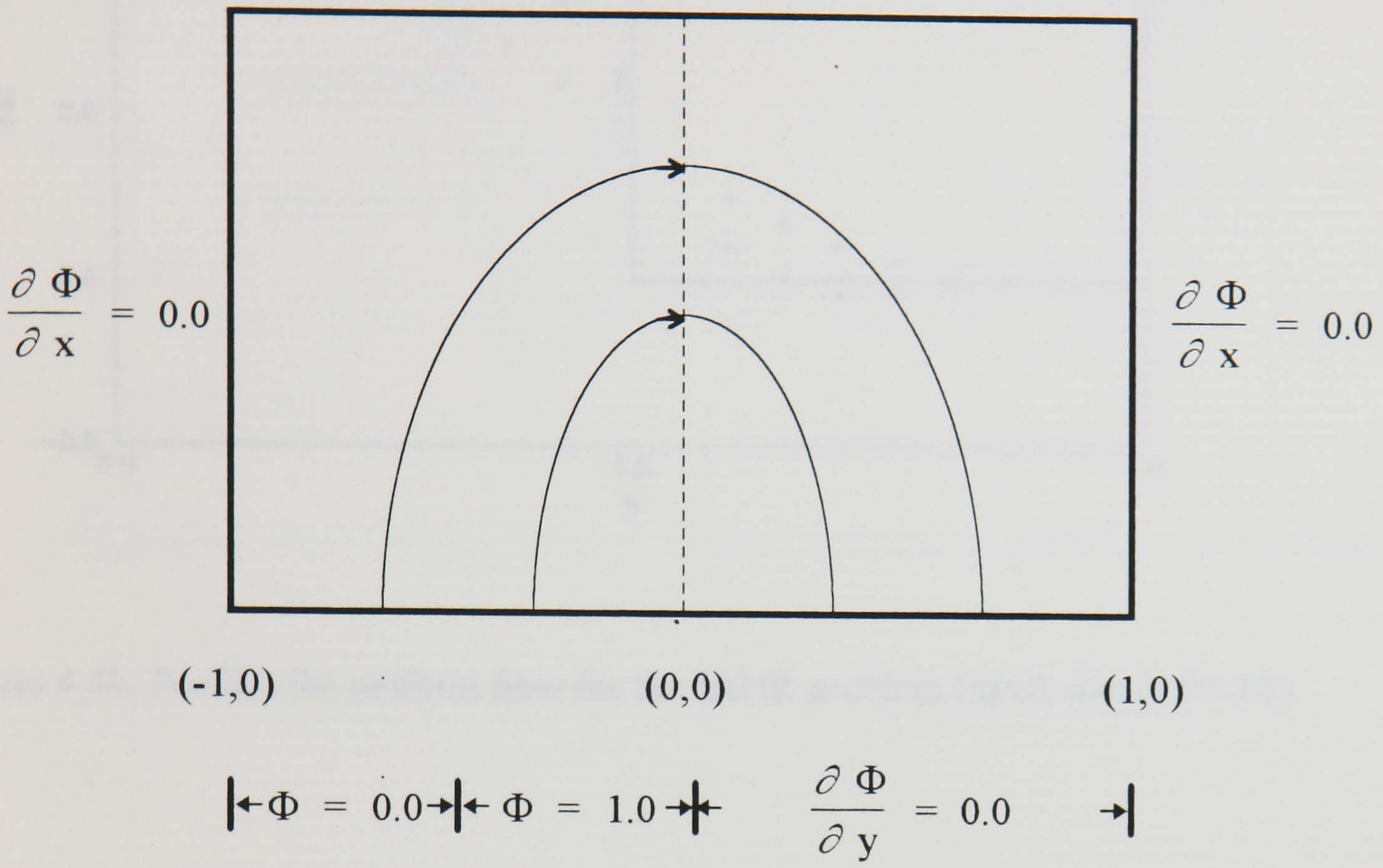



Figure.4.3. Uniform flow for the IAHR problem.

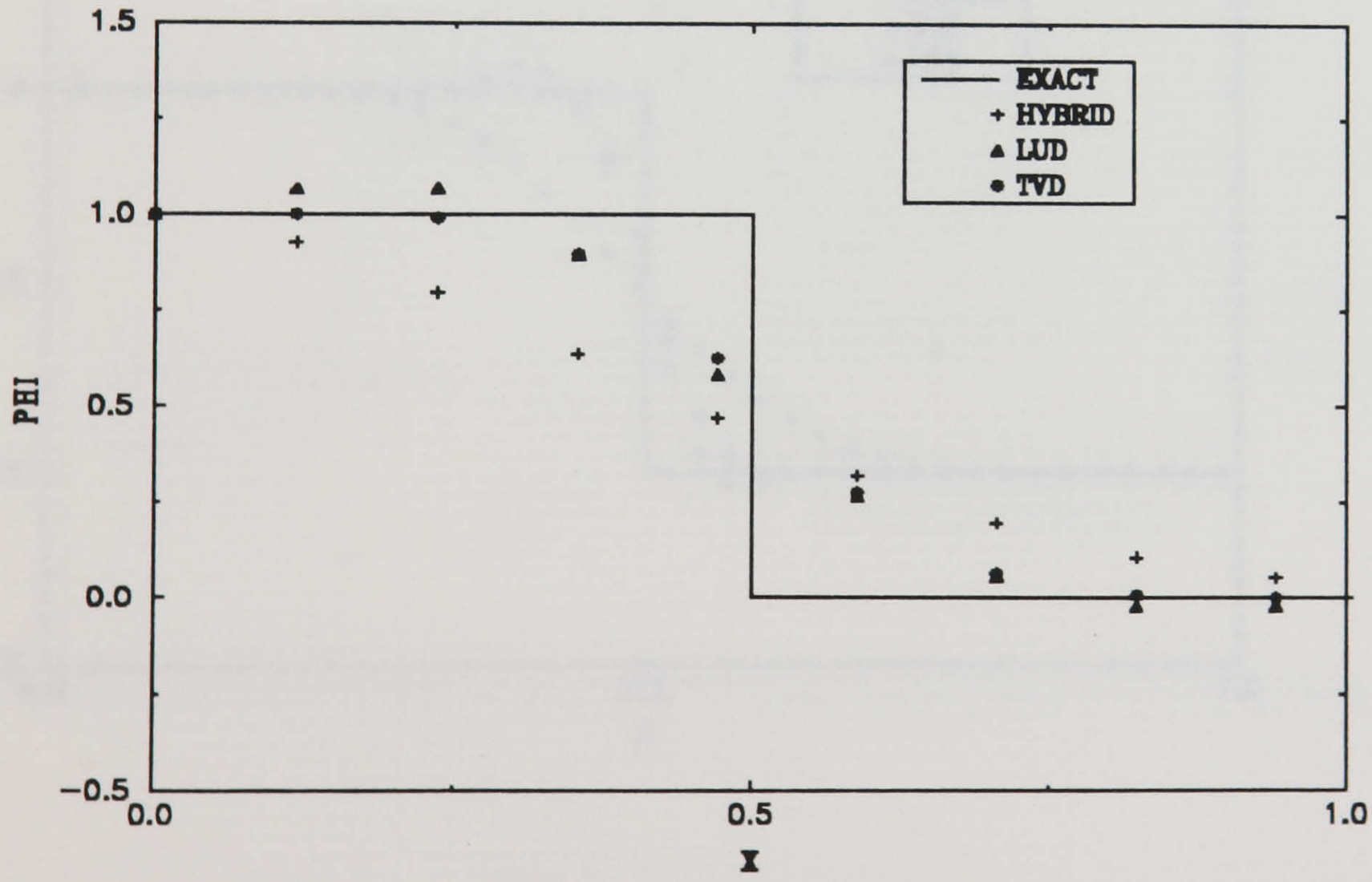



Figure.4.4a. Profiles for uniform flow for the IAHR problem (mesh size is 19x9).

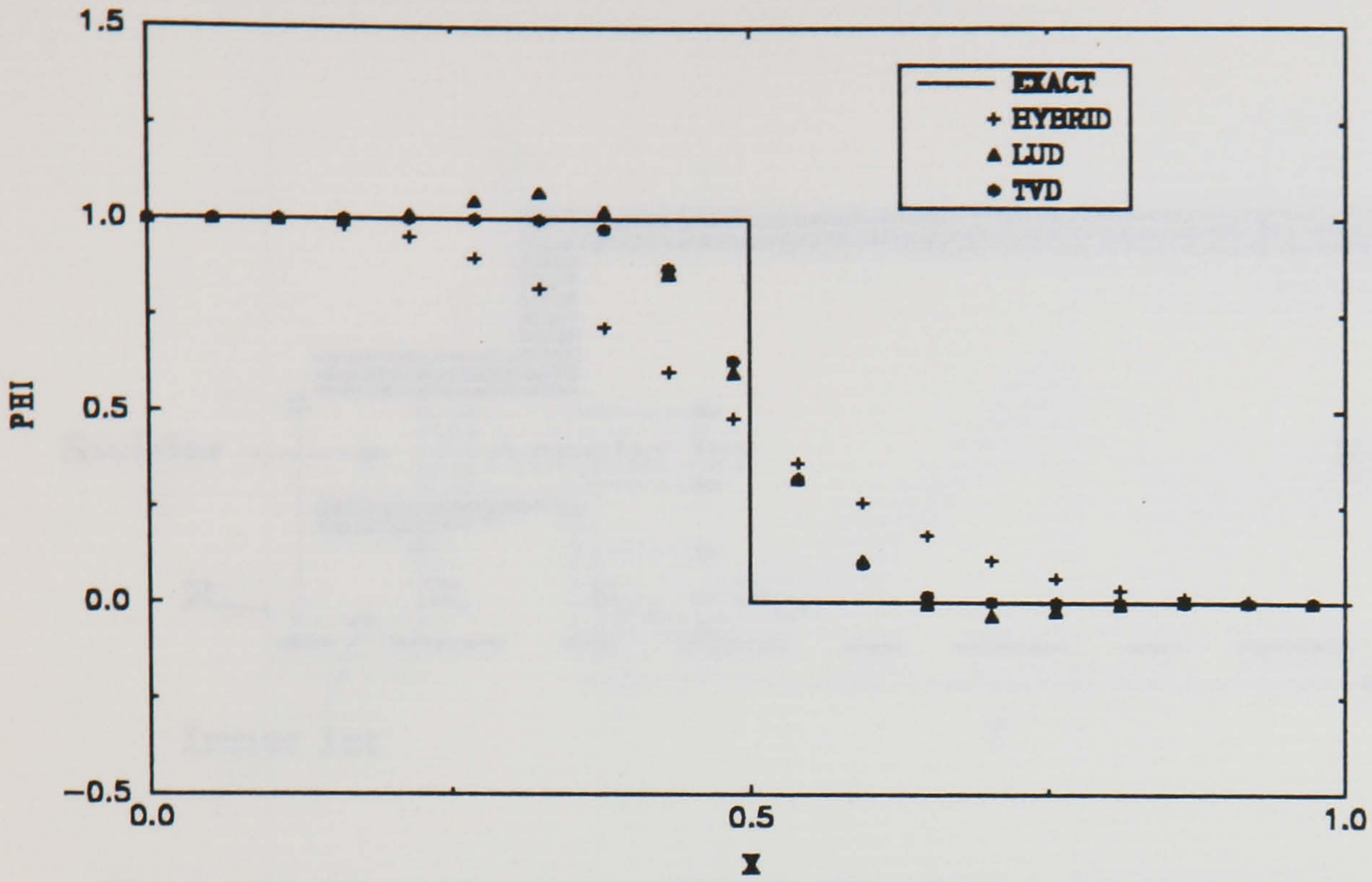



Figure.4.4b. Profiles for uniform flow for the IAHR problem (mesh size is 39x19).

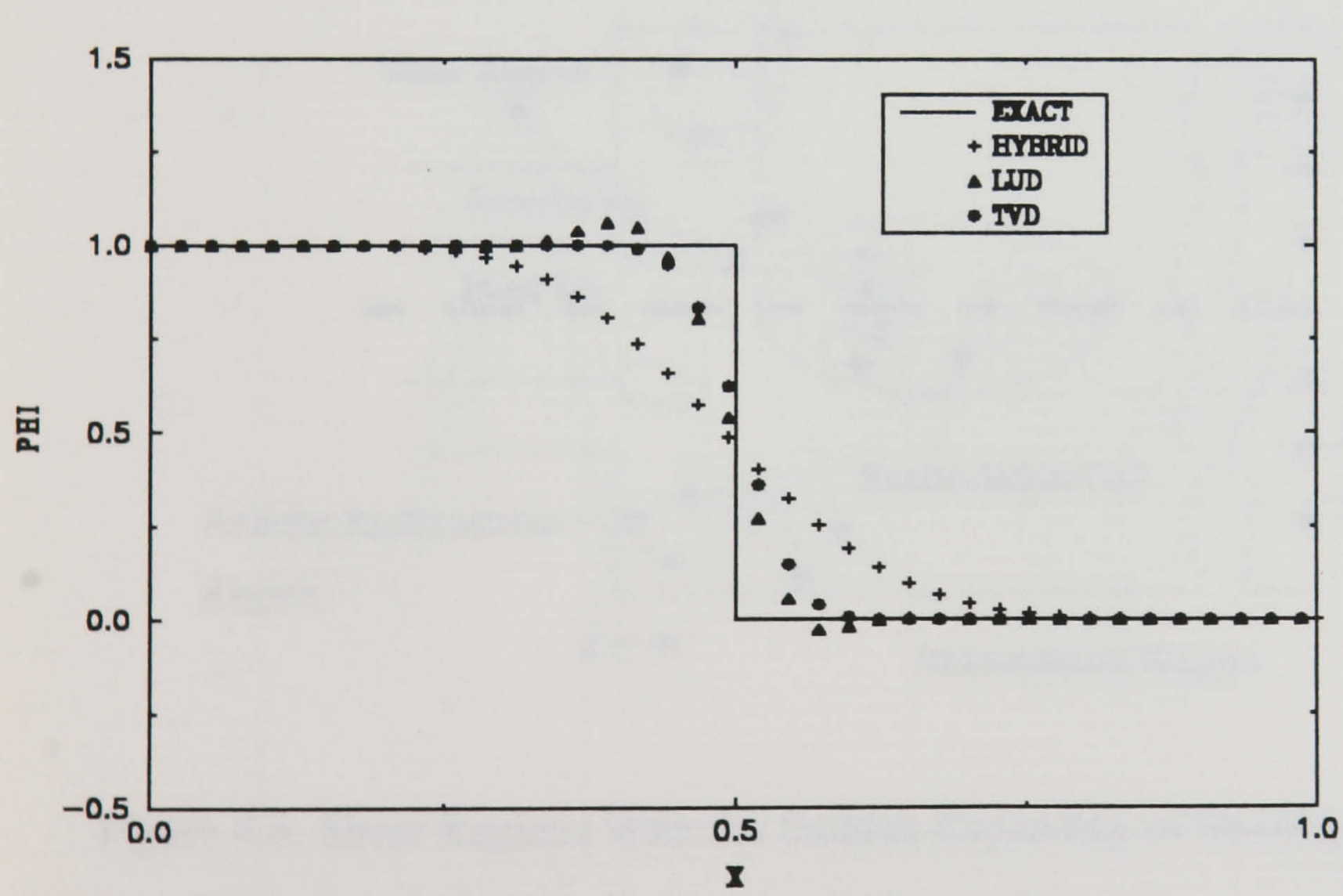



Figure.4.4c. Profiles for uniform flow for the IAHR problem (mesh size is 79x39).

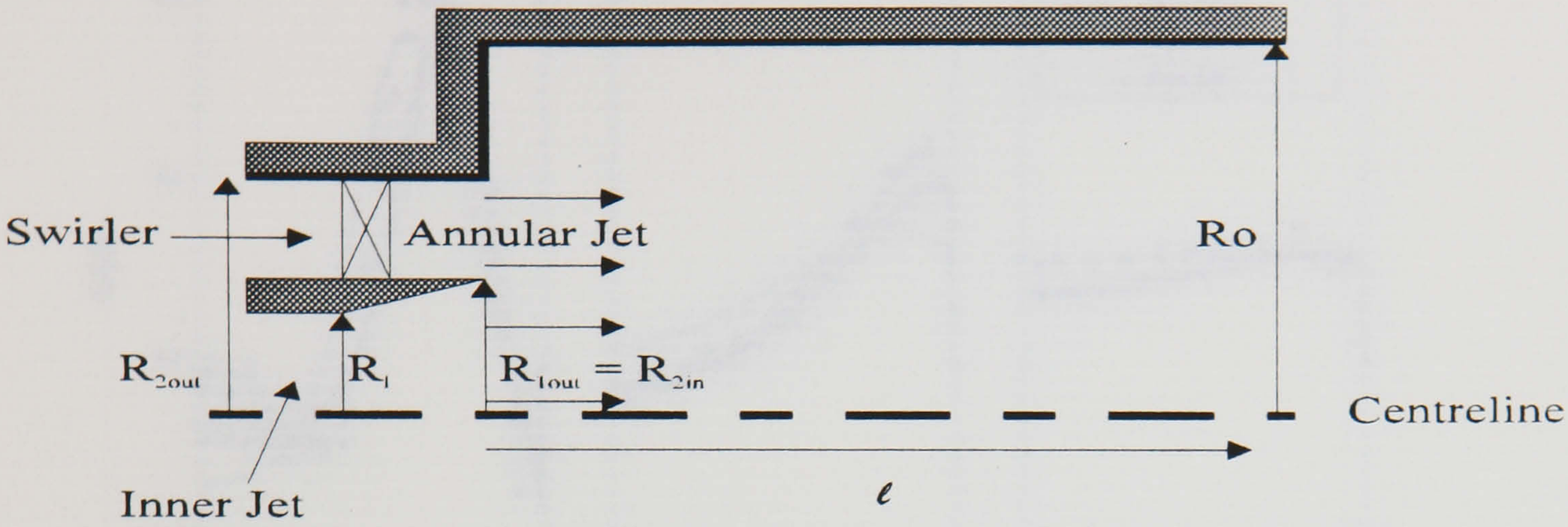



Figure.4.5. Flow Geometry of the Sudden Expansion of Swirling Coaxial Water Jets.

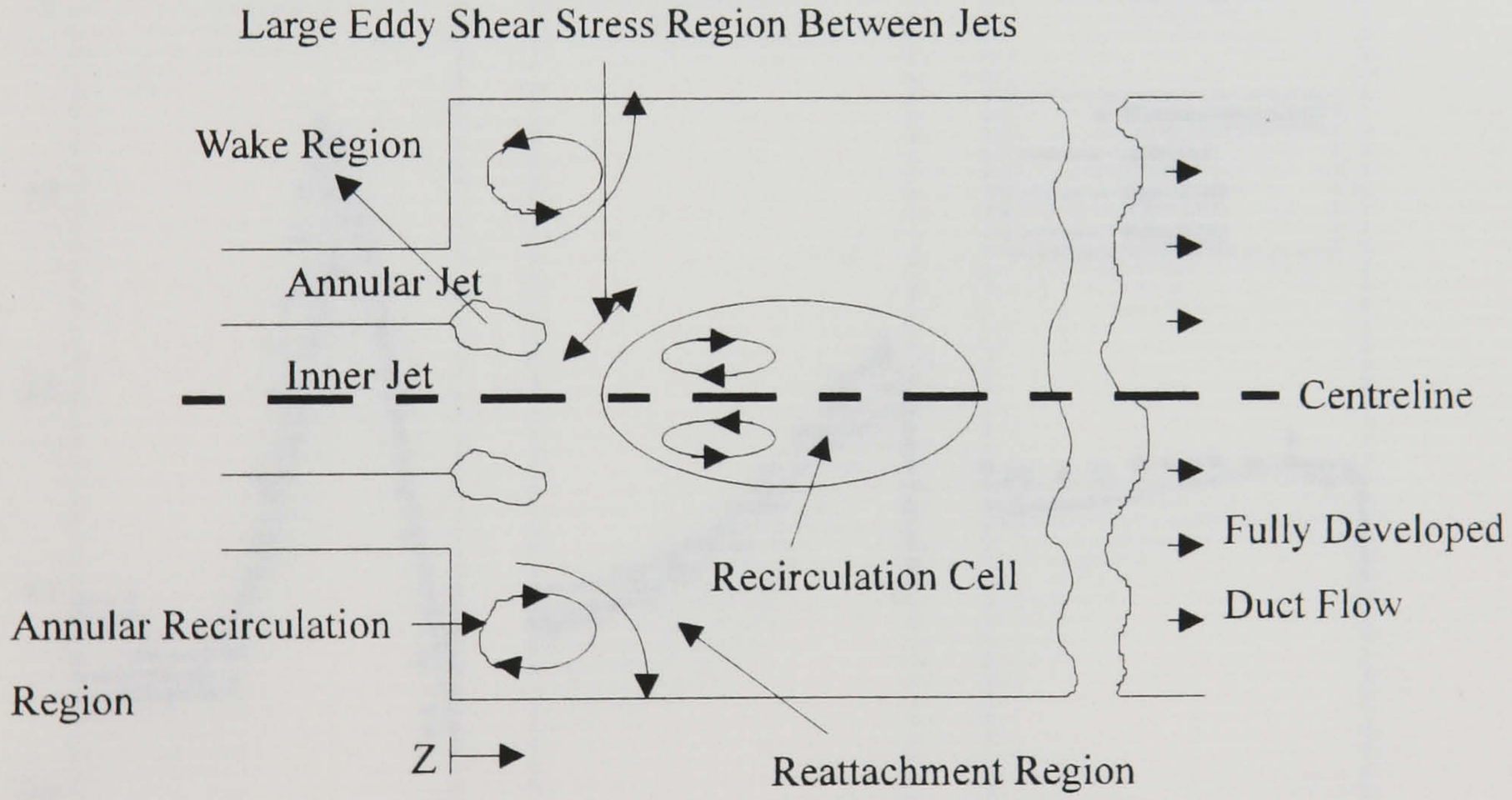



Figure.4.6. Shear Regions With the Sudden Expanding of Swirling Coaxial Water Jets.

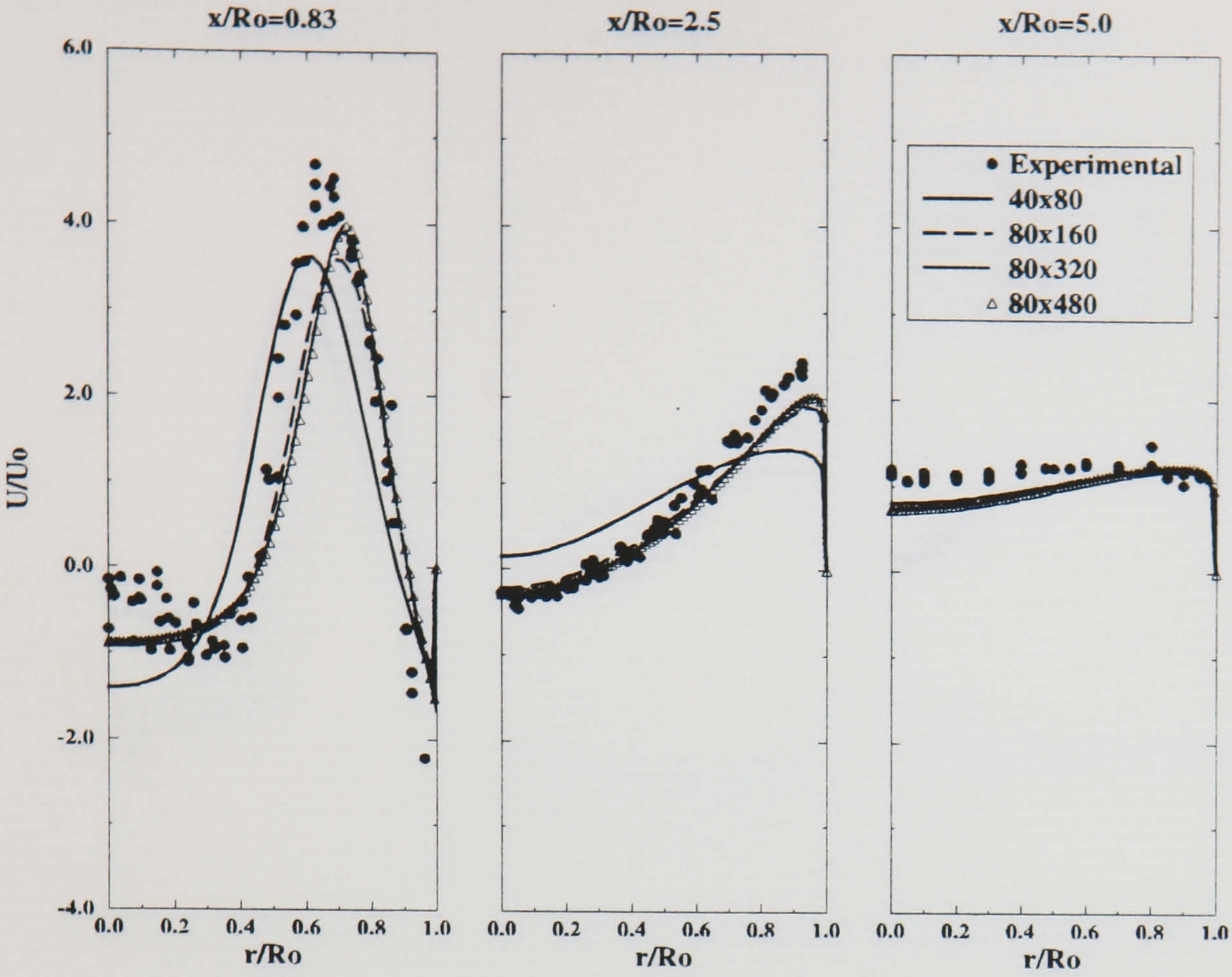



Figure.4.7a. Prediction of the U axial velocity using $\kappa$ - $\varepsilon$ turbulence model and Hybrid scheme.

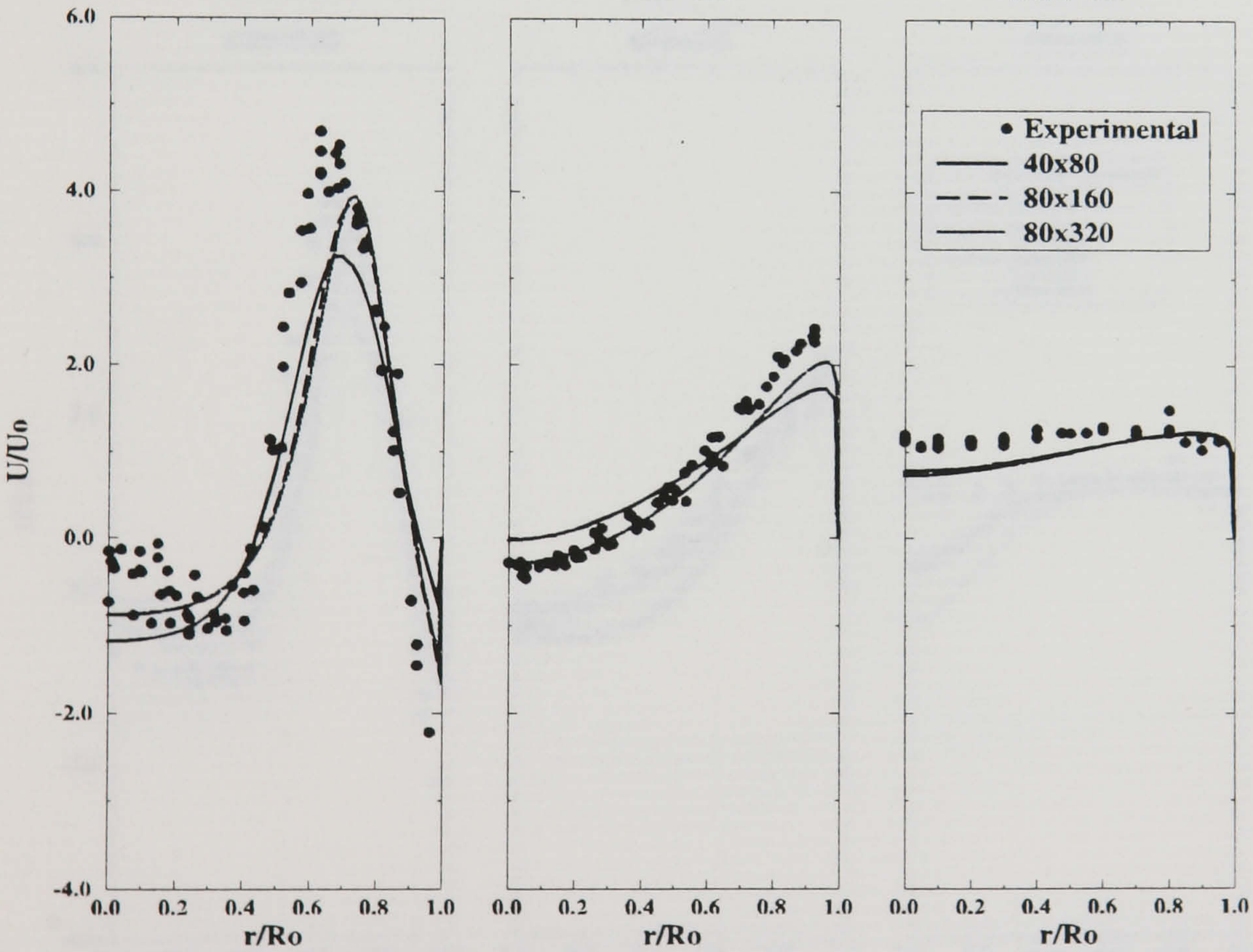



Figure.4.7b. Prediction of the U axial velocity using $\kappa$ - $\varepsilon$ turbulence model and TVD scheme.

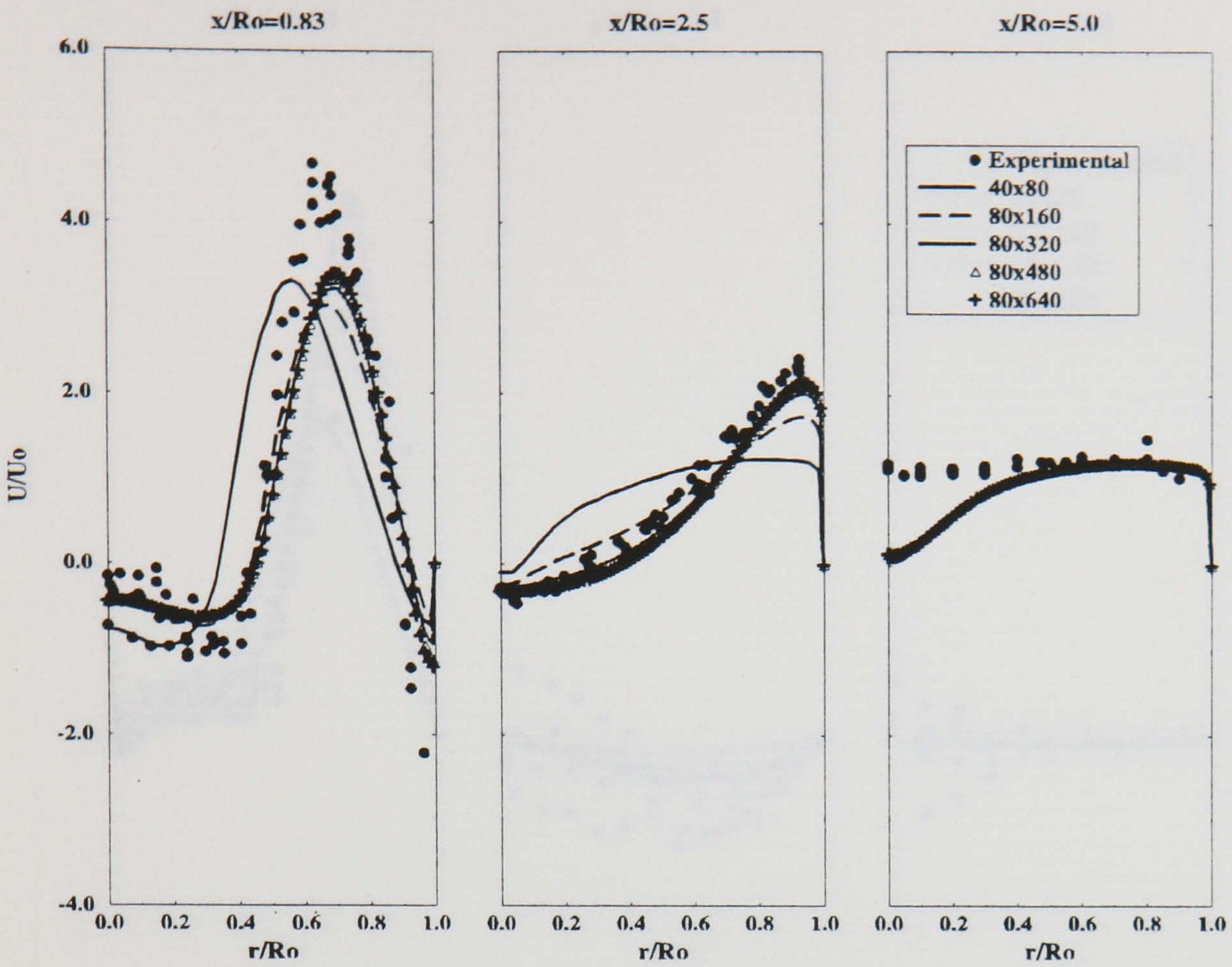



Figure.4.7c. Prediction of the U axial velocity using Reynolds Stress turbulence model and Hybrid scheme.

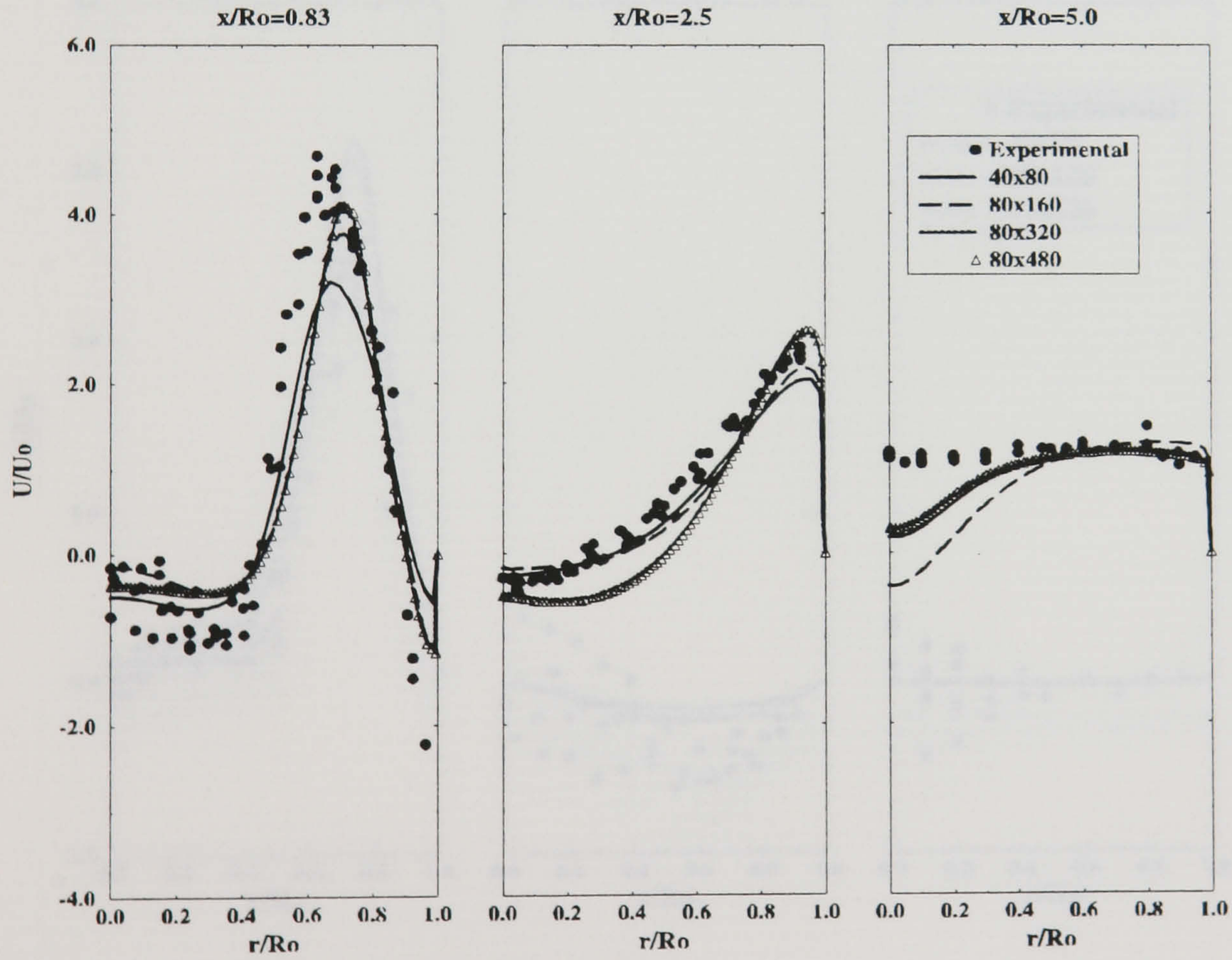



Figure.4.7d. Prediction of the U axial velocity using Reynolds Stress turbulence model and TVD scheme.

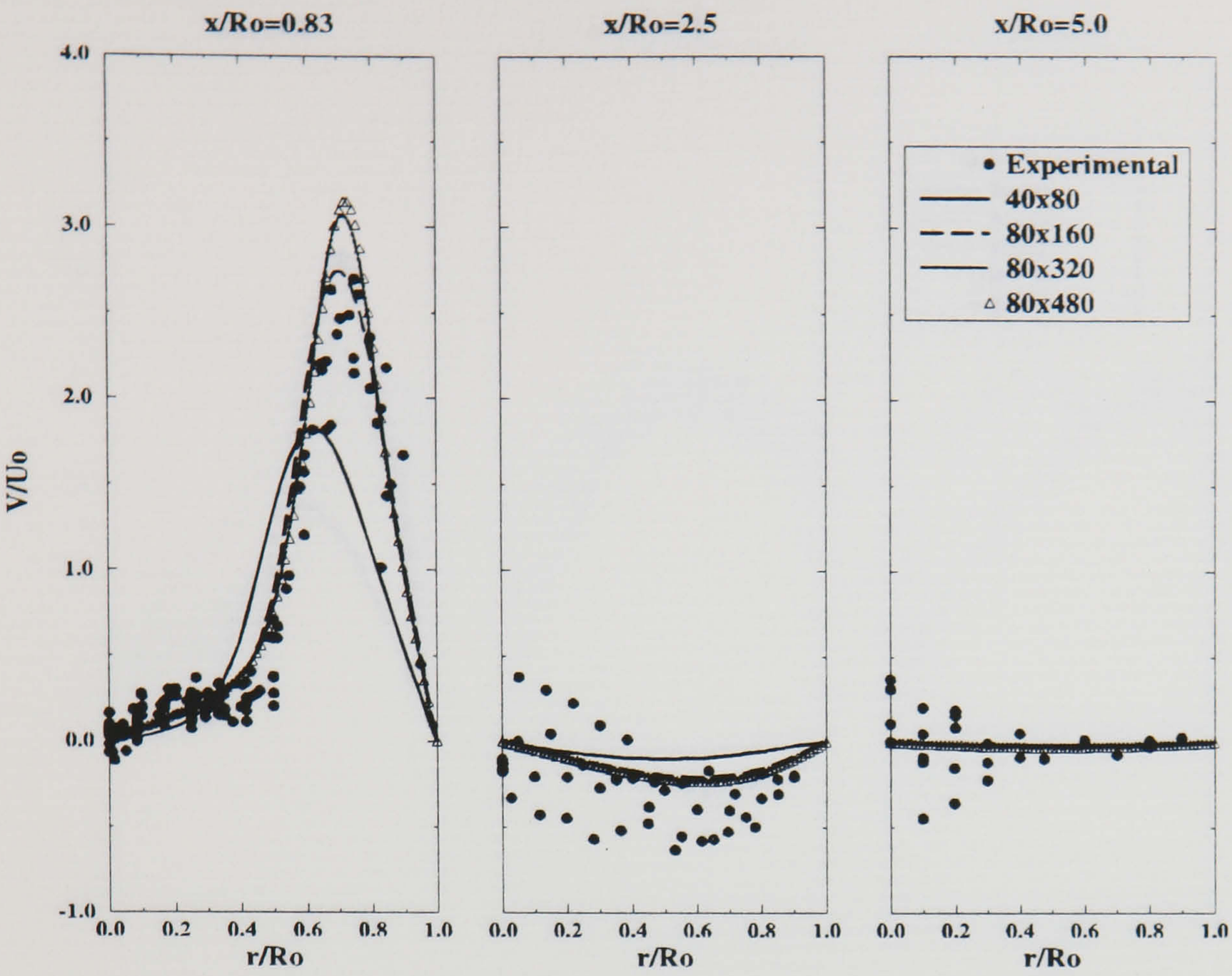



Figure.4.8a. Prediction of the V radial velocity using $\kappa$ - $\varepsilon$ turbulence model and Hybrid scheme.

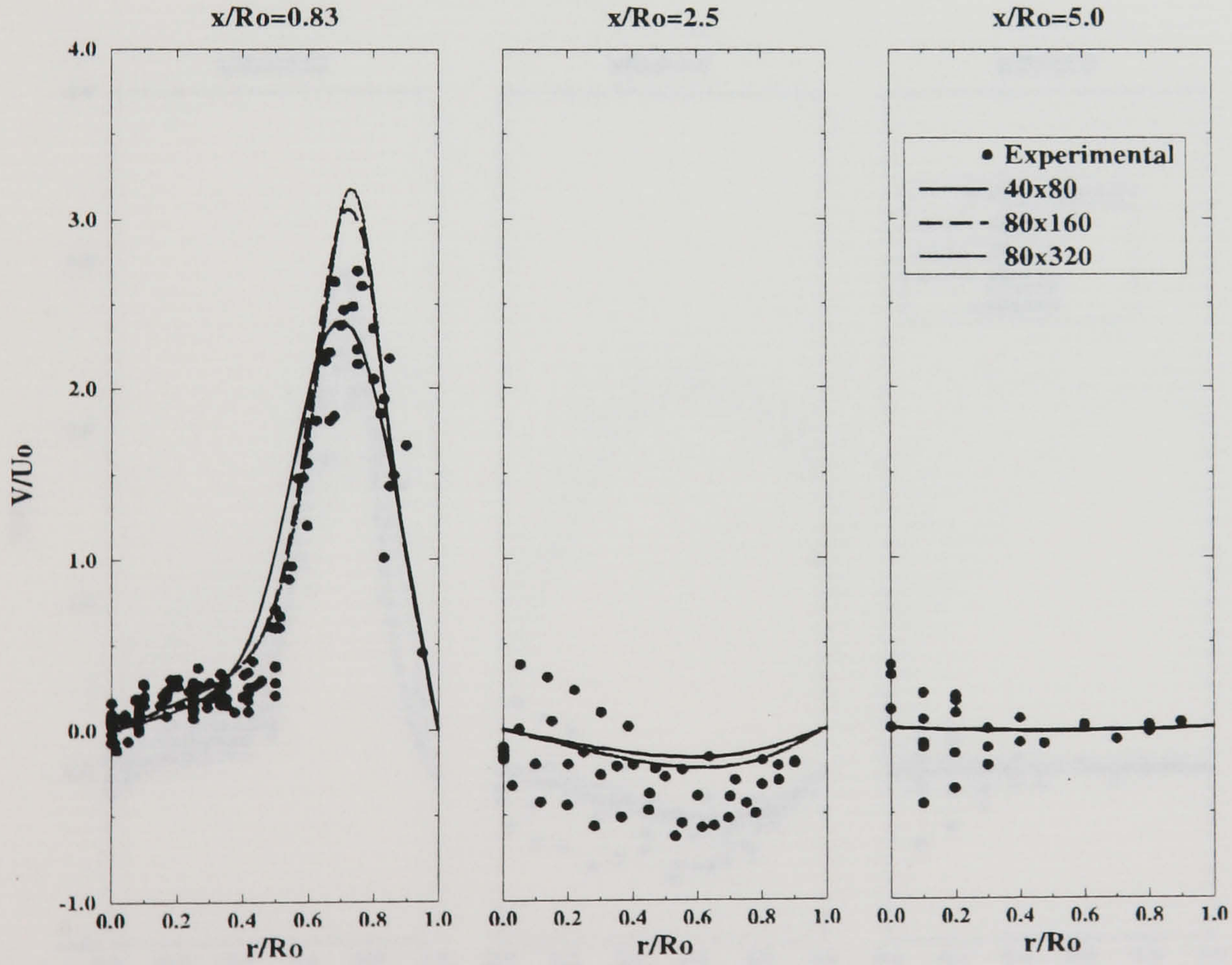



Figure.4.8b. Prediction of the V radial velocity using $\kappa$ - $\varepsilon$ turbulence model and TVD scheme.

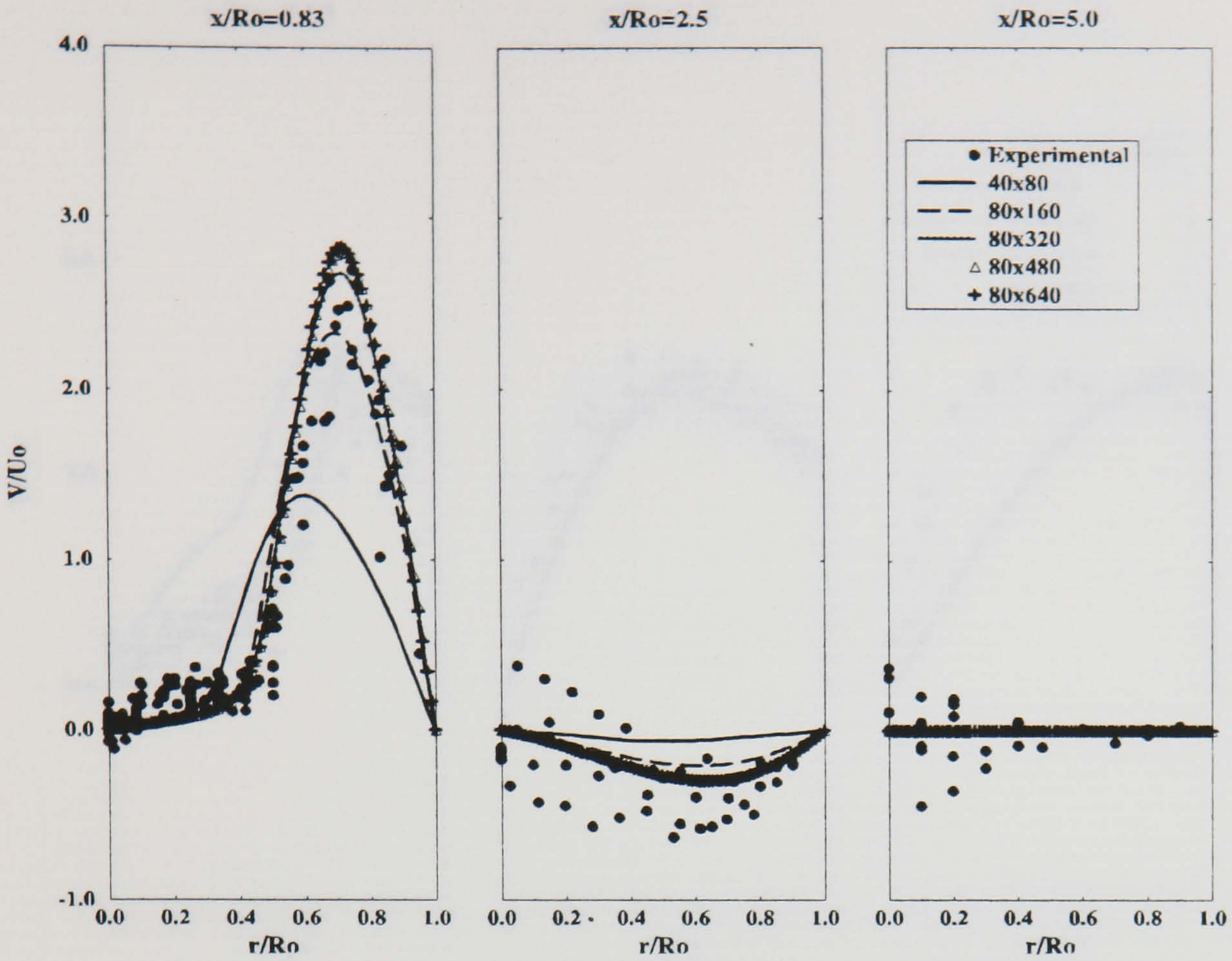



Figure.4.8c. Prediction of the V radial velocity using Reynolds Stress turbulence model and Hybrid scheme.

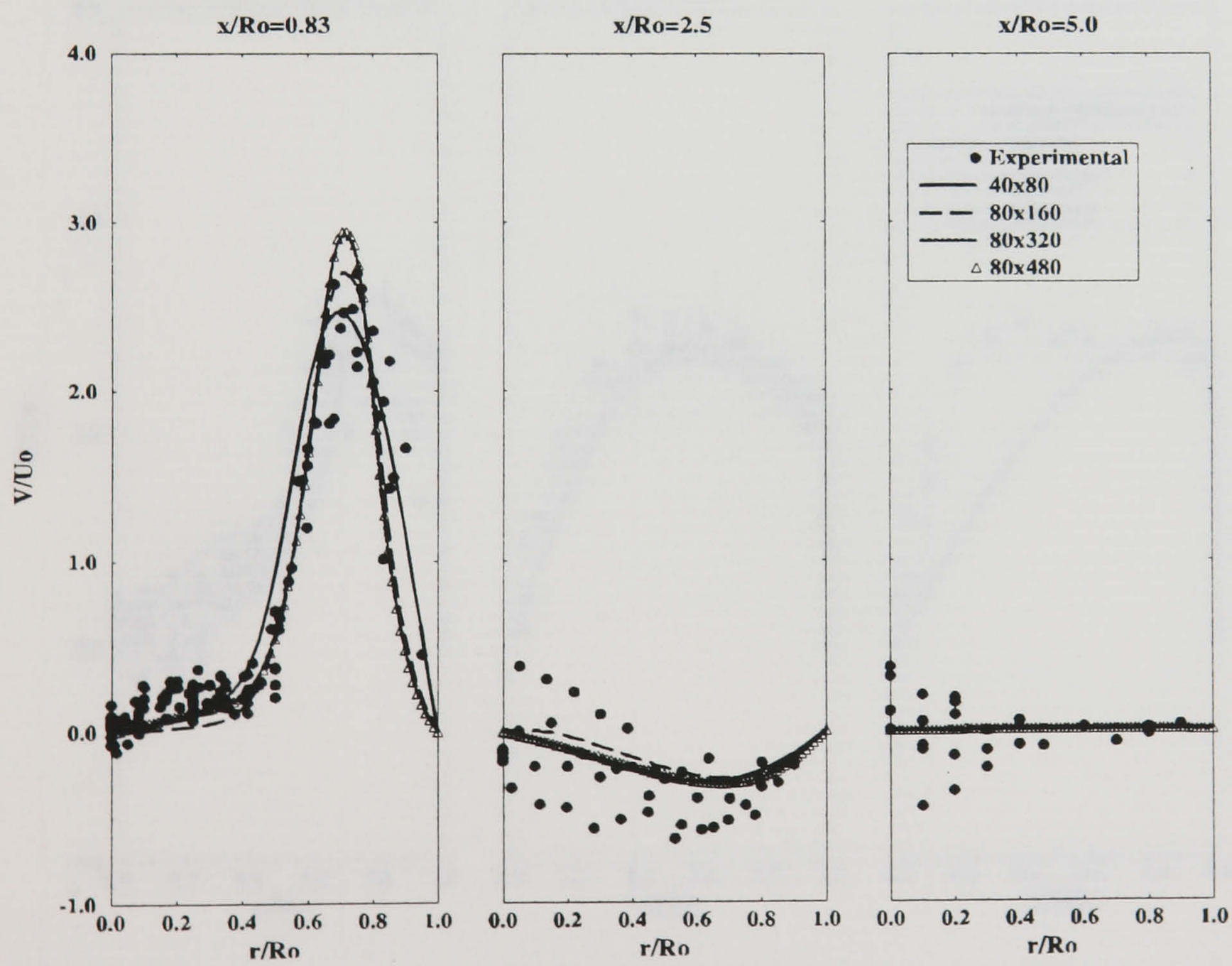



Figure.4.8d. Prediction of the V radial velocity using Reynolds Stress turbulence model and TVD scheme.

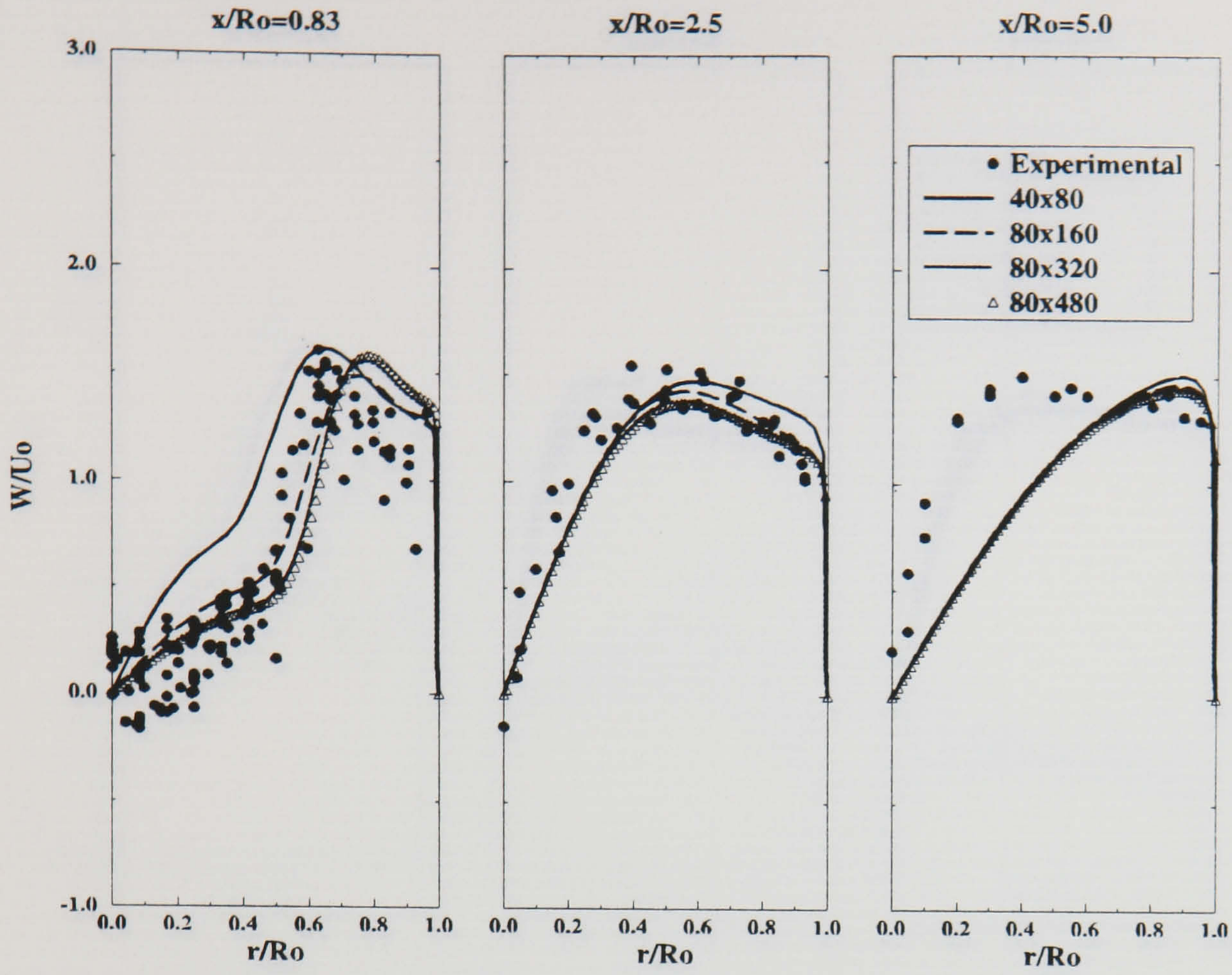



Figure.4.9a. Prediction of the W angular velocity using $\kappa$ - $\varepsilon$ turbulence model and Hybrid scheme.

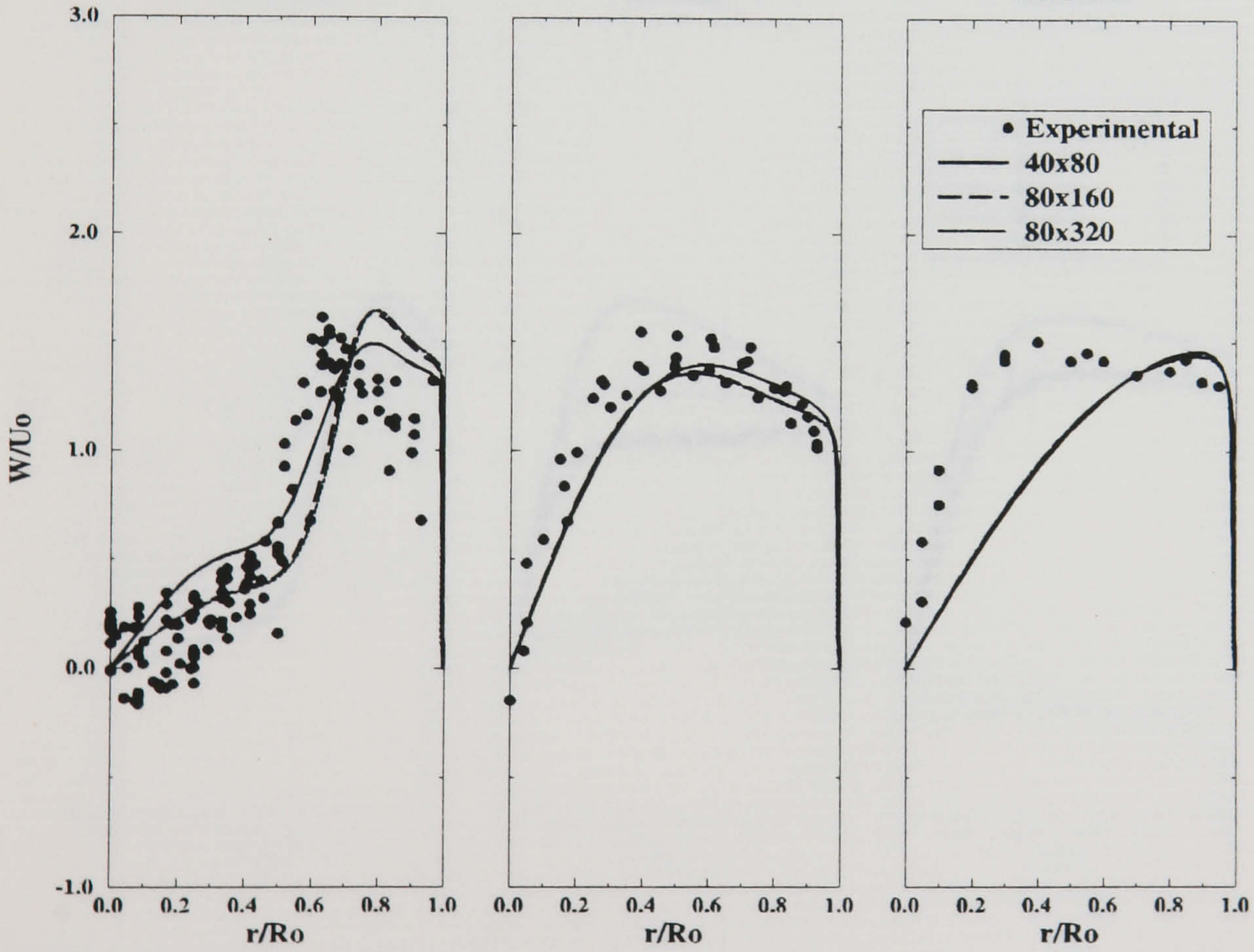



Figure.4.9b. Prediction of the W angular velocity using $\kappa$ - $\varepsilon$ turbulence model and TVD scheme.

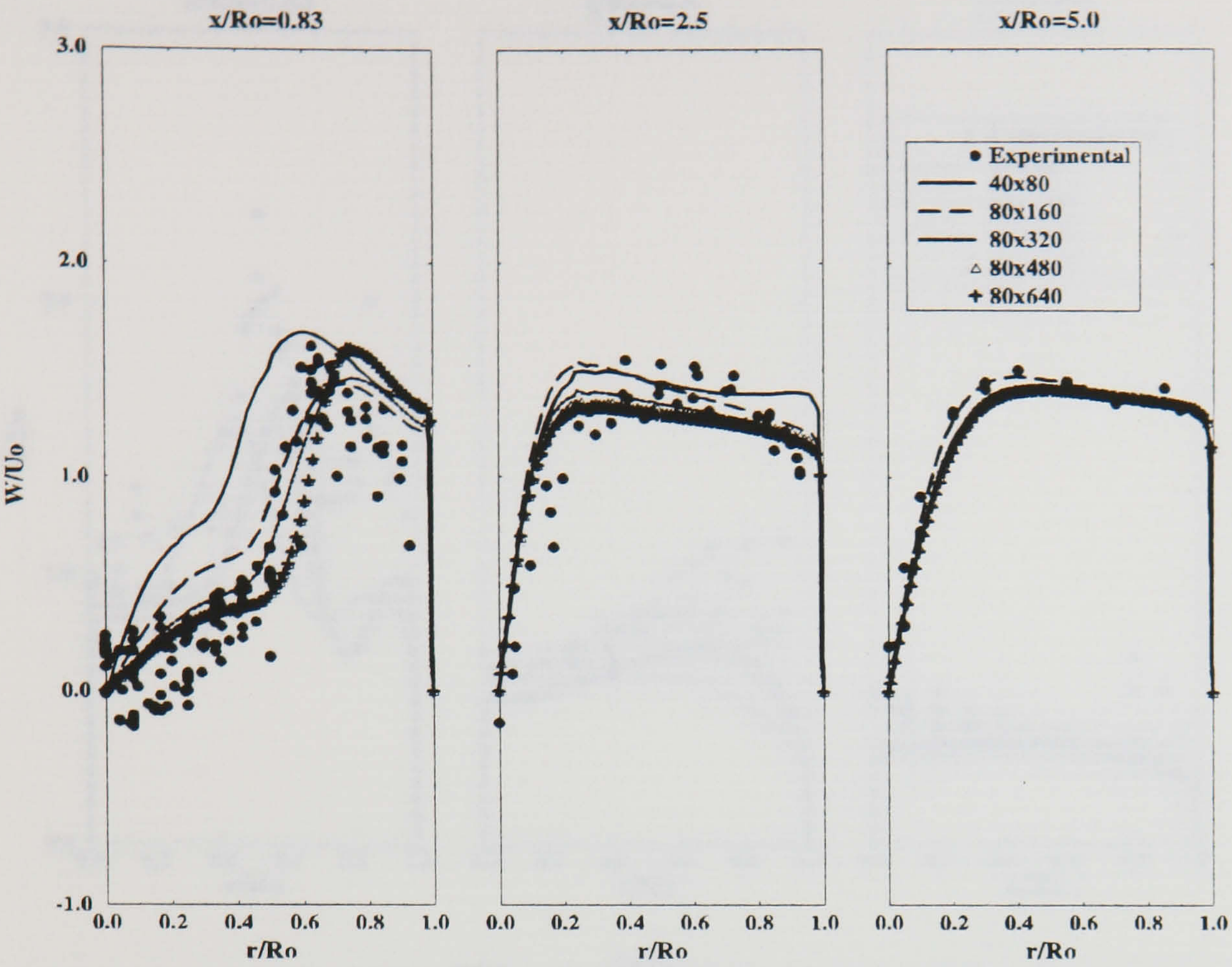



Figure.4.9c. Prediction of the W angular velocity using Reynolds Stress turbulence model and Hybrid scheme.

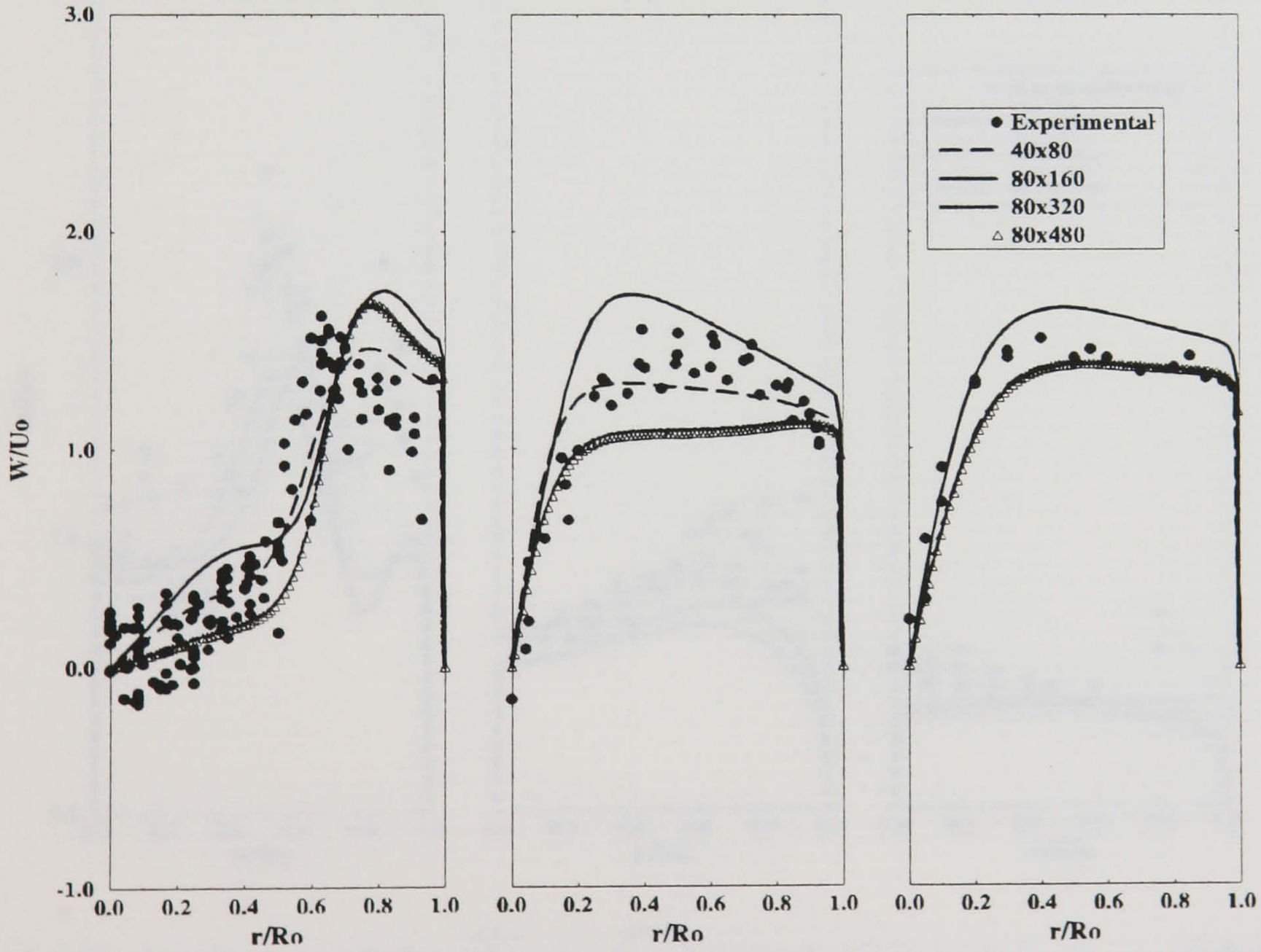



Figure.4.9d. Prediction of the W angular velocity using Reynolds Stress turbulence model and TVD scheme.

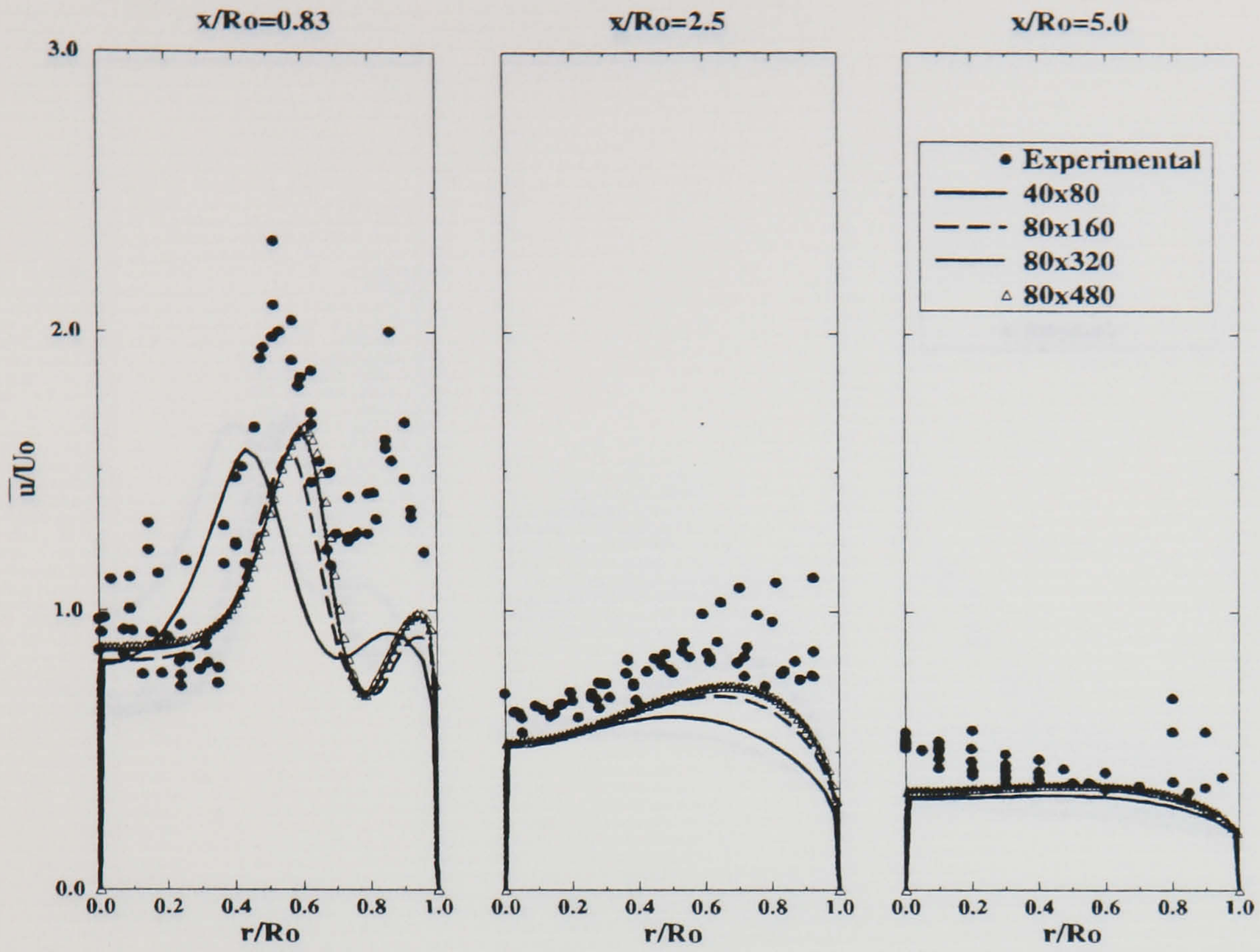



Figure.4.10a. Prediction of the $\bar{u}\left(\bar{u} = \sqrt{\overline{uu}}\right)$ normal stress using $\kappa$ - $\varepsilon$ turbulence model and Hybrid scheme.

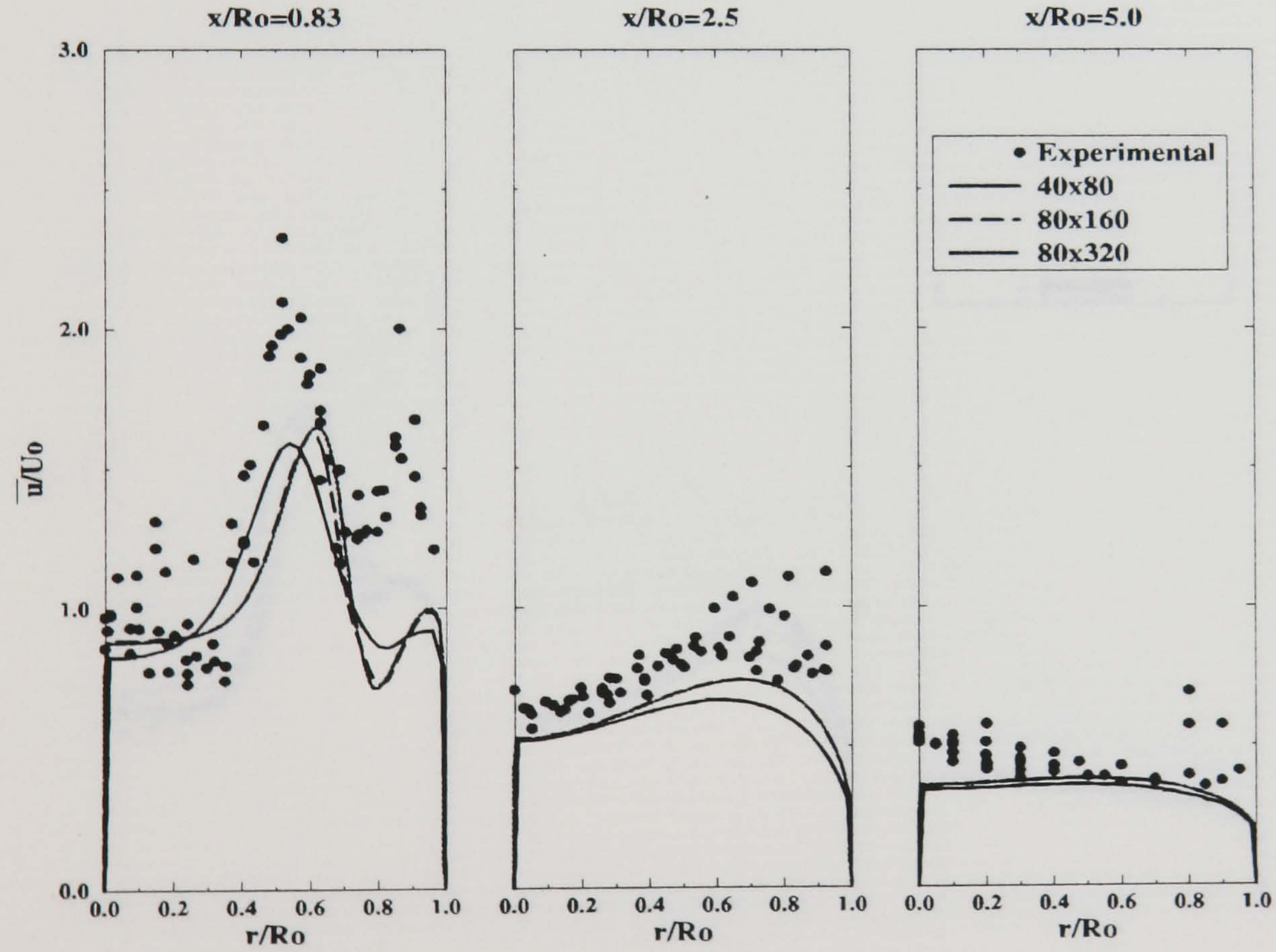



Figure.4.10b. Prediction of the $\bar{u}\left(\bar{u} = \sqrt{\overline{uu}}\right)$ normal stress using $\kappa$ - $\varepsilon$ turbulence model and TVD scheme.

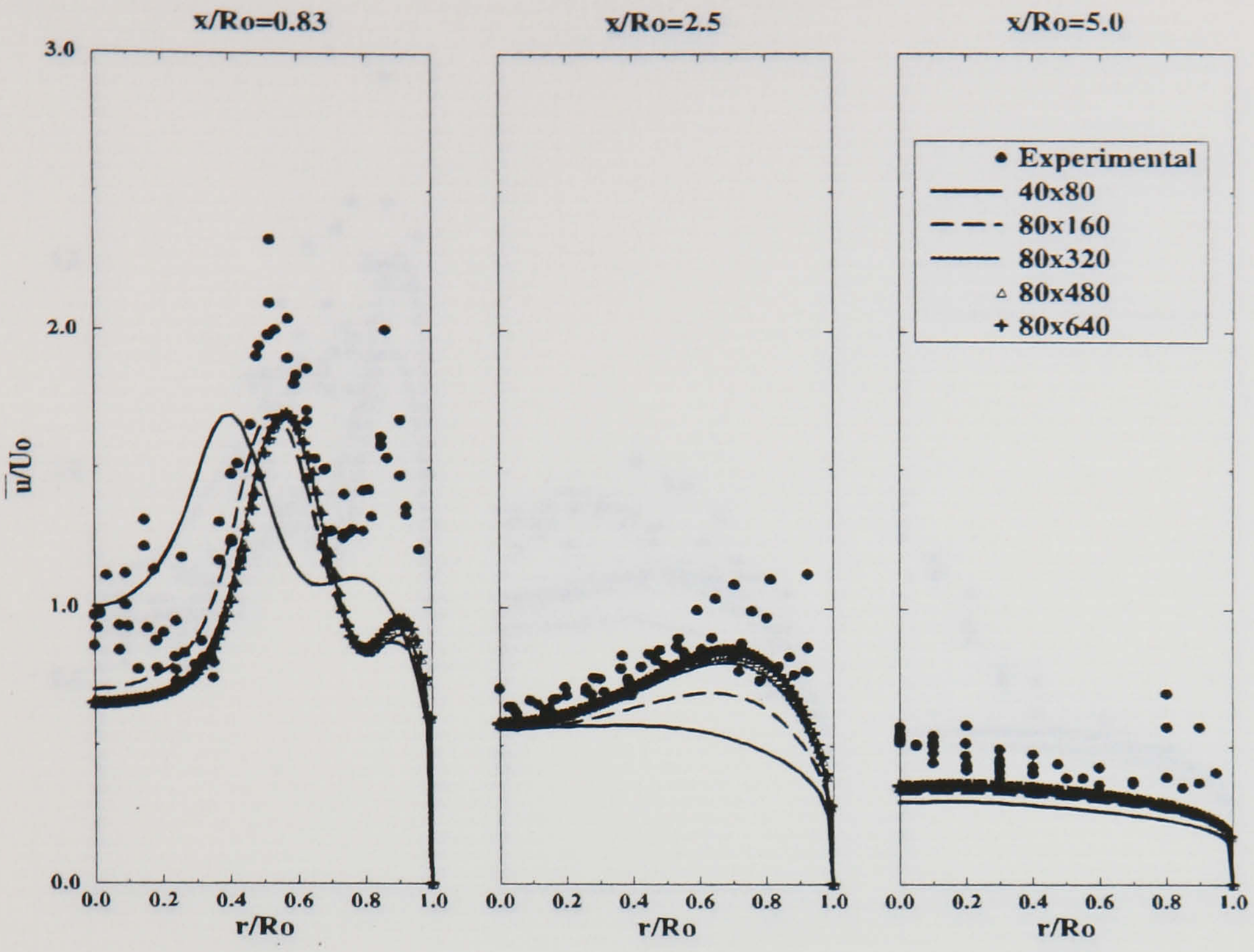



Figure.4.10c. Prediction of the $\bar{u}\left(\bar{u} = \sqrt{\overline{uu}}\right)$normal stress using Reynolds Stress turbulence model and Hybrid scheme.

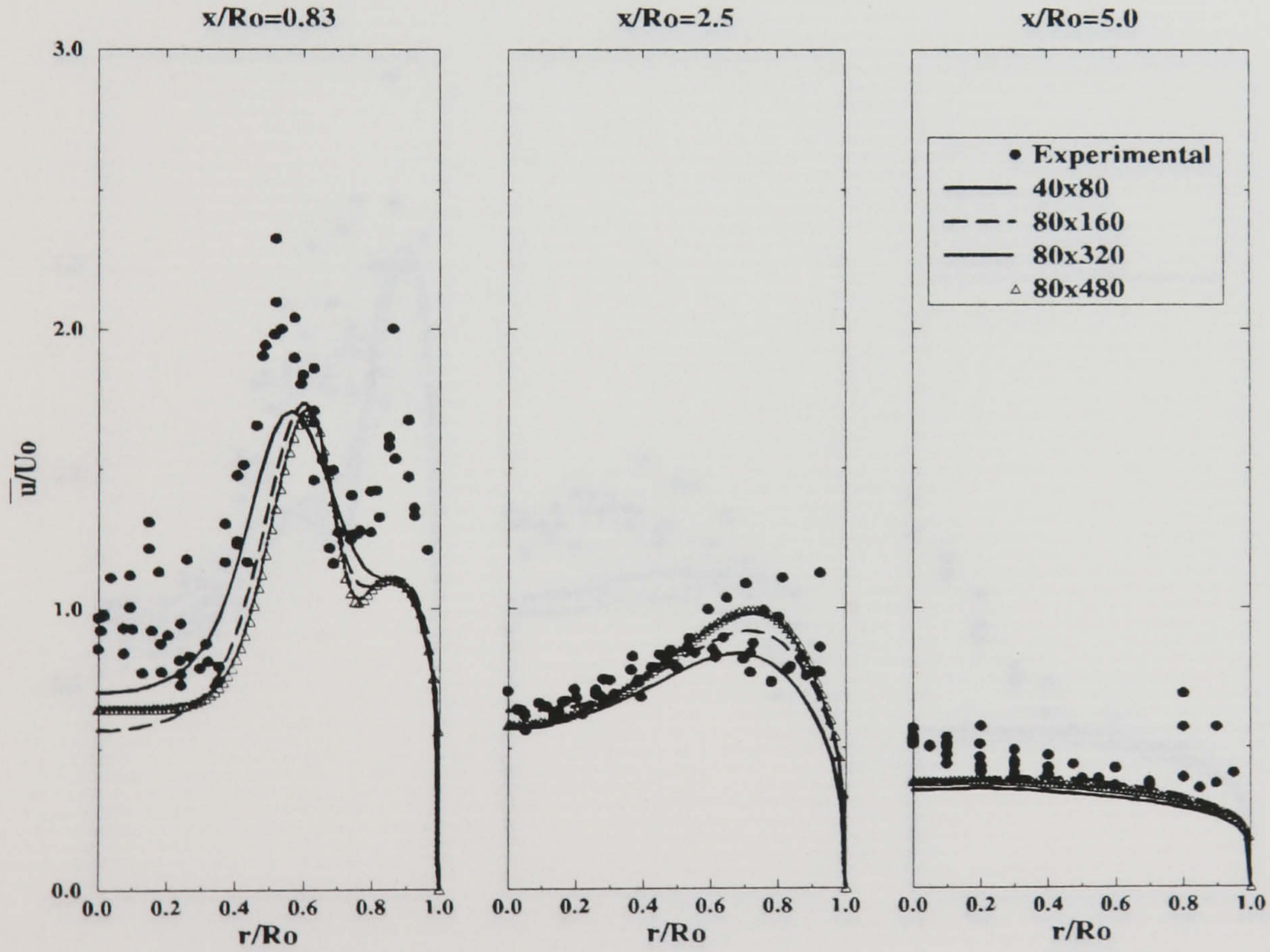



Figure.4.10d. Prediction of the $\bar{u}\left(\bar{u} = \sqrt{\overline{uu}}\right)$normal stress using Reynolds Stress turbulence model and TVD scheme.

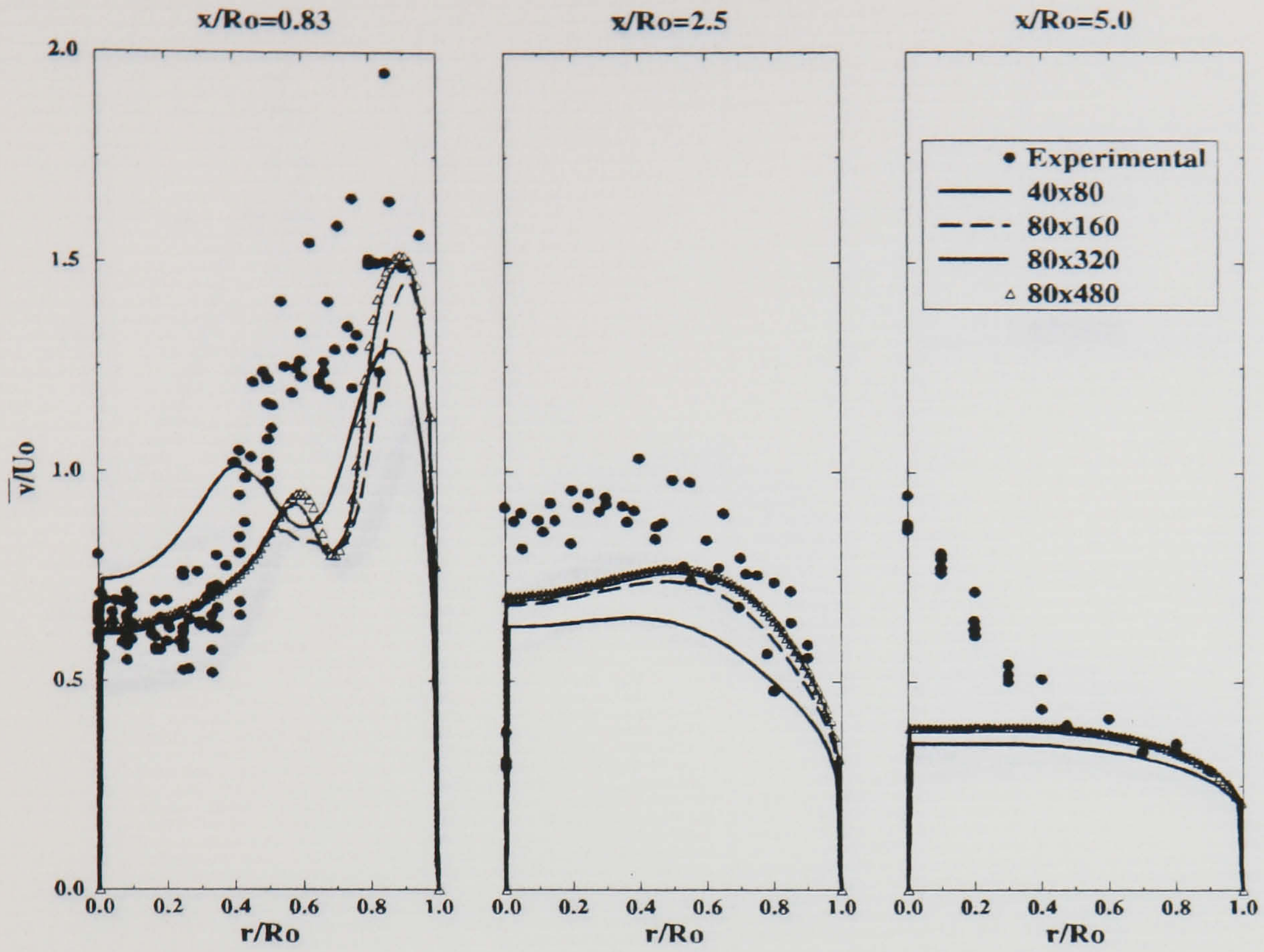



Figure.4.11a. Prediction of the $\bar{v}\left(\bar{v} = \sqrt{\overline{vv}}\right)$ normal stress using $\kappa$ - $\varepsilon$ turbulence model and Hybrid scheme.

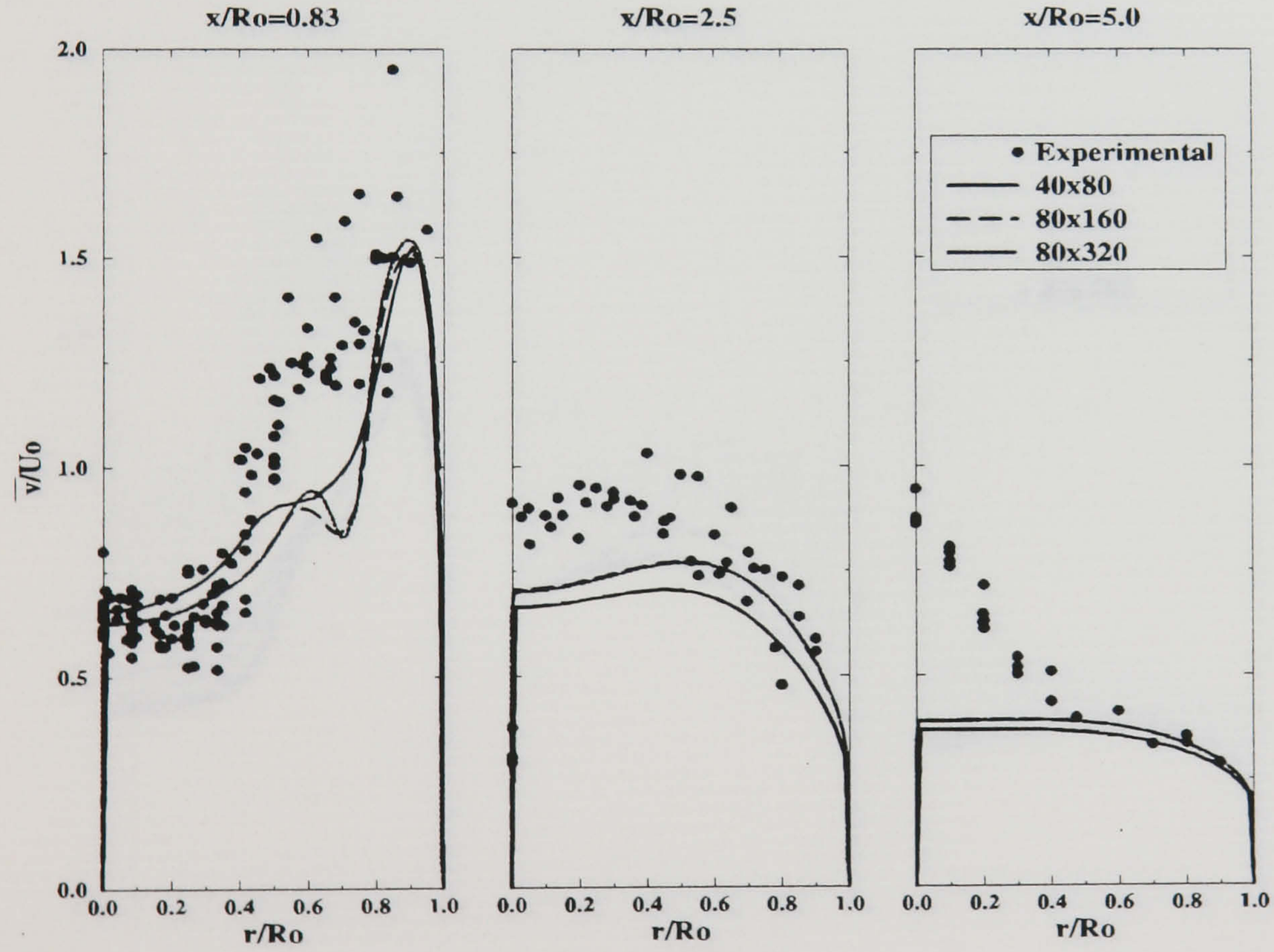



Figure.4.11b. Prediction of the $\bar{v}\left(\bar{v} = \sqrt{\overline{vv}}\right)$ normal stress using $\kappa$ - $\varepsilon$ turbulence model and TVD scheme.

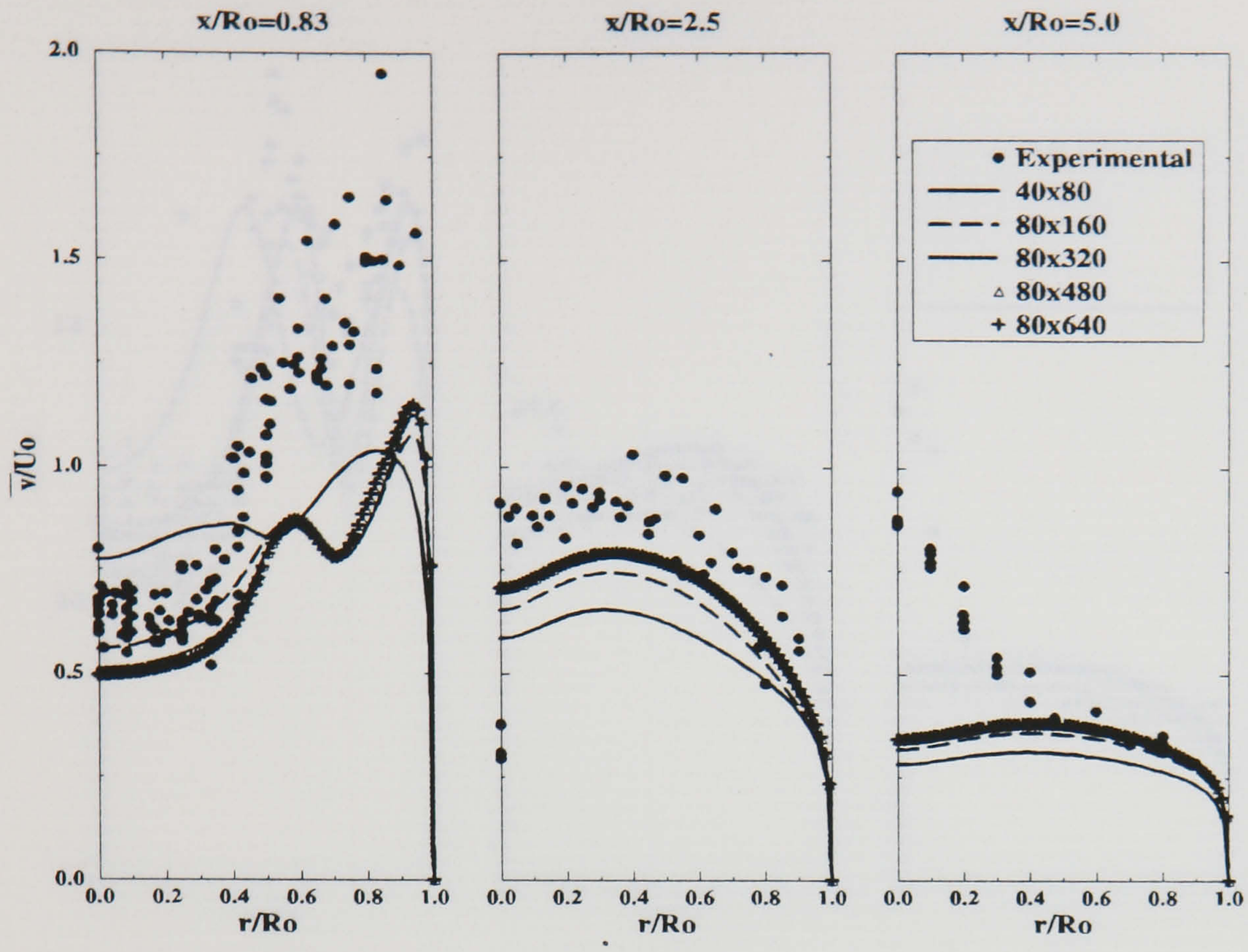



Figure.4.11c. Prediction of the $\overline{v}\left(\overline{v} = \sqrt{\overline{vv}}\right)$ normal stress using Reynolds Stress turbulence model and Hybrid scheme.

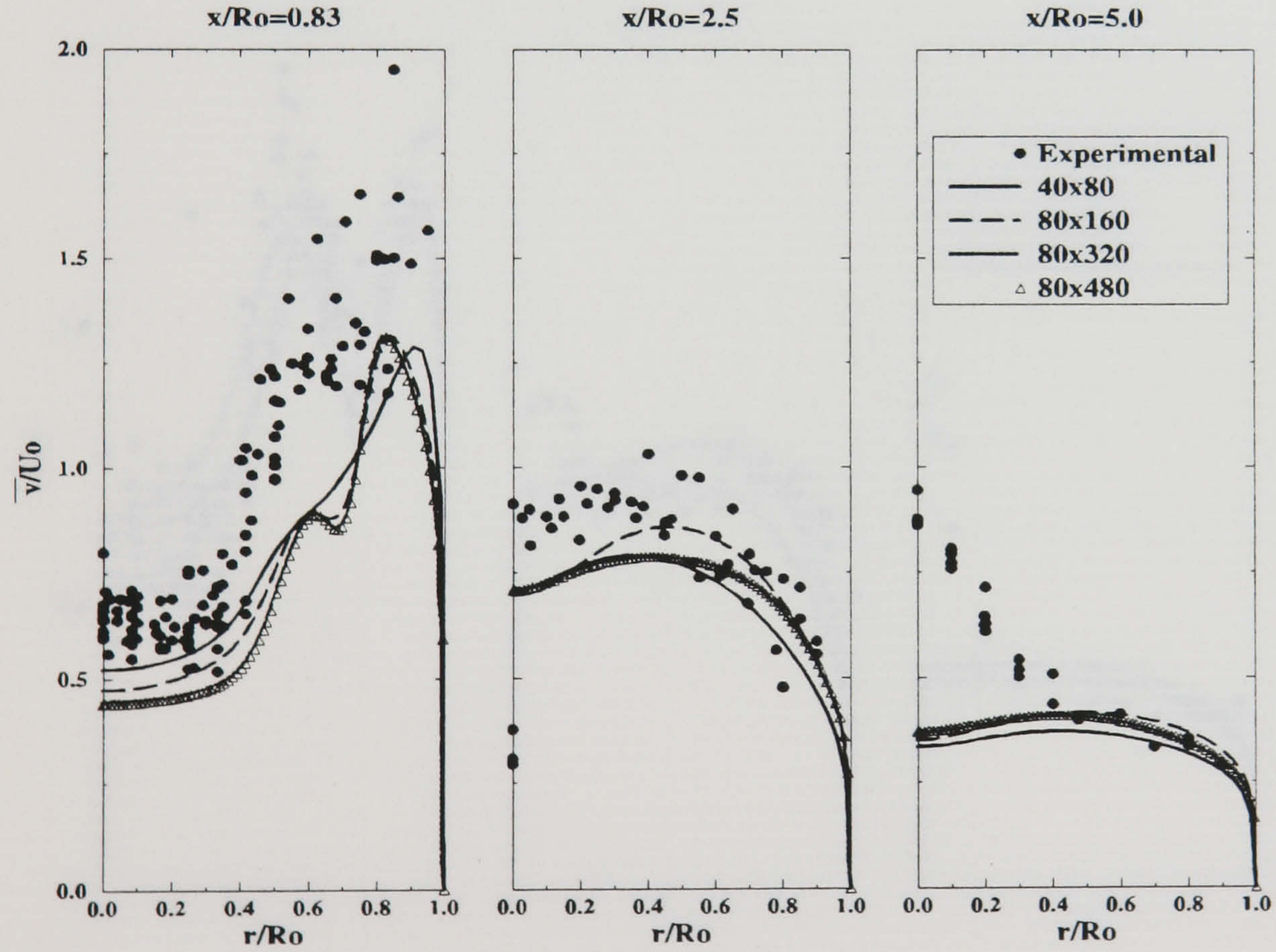



Figure.4.11d. Prediction of the $\overline{v}\left(\overline{v} = \sqrt{\overline{vv}}\right)$ normal stress using Reynolds Stress turbulence model and TVD scheme.

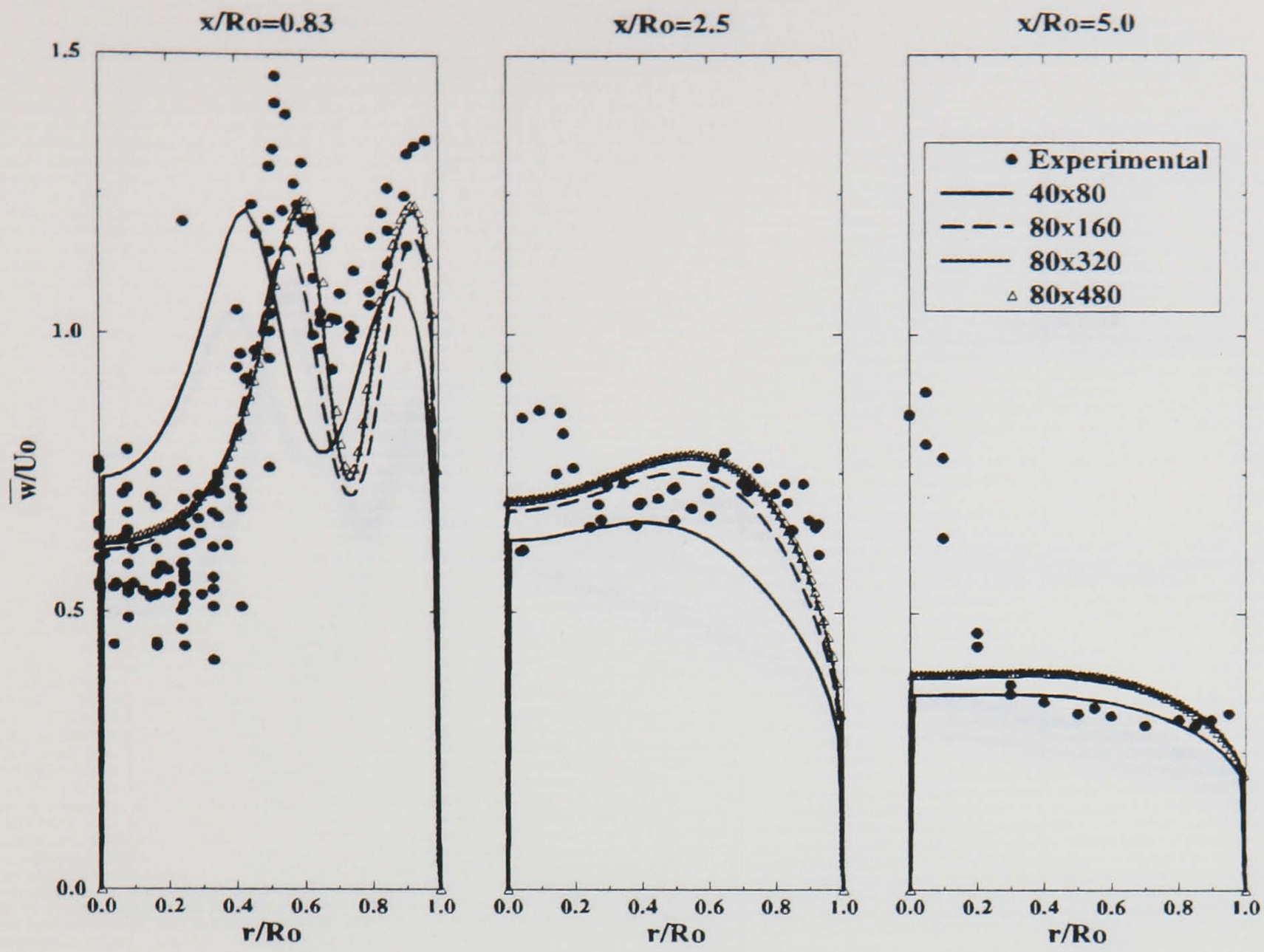



Figure.4.12a. Prediction of the $\overline{w}\left(\overline{w} = \sqrt{\overline{ww}}\right)$ normal stress using $\kappa$ - $\varepsilon$ turbulence model and Hybrid scheme.

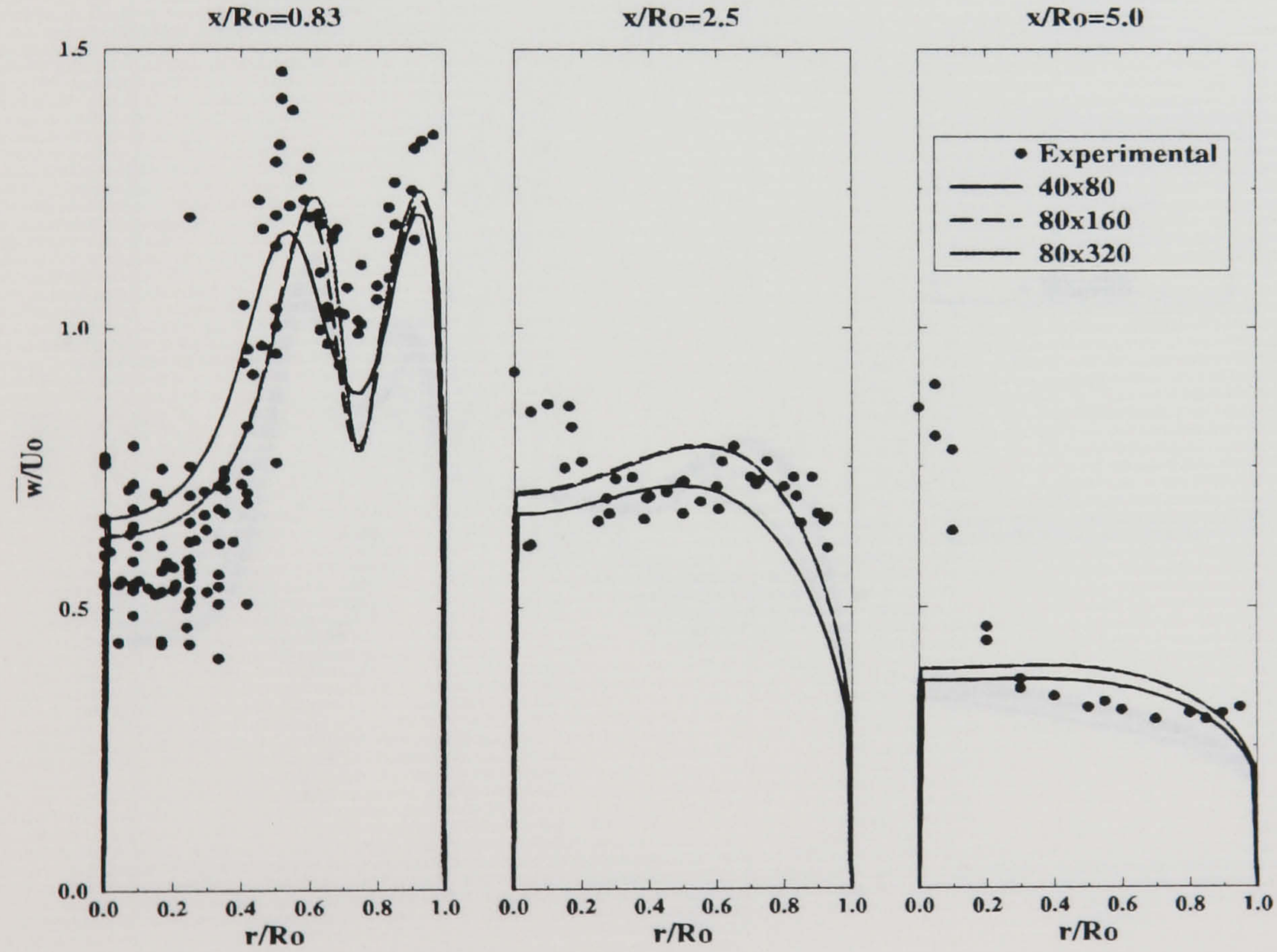



Figure.4.12b. Prediction of the $\overline{w}\left(\overline{w} = \sqrt{\overline{ww}}\right)$ normal stress using $\kappa$ - $\varepsilon$ turbulence model and TVD scheme.

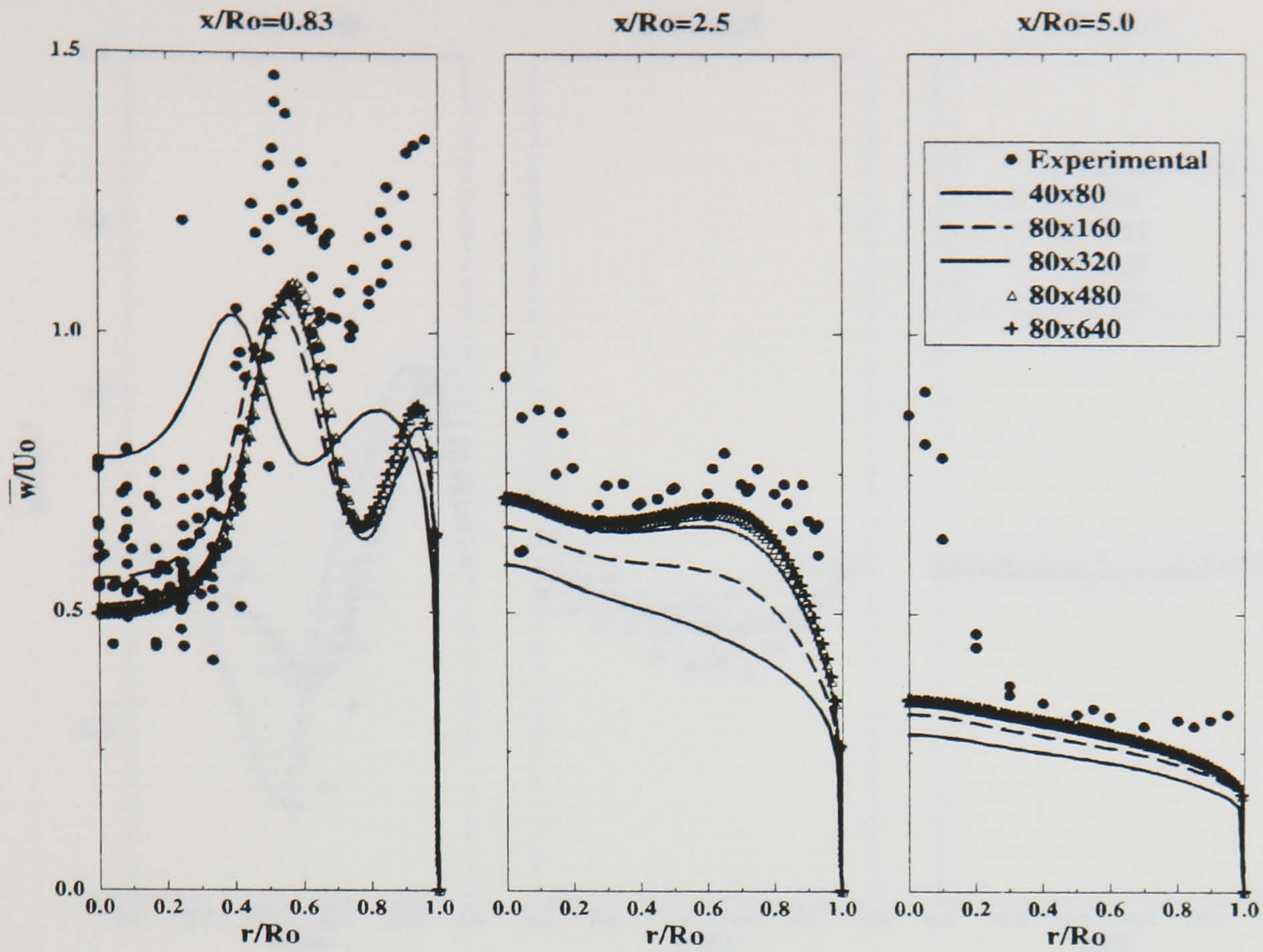



Figure.4.12c. Prediction of the $\overline{w}\left(\overline{w} = \sqrt{\overline{ww}}\right)$ normal stress using Reynolds Stress turbulence model and Hybrid scheme.

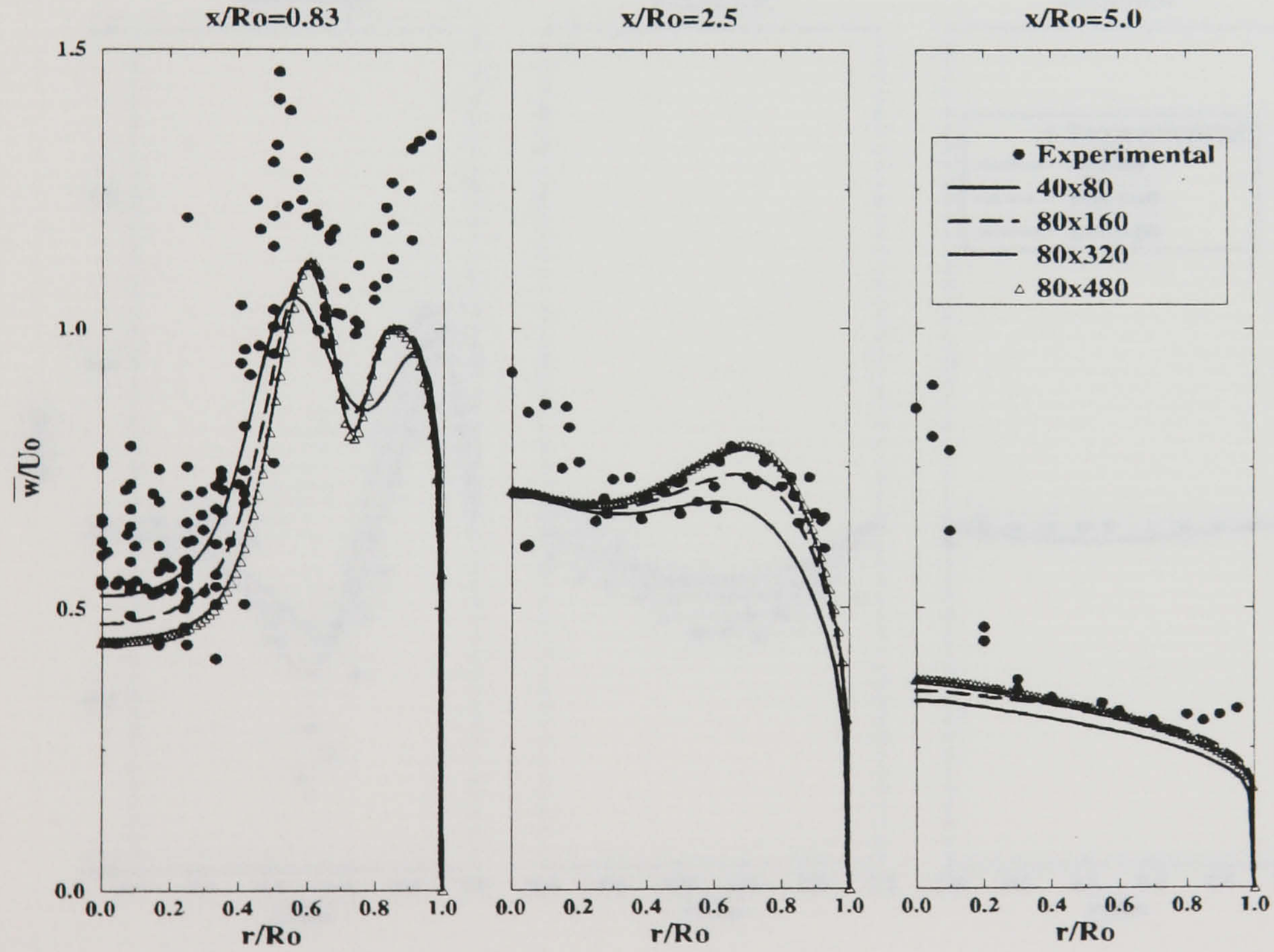



Figure.4.12d. Prediction of the $\overline{w}\left(\overline{w} = \sqrt{\overline{ww}}\right)$ normal stress using Reynolds Stress turbulence model and TVD scheme.

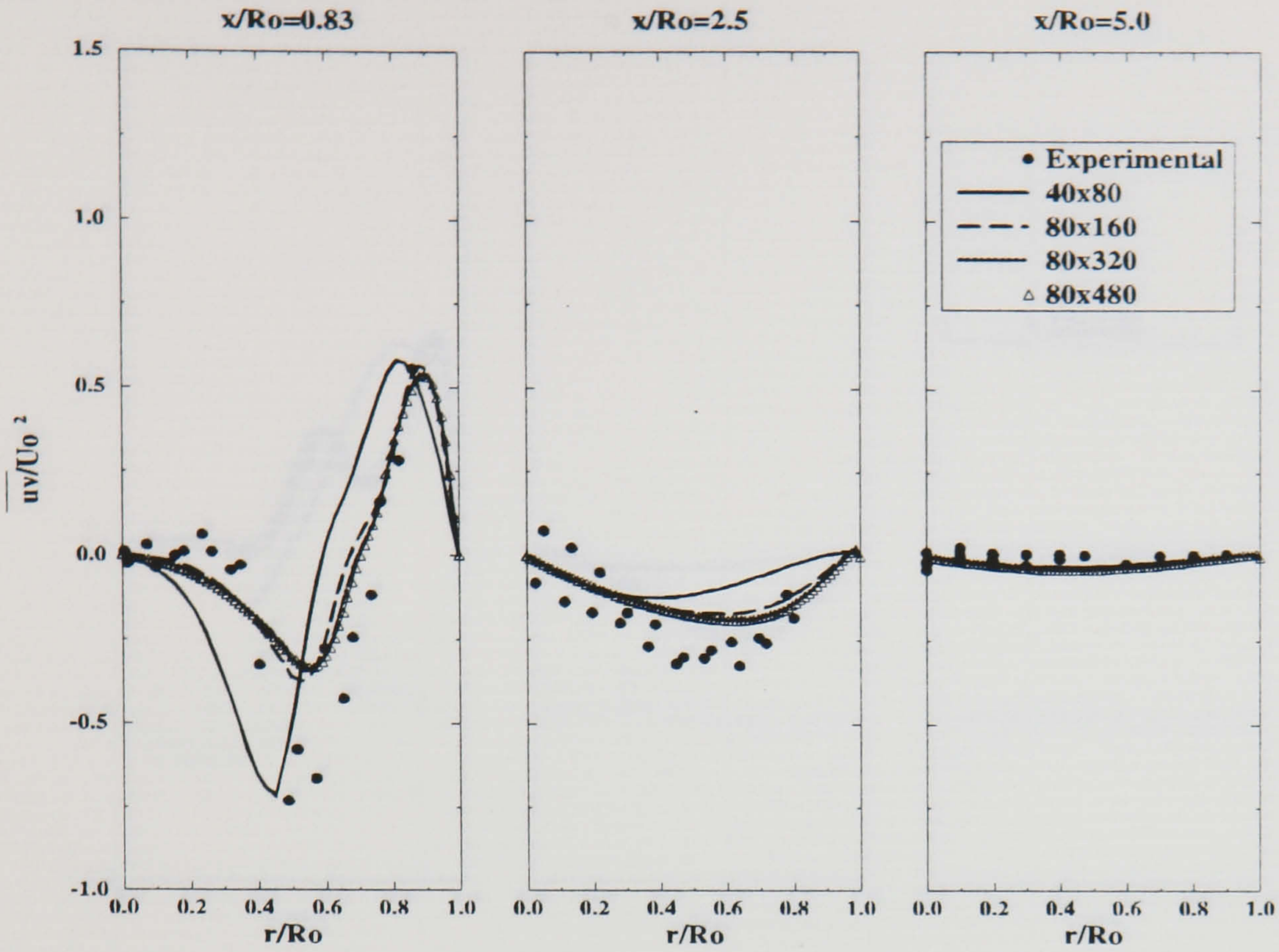



Figure.4.13a. Prediction of the $\overline{uv}$ shear stress using $\kappa$ - $\varepsilon$ turbulence model and Hybrid scheme.

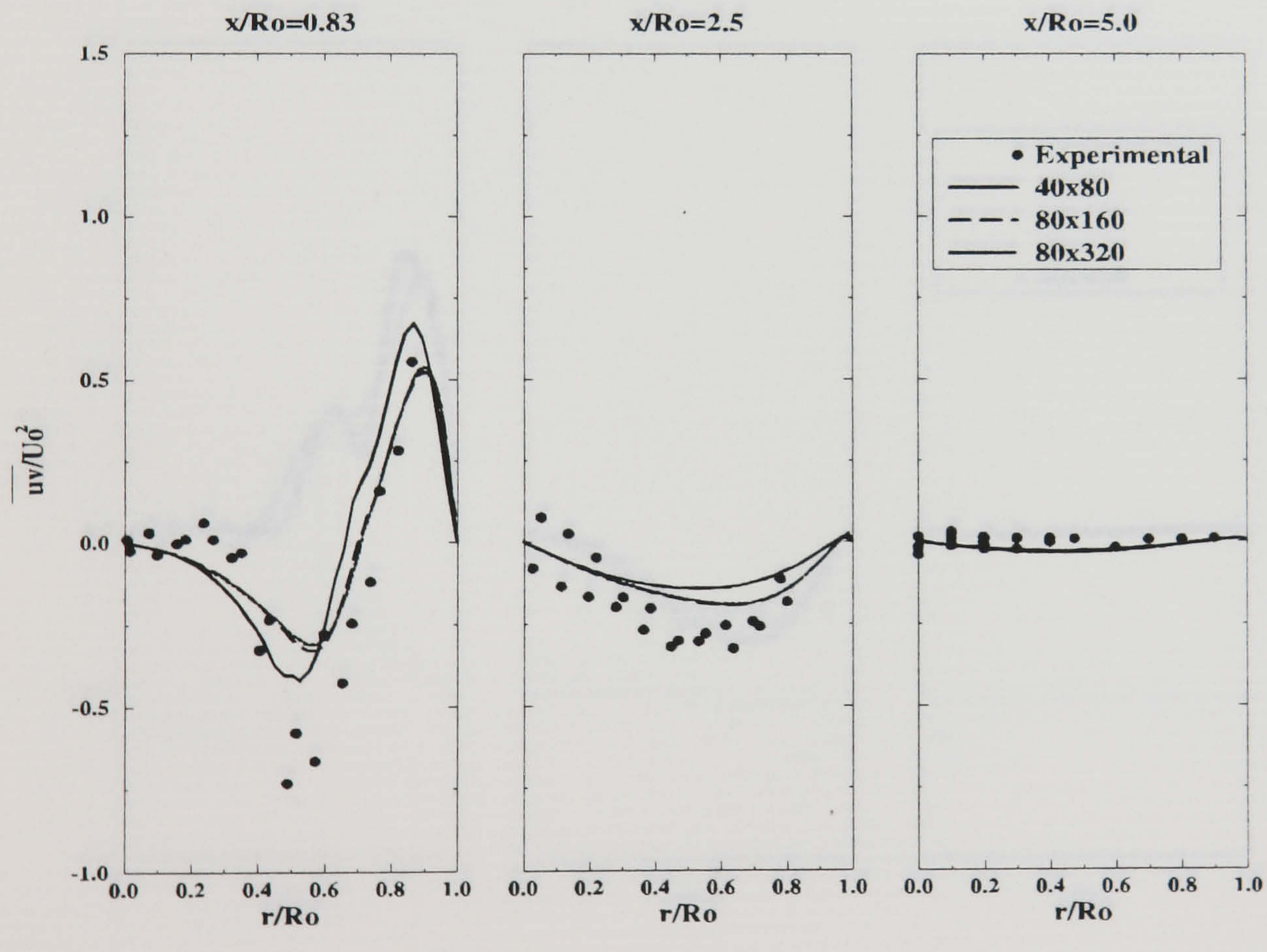



Figure.4.13b. Prediction of the $\overline{uv}$ shear stress using $\kappa$ - $\varepsilon$ turbulence model and TVD scheme.

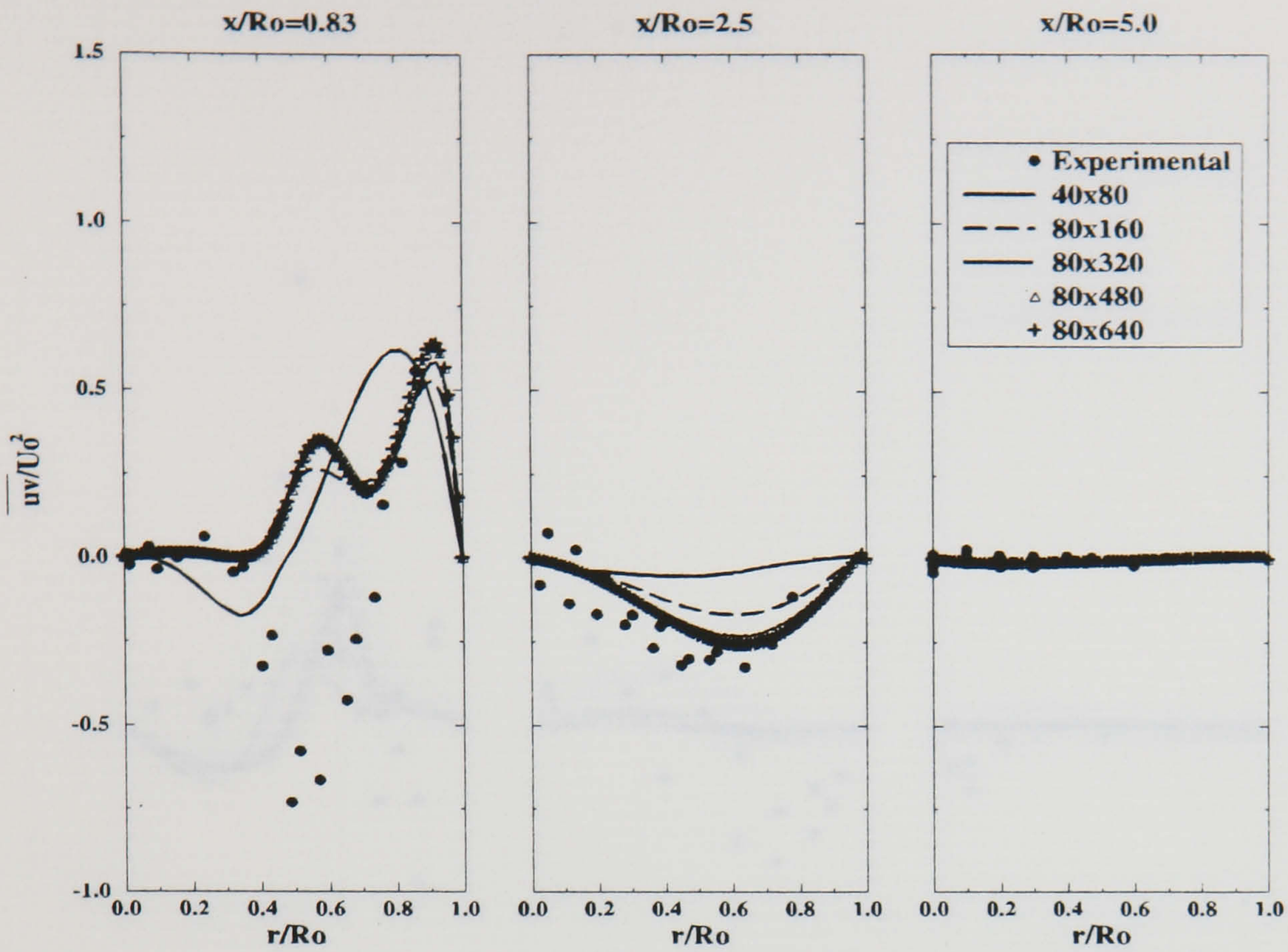



Figure.4.13c. Prediction of the $\overline{uv}$ shear stress using Reynolds Stress turbulence model and Hybrid scheme.

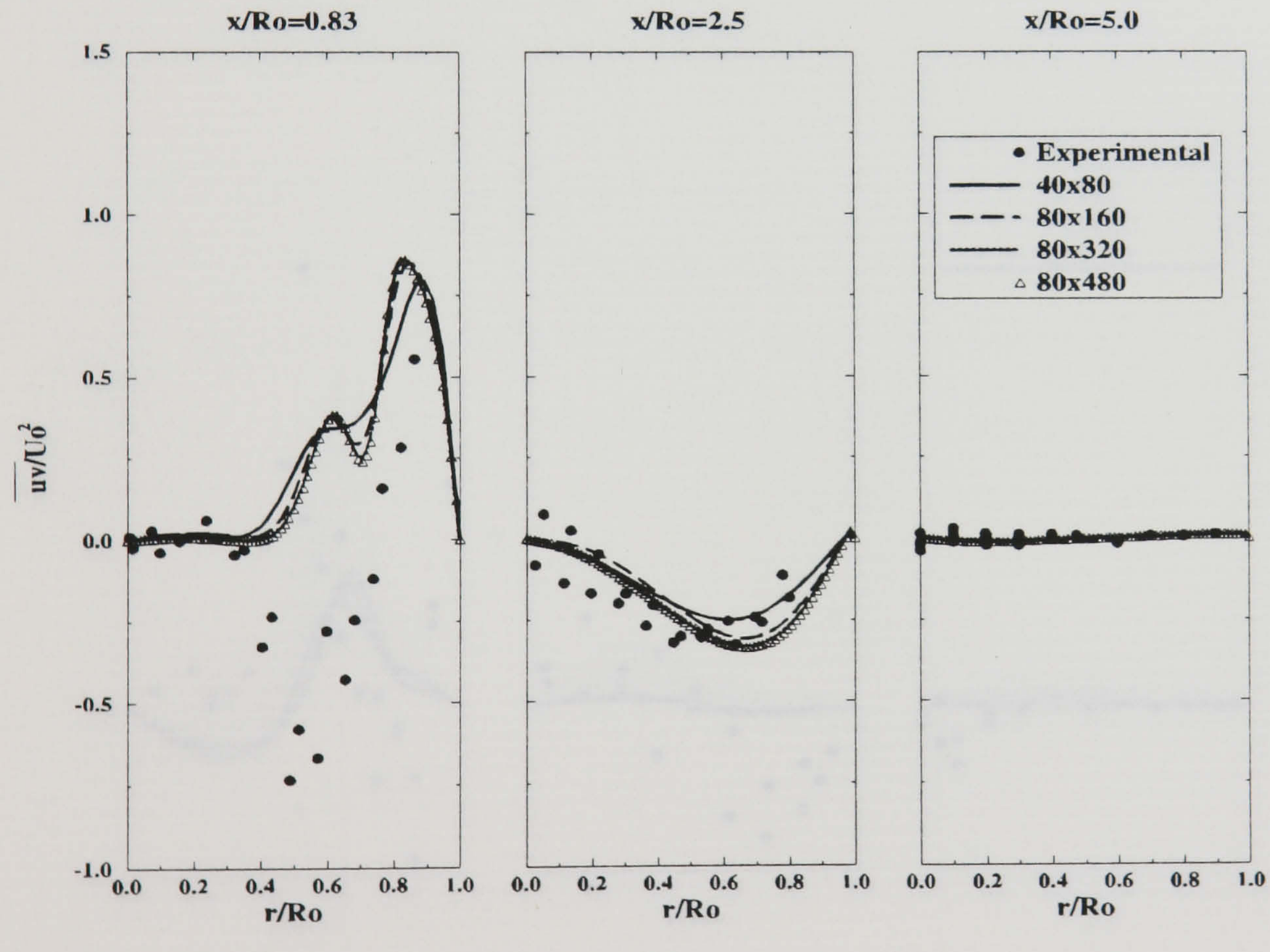



Figure.4.13d. Prediction of the $\overline{uv}$ shear stress using Reynolds Stress turbulence model and TVD scheme.

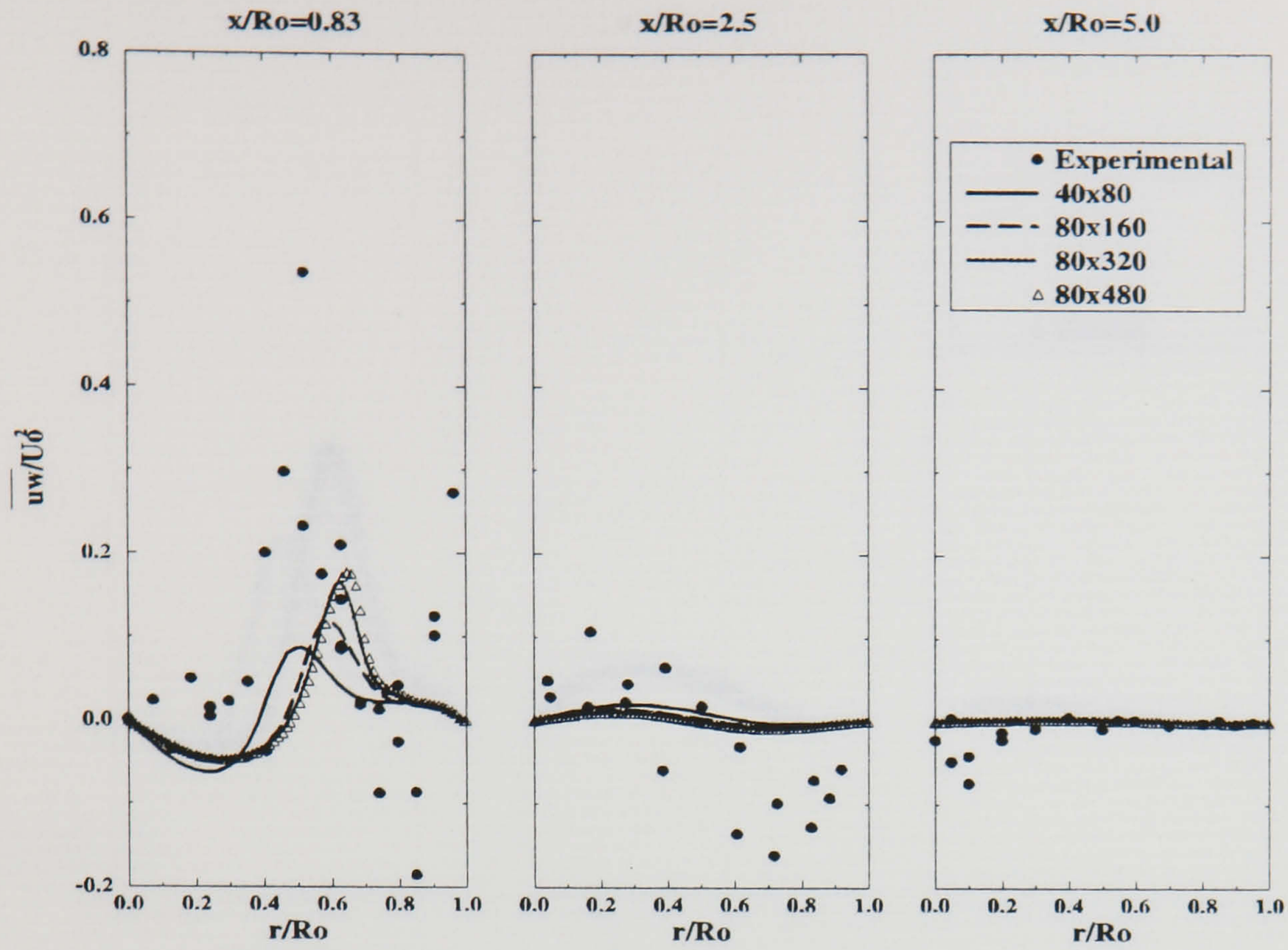



Figure.4.14a. Prediction of the $\overline{uw}$ shear stress using $\kappa$ - $\varepsilon$ turbulence model and Hybrid scheme.

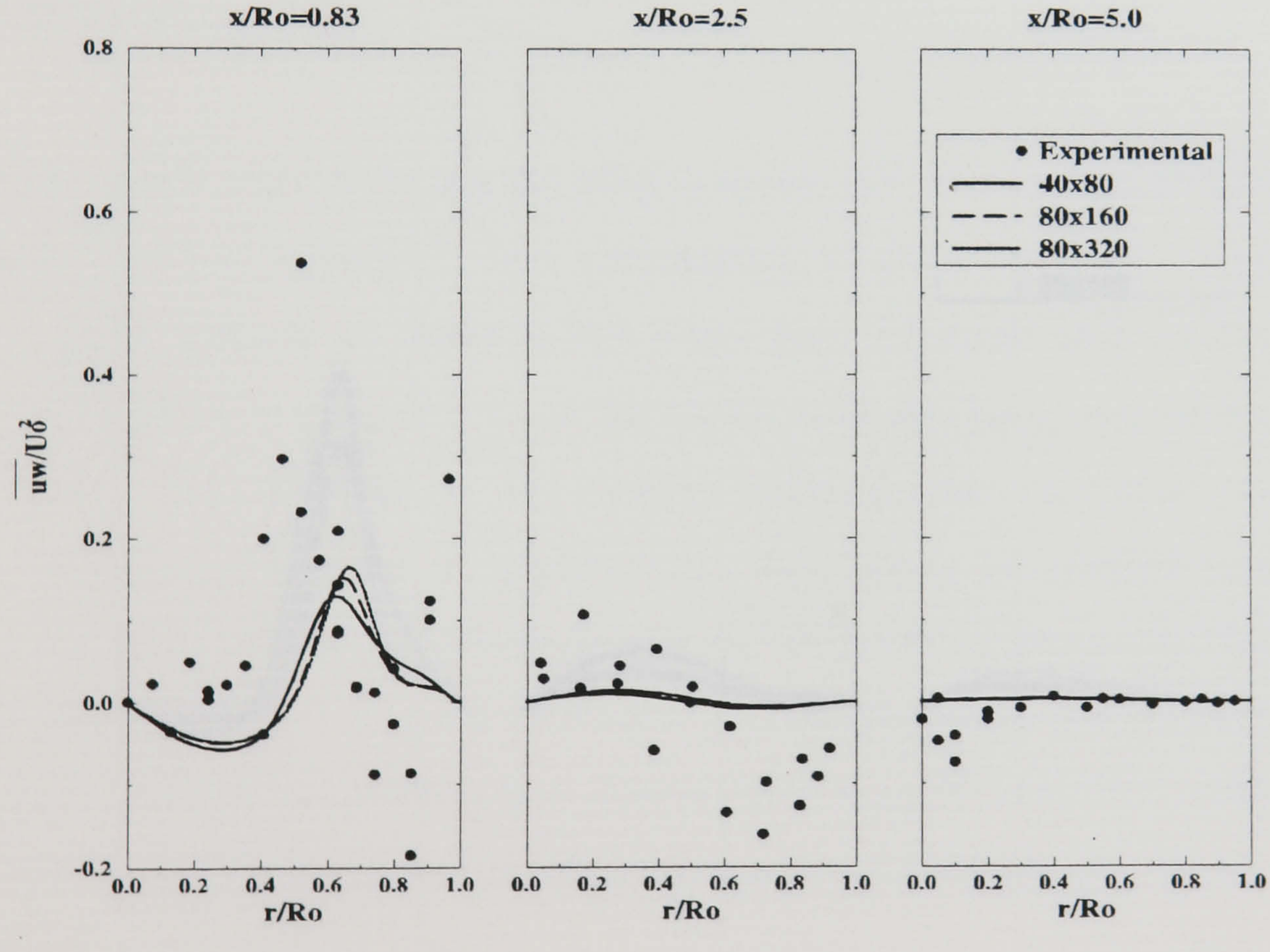



Figure.4.14b. Prediction of the $\overline{uw}$ shear stress using $\kappa$ - $\varepsilon$ turbulence model and TVD scheme.

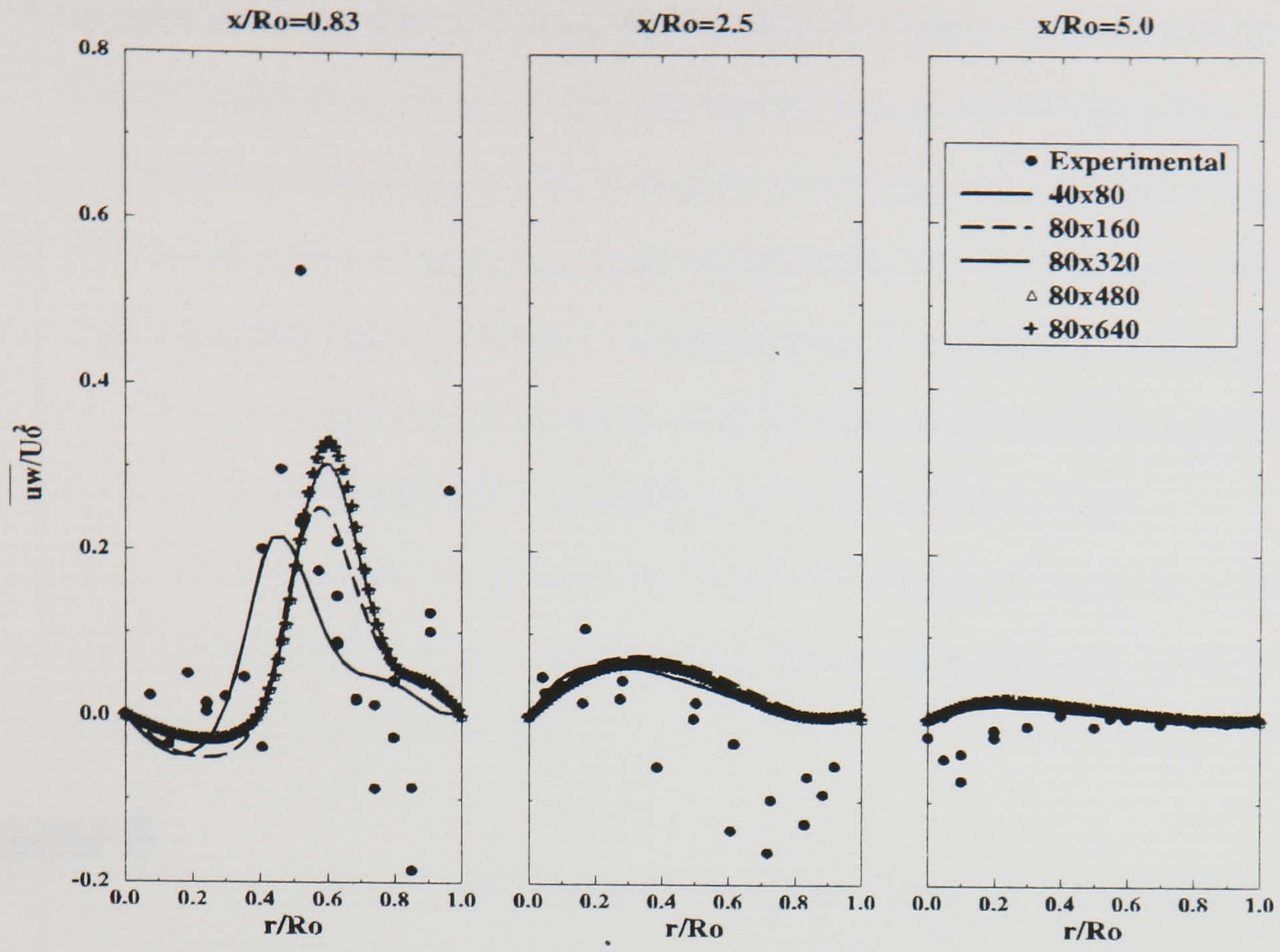



Figure.4.14c. Prediction of the $\overline{uw}$ shear stress using Reynolds Stress turbulence model and Hybrid scheme.

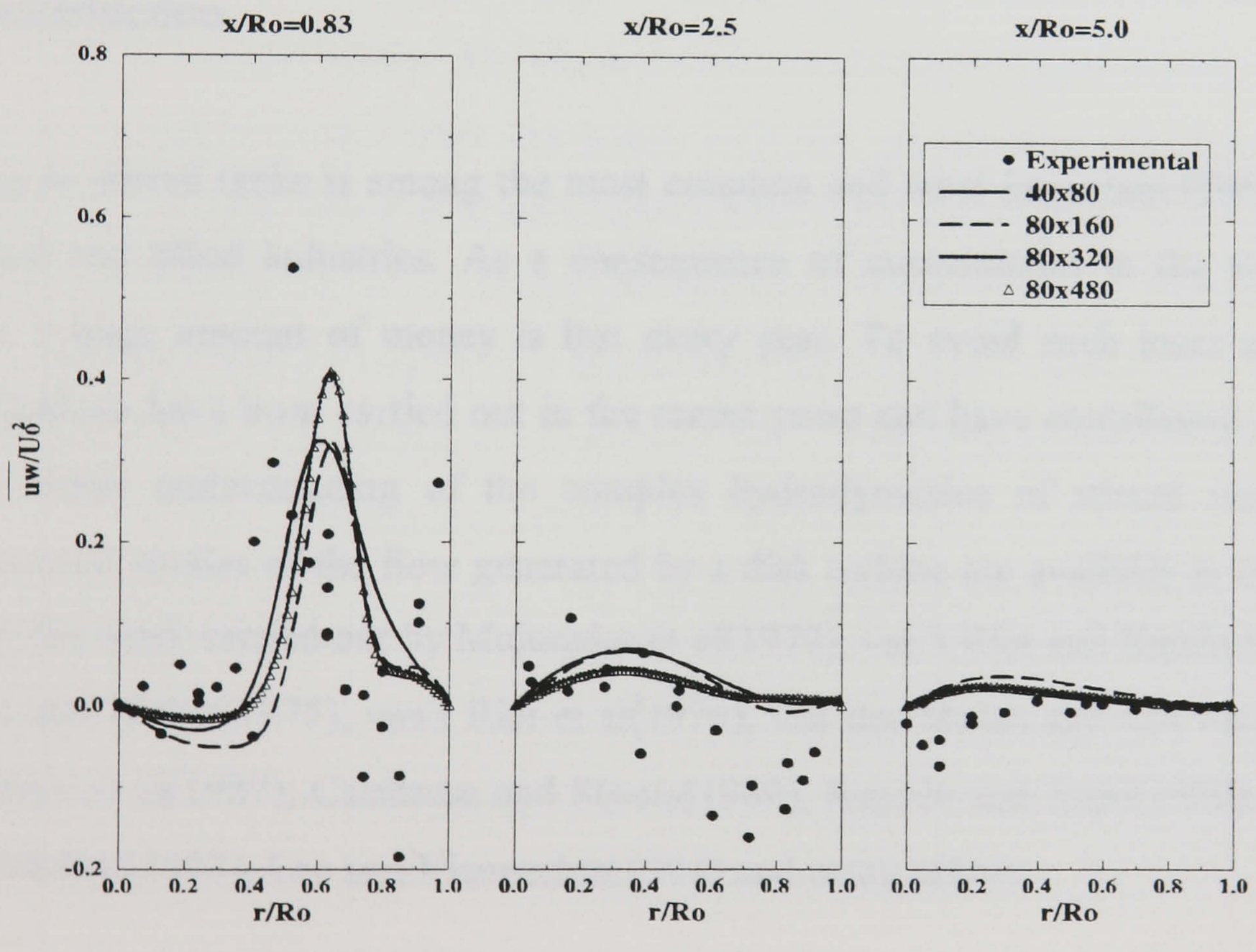



Figure.4.14d. Prediction of the $\overline{uw}$ shear stress using Reynolds Stress turbulence model and TVD scheme.

# Chapter 5

# Fluid Flow in Stirred Tanks

## 5.1 Introduction

Stirring in stirred tanks is among the most common and most important operations in the chemical and allied industries. As a consequence of uncertainties in the stirred vessel design, a huge amount of money is lost every year. To avoid such loses experimental investigations have been carried out in the recent years and have contributed significantly to the better understanding of the complex hydrodynamics of stirred vessels. Many experimental studies of the flow generated by a disk turbine are available in the literature such as the work carried out by Mujumdar et al(1970), van't Riet and Smith(1973, 1975), Gunkel and Weber(1975), van't Riet et al(1976), van der Molen and van Maanen(1978), Yianneskis et al(1987), Calabrese and Stoots(1989), Ranade and Joshi(1990), Yianneskis and Whitelaw(1993), Lee and Yianneskis(1994) and many others.

Based on the information and data made available by the experimental workers, a significant improvement in stirred vessels design can be obtained by developing models

which take into account the real flow field inside the vessel. These models employ the method of finite difference to solve the governing conservation equations subject to the appropriate boundary conditions. The boundary conditions of a baffled tank stirred by an impeller consist of a line of symmetry and solid walls (the top, bottom and outer wall), baffles and the impeller disk and blades. These boundary conditions except for the impeller blades, are well established and have been used by many workers, for example, Pericleous and Patel(1987) and Ranade and Joshi(1990) and have already been described earlier in this work (section 4.3.2) and are further elaborated upon in section 5.3. The impeller region in a vessel has been approached differently by several workers and some of these approaches are described below.

Investigators such as Harvey and Greaves(1982) have treated the rotating impeller as a black box and required the impeller boundary conditions as experimentally determined input. Although this approach has been found to be useful in predicting the flow characteristics in the bulk of the vessel, it can not capture the details of the flow between and around the impeller blades. Harvey and Greaves used the Hybrid differencing scheme and their numerical results were compared with the experimental data of Gunkel and Weber(1975). It was found that the experimental data of the mean velocity were not quantitatively satisfactory when compared with the calculated values. Placek et al(1986) did not treat the impeller region as a black box, but they have solved for $\kappa_T$(turbulence kinetic energy of transfer eddies per unit mass) and $\varepsilon$ using transport equations. Placek et al used the Upwind differencing scheme and indicated that their results of the mean velocity are in reasonable agreement with experimental data at the tank wall, however, for $\kappa_T$ and $\varepsilon$ no quantitative comparison was reported.

The two impeller approaches described above were unable to predict the flow field around the impeller region correctly. Therefore, an attempt towards a more fundamental technique which tackles the time averaged Navier-Stokes equations describing the flow in the vessel was carried out by Pericleous and Patel(1987). In their work, they have presented a numerical simulation of a biochemical reactor stirred by two tangential and

one axial impeller attached to a common shaft. They modelled each impeller and compared the numerical data obtained against the experimental data of Bertrand et al(1980). The different submodels were joined to simulate the multi-impeller biochemical reactor. PHOENICS by Rosten and Spalding(1985) was used to solve the Navier-Stokes equations, where the different impeller types appeared as sources of angular or axial momentum or both depending on the type of impeller being used. The authors indicated that the numerical data obtained using their technique showed a general agreement with experimental data.

Ranade and Joshi(part II, 1990), presented three-dimensional computations for the flow in a fully baffled cylindrical tank stirred by a Rushton turbine. Two types of boundary conditions were imposed on the impeller region. In the first, the impeller region was considered as bounded by two surfaces, one horizontal and one vertical. The parabolic profiles of U and V were imposed on the vertical surface and the boundary conditions used for $\kappa$ and $\varepsilon$ were obtained from experimental data. In the second, boundary conditions were imposed only on the vertical surface and the equations for all variables were solved in the domain of the entire vessel, including the interior region of the impeller. Their numerical results showed a good agreement with the experimental data obtained by the same authors(part I, 1990), however, the vortices behind a baffle were not predicted.

Smith et al(1990) demonstrated the use of the numerical model of Placek et al(1985) for computing the hydrodynamics during the scale-up of a Rushton turbine agitated vessels by two orders of magnitude. Three different scaling criteria were considered; constant impeller Reynolds number, constant power input per unit mass and impeller tip speed. The calculations were carried out for two-dimensional axi-symmetric tank. The predictions obtained show the expected flow patterns generated by a Rushton and concluded that the Reynolds number scaling was the most appropriate.

The numerical simulations for stirred vessels discussed above depended on experimental data for the boundary conditions around the impeller which is a disadvantage if these data were not accurately measured or new forms of impellers are being considered.

Workers such as Brucato et al(1994) and Jayathi et al(1994), have developed a new approach to overcome the need for experimental data for numerical solution of a baffled stirred tank. In this approach, the whole volume of the tank is divided into an inner zone (containing the impeller) and an outer zone. In the inner zone, the flow field is simulated in using a rotating reference frame with respect to the outer zone. Information is iteratively exchanged between the zones after azimuthally-averaging and correcting for the relative motion. The above approach has been applied to a fully baffled tank stirred by a Rushton turbine. Brucato et al used the Harwell-Flow3D (Release 2) code while Jayathi et al used a code based on the SIMPLE algorithm by Patankar(1980) for the pressure-velocity coupling. The numerical data of Brucato et al were compared with the Stoots and Calabrese(1989) and showed a satisfactory qualitative agreement. Jayathi et al did not compare their predictions with experimental data, however, the authors indicated that the numerical data obtained captured the characteristic flow features correctly without the need of experimental data.

This chapter deals with numerical simulation of a cylindrical tank stirred by single and double Rushton impellers using three-dimensional finite difference solution of the time averaged conservation equations. The impeller blades in this study were represented by three different mathematical models as a source term in the tangential momentum equation. These impeller models together with different combinations of differencing scheme and turbulence model used in this study are described later in more detail.

Sections 5.2 and 5.3 present a detailed description of the tank, single Rushton turbine, double Rushton turbine and the boundary conditions used for the simulation. The Rushton turbine impeller mathematical models are discussed in section 5.4 and the numerical data obtained using a single and double Rushton turbine are discussed and compared with

experimental data of Lee(1995) in sections 5.5 and 5.6 respectively. The influence of grid refinement on the computations, computational time, circumferential effect of the impeller models and the conclusions are presented in sections 5.7, 5.8, 5.9 and 5.10 respectively.

## 5.2 Flow Configuration

The flow configurations considered in this work are those studied experimentally by Lee(1995). The cylindrical tank of diameter T = 100 mm and height H = 100 mm was fitted with four equally spaced baffles of width B = T/10 and thickness of T/100 mounted on the wall of the vessel. The working fluid, distilled water, was stirred by a single or a double Rushton impeller. The impellers were of diameter D = T/3 and had six flat blades of height = D/5, width = D/4, and thickness 1mm mounted on a disk also 1mm thick. The clearance between the bottom of the vessel and the mid-section of the impeller, C1 = T/3, and the separation between the impellers in case of double impellers, C2 = T/3. The shaft was rotated with a rotational speed of 2165 ± 10 rpm which resulted in an impeller Reynolds number of 40,000. The dimensions of the tank and the impellers are summarised in figures 5.1 and 5.2. Measurements of the three mean and fluctuating velocity components were made with an LDA system and the accuracy of the mean and fluctuating components was reported as 1-5% and 5-10% respectively.

## 5.3 Boundary Conditions

The boundary conditions used for the numerical computations of the tank stirred by either one or two Rushton turbines consist of a line of symmetry and solid walls (consisting of the top, bottom and outer walls, baffles and impeller the disk but not the impeller blades). As the impeller blades are not represented exactly a model is needed and this will be presented in section 5.4.

### 5.3.1 Symmetry

$$r = 0 \qquad U = V = 0$$

$$\overline{uv} = \overline{vw} = 0$$

$$\frac{\partial}{\partial r} = 0 \qquad \text{otherwise}$$

**Top Surface**

$$x = H \qquad U = 0$$

$$\overline{uv} = \overline{uw} = 0$$

$$\frac{\partial .}{\partial x} = 0 \qquad \text{otherwise}$$

### 5.3.2 Wall

The no-slip conditions have been employed and in order to account for the presence of the wall and the shear stress at the wall has been specified using well known law of the wall profiles. The shear stresses are related to the resultant velocity tangential to the wall (Launder and Spalding (1974) and Amano (1984)), $U_w$ through the following equation

$$\tau_w = \frac{|U_w| \left(C_D^{1/2} \kappa^{1/2}\right)^{1/4}}{K \ln\left(E\, y^+\right)} \qquad (5.1)$$

where $U_w$ is the velocity vector tangential to the wall, E is the roughness constant ( E = 9, for a smooth surface), $K$ is Von Karman's constant ($K$ = 0.4) and $y^+$ is the dimensionless distance from the wall, which is given as

$$y^+ = \frac{\rho U^* y}{\mu} \qquad (5.2)$$

where the friction velocity $U^*$ is given by

$$U^* = \left(\frac{\tau_w}{\rho}\right)^{1/2} \tag{5.3}$$

The derivation of the wall function assumes a local equilibrium between the generation and dissipation of turbulence energy, which leads to the following boundary conditions for $\kappa$ and $\varepsilon$

$$y = 0, \qquad \frac{\partial \kappa}{\partial y} = 0$$

where y is the distance of the near wall node from the wall.

$$\varepsilon = \frac{C_D^{3/4}\, \kappa^{3/2}}{K\, y_1} \tag{5.4}$$

The mean rate of generation, $G_w$, and dissipation of turbulence, $\varepsilon_w$, energy near the wall may be obtained from the following

$$G_w = \frac{\tau_w^2}{\rho\, y_1 \kappa^{1/2} C_D^{1/4} K} \tag{5.5}$$

$$\varepsilon_w = \frac{C_D\, \kappa^{3/2}}{K y} \ln\left(\frac{E\, y_1\, C_D^{1/4}\, \kappa^{1/2} \rho}{\mu}\right) \tag{5.6}$$

**Outer Wall**

at $r = R$ $U = V = W = 0$

$$\frac{\partial}{\partial r} = 0 \quad \text{otherwise}$$

For the shear stresses $\overline{uv}$ and $\overline{vw}$, the law of the wall is applied.

**Bottom Wall**

at $x = 0$ $U = V = W = 0$

$$\frac{\partial}{\partial x} = 0 \quad \text{otherwise}$$

For the shear stresses $\overline{uv}$ and $\overline{uw}$, the law of the wall is again applied.

### 5.3.3 Baffles and Impeller Disk

The baffles which are attached vertically to the wall of the tank and the impeller disk for the single Rushton and double Rushton impellers are considered as solid blockages to the flow, the outer surfaces of which are treated as walls, moving walls with a velocity equal to $\omega r$ (where $\omega$ = the rotational velocity of the impeller (rad/s) and r is the radial distance of the blockage from the centreline) in the case of the impeller disk. The rest of the treatment for walls surfaces follows that for the walls of the tank.

## 5.4 Impeller Models

This section describes the models used to represent the impeller in a tank stirred by one or two Rushton turbine and are referred to as the Simple, Drag force and Dynamic models.

### 5.4.1 Simple Model

Within the impeller blade region the angular velocity of the fluid is set explicitly to

$$W = \omega r \tag{5.7}$$

where $\omega$ = the rotational velocity of the impeller (rad/s) and r is the radial location.

### 5.4.2 Drag Force Model

This model was used by Pericleous and Patel(1987) to simulate a stirred biochemical reactor by three impellers two tangential and one axial, attached to a common shaft. The blades mounted on a central disc were represented as a quadratic source for the tangential momentum equation. The quadratic term arising from the difference of the squares of the fluid and impeller velocities may be written as

$$S_W = \frac{1}{2} \rho \left[ (\omega r)^2 - W^2 \right] C_D N A_f \tag{5.8}$$

where $C_D$ is the drag coefficient of a flat blade perpendicular to a stream of fluid, N is the number of blades, W is the mean tangential velocity of the fluid and $A_f$ is the time averaged blade area.

The model adopted here uses a similar approach but attached a different interpretation to $A_f$ or more correctly $C_D N A_f$.

As a flat plate moves through a fluid in a direction normal to the plate a force is exerted on the fluid in exactly the same manner that a moving fluid exerts a force on a stationary plate. If the impeller blade is moving "linearly" through a stationary fluid the drag force acting on one blade may be written as

$$F_D = \frac{1}{2}\rho\left(r_T\,\omega\right)^2 C_D A_B \qquad (5.9)$$

where $F_D$ is the drag force, $A_B$ is the area of the impeller blade ($A_B$ = blade height x blade width) and $r_T$ is the mean impeller blade radius, given by

$$r_T = \frac{1}{2}\left(r_{out} + r_{in}\right)$$

Then the total drag force, $F_{DT}$, on the impeller with N blades is

$$F_{DT} = N F_D \qquad (5.10)$$

In the model, the impeller blades which spread over the impeller swept volume are represented by

$$F'_D = \frac{1}{2}\rho\left(r\,\omega\right)^2 C'_D A \qquad (5.11)$$

where $F'_D$ is the drag force acting on each impeller control volume, $C'_D$ is the mean drag coefficient for each impeller control volume within the impeller region and A is the cross-sectional area of the control volume normal to the direction of motion of the impeller. The total drag, $F'_{DT}$, is

$$F'_{DT} = C'_D \sum \frac{1}{2}\rho\left(r\,\omega\right)^2 A \qquad (5.12)$$

where the summation is carried out over all the cells contained within the impeller swept volume.

The total drag force on the model equals the total drag on the real impeller, therefore

$$F'_{DT} = F_{DT} \tag{5.13}$$

After rearranging the above equation, the mean drag coefficient for each impeller control volume can be written as

$$C'_D = \frac{F_{DT}}{\sum \frac{1}{2} \rho (r\,\omega)^2 A} \tag{5.14}$$

which for a given rotational speed, $\omega$, is known if $C_D$ is known. In the case of a flat plate $C_D$ is in the range of 1-2 depending on the Reynolds number (Houghton and Brock , 1970).

The drag force on each impeller control volume is then

$$F'_D = \frac{1}{2} \rho\ C'_D A\left[(r\,\omega)^2 - W^2\right] \tag{5.15}$$

where $(r\,\omega)^2 - W^2$ represents the relative velocity between the impeller and the fluid. In the computer program the source term for the angular momentum equation is written as force/unit volume, therefore the source term is

$$S_w = \frac{\frac{1}{2} \rho\ C'_D A\left[(r\,\omega)^2 - W^2\right]}{\Delta V} \tag{5.16}$$

where $\Delta V$ is the volume of the control volume = $r\,\delta_r\delta_\theta\,\delta_x$, but $A = \delta_r\delta_x$ therefore the fluid source term may be written in the following final form

$$S_W = \frac{\frac{1}{2}\rho\, C'_D\, \left[(r\,\omega)^2 - W^2\right]}{r\,\delta_\theta} \qquad (5.17)$$

### 5.4.3 Dynamic Model

The drag force acting on one blade, $F_D$, and the total drag force acting on the impeller with N blades are given in equations (5.9) and (5.10) respectively. In the Dynamic model an impeller function, $F_{DS}$, is added to equation (5.11) which now may be written as

$$F'_D = \frac{1}{2}\rho\,(r\,\omega)^2\, C'_D A F_{DS} \qquad (5.18)$$

where, $F_{DS}$, is given by

$$F_{DS} = \sin^2\left(\frac{N\,\theta}{2} + \omega\, T\right) \qquad (5.19)$$

where $\theta$ is the angular location in the tank and T is the actual time. The Rushton impeller used in this study contained 6 equally spaced blades and these were represented by the six peaks in the above function. This formulation was chosen because it is well behaved and easy to compute.

The total drag force, $F'_{DT}$, is then

$$F'_{DT} = C'_D \sum \frac{1}{2}\rho\,(r\,\omega)^2\, A\, F_{DS} \qquad (5.20)$$

where the summation is again over all the cells swept by the impeller.

The total drag force in the model equals the total drag acting on the real impeller. therefore, equation (5.13) is applied again and with some rearrangement, the mean drag coefficient, $C'_D$, acting on each impeller blade control volume is

$$C'_D = \frac{F_{DT}}{\sum \frac{1}{2} \rho (r\,\omega)^2 A F_{DS}} \qquad (5.21)$$

The drag force acting on each impeller blade control volume is again given by

$$F'_D = \frac{1}{2} \rho\ C'_D A\left[(r\,\omega)^2 - W^2\right]$$

and the source term by

$$S_W = \frac{\frac{1}{2} \rho\ C'_D A F_{DS}\left[(r\,\omega)^2 - W^2\right]}{\Delta V} \qquad (5.22)$$

where $(r\,\omega)^2 - W^2$ again represents the relative velocity between the impeller and the fluid and $\Delta V$ is the volume of the control volume = $r\,\delta_r \delta_\theta\ \delta_x$, but again $A = \delta_r \delta_x$ therefore the fluid source term for this model may be written in the following final form

$$S_W = \frac{\frac{1}{2} \rho\ C'_D\ F_{DS}\left[(r\,\omega)^2 - W^2\right]}{r\,\delta_\theta} \qquad (5.23)$$

## 5.5 Single Rushton Turbine

The Rushton turbine consists of an impeller disc, mounted on a rotating vertical shaft, which carries a number of blades which agitate the flow. When the impeller rotates it imparts angular momentum to the fluid forcing it to rotate with the impeller. This rotation generates a radial pressure gradient, which forces a radial jet of fluid outwards on both sides of the impeller disc. The flow generated by a single Rushton impeller in the $\theta = 0°$ plane i.e. mid way between the baffles and at x = C, i.e. the centre of the impeller, is shown in figure 5.3a. The measurements of Reed et al(1977), Yianneskis et al(1987), Nouri(1988), Hockey(1990) and others indicate that the flow generated by a Rushton turbine in a Newtonian fluid is strongly three-dimensional with radial jet emanating from the impeller that divides upon reaching the tank wall into two jets above and below the impeller which generate two main ring vortices. In the following section the computed results obtained for the single Rushton impeller are discussed and compared with the experimental data of Lee(1995).

### 5.5.1 Results and Discussion

In the results to be compared and described below, all velocities have been normalised with the impeller tip speed (3.77m/s). Figures 5.5-5.20 present axial profiles of the mean axial, radial, tangential and tangential fluctuating velocities in the planes $\theta = 0°$ and $\theta = 45°$. Each figure contains five profiles taken at radial locations of 17 (near the impeller blade), 20, 25, 30 and 35mm (almost mid way between the impeller blade and the wall of the tank) and each radial location contains two predicted profiles using the $\kappa$ - $\varepsilon$ and Reynolds Stress turbulence models and the experimental data. The computed results, were obtained using a computational meshes of 55x29x51, where each number represent the number of nodes in the axial, radial and circumferential directions respectively. Figures 5.3c and 5.3d depict the distribution of the nodes used to map the flow domain in the mixing tank in the axial-radial plane and the radial-tangential plane respectively. The calculations carried out using the three impeller models (Simple, Drag and Dynamic)

together with the Hybrid and TVD differencing schemes and the $\kappa$ - $\varepsilon$ and Reynolds Stress turbulence models are listed in table 5.1.

| Turbulence model | Plane | Impeller model | Velocities | Figure number | Differencing scheme |
|---|---|---|---|---|---|
| $\kappa$ - $\varepsilon$ and RS/SF | $\theta = 0°$ | Simple | U | 5.5a | Hybrid |
| | | | U | 5.5b | TVD |
| | | Drag | U | 5.6a | Hybrid |
| | | Dynamic | U | 5.6b | TVD |
| | | Simple | V | 5.7a | Hybrid |
| | | | V | 5.7b | TVD |
| | | Drag | V | 5.8a | Hybrid |
| | | Dynamic | V | 5.8b | TVD |
| | | Simple | W | 5.9a | Hybrid |
| | | | W | 5.9b | TVD |
| | | Drag | W | 5.10a | Hybrid |
| | | Dynamic | W | 5.10b | TVD |
| | $\theta = 45°$ | Simple | U | 5.11a | Hybrid |
| | | | U | 5.11b | TVD |
| | | Drag | U | 5.12a | Hybrid |
| | | Dynamic | U | 5.12b | TVD |
| | | Simple | V | 5.13a | Hybrid |
| | | | V | 5.13b | TVD |
| | | Drag | V | 5.14a | TVD |
| | | Dynamic | V | 5.14b | Hybrid |
| | | Simple | W | 5.15a | Hybrid |
| | | | W | 5.15b | TVD |
| | | Drag | W | 5.16a | Hybrid |
| | | Dynamic | W | 5.16b | TVD |
| | $\theta = 0°$ | Simple | $\overline{w}$ | 5.17a | Hybrid |
| | | | $\overline{w}$ | 5.17b | TVD |
| | | Drag | $\overline{w}$ | 5.18a | Hybrid |
| | | Dynamic | $\overline{w}$ | 5.18b | TVD |
| | $\theta = 45°$ | Simple | $\overline{w}$ | 5.19a | Hybrid |
| | | | $\overline{w}$ | 5.19b | TVD |
| | | Drag | $\overline{w}$ | 5.20a | Hybrid |
| | | Dynamic | $\overline{w}$ | 5.20b | TVD |

Table 5.1. A summary of the different impeller model, differencing scheme, turbulence model combinations presented in figures 5.5-5.20.

## Mean Velocities

The experimental data obtained by Lee(1995) for the single Rushton impeller indicates that the mean velocities near the blade tip vary with circumferential location, $\theta$, which is indicative of the complex variation of the mean flow behind the blade. The velocity vectors in the different $\theta$ planes (0°, 15°, 30° and 45°) show that the flow discharged by the single Rushton impeller is directed towards the tank wall with a slight upward inclination. As the wall is approached the flow divides into two ring vortices above and below the impeller and has also been documented by several workers, e.g. Yianneskis et al(1987).

### *The Plane $\theta = 0°$ (Mid way between the baffles)*

Figure 5.5a presents the mean axial velocity profiles predicted using the Simple impeller model with the Hybrid differencing scheme and the $\kappa$ - $\varepsilon$ and Reynolds Stress turbulence models in the plane $\theta = 0°$. Close to the impeller blade, r = 17mm, the agreement between the predictions obtained using either turbulence model and the experimental data in the upper region of the impeller blade is poor and at the lower edge of the impeller the predictions have overpredicted the experimental data by 71.5 percent. At r = 20mm, the predicted profiles using either turbulence model agree with the experimental data above the impeller and have underpredicted the experimental data by approximately 73 percent at the lower edge of the impeller. The predicted profiles obtained using the $\kappa$ - $\varepsilon$ model coincide with the experimental data in the lower region of the impeller blade whereas the predicted profile obtained using the Reynolds Stress model have underpredicted the experimental data by approximately 39 percent. At r = 25mm, the predictions agreed well with experimental except at x = 36mm, where the peak in the experimental data has not been predicted. At r = 30 and 35mm, both the experimental data and the predictions obtained using either turbulence model agree well although the profile obtained using the $\kappa$ - $\varepsilon$ model at r = 30mm have slightly overpredicted the experimental data.

Figure 5.5b presents the mean axial velocity profiles predicted using the Simple impeller model with TVD differencing scheme and the $\kappa$ - $\varepsilon$ and Reynolds Stress turbulence models in the plane $\theta$ = 0°. At r = 17mm, the agreement between the experimental data and the predictions in the upper region of the impeller blade is again poor. The predicted profile obtained using the Reynolds Stress model agrees more closely with the experimental data compared with the predicted profile obtained using the $\kappa$ - $\varepsilon$ model in the lower part of the impeller blade. At the same location, the predictions obtained using the $\kappa$ - $\varepsilon$ model with the Hybrid scheme, figure 5.5a, are closer to the experimental data than the predictions obtained using the same model but with the TVD scheme, figure 5.5b. At r = 20 and 25mm, the profiles predicted using the Reynolds Stress model shown in this figure have the same features as those shown in figure 5.5a. However, the predicted profiles obtained using the TVD scheme with $\kappa$ - $\varepsilon$ model, figure 5.5b, moved closer to the experimental data between x = 29mm and 33.3mm for r = 20mm and between x = 33 and 36mm for r = 25mm compared with figure 5.5a. No major changes were noted for r > 25mm between the predictions obtained using either differencing scheme and turbulence model shown in this figure and figure 5.5a.

Figure 5.6a presents the mean axial velocity profiles predicted using the Drag impeller model with the Hybrid differencing scheme and the $\kappa$ - $\varepsilon$ and Reynolds Stress turbulence models in the plane $\theta$ = 0°. The predicted profiles using both turbulence models are coincident at all locations and show poor agreement with the experimental data close to the impeller. At r = 17mm, the predicted profiles have moved towards the experimental data by few percent compared with the predicted profiles presented in figures 5.5a and 5.5b in the regions adjacent to the impeller edges. In the lower part of the tank the predicted profiles underpredict the experimental data by approximately 40 percent, while those presented in figures 5.5a and 5.5b agree closely with the experimental data. At r = 20mm, the predicted profiles show poor agreement with the experimental data in the lower region of the impeller disk compared with the predictions shown in figures 5.5a and 5.5b. For r > 20mm, no significant changes were noted between the predictions shown in this figure and figures 5.5a and 5.5b.

Figure 5.6b presents the mean axial velocity profiles predicted using the Dynamic impeller model with the TVD differencing scheme and the $\kappa$ - $\varepsilon$ and Reynolds Stress turbulence models in the plane $\theta$ = 0°. The only major difference between the predictions shown in this figure compared with figure 5.5b were noted at r = 20mm. At this radial location the profile predicted using the Reynolds Stress model, figure 5.6b, moved closer to the experimental data in the lower part of the impeller compared with the predicted profile obtained using the same turbulence model shown in figure 5.5b.

Figure 5.7a presents the mean radial velocity profiles predicted using the Simple impeller model with Hybrid differencing scheme and the $\kappa$ - $\varepsilon$ and Reynolds Stress turbulence models in the plane $\theta$ = 0°. In general the predictions at the different radial locations follow the same trends as the experimental data. At r = 17mm, both turbulence models agree well with the experimental data except at the lower edge of the impeller. At r = 20mm, the predictions again agree well with the experimental data, although, the predicted profile obtained using the Reynolds Stress model is closer to the experimental data than that obtained using the $\kappa$ - $\varepsilon$ model between x = 32 and 35mm. At r = 25, 30 and 35mm, the predictions obtained using either turbulence model have overpredicted the experimental data at x = 34mm by about 18, 30 and 28 percent respectively. At these locations, the predictions obtained using the Reynolds Stress model are closer to the experimental data than those of the $\kappa$ - $\varepsilon$ model above the impeller disk.

Figure 5.7b presents the mean radial velocity profiles predicted using the Simple impeller model with TVD differencing scheme and the $\kappa$ - $\varepsilon$ and Reynolds Stress turbulence models in the plane $\theta$ = 0° and follow similar trends to those in figure 5.7a. The only major difference between the predictions shown in this figure and those in figure 5.7a were noted for r > 17mm with the predictions obtained using $\kappa$ - $\varepsilon$ model which moved further away from the experimental data compared with figure 5.7a, at the upper part of the impeller centre plane.

Figure 5.8a presents the mean radial velocity profiles predicted using the Drag impeller model with the Hybrid differencing scheme and the $\kappa$ - $\varepsilon$ and Reynolds Stress turbulence models in the plane $\theta$ = 0°. In this figure, no significant differences were noted between the predictions obtained using either turbulence models. At r = 17 and 20mm, the predicted profiles have underpredicted the experimental data peaks by 36 and 39 percent respectively and they are less accurate compared with the predicted profiles shown in figures 5.7a and 5.7b. The predictions for r > 20mm, figure 5.7a, obtained using either turbulence model are coincident and agree more with the experimental data compared with predictions presented again in figures 5.7a and 5.7b.

Figure 5.8b presents the mean radial velocity profiles predicted using the Dynamic impeller model with the TVD differencing scheme and the $\kappa$ - $\varepsilon$ and Reynolds Stress turbulence models in the plane $\theta$ = 0°. In general, the predictions in this figure obtained using either turbulence model follow similar trends as the predicted profiles obtained using the Simple impeller model with TVD scheme presented in figure 5.7b. Therefore, comparison between the predictions obtained using either turbulence model with either impeller model and differencing scheme are similar to those discussed above in figures 5.7b and 5.8a.

Figure 5.9a presents the mean tangential velocity profiles predicted using the Simple impeller model with Hybrid differencing scheme and the $\kappa$ - $\varepsilon$ and Reynolds Stress turbulence models in the plane $\theta$ = 0°. There is no major differences between the predicted profiles obtained using either turbulence model at all radial locations and at r = 17 and 20mm the predictions have underpredicted the experimental data peak by about 35 and 39 percent respectively. For r > 20mm, the predictions agree well with the experimental data.

Figure 5.9b presents the mean tangential velocity profiles predicted using the Simple impeller model with TVD differencing scheme and the $\kappa$ - $\varepsilon$ and Reynolds Stress turbulence models in the plane $\theta$ = 0°. The predicted profiles presented in this figure show small differences at all radial locations except r = 35mm compared with the

predictions presented in figure 5.9a. These differences are located close to the top and bottom edges of the radial jet near the impeller. The predictions at r = 35mm obtained using either turbulence model are coincident with the experimental data and are similar to those shown in figure 5.9a.

Figure 5.10a presents the mean tangential velocity profiles predicted using the Drag impeller model with the Hybrid differencing scheme and the $\kappa$ - $\varepsilon$ and Reynolds Stress turbulence models in the plane $\theta$ = 0°. The predicted profiles show a very close agreement with the experimental data at all radial locations with approximately 10 percent differences in the upper part of the radial jet close to the impeller.

Figure 5.10b presents the mean tangential velocity profiles predicted using the Dynamic impeller model with the TVD differencing scheme and the $\kappa$ - $\varepsilon$ and Reynolds Stress turbulence models in the plane $\theta$ = 0°. No significant differences were observed between the predictions presented in this figure and the predictions obtained using the Simple impeller model shown in figures 5.9a and 5.9b.

***The Plane $\theta$ = 45° (In the plane of the baffles)***

Figure 5.11a presents the mean axial velocity profiles predicted using the Simple impeller model with the Hybrid differencing scheme and the $\kappa$ - $\varepsilon$ and Reynolds Stress turbulence models in the plane $\theta$ = 45°. At all radial locations shown in this figure, the predicted profiles using both turbulence models are very close to each other. At r = 17mm, both turbulence models have underpredicted the experimental data peaks at x = 31 and 36mm by about 40 and 21 percent respectively. The predicted profiles at r = 20mm are poor compared with the experimental data and fail to reproduce the experimental data peaks at x = 31 and 37mm. At r = 25mm, the profiles are generally coincident with the experimental data, however, they fail to predict the experimental data peak between x = 35 and 36mm. The predicted profiles at r = 30 and 35mm are flat and at r = 35mm, the predicted profiles are coincident with the experimental data.

Figure 5.11b presents the mean axial velocity profiles predicted using the Simple impeller model with the TVD differencing scheme and the $\kappa$ - $\varepsilon$ and Reynolds Stress turbulence models in the plane $\theta$ = 45°. No changes were noted between the predictions obtained using the Reynolds Stress model shown in this figure and those shown in figure 5.11a. At r = 17 and 20mm, the predicted profiles obtained using the $\kappa$ - $\varepsilon$ model have moved closer to the experimental data compared to that of the Reynolds Stress model presented in this figure and with the predictions shown in figure 5.11a. At r = 25 and 30mm, the $\kappa$ - $\varepsilon$ model predicted profiles have overpredicted the experimental data by 10 and 18 percent respectively in the lower part of the impeller, whereas at r = 35mm it has overpredicted the experimental data by 8 percent compared to those shown in figure 5.11a.

Figure 5.12a presents the mean axial velocity profiles predicted using the Drag impeller model with the Hybrid differencing scheme and the $\kappa$ - $\varepsilon$ and Reynolds Stress turbulence models in the plane $\theta$ = 45°. The predictions at r = 17, 20 and 25mm failed to predict the experimental peak values and are flatter than those shown in figures 5.11a and 5.11b. At r = 30mm, the predicted profiles agree more with the experimental data in the upper part of the impeller compared with figure 5.11a. At r = 35mm, no significant change were noted with the predictions compared with figure 5.11a.

Figure 5.12b presents the mean axial velocity profiles predicted using the Dynamic impeller model with the TVD differencing scheme and the $\kappa$ - $\varepsilon$ and Reynolds Stress turbulence models in the plane $\theta$ = 45°. The predictions in this case are very similar to those obtained using the Simple impeller model with either turbulence model presented in figure 5.11b except at r = 25mm. The profile predicted at r = 25mm using the Reynolds Stress model, figure 5.12b, have moved 17 percent further from the experimental data compared with figure 5.11b.

Figure 5.13a presents the mean radial velocity profiles predicted using the Simple impeller model with the Hybrid differencing scheme and the $\kappa$ - $\varepsilon$ and Reynolds Stress turbulence

models in the plane $\theta$ = 45°. At all radial locations, the predictions obtained using either turbulence model are similar to the experimental data, however, the predicted profiles obtained using the Reynolds Stress model agrees more with the experimental data than the $\kappa$ - $\varepsilon$ model predictions particularly at the lower edge of the radial jet. The predicted profiles obtained using the Reynolds Stress model have underpredicted the experimental data peaks at r = 17, 25, 30 and 35mm by about 26, 33, 35 and 34 percent respectively.

Figure 5.13b presents the mean radial velocity profiles predicted using the Simple impeller model with the TVD differencing scheme and the $\kappa$ - $\varepsilon$ and Reynolds Stress turbulence models in the plane $\theta$ = 45°. In general, the TVD scheme did not have a significant effect on the Reynolds Stress predicted profiles except at r = 35mm bringing a closer agreement with the experimental data compared with figure 5.13a. However, for r > 17mm, the TVD scheme has significantly affected the $\kappa$ - $\varepsilon$ model predicted profiles above the impeller centre plane bringing a greater disagreement with the experimental data compared with figure 5.13a. It was noted that the profiles obtained in this figure and figure 5.13a using the Reynolds Stress model, agree more closely with the experimental data than those profiles predicted using the $\kappa$ - $\varepsilon$ model. The predicted profiles obtained using the $\kappa$ - $\varepsilon$ model with the Hybrid scheme agrees more with the experimental data than those predicted using the $\kappa$ - $\varepsilon$ model with the TVD scheme.

Figure 5.14a presents the mean radial velocity profiles predicted using the Drag impeller model with the TVD differencing scheme and the $\kappa$ - $\varepsilon$ and Reynolds Stress turbulence models in the plane $\theta$ = 45°. The predictions at all radial locations agree with the experimental data in the upper and lower parts of the impeller blade and underpredicts the central peak of the experimental data in contrast to the predictions shown in figures 5.13a and 5.13b which overpredict the experimental data. At r = 17, 20, 25 and 30mm, figure 5.14a, the predictions have underpredicted the experimental data peak by 32, 50 , 23 and 21 percent respectively. At r = 35mm, the profile predicted using the Reynolds Stress model agrees more with the experimental data at the lower edge of the impeller than the profile predicted using the $\kappa$ - $\varepsilon$ model, whereas the $\kappa$ - $\varepsilon$ profile is the closer to the

experimental data at the upper part of the impeller. The profiles obtained using the Reynolds Stress model presented in figures 5.13a and 5.13b are closer to the experimental data than the predictions shown in this figure.

Figure 5.14b presents the mean radial velocity profiles predicted using the Dynamic impeller model with the Hybrid differencing scheme and the $\kappa$ - $\varepsilon$ and Reynolds Stress turbulence models in the plane $\theta$ = 45°. The predicted profiles obtained using the Reynolds Stress model agree more closely with the experimental data than those of the $\kappa$ - $\varepsilon$ model and closely resemble those of figure 5.13a. The Dynamic impeller model has improved the agreement between the predicted profiles using the $\kappa$ - $\varepsilon$ model and the experimental data (compared with figure 5.13a).

Figure 5.15a presents the mean tangential velocity profiles predicted using the Simple impeller model with the Hybrid differencing scheme and the $\kappa$ - $\varepsilon$ and Reynolds Stress turbulence models in the plane $\theta$ = 45°. In general, the predictions presented in this figure follow the trends of the experimental data. At r = 17, 20, 25, 30 and 35mm, the predictions are coincident between the upper and lower edges of the impeller blade and have overpredicted the experimental data by 87, 12, 25, 19 and 13.5 percent respectively. At these locations, the predictions obtained using both turbulence models are coincident above the impeller and differ by few percent below the impeller.

Figure 5.15b presents the mean tangential velocity profiles predicted using the Simple impeller model with the TVD differencing scheme and the $\kappa$ - $\varepsilon$ and Reynolds Stress turbulence models in the plane $\theta$ = 45°. In general, the TVD scheme did not significantly effect the performance of the predictions obtained using the Reynolds Stress model compared with figure 5.15a. For r $\geq$ 17mm, the predicted profiles obtained using the $\kappa$ - $\varepsilon$ model are few percent less accurate in the upper part of the impeller centre plane and moved closer to the experimental data for r > 17mm in the lower part of the impeller centre plane compared to those shown in figure 5.15a.

Figure 5.16a presents the mean tangential velocity profiles predicted using the Drag impeller model with the Hybrid differencing scheme and the $\kappa$ - $\varepsilon$ and Reynolds Stress turbulence models in the plane $\theta$ = 45°. In general, the predictions obtained using either turbulence model presented in this figure agree well with the experimental data at all radial locations except at r = 20mm where the predicted profiles have underpredicted the experimental data between x = 31 and 37mm by 40 percent. Compared to the predictions obtained using the Simple impeller model, figures 5.15a and 5.15b, the Hybrid differencing with the Drag impeller model, figure 5.16a, have affected the performance of the predictions obtained using both turbulence models bringing good agreement with the experimental data except at r = 20mm. At r = 20mm the profiles predicted using either turbulence model with the Simple impeller agree more with the experimental data than those shown in this figure in the impeller centre plane.

Figure 5.16b presents the mean angular velocity profiles predicted using the Dynamic impeller model with the TVD differencing scheme and the $\kappa$ - $\varepsilon$ and Reynolds Stress turbulence models in the plane $\theta$ = 45°. The predictions obtained using both turbulence models are coincide in this figure and closely follow the predictions shown in figure 5.15a. The profiles predicted using the Drag impeller model with either turbulence model presented in figure 5.16a agree more with the experimental data compared with this figure and figures 5.15a and 5.15b at all radial locations except at r = 20mm, where the predictions obtained using this impeller model and the Simple impeller model agrees more with the experimental data than the profiles predicted using the Drag impeller model, figure 5.16a.

**Fluctuating Velocities**

Lee(1995), indicates that the high levels of axial normal stresses in the $\theta$ = 0° plane show the presence of the trailing vortices generated by the previous blade. These stresses are located radially between r = 22 and 27mm and axially between the upper and lower edges of the impeller blade. As the vortex moves away from the blade and into the impeller

stream, the axial normal stresses maxima move accordingly, from r = 17mm at $\theta$ = 15° plane to r = 19mm at $\theta$ = 30° plane and r = 21mm at $\theta$ = 45° plane. These high level of turbulence tends to diminish as the radial distance increases.

The level of the radial normal stresses behind the leading blade are higher than the axial normal stresses due to the velocity gradients which are more pronounced in the radial direction than in the axial. The level obtained for the tangential normal stresses was a little higher than the radial normal stresses and due to this reason the results selected and discussed below are those obtained for the tangential normal stresses. Comparisons of the axial, radial and tangential normal stresses obtained in the $\theta$ planes indicate that the turbulence is in general anisotropic in the impeller stream.

***The Plane $\theta$ = 0° (Mid way between the baffles)***

Figure 5.17a presents the fluctuating tangential velocity profiles predicted using the Simple impeller model with Hybrid differencing scheme and the $\kappa$ - $\varepsilon$ and Reynolds Stress turbulence models in the plane $\theta$ = 0°. At r = 17mm, the experimental data shows high peaks adjacent to the top and bottom edges of the impeller blade. The upper experimental data peak has been underpredicted by 30 percent and the lower peak has been overpredicted by the Reynolds Stress model and well reproduced by the $\kappa$ - $\varepsilon$ model. For r > 17mm, the predictions using both turbulence models agree well with the experimental data, however, the profile predicted using the Reynolds Stress model shows closer agreement with the experimental data compared to the $\kappa$ - $\varepsilon$ model in the lower part of the impeller, however, the reverse applies in the upper part of the impeller. At r = 25mm, the predictions obtained using either turbulence model has underpredicted the experimental data peak by 18 percent, whereas for r > 25mm the predictions are coincident with the experimental data at the impeller blade centre.

Figure 5.17b presents the fluctuating tangential velocity profiles predicted using the Simple impeller model with TVD differencing scheme and the $\kappa$ - $\varepsilon$ and Reynolds Stress

turbulence models in the plane $\theta$ = 0°. At r = 17mm, the upper peak obtained using the Reynolds Stress model has moved closer to the experimental data and the lower peak has moved further from the experimental data compared with figure 5.17a. The predictions in the lower part of the impeller obtained using either turbulence model moved closer to the experimental data at all radial locations compared with figure 5.17a. For r > 17mm, no significant differences were noted in the upper region of the impeller disk between the predictions shown in this figure and those of figure 5.17a. However, for r > 20mm, the profiles predicted using the $\kappa$ - $\varepsilon$ model have shown a greater deviation from the experimental data at the lower edge of the impeller compared with figure 5.17a.

Figure 5.18a presents the tangential fluctuating velocity profiles predicted using the Drag impeller model with the Hybrid differencing scheme and the $\kappa$ - $\varepsilon$ and Reynolds Stress turbulence models in the plane $\theta$ = 0°. No significant differences were noted between the predictions obtained using either turbulence model and in general considerably underpredict the experimental data and are lower than the predictions shown in figures 5.17a and 5.17b.

Figure 5.18b presents the tangential fluctuating velocity profiles predicted using the Dynamic impeller model with the TVD differencing scheme and the $\kappa$ - $\varepsilon$ and Reynolds Stress turbulence models in the plane $\theta$ = 0°. In general, the predictions presented in this figure follow similar trends as the predictions presented in 5.17b, although at r = 17mm the upper peak predicted by the Reynolds Stress model shown in this figure is closer to the experimental data than that presented in figure 5.17b.

***The Plane $\theta$ = 45° (In the plane of the baffles)***

Figure 5.19a presents the tangential fluctuating velocity profiles predicted using the Simple impeller model with the Hybrid differencing scheme and the $\kappa$ - $\varepsilon$ and Reynolds Stress turbulence models in the plane $\theta$ = 45°. At r = 17mm, the predictions have overpredicted the experimental data at the upper edge of the impeller by 10 percent and

underpredicted the experimental data at the lower edge by 6.5 percent. At r = 20mm, the predictions obtained using both turbulence models have underpredicted the experimental data below the impeller blade centre by about 45 percent. For r > 20mm, the predictions agree with the experimental data, however, at r = 25mm the profile predicted using the $\kappa$ - $\varepsilon$ model has moved by few percent closer to the experimental data than the predicted profile obtained using the Reynolds Stress model at the upper part of the impeller.

Figure 5.19b presents the tangential fluctuating velocity profiles predicted using the Simple impeller model with the TVD differencing scheme and the $\kappa$ - $\varepsilon$ and Reynolds Stress turbulence models in the plane $\theta$ = 45°. At r = 17mm, the predictions obtained using the Reynolds Stress model adjacent to the upper and lower edges of the impeller have moved further from the experimental data compared with figure 5.19a. However, the predicted profile obtained using the $\kappa$ - $\varepsilon$ model remains unchanged compared with figure 5.19a. At r = 20mm, the predicted profile obtained using the Reynolds Stress model has moved closer to the experimental data at the lower edge of the impeller compared with figure 5.19a. No significant changes were noted for r > 20mm between the predictions shown in this figure and those of figure 5.19a.

Figure 5.20a presents the angular fluctuating velocity profiles predicted using the Drag impeller model with the Hybrid differencing scheme and the $\kappa$ - $\varepsilon$ and Reynolds Stress turbulence models in the plane $\theta$ = 45°. For r > 17mm, the predictions obtained using either turbulence model are almost coincident and are in poor agreement with the experimental data and with the predictions shown in figures 5.19a and 5.19b. At r = 17mm, the predicted profile using the Reynolds Stress model agrees more with the experimental data than the predicted profiles obtained using the $\kappa$ - $\varepsilon$ model although both have underpredicted the experimental data by 30 percent at x = 33.3mm. The profile predicted at r = 17mm using the Reynolds Stress model is closer to the experimental data above the impeller disk compared with figures 5.19a and 5.19b.

Figure 5.20b presents the tangential fluctuating velocity profiles predicted using the Dynamic impeller model with the TVD differencing scheme and the $\kappa$ - $\varepsilon$ and Reynolds Stress turbulence models in the plane $\theta = 45°$. The predictions shown in this figure follow similar trends as the predictions shown in figure 5.20b. No significant differences were noted for r > 20mm between the predicted profiles presented in this figure and those shown in figure 5.19b. At r = 17mm, the upper and lower peaks of the predicted profile obtained using the Reynolds Stress model shown in this figure are closer to the experimental data compared with those shown in figure 5.19b.

## 5.6 Double Rushton Turbine

The double Rushton turbine consists of two impellers discs, mounting on a common rotating vertical shaft, each impeller disc carries a number of blades which agitate the flow. When the impellers rotate they impart angular momentum to the fluid forcing it to rotate with the impellers. Many experimental studies were concerned primarily with large impeller clearances and separations (C1 and C2 shown in figure 5.2), where there is little or no interaction between the flows generated by individual impellers. For example, Crozier(1989) studied the flow generated by two Rushton impellers located at C1 = T/3 and C2 = T. The flow generated by the impellers showed an independent behaviour as if the vessel was divided into two equal parts, where each part is agitated by single impeller. Mahmoudi and Yanneskis(1991, 1992) and Mahmoudi(1994) investigated the effect of different impeller spacing with the double Rushton turbine, where they observed three stable and four unstable flow patterns. Of the three stable patterns, the merging flow pattern, which is used in this study, occurred with impeller clearances of C1 = C2 = T/3. This impeller separation causes the impeller streams to incline towards each other and merge half way between the two impellers and generally produces the lowest mixing time. In the following section the computed results obtained for the double Rushton impeller are discussed and compared with the experimental data of Lee(1995).

### 5.6.1 Results and Discussion

In the results to be compared and described below, all the velocities have been normalised with the impeller tip speed (3.77m/s). Figures 5.21-5.36 present axial profiles for the mean axial, radial, tangential and tangential fluctuating velocities in the planes $\theta$ = 0° and $\theta$ = 45°. Each figure contains five profiles taken at radial locations of 17 (near the impeller blade), 20, 25, 30 and 35mm (approximately mid way between the impeller blade and the wall of the tank) and each radial location contains two predicted profiles using the $\kappa$ - $\varepsilon$ and Reynolds Stress turbulence models and the experimental data. The computed results were obtained on a computational mesh of 64x29x51, where the first, second and third

numbers represent the number of nodes in the axial, radial and circumferential directions respectively. Figures 5.4c and 5.4d shows the distribution of the nodes used to map the flow domain in the mixing tank in the axial-radial plane and the radial-tangential plane respectively. The calculations were carried out using the three impeller models (Simple. Drag and Dynamic) together with the Hybrid and TVD differencing schemes and the $\kappa$ - $\varepsilon$ and Reynolds Stress turbulence models and are listed in table 5.2.

| Turbulence model | Plane | Impeller model | Velocities | Figure number | Differencing scheme |
|---|---|---|---|---|---|
| $\kappa$ - $\varepsilon$ and RS/SF | $\theta = 0°$ | Simple | U | 5.21a | Hybrid |
| | | | U | 5.21b | TVD |
| | | Drag | U | 5.22a | Hybrid |
| | | Dynamic | U | 5.22b | TVD |
| | | Simple | V | 5.23a | Hybrid |
| | | | V | 5.23b | TVD |
| | | Drag | V | 5.24a | Hybrid |
| | | Dynamic | V | 5.24b | TVD |
| | | Simple | W | 5.25a | Hybrid |
| | | | W | 5.25b | TVD |
| | | Drag | W | 5.26a | Hybrid |
| | | Dynamic | W | 5.26b | TVD |
| | $\theta = 45°$ | Simple | U | 5.27a | Hybrid |
| | | | U | 5.27b | TVD |
| | | Drag | U | 5.28a | Hybrid |
| | | Dynamic | U | 5.28b | TVD |
| | | Simple | V | 5.29a | Hybrid |
| | | | V | 5.29b | TVD |
| | | Drag | V | 5.30a | Hybrid |
| | | Dynamic | V | 5.30b | TVD |
| | | Simple | W | 5.31a | Hybrid |
| | | | W | 5.31b | TVD |
| | | Drag | W | 5.32a | Hybrid |
| | | Dynamic | W | 5.32b | TVD |
| | $\theta = 0°$ | Simple | $\overline{w}$ | 5.33a | Hybrid |
| | | | $\overline{w}$ | 5.33b | TVD |
| | | Drag | $\overline{w}$ | 5.34a | Hybrid |
| | | Dynamic | $\overline{w}$ | 5.34b | TVD |
| | $\theta = 45°$ | Simple | $\overline{w}$ | 5.35a | Hybrid |
| | | | $\overline{w}$ | 5.35b | TVD |
| | | Drag | $\overline{w}$ | 5.36a | Hybrid |
| | | Dynamic | $\overline{w}$ | 5.36b | TVD |

Table 5.2. A summary of the different impeller model, differencing scheme, turbulence model combinations presented in figures 5.22-5.36.

**Mean Velocities**

The mean velocity data obtained by Lee(1995) indicates that the discharge flow is oriented at about 45° to the horizontal in all measurement planes ($\theta$ = 0°, 15°, 30° and 45°) in contrast with the near horizontal discharge flow when a single Rushton impeller is used.

The addition of the upper impeller prevented the formation of a large ring vortex above the lower impeller as in the single impeller case although the presence of two impellers formed two smaller ring vortices near the shaft between the two impellers. The discharge streams are inclined at 45° towards one another and meet in a plane half-way between the impellers. The same conditions where also noted by Mahmoudi and Yanneskis(1991) and Mahmoudi(1994).

***The Plane $\theta = 0°$ (Mid way between the baffles)***

Figure 5.21a presents the mean axial velocity profiles predicted using the Simple impeller model with Hybrid differencing scheme and the $\kappa$ - $\varepsilon$ and Reynolds Stress models in the plane $\theta$ = 0°. At r = 17mm, the predicted profile obtained using the Reynolds Stress model is closer to the experimental data than that obtained using the $\kappa$ - $\varepsilon$ model except near the centre of the impeller, where the reverse applies. The Reynolds Stress model overpredicted the experimental data by approximately 85 percent at x = 40mm and underpredicted the experimental data by 55 percent at the impeller blade centre. At r = 20mm, the predictions are in general poor compared to the experimental data, although the profile predicted using the Reynolds Stress model is closer to the experimental data than that of the $\kappa$ - $\varepsilon$ model for x > 40mm and at the impeller centre. For r > 20mm, the predictions agree well with the experimental data.

Figure 5.21b presents the mean axial velocity profiles predicted using the Simple impeller model with TVD differencing scheme and the $\kappa$ - $\varepsilon$ and Reynolds Stress models in the plane $\theta$ = 0°. At r = 17 and 20mm, the predicted profile obtained using the Reynolds Stress model have moved by few percent closer to the experimental data and the predicted profile obtained using the $\kappa$ - $\varepsilon$ model moved away from the experimental data in the upper part of the impeller compared with figure 5.21a. For r > 20mm, no significant differences were noted between the predictions except at r = 25mm, where the predicted profile obtained using the $\kappa$ - $\varepsilon$ model at x = 47.5 has overpredicted the experimental data by approximately 35 percent compared with that of figure 5.21a.

Figure 5.22a presents the mean axial velocity profiles predicted using the Drag impeller model with Hybrid differencing scheme and the $\kappa$ - $\varepsilon$ and Reynolds Stress models in the plane $\theta$ = 0°. At r = 17mm, the profile predicted using the Reynolds Stress model is coincident with the experimental data in the upper part of the impeller, while the profile predicted using the $\kappa$ - $\varepsilon$ model has overpredicted the experimental data. At the same radial location, the predictions obtained using either turbulence model have failed to reproduce the experimental data at the impeller blade centre. The agreement between the experimental data and the predictions at r = 20mm is good compared with those of figures 5.21a and 5.21b. At r > 20mm, no significant changes were noted between the predictions shown in this figure and those in figure 5.21a.

Figure 5.22b presents the mean axial velocity profiles predicted using the Dynamic impeller model with TVD differencing scheme and the $\kappa$ - $\varepsilon$ and Reynolds Stress models in the plane $\theta$ = 0°. At r = 17 and 20mm, the profiles predicted using the Reynolds Stress model are closer to the experimental data than those obtained using the $\kappa$ - $\varepsilon$ model except near the impeller centre plane at r = 17mm, where the reverse applies. At the same radial locations, the profiles predicted using the Reynolds Stress model shown in this figure are closer to the experimental data than those obtained using the Simple impeller model shown in figures 5.21a and 5.21b. The $\kappa$ - $\varepsilon$ model predictions presented in figure 5.22a agree more closely with the experimental data than those shown in this figure and figures 5.21a and 5.21b. For r > 20mm, the predictions are similar to those shown in figure 5.22a.

Figure 5.23a presents the mean radial velocity profiles predicted using the Simple impeller model with Hybrid differencing scheme and the $\kappa$ - $\varepsilon$ and Reynolds Stress models in the plane $\theta$ = 0°. In general, the predicted profiles obtained using the Reynolds Stress model agree more with the experimental data than those obtained using the $\kappa$ - $\varepsilon$ model. At r = 17mm, the predictions obtained using the Reynolds Stress and $\kappa$ - $\varepsilon$ models agreed well with the experimental data in the upper part of the impeller, but underpredicted the experimental data in the impeller centre plane by 32 and 53 percent respectively. At

r = 20mm, the predicted profile obtained using the Reynolds Stress model follow a similar trend as the experimental data, but it underpredicts the experimental data by 30 percent in the upper edge of the impeller blade. At r > 20mm, the predicted profiles obtained using the Reynolds Stress model agree well with the experimental data except at x > 40mm, where the predictions have slightly overpredicted the experimental data. At r = 30 and 35mm, the predictions obtained using the $\kappa$ - $\varepsilon$ model at x = 50mm have overpredicted the experimental data by approximately 46 and 37 percent respectively.

Figure 5.23b presents the mean radial velocity profiles predicted using the Simple impeller model with TVD differencing scheme and the $\kappa$ - $\varepsilon$ and Reynolds Stress models in the plane $\theta$ = 0°. No major changes were noted with the predictions obtained using the $\kappa$ - $\varepsilon$ model at all radial locations compared with those shown in figure 5.23a except at r = 35mm, where the predicted profile at x = 50mm shown in this figure has 23 percent closer to the experimental data. The predicted profile obtained using the Reynolds Stress model shown in figure 5.23a is closer to the experimental data in the impeller region for r = 17mm and at all predicted points for r = 20mm compared to those shown in this figure. For r > 20mm, the predictions obtained using the Reynolds Stress model shown in this figure agree more closely with the experimental data near the impeller centre plane and the reverse applies at x > 40mm compared with figure 5.23a.

Figure 5.24a presents the mean radial velocity profiles predicted using the Drag impeller model with Hybrid differencing scheme and the $\kappa$ - $\varepsilon$ and Reynolds Stress models in the plane $\theta$ = 0°. In this figure, the predictions obtained using the Reynolds Stress model for r > 20mm are in a closer agreement with the experimental data compared to those of the $\kappa$ - $\varepsilon$ model. At r = 17 and 20mm, the profiles followed a similar trend as those shown in figure 5.23a. For r > 20mm the predictions obtained using either turbulence model shown in this figure have moved closer to the experimental data compared with those obtained using the Simple impeller model shown in figures 5.23a and 5.23b.

Figure 5.24b presents the mean radial velocity profiles predicted using the Dynamic impeller model with TVD differencing scheme and the $\kappa$ - $\varepsilon$ and Reynolds Stress models in the plane $\theta$ = 0°. At r = 17 and r = 20mm, no major changes were noted between the profiles predicted using the $\kappa$ - $\varepsilon$ model shown in this figure and those obtained using the Simple and Drag impeller models shown in figures 5.23a, 5.23b and 5.24a. At the same radial locations, the predictions obtained using the Reynolds Stress model agree more closely with the experimental data in the impeller region compared to those shown in figures 5.23a, 5.23b and 5.24a. In this figure, for r > 20mm, the profile predicted using the $\kappa$ - $\varepsilon$ model moved a few percent further from the experimental data at x = 50mm, whereas the predictions obtained using the Reynolds Stress model are in a closer agreement with the experimental data compared with those shown in figures 5.23a and 5.23b.

Figure 5.25a presents the mean tangential velocity profiles predicted using the Simple impeller model with Hybrid differencing scheme and the $\kappa$ - $\varepsilon$ and Reynolds Stress models in the plane $\theta$ = 0°. In general, the predictions obtained using the Reynolds Stress model agree more with the experimental data than those obtained using the $\kappa$ - $\varepsilon$ model although at r = 35mm both predicted profiles are coincident with the experimental data. The predictions at r = 17mm are poor compared with the experimental data and overpredicted the experimental data by 30 percent at the impeller centre plane. At r = 20, 25 and 30mm, the predicted profiles obtained using the Reynolds Stress model agree more closely with the experimental data than those of the $\kappa$ - $\varepsilon$ model. At r = 25mm, the predicted profile obtained using the $\kappa$ - $\varepsilon$ model has underpredicted the experimental data between the upper edge of the impeller blade and x = 40mm by 27 percent.

Figure 5.25b presents the mean tangential velocity profiles predicted using the Simple impeller model with TVD differencing scheme and the $\kappa$ - $\varepsilon$ and Reynolds Stress models in the plane $\theta$ = 0°. At r = 17mm, the predicted profile obtained using the Reynolds Stress model moved a few percent further from the experimental data, whereas those of the $\kappa$ - $\varepsilon$ model remained unchanged compared with figure 5.25a. The predictions at r = 20mm

agree more closely with the experimental data near the impeller region compared to those shown in figure 5.25a. For r > 20mm, no significant differences were noted between the predictions shown in this figure and those of figure 5.25a.

Figure 5.26a presents the mean tangential velocity profiles predicted using the Drag impeller model with Hybrid differencing scheme and the $\kappa$ - $\varepsilon$ and Reynolds Stress models in the plane $\theta$ = 0°. The most significant changes in this figure to that of figures 5.25a and 5.25b have occurred at r = 17 and 20mm. At r = 17mm, the predictions obtained using either turbulence model are coincident and agree well with the experimental data compared with figures 5.25a and 5.25b. In this figure, the profile predicted using the Reynolds Stress model at r = 20mm agrees more closely with the experimental data in the impeller region than that of the $\kappa$ - $\varepsilon$ model. At the same radial location, the profile predicted using the $\kappa$ - $\varepsilon$ model shown in this figure agree more closely with the experimental data for x > 40mm than those of figures 5.25a and 5.25b and the reverse applies in the impeller region compared to that shown in figure 5.25b.

Figure 5.26b presents the mean tangential velocity profiles predicted using the Dynamic impeller model with TVD differencing scheme and the $\kappa$ - $\varepsilon$ and Reynolds Stress models in the plane $\theta$ = 0°. The predictions obtained using the Reynolds Stress model agree more closely with the experimental data at r = 17, 20 and 25mm than those predicted using the $\kappa$ - $\varepsilon$ model and no significant changes were noted between the predictions for r > 25mm. At r = 17mm, the predicted profiles obtained using the Reynolds Stress model in the upper part of the impeller agree more closely with the experimental data than those obtained using the Simple impeller model shown in figures 5.25a and 5.25b, however, in the impeller region the predicted profile obtained by the Drag impeller model, figure 5.26a, was the closest to the experimental data. The predictions at r = 20mm are similar to those presented in figure 5.25a, however, the predictions obtained using the Reynolds Stress model agree more closely with the experimental data than that of figure 5.25a. For r > 20mm, no significant changes were noted between the predictions shown in this figure and those shown in figure 5.25b.

***The Plane $\theta = 45°$ ( In the plane of the baffles)***

Figure 5.27a presents the mean axial velocity profiles predicted using the Simple impeller model with Hybrid differencing scheme and the $\kappa$ - $\varepsilon$ and Reynolds Stress models in the plane $\theta$ = 45°. At r = 17 and 20mm, the predictions reproduce the experimental data at the impeller centre plane, however, in the upper part of the impeller blade the predictions obtained using the Reynolds Stress model agrees more closely with the experimental data than those of the $\kappa$ - $\varepsilon$ model. At r = 25mm, the predictions overpredicted the experimental data between x = 42.5 and 45mm by 33 percent and at r = 35mm the predictions underpredicted the experimental data in the impeller centre plane by 39 percent. The predictions obtained by either turbulence model at r = 30mm agreed well with the experimental data.

Figure 5.27b presents the mean axial velocity profiles predicted using the Simple impeller model with TVD differencing scheme and the $\kappa$ - $\varepsilon$ and Reynolds Stress models in the plane $\theta$ = 45°. In general, the predictions obtained using the Reynolds Stress model agree more with the experimental data than those obtained using the $\kappa$ - $\varepsilon$ model, but at r = 17mm the prediction obtained using the Reynolds Stress model underpredicted the experimental data by 57 percent in the upper edge of the impeller blade. Compared to the predictions using the Hybrid differencing, figure 5.27a, the predictions obtained using the TVD scheme with the Reynolds Stress model agree more closely with the experimental data at r = 17, 20, 25 and 35mm than those shown in figure 5.27a. The predictions obtained using the $\kappa$ - $\varepsilon$ model at r = 17 and 20mm in this figure have moved further from the experimental data in the upper part of the impeller, whereas no significant changes were noted for r > 20mm compared with those shown in figure 5.27a.

Figure 5.28a presents the mean axial velocity profiles predicted using the Drag impeller model with Hybrid differencing scheme and the $\kappa$ - $\varepsilon$ and Reynolds Stress models in the plane $\theta$ = 45°. The predicted profile obtained using the Reynolds Stress model agree more closely with the experimental data at r = 17mm than those obtained using the $\kappa$ - $\varepsilon$

model in the upper part of the impeller and both predicted profiles underpredicted the experimental data at the impeller centre plane by 67 percent. For r > 17mm, the predictions in this figure agree well with the experimental data and the predictions located at r = 20, 25 and 35mm agree more closely with the experimental data than those obtained using the Simple impeller model shown in figure 5.27a.

Figure 5.28b presents the mean axial velocity profiles predicted using the Dynamic impeller model with TVD differencing scheme and the $\kappa$ - $\varepsilon$ and Reynolds Stress models in the plane $\theta$ = 45°. At r = 17, 20, 25 and 30mm, the predictions are similar to those obtained using the Simple impeller model with TVD scheme, figure 5.27b, but at r = 17mm the prediction obtained using the Reynolds Stress model shown in this figure have predicted the experimental data in the upper edge of the impeller blade. At r = 35mm, the predictions obtained using the $\kappa$ - $\varepsilon$ and Reynolds Stress models have underpredicted the experimental data in the impeller region by 39 and 43 percent respectively. The predictions obtained at r = 17mm using the TVD scheme with Reynolds Stress model shown in this figure is the closer to the experimental data than those of figures 5.27a, 5.27b and 5.28a. At r = 17 and 20mm, the predictions obtained using the Hybrid differencing with $\kappa$ - $\varepsilon$ model shown in figure 5.28a are the closer to the experimental data than those shown in this figure and figures 5.27a, 5.27b.

Figure 5.29a presents the mean radial velocity profiles predicted using the Simple impeller model with Hybrid differencing scheme and the $\kappa$ - $\varepsilon$ and Reynolds Stress models in the plane $\theta$ = 45°. In general, the predictions obtained using the Reynolds Stress model agree more closely with the experimental data at all radial locations than those of the $\kappa$ - $\varepsilon$ model. At r = 17 and 20mm, the predictions obtained using the Reynolds Stress model underpredicted the experimental data peaks in the impeller region by 33 and 37 percent respectively. At r = 20, 25, 30 and 35mm, the predictions obtained using the $\kappa$ - $\varepsilon$ model have overpredicted the experimental data at x = 50mm by 27, 40, 34 and 28 percent respectively.

Figure 5.29b presents the mean radial velocity profiles predicted using the Simple impeller model with TVD differencing scheme and the $\kappa$ - $\varepsilon$ and Reynolds Stress models in the plane $\theta$ = 45°. No significant changes were noted between the predictions obtained using the $\kappa$ - $\varepsilon$ model and those shown in figure 5.29a. The predicted profile obtained using the Reynolds Stress model moved closer to the experimental data between the centre of the impeller blade and x = 40mm for r = 17mm and in the impeller centre plane for r = 20mm than those shown in figure 5.29a. At r = 17mm the prediction obtained using the Reynolds Stress model overpredicted the experimental data by 37.4 percent at the centre of the impeller blade and by approximately 36 percent for r > 17mm in the upper edge of the impeller.

Figure 5.30a presents the mean radial velocity profiles predicted using the Drag impeller model with Hybrid differencing scheme and the $\kappa$ - $\varepsilon$ and Reynolds Stress models in the plane $\theta$ = 45°. The predictions obtained using the Reynolds Stress model at r = 17, 20 and 25mm agree more closely with the experimental data than those of the $\kappa$ - $\varepsilon$ model. At r = 17 and 20mm, the predictions obtained using the Reynolds Stress model underpredicted the experimental data peaks in the impeller region by 60 and 64 percent respectively. For r > 20mm, the predictions obtained using either turbulence model agree more closely with the experimental data compared to those obtained using the Simple impeller model shown in figures 5.29a and 5.29b.

Figure 5.30b presents the mean radial velocity profiles predicted using the Dynamic impeller model with TVD differencing scheme and the $\kappa$ - $\varepsilon$ and Reynolds Stress models in the plane $\theta$ = 45°. The predictions obtained using the $\kappa$ - $\varepsilon$ model are similar to those obtained using the Simple impeller model shown in figures 5.29a and 5.29b except at x = 50mm, where the predictions presented in this figure moved further from the experimental data by approximately 22 percent for r > 20mm. The predictions obtained using the Reynolds Stress model shown in this figure at r = 17 and 20mm are the closes to the experimental data than those shown in figures 5.29a, 5.29b and 5.30a. The predictions obtained for r > 20mm using the same turbulence model agree more closely

with the experimental data between x = 42.5mm and above the centre of the impeller blade than those shown in figure 5.29b. No significant changes were noted when compared with the predictions of figure 5.30b except at r = 35mm, where the prediction shown in this figure underpredicts the experimental data at x = 50mm by 24 percent.

Figure 5.31a presents the mean tangential velocity profiles predicted using the Simple impeller model with Hybrid differencing scheme and the $\kappa$ - $\varepsilon$ and Reynolds Stress models in the plane $\theta$ = 45°. The predictions obtained using the Reynolds Stress model at r = 17 and 20mm agree more closely with the experimental data than those of the $\kappa$ - $\varepsilon$ model, however, the predictions obtained at r = 17mm using the Reynolds Stress model has overpredicted the experimental data by approximately 23 percent. The predictions for r > 20mm obtained by either turbulence model agree well with the experimental data.

Figure 5.31b presents the mean tangential velocity profiles predicted using the Simple impeller model with TVD differencing scheme and the $\kappa$ - $\varepsilon$ and Reynolds Stress models in the plane $\theta$ = 45°. No significant differences were noted between the predictions obtained using the $\kappa$ - $\varepsilon$ model shown in this figure and those of figure 5.31a. The predictions obtained using the Reynolds Stress model moved further from the experimental data by approximately 69 percent in the impeller centre plane at r = 17mm and by few percent between the upper edge of the impeller blade and x = 47.5mm for r > 20mm than those shown in figure 5.31a.

Figure 5.32a presents the mean tangential velocity profiles predicted using the Drag impeller model with Hybrid differencing scheme and the $\kappa$ - $\varepsilon$ and Reynolds Stress models in the plane $\theta$ = 45°. At r = 17mm, the predictions obtained using the Reynolds Stress and $\kappa$ - $\varepsilon$ models agree well with the experimental data above the impeller centre than those obtained using the Simple impeller model shown in figures 5.31a and 5.31b, however, they underpredicted the experimental data in the impeller centre by 26 and 52 percent respectively. The predictions agreed well with the experimental data at r = 20mm in the upper part of the impeller blade, but failed to predict the experimental data in the

impeller centre plane. For r > 20mm, no significant differences were noted between the predictions shown in this figure and those shown in figure 5.31a.

Figure 5.32b presents the mean tangential velocity profiles predicted using the Dynamic impeller model with TVD differencing scheme and the $\kappa$ - $\varepsilon$ and Reynolds Stress models in the plane $\theta$ = 45°. The predictions obtained using the $\kappa$ - $\varepsilon$ model shown in this figure are similar to those obtained using the Hybrid differencing with the Simple impeller model shown in figure 5.31a. The predictions obtained using the Reynolds Stress model agree more closely with the experimental data than those obtained using the TVD scheme with the Simple impeller model shown in figure 5.31b. At r = 17mm, the predictions obtained using the Reynolds Stress and Drag impeller models, figure 5.32a, agree more closely with the experimental data between the centre and the edge of the impeller than that shown in this figure and the reverse applies at r = 20mm.

**Fluctuating Velocities**

Lee(1995), indicated that the high turbulence levels for the fluctuating axial, radial and tangential velocities are observed next to the leading blade indicating the presence of the trailing vortex generated by the preceding blade. The experimental data of Lee also show that the level of the radial fluctuating velocities are higher than the axial fluctuating velocities and that the level obtained for the tangential fluctuating velocities was a little higher than those of the radial fluctuating velocities. The differences between the fluctuating velocities indicate that the turbulence in the vicinity of the impeller blades is considered anisotropic.

In the $\theta$ = 0° plane, the high levels of the axial fluctuating velocity around r = 20mm are associated with the flow produced by the preceding blade and are higher than those measured for the single impeller. The axial fluctuating velocities in all $\theta$ planes ( 0°, 15°, 30° and 45°) extend outward from the blade at an angle of around 45° to the horizontal and are located axially between the impeller blade centre and x = 50mm. The high levels of the

radial and tangential fluctuating velocities associated with the flow produced by the preceding and the leading blade are less than the axial fluctuating velocity at x = 50mm. The high levels of turbulence tends to diminish as the radial distance increases similar to those of the single impeller.

***The Plane $\theta = 0°$ (Mid way between the baffles)***

Figure 5.33a presents the tangential fluctuating velocity profiles predicted using the Simple impeller model with Hybrid differencing scheme and the $\kappa$ - $\varepsilon$ and Reynolds Stress models in the plane $\theta = 0°$. In general, the predictions obtained at r = 17, 20, 25 and 30mm using the Reynolds Stress model agree more closely with the experimental data than those of the $\kappa$ - $\varepsilon$ model. At r = 25mm, the predictions failed to reproduce the experimental data between the centre of the impeller blade and x = 40mm and at r = 35mm the predicted profiles obtained using either turbulence model agree well with the experimental data.

Figure 5.33b presents the tangential fluctuating velocity profiles predicted using the Simple impeller model with TVD differencing scheme and the $\kappa$ - $\varepsilon$ and Reynolds Stress models in the plane $\theta = 0°$. The predictions presented in this figure are similar to those shown in figure 5.33a except for a few differences at r = 17, 20 and 25mm. In this figure, the profiles predicted using the $\kappa$ - $\varepsilon$ model at these radial locations moved by few percent closer to the experimental data in the impeller blade region than those shown in figure 5.33a. At r = 20 and 25mm, the predictions obtained using the Reynolds Stress model presented in this figure also moved closer to the experimental data by 20 percent at the impeller blade centre and by 49 percent between the centre and the upper edge of the impeller blade compared with those shown in figure 5.33a.

Figure 5.34a presents the tangential fluctuating velocity profiles predicted using the Drag impeller model with Hybrid differencing scheme and the $\kappa$ - $\varepsilon$ and Reynolds Stress models in the plane $\theta = 0°$. In general, no significant differences were noted between the

predictions obtained using either turbulence model at all radial locations except at r = 20mm. At this radial location the Reynolds Stress predicted profile is 12 percent closer to the experimental data in the impeller blade region than that of the $\kappa$ - $\varepsilon$ model. Compared to the predictions using the Simple impeller model, figure 5.33a, it was noted that at r = 17mm the predictions shown in this figure moved by more than 50 percent further from the experimental data in the impeller blade centre than that shown in figure 5.33a. For r > 17mm, the predictions obtained using the Reynolds Stress model also moved by approximately 27 percent further from the experimental data above the impeller blade than those shown again in figure 5.33a.

Figure 5.34b presents the tangential fluctuating velocity profiles predicted using the Dynamic impeller model with TVD differencing scheme and the $\kappa$ - $\varepsilon$ and Reynolds Stress models in the plane $\theta$ = 0°. The predictions obtained using the Reynolds Stress model at all radial locations agree well with the experimental data and are similar to those obtained using the Simple impeller model presented in figure 5.33b. The predicted profiles obtained using the $\kappa$ - $\varepsilon$ model shown in this figure followed a similar trend as those presented again in figure 5.33b.

***The Plane $\theta$ = 45° (In the plane of the baffles)***

Figure 5.35a presents the tangential fluctuating velocity profiles predicted using the Simple impeller model with Hybrid differencing scheme and the $\kappa$ - $\varepsilon$ and Reynolds Stress models in the plane $\theta$ = 45°. The predictions obtained using either turbulence model agree well with the experimental data at r = 17mm, where the profile predicted using the $\kappa$ - $\varepsilon$ model overpredicted the experimental data at x = 50mm by 15 percent. At r = 20mm, the predictions obtained using the Reynolds Stress model agree more closely with the experimental data between the impeller blade centre and x = 40mm than that of the $\kappa$ - $\varepsilon$ model, while it underpredicted the experimental data by 52 percent at the impeller blade centre. For r > 20mm, no significant changes were noted between the predictions obtained using either turbulence model except at r = 25mm, where the profile

predicted using the Reynolds Stress model agree more closely with the experimental data between the upper part of the impeller blade and x = 42.5mm than that of the $\kappa$ - $\varepsilon$ model.

Figure 5.35b presents the tangential fluctuating velocity profiles predicted using the Simple impeller model with TVD differencing scheme and the $\kappa$ - $\varepsilon$ and Reynolds Stress models in the plane $\theta$ = 45°. At r = 17mm, the predictions in the upper edge of the impeller blade moved by 10 percent closer to the experimental data than those shown in figure 5.35a. The prediction obtained using the Reynolds Stress model was able to predict the experimental data at the impeller blade centre, while no changes were noted with the prediction obtained using the $\kappa$ - $\varepsilon$ model compared with those shown in figure 5.35a. For r > 20mm, the predictions agree more closely with the experimental data than those shown in figure 5.35a.

Figure 5.36a presents the tangential fluctuating velocity profiles predicted using the Drag impeller model with Hybrid differencing scheme and the $\kappa$ - $\varepsilon$ and Reynolds Stress models in the plane $\theta$ = 45°. In general, no significant differences were noted between the predictions in this figure except at r = 17mm, where the profile predicted using the Reynolds Stress model agrees more closely with the experimental data than that of the $\kappa$ - $\varepsilon$ model at the impeller blade centre. The predictions at this radial location moved by approximately 18 percent further from the experimental data in the impeller blade region than those obtained using the Simple impeller model, figure 5.35a. At r = 20mm, the predictions are in general poor between the impeller blade centre and x = 42.5mm compared with those shown in figure 5.35a. At r = 25, 30 and 35mm, the predictions are coincident with each other and moved further from the experimental data between the impeller blade centre and x = 45mm by 10, 8.5 and 5.3 percent respectively to those of figure 5.53a.

Figure 5.36b presents the tangential fluctuating velocity profiles predicted using the Dynamic impeller model with TVD differencing scheme and the $\kappa$ - $\varepsilon$ and Reynolds

Stress models in the plane $\theta$ = 45°. The predictions shown in this figure are similar to those obtained using the Simple impeller model, figure 5.35b and the only major difference was observed at r = 17mm. At this radial location, the profile predicted using the Reynolds Stress model overpredicted the experimental data at the impeller blade centre by 57 percent compared with that of figure 5.35b.

## 5.7 Influence of Grid Refinement on the Computations

The purpose of the work in this section was to investigate the effect of refining the mesh on the predictions of a cylindrical tank stirred by a single Rushton impeller discussed in section 5.5. In the process of investigating the grid independency of the solution the grid was refined in each direction separately in order to reduce the computer storage and running time. In the following section the computed results obtained using the refined meshes with single Rushton impeller are discussed.

### 5.7.1 Results and Discussion

The calculations in this investigation was carried out using the meshes 98x29x51, 55x58x51 and 55x29x96 and the Dynamic impeller model together with the following combinations of differencing scheme and turbulence model:

i) Hybrid scheme and $\kappa$ - $\varepsilon$ turbulence model.
ii) Hybrid scheme and Reynolds Stress turbulence model.
iii) TVD scheme and $\kappa$ - $\varepsilon$ turbulence model.
iv) TVD scheme and Reynolds Stress turbulence model.

In the results described below, all velocities were normalised with the impeller tip speed of 3.77m/s. Figures 5.37 and 5.38 present axial profiles for the mean radial and fluctuating tangential velocities. Each figure contains five profiles taken at radial locations of 17, 20,

25, 30 and 35mm and each radial location contains the predictions obtained before and after mesh refinement and the experimental data obtained by Lee(1995).

Most results obtained using refined grids in the axial, radial and tangential directions were coincident with the predictions obtained using grid size of 55x29x51 or the differences between them were very small. However, the results shown in figures 5.37 and 5.38 showed some differences between the predictions obtained before and after grid refinement and have been selected for discussion.

Figures 5.37a and 5.37b present the mean radial velocity profiles predicted using the Dynamic impeller model, TVD scheme with Reynolds Stress turbulence model and refined mesh sizes of 55x29x96 and 55x58x51 in the planes $\theta = 0°$ and $\theta = 45°$respectively. In general the differences at all radial locations between the predictions obtained using mesh, 55x29x51, and the refined mesh in either plane were very small if any. For example, the differences, figure 5.37a, can be seen for r > 20mm whereas the only differences between the predictions, figure 5.37b, were noted at r = 17 and 35 mm and have occurred in regions of steep gradients.

Figure 5.38 presents the tangential fluctuating velocity profiles predicted using the Dynamic impeller model, Hybrid differencing with $\kappa$ - $\varepsilon$ turbulence model and refined mesh size of 55x58x51 in the plane $\theta = 0°$. The only differences between the predictions presented in this figure were small and noted above the impeller disk centre at all radial locations.

Comparing the predictions discussed above with the experimental data, it was noted that the predicted profile obtained using the refined mesh, figure 5.37b, moved closer to the experimental data than those predicted using the 55x29x51 mesh at the impeller blade centre. However, the predictions above the impeller disk centre, figure 5.38, obtained using mesh 55x29x51 agreed more with the experimental data compared with the predictions obtained using the refined mesh, 55x58x51.

The minor differences that were observed in the above figures indicate that refining the grid individually showed little change to the numerical solution compared with the predictions obtained using the original mesh 55x29x51. At this point the predictions shown in the figures discussed above might represent a grid independent solution, however, to make sure that a grid independent solution is reached the grid refinement must be applied together to all three directions. In this case, to run each one of the above differencing scheme and models combinations might take several months before obtaining a converged solution and this was not performed.

## 5.8 Computational Effort

The calculations carried out in this study for the single and double impellers shown in tables 5.1 and 5.2 respectively were computed on a DEC Alpha workstation. Tables 5.3 and 5.4 present the CPU time, in seconds, required to complete one iteration for the different combinations of impeller model, differencing scheme and turbulence model. Table 5.5 shows the velocity variables for which transport equations are solved for either the single or double impellers.

| Impeller model | Differencing scheme | Turbulence model | CPU time/iteration (seconds) |
|---|---|---|---|
| Simple | Hybrid | $\kappa$ - $\varepsilon$ | 15.4 |
| | | Reynolds Stress | 36.2 |
| | TVD | $\kappa$ - $\varepsilon$ | 17.35 |
| | | Reynolds Stress | 41.37 |
| Drag | Hybrid | $\kappa$ - $\varepsilon$ | 15.2 |
| | | Reynolds Stress | 36.0 |
| | TVD | $\kappa$ - $\varepsilon$ | 17.5 |
| | | Reynolds Stress | 41.2 |
| Dynamic | Hybrid | $\kappa$ - $\varepsilon$ | 15.4 |
| | | Reynolds Stress | 36.3 |
| | TVD | $\kappa$ - $\varepsilon$ | 17.4 |
| | | Reynolds Stress | 41.5 |

Table 5.3. Flow field CPU time required to complete one iteration for the single Rushton impeller calculations (refer to footnote on page 69).

| Impeller model | Differencing scheme | Turbulence model | CPU time/iteration (seconds) |
|---|---|---|---|
| Simple | Hybrid | $\kappa$ - $\varepsilon$ | 22.8 |
| | | Reynolds Stress | 53.7 |
| | TVD | $\kappa$ - $\varepsilon$ | 25.2 |
| | | Reynolds Stress | 59.93 |
| Drag | Hybrid | $\kappa$ - $\varepsilon$ | 22.4 |
| | | Reynolds Stress | 53.5 |
| | TVD | $\kappa$ - $\varepsilon$ | 25.7 |
| | | Reynolds Stress | 60.5 |
| Dynamic | Hybrid | $\kappa$ - $\varepsilon$ | 22.74 |
| | | Reynolds Stress | 53.73 |
| | TVD | $\kappa$ - $\varepsilon$ | 25.6 |
| | | Reynolds Stress | 60.7 |

Table 5.4. Flow field CPU time required to complete one iteration for the double Rushton impeller calculations.

| Turbulence models | $\kappa$ - $\varepsilon$ | Reynolds Stress |
|---|---|---|
| Velocity variables | U, V, W. $\delta$P, $\kappa$, $\varepsilon$ | U, V, W, $\delta$P, $\varepsilon$, $\overline{uu}$, $\overline{vv}$, $\overline{ww}$, $\overline{uv}$, $\overline{uw}$, $\overline{vw}$ |
| Number of transport equations | 6 | 11 |

Table 5.5. Velocity variables for which transport equations are solved for either the single or double impellers.

Tables 5.3 and 5.4 show that the Reynolds Stress turbulence model has used more CPU time than the $\kappa$ - $\varepsilon$ turbulence model to complete one iteration. The ratio of CPU time between the Reynolds Stress and $\kappa$ - $\varepsilon$ turbulence models is constant at around 2.4 and is consistent with the increase in the number of equations and the increased complexity of the Reynolds Stress transport equations. For example, using the $\kappa$ - $\varepsilon$ and Reynolds Stress turbulence models with the Simple impeller model and Hybrid differencing, table 5.3, have used 15.4 and 36.2 seconds of CPU time respectively. As shown in table 5.5, the Reynolds Stress turbulence model solves 11 equations, while only 6 equations are solved by the $\kappa$ - $\varepsilon$ turbulence model resulting in the increase in the CPU time.

The effect of the different impeller models on the CPU time were very small as shown in tables 5.3 and 5.4. For example, the Simple, Drag and Dynamic impeller models with the Hybrid and Reynolds Stress turbulence model, table 5.4, have used 53.7, 53.5 and 53.73 seconds of CPU time respectively.

Tables 5.3 and 5.4 show that the TVD scheme takes more CPU time per iteration than the Hybrid differencing because the convection terms containing flux limiters were added to the source term explicitly and represent an increase in effort.

Tables 5.3 and 5.4 also show that the CPU times produced by the double impeller are greater than those of the single impeller which is caused by the addition of the second

impeller and the increase in the number of nodes in the I-direction from 55 nodes in the single impeller to 64 nodes in the double impellers.

## 5.9 Circumferential Effect of the Impeller Models

In this section the effect of the Drag and Dynamic impeller models on the periodicity of the flow in a vessel stirred by a single Rushton impeller is discussed with respect to the mean tangential velocity. Figures 5.39a, b and c present the circumferential profiles of predicted mean tangential velocities and the experimental data of Lee(1995) over 180° in the x = 33.5 plane at r = 17mm.

Figure 5.39a presents the circumferential profiles of the mean tangential velocity obtained experimentally by Lee(1995), where the impeller blades are located at 0°, 60°, 120° and 180°. The data shows large velocity fluctuations in the circumferential direction with a distinct periodicity exhibiting three cycles in the 180°. Each cycle covers a 60° sector and corresponds to the passage of an impeller blade where the tangential velocity reaches a minimum value of -0.14 at 7.5° and a maximum value of 0.27 at 27.7°. The peaks located at 0°, 60°, 120° and 180° reflects the positions of the impeller blades, whereas the velocity variations between the blades correspond to the trailing vortex generated behind each blade.

Figures 5.39b and 5.39c present the circumferential mean tangential velocity profiles obtained using the Drag and Dynamic impeller models respectively with Hybrid differencing and $\kappa$ - $\varepsilon$ turbulence model. The predicted profile obtained using the Drag impeller model shows only two cycles per half revolution where each cycle occupies a 90° sector in contrast to the experimental data, figure 5.39a. The first cycle has reached a minimum value of 0.37 at 26.25° and a maximum value of 0.47 at 71.25°, whereas the minimum of the second cycle has reached a value of 0.38 at 116.25° and a maximum of 0.38 at 161.25°.

The predicted profile obtained using the Dynamic impeller model, figure 5.39c. has generated what appears to be three cycles per half revolution, however, these cycles have higher velocities and are not as regular as the cycles shown in figures 5.39a and 5.39b although the predicted velocity fluctuations shown in this figure shows a similar variation to that of the experimental data in terms of the number of maximum and minimum peaks. It is noted that the first, second and third predicted and experimental data velocity peaks have occurred at 32° and 27.7°, 90° and 87.7° and 150° and 147.7° respectively. The predictions show three minimum velocity values of 0.818 at 46° and 0.806 at about 107° and 0.81 at about 170°, while the experimental data minimum velocity value of -0.14 is observed at 7.5°, 67.5° and 127.5°.

Figure 5.39d presents the impeller function, $F_{DS}$, used in modelling the Dynamic impeller model, section 5.4.3. The impeller function shows a distinct periodicity exhibiting three cycles per half revolution and each cycle covers a 60° sector with maximum and minimum values of 1.0 and 0.0.

In conclusion the predictions obtained using the Drag impeller model, figure 5.39b. shows a periodic variation and the peak located at 60° reflect the position of one impeller blade compared to the experimental data. The use of an impeller function, $F_{DS}$, has helped the Dynamic impeller model to produce a similar behaviour to that of the experimental data, figure 5.39c, showing high velocity levels at 60° and 120° coinciding with the impeller blade positions and the velocity variation occurring between 0° to 60°, 60° to 120° and 120° to 180° reflects the trailing vortex and compares with the experimental data, figure 5.39a. However, the actual values of the predicted velocity variations produced by the Drag impeller model agree more closely to the experimental data than those of the Dynamic impeller model although large differences remain.

## 5.10 Conclusions

In this section, the main conclusions are summarised for grid refinement, single and double Rushton impellers and circumferential effect of the impeller models.

***Grid Refinement***

To assess the grid independency of the solution the grid may refined in each individual (I, J, K) direction one at a time. The comparison between the refined and unrefined predictions showed almost no variation differences and it is possible therefore that a grid independent solution has been reached which ideally should be confirmed by repeating the calculations on a mesh that has been refined in all three directions simultaneously.

***Single Rushton Turbine***

***The Plane $\theta = 0°$ (Mid way between the baffles)***

The differences between the predictions adjacent to the impeller obtained using the Simple and Dynamic impeller models were small irrespective of the differencing scheme or turbulence model used and generally agreed more closely with the experimental data than those of the Drag impeller model; except for the mean tangential velocity profiles, where the predictions obtained using the Drag impeller model were the closest to the experimental data. Far from the impeller, the predicted mean radial velocity profiles obtained using the Simple and Dynamic impeller models with the Reynolds Stress turbulence model agree more closely with the experimental data than those of the $\kappa$ - $\varepsilon$ turbulence model. In contrast no differences were noted between the predictions obtained using the Drag impeller model with either turbulence model and are closer to the experimental data at the impeller blade centre than those of the Simple and Dynamic impeller models. No significant differences were noted between the predictions of the mean axial and tangential velocities obtained irrespective of the differencing scheme or

turbulence model or impeller model used. The predictions of the tangential fluctuating velocity obtained using the Simple and Dynamic impeller models with the Reynolds Stress model agreed more closely with the experimental data in the lower edge of the impeller blade than those of the $\kappa$ - $\varepsilon$ turbulence model and the reverse applies in the upper edge of the impeller blade. In general the predictions of the tangential fluctuating velocity obtained by the Simple and Dynamic impeller models are closer to the experimental data than those of Drag impeller model.

***The Plane $\theta = 45°$ (In the plane of the baffles)***

In this plane the mean axial velocity profiles close to the impeller were best predicted using the Simple and Dynamic impeller models with TVD scheme and the $\kappa$ - $\varepsilon$ turbulence model, whereas far from the impeller the predictions obtained using the Simple and Drag impeller models with the $\kappa$ - $\varepsilon$ turbulence model agree more closely with the experimental data than those obtained using the Simple and Dynamic impeller models with TVD scheme. The predicted mean radial velocity profiles obtained using the Simple and Dynamic impeller models with the Reynolds Stress turbulence model agree more closely with the experimental data than any of those using the $\kappa$ - $\varepsilon$ turbulence model and any of those using the Drag impeller model. Predictions of the mean tangential velocity obtained by the Drag impeller model have moved closer to the experimental data than those of the Simple and Dynamic impeller models; except at r = 20mm where the reverse applies. The differences between the predictions of the tangential fluctuating velocity obtained using the Simple and Dynamic impeller models are small; except at r = 20mm where the predictions obtained using the Simple and Dynamic impeller models with the Reynolds Stress turbulence model and TVD scheme in the lower edge of the impeller blade agree more closely with the experimental data than those of the Simple impeller model with either turbulence model and Hybrid differencing and moved closer to the experimental data than those of the Drag impeller model.

In the above conclusions it was noted that in most cases the differences between the predictions obtained using the Simple and Dynamic impeller models were small irrespective of the differencing scheme or turbulence model used and generally agreed more closely with the experimental data than those of the Drag impeller model; except in the predictions of the mean tangential velocity where the reverse applies (does not apply for predictions obtained at r = 20mm in the $\theta$ = 45°). This indicate that the predictions were mostly effected by the impeller models.

***Double Rushton Turbine***

***The Plane $\theta$ = 0° (Mid way between the baffles)***

The predictions obtained using the Reynolds Stress turbulence model generally agree more closely with the experimental data than those of the $\kappa$ - $\varepsilon$ turbulence model, however, it was noted that in few cases, e.g., the mean axial velocities, the differences located far from the impeller are small between the predictions obtained using either turbulence model. The predictions obtained using the Dynamic impeller model with the Reynolds Stress turbulence model and TVD scheme agree more closely with the experimental data especially close to the impeller; except with the predictions of the mean tangential velocity where the predictions obtained by the Drag impeller model with the Reynolds Stress turbulence model agreed the most with the experimental data. The predictions of the mean axial and tangential velocities obtained using the $\kappa$ - $\varepsilon$ turbulence model with the Drag impeller model moved closer to the experimental data than those of the $\kappa$ - $\varepsilon$ turbulence model with either the Simple or Dynamic impeller model.

***The Plane $\theta$ = 45° (In the plane of the baffles)***

In this plane, the predictions obtained using the Reynolds Stress turbulence model again agree more closely with the experimental data than those of the $\kappa$ - $\varepsilon$ turbulence model especially close to the impeller. The predictions obtained using the Dynamic impeller

model with the Reynolds Stress turbulence model and TVD scheme are generally the closest to the experimental data again especially close to the impeller. The differences between the predictions obtained using either turbulence model and the Drag impeller model located far from the impeller are small. A similar behaviour was again noted with the predictions of the mean tangential velocity obtained using the Simple impeller model with Hybrid differencing and the Dynamic impeller model with TVD scheme and the tangential fluctuating velocities obtained using either differencing scheme with the Simple and Dynamic impeller models. The prediction of the tangential fluctuating velocity at r = 17mm obtained using the Reynolds Stress turbulence model and TVD scheme with the Simple impeller model is the closest to the experimental data.

The conclusions above indicate that in both planes that the predictions close to the impeller were best predicted using the Reynolds Stress turbulence model and TVD scheme with the Dynamic impeller model and that obtained using the Reynolds Stress turbulence model agree more closely with the experimental data than those of the $\kappa$ - $\varepsilon$ turbulence model. The conclusions also show that the differences between the predictions obtained by either turbulence model located far from the impeller are in many cases small.

***Circumferential Effect of the Impeller Models***

The use of an impeller function, $F_{DS}$, has helped the Dynamic impeller model to produce a similar behaviour to that of the experimental data as showing high velocity levels at 60° and 120° coinciding with the impeller blade locations. However, the values of the predicted velocity variation obtained by the Drag impeller model agree more closely to the experimental data than those of the Dynamic impeller model.

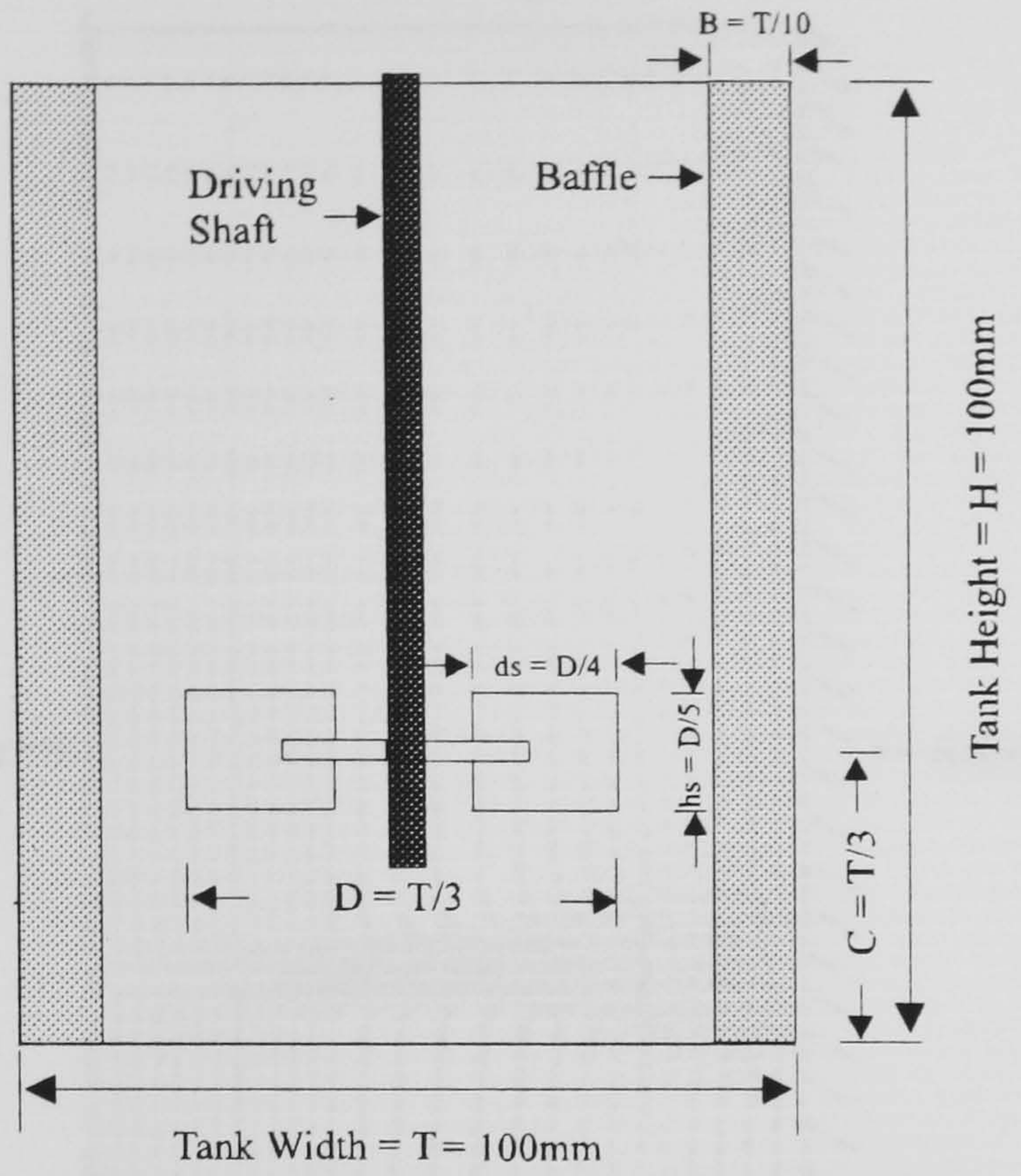



Figure.5.1. Cylindrical tank with single Rushton turbine impeller.

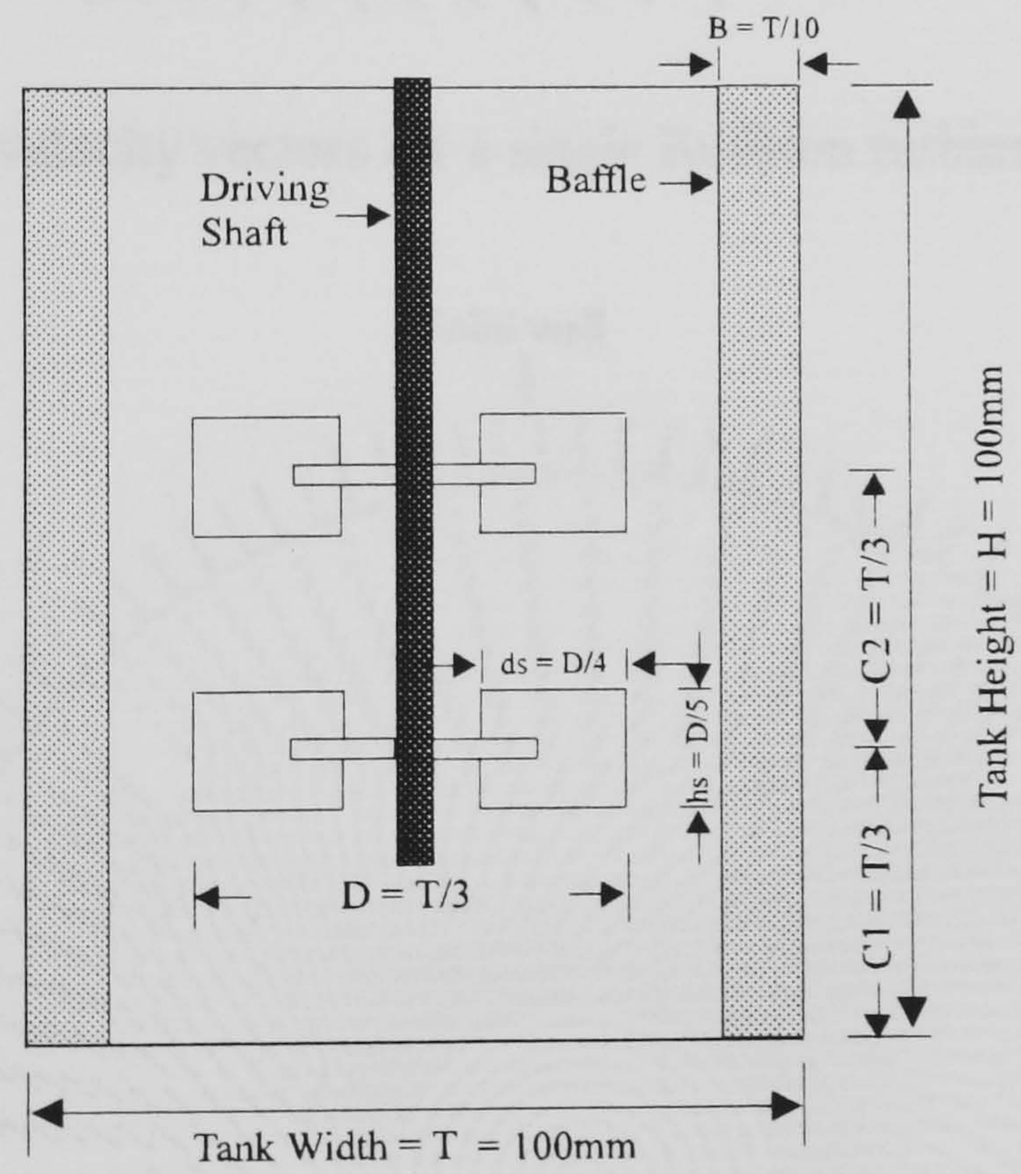



Figure.5.2. Cylindrical tank with double Rushton turbine impeller.

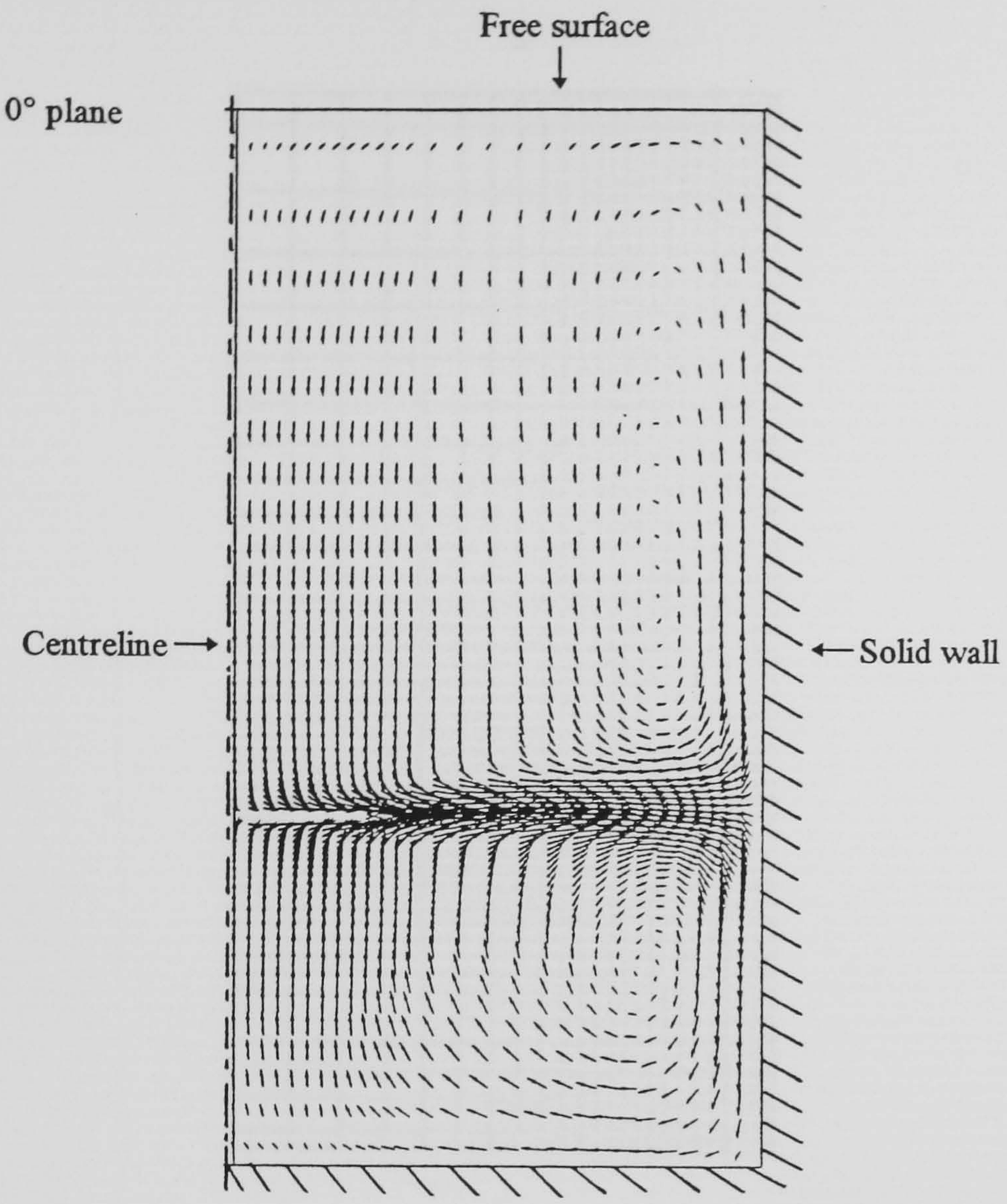



Figure.5.3a. Mean velocity vectors for a single Rushton turbine in the $\theta = 0°$ plane.

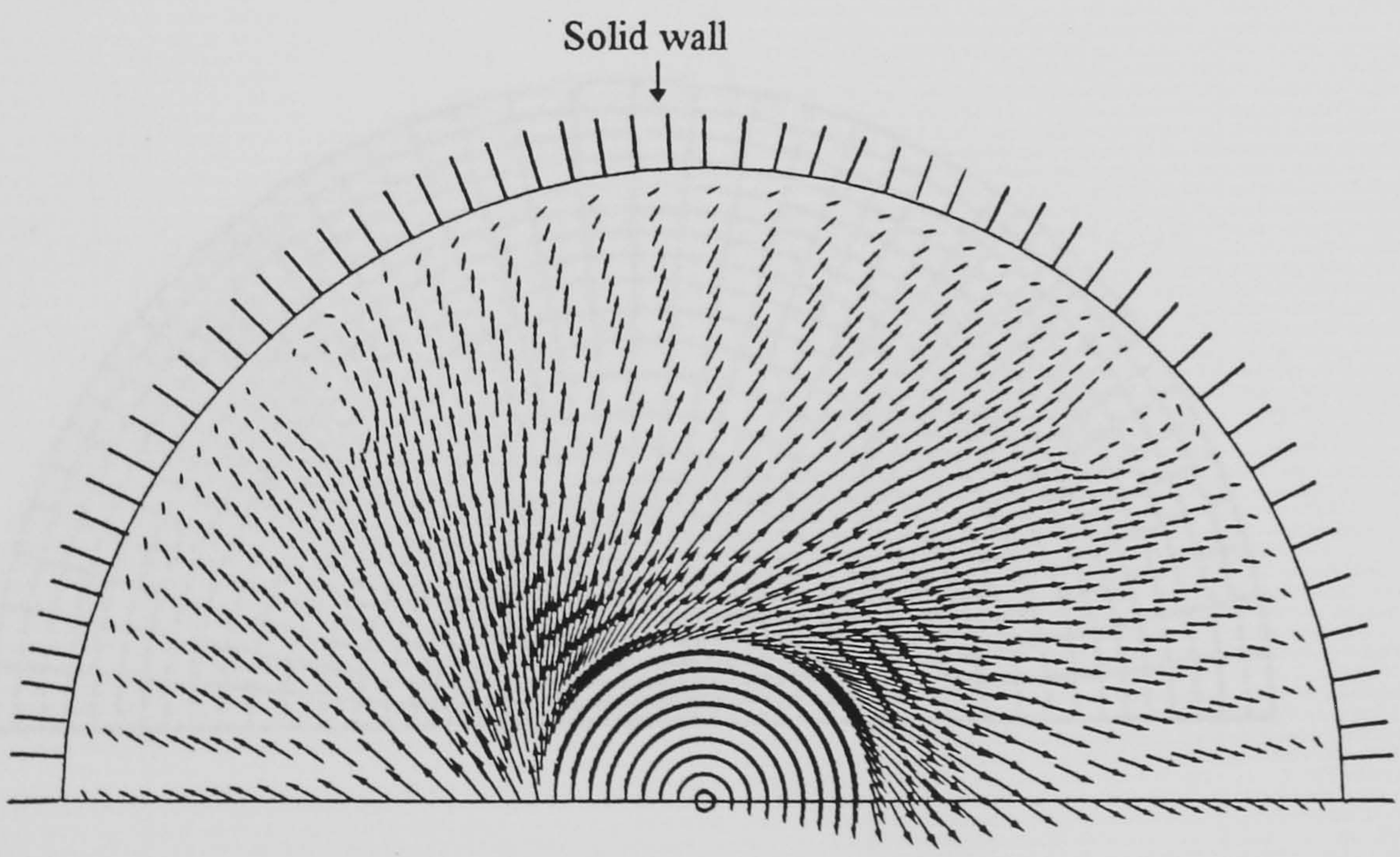



Figure.5.3b. Mean velocity vectors for a single Rushton turbine in the x = 33.5mm plane.

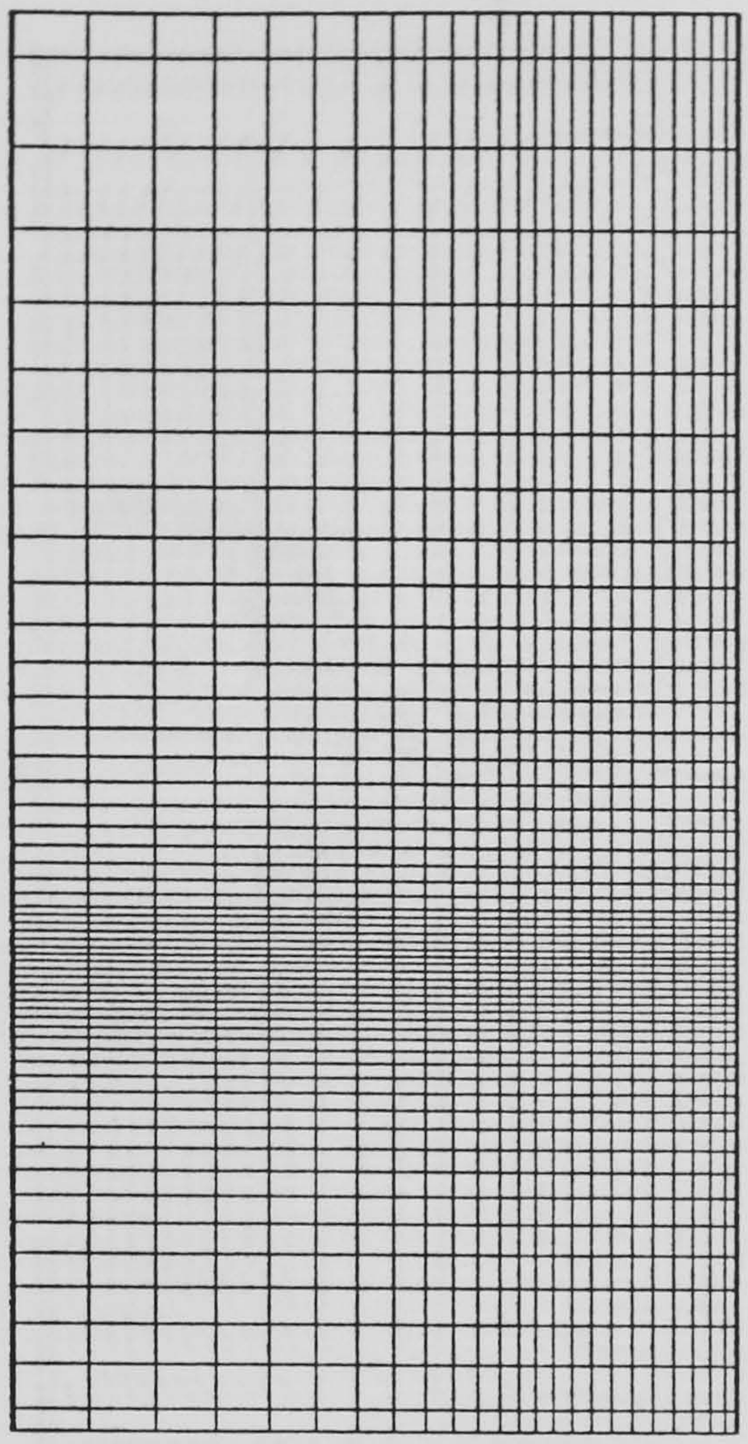


Figure.5.3c. Node distribution for a single Rushton turbine in the axial-radial plane.

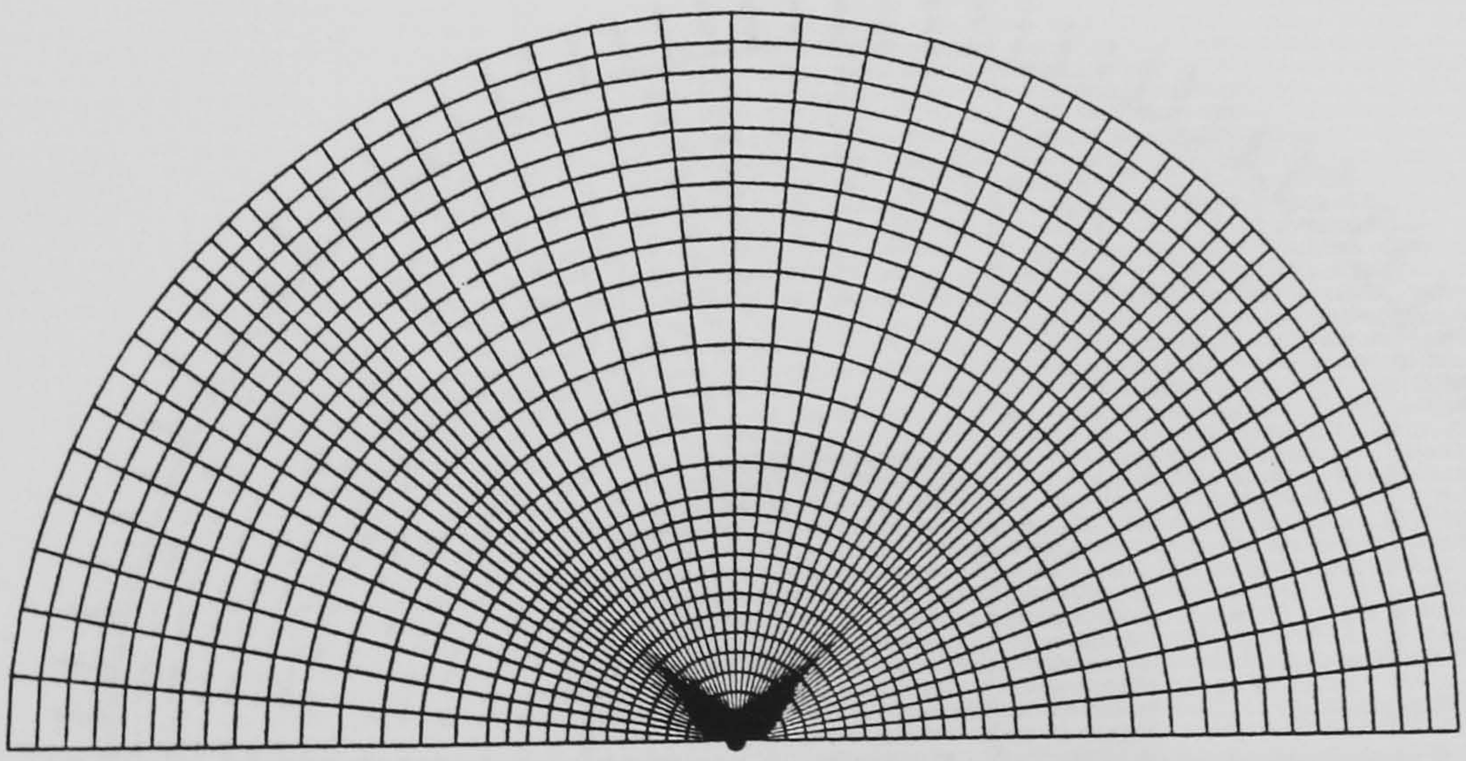


Figure.5.3d. Node distribution for a single Rushton turbine in the radial-tangential plane.

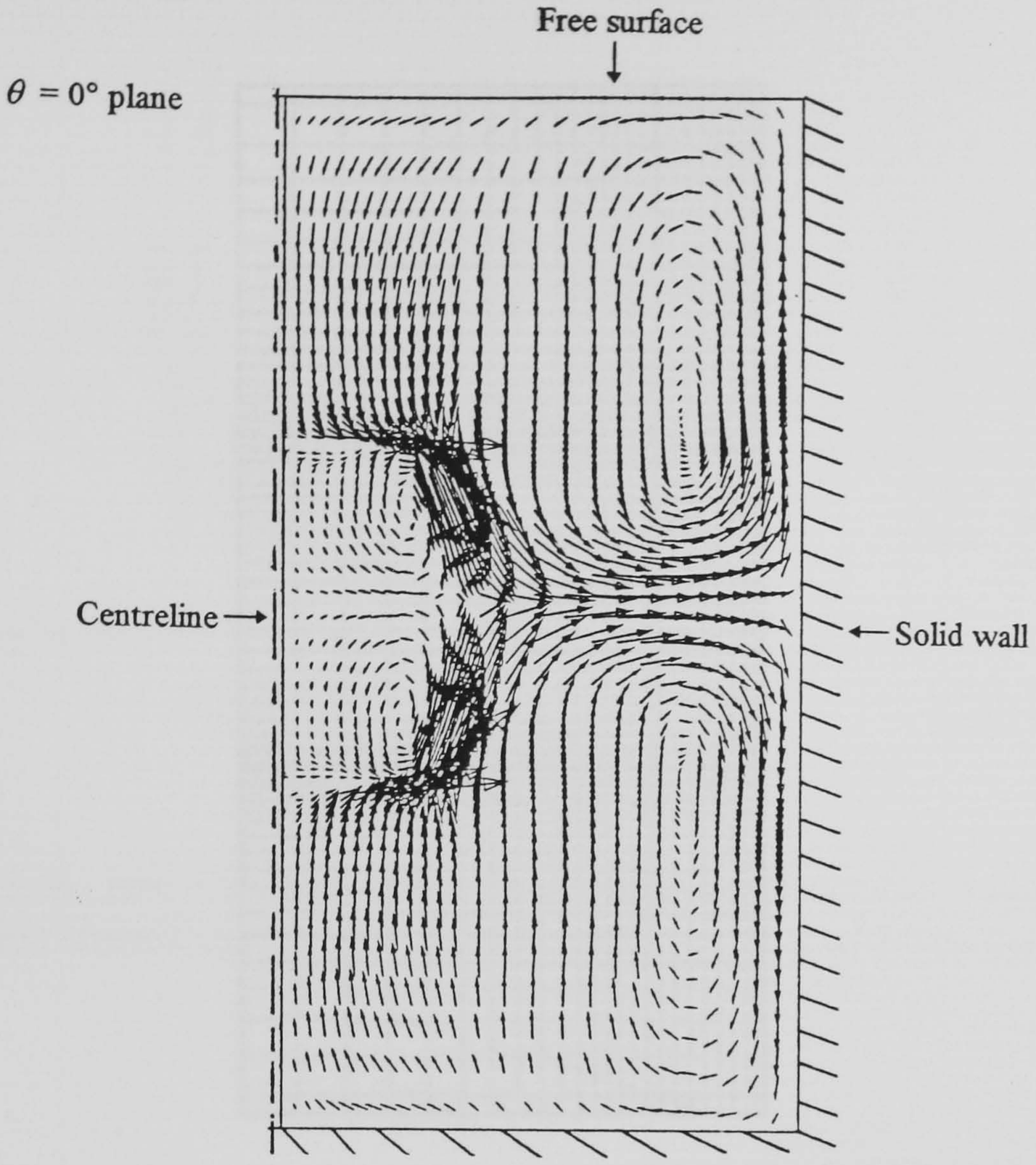



Figure.5.4a. Mean velocity vectors for a double Rushton turbine in the $\theta = 0°$ plane.

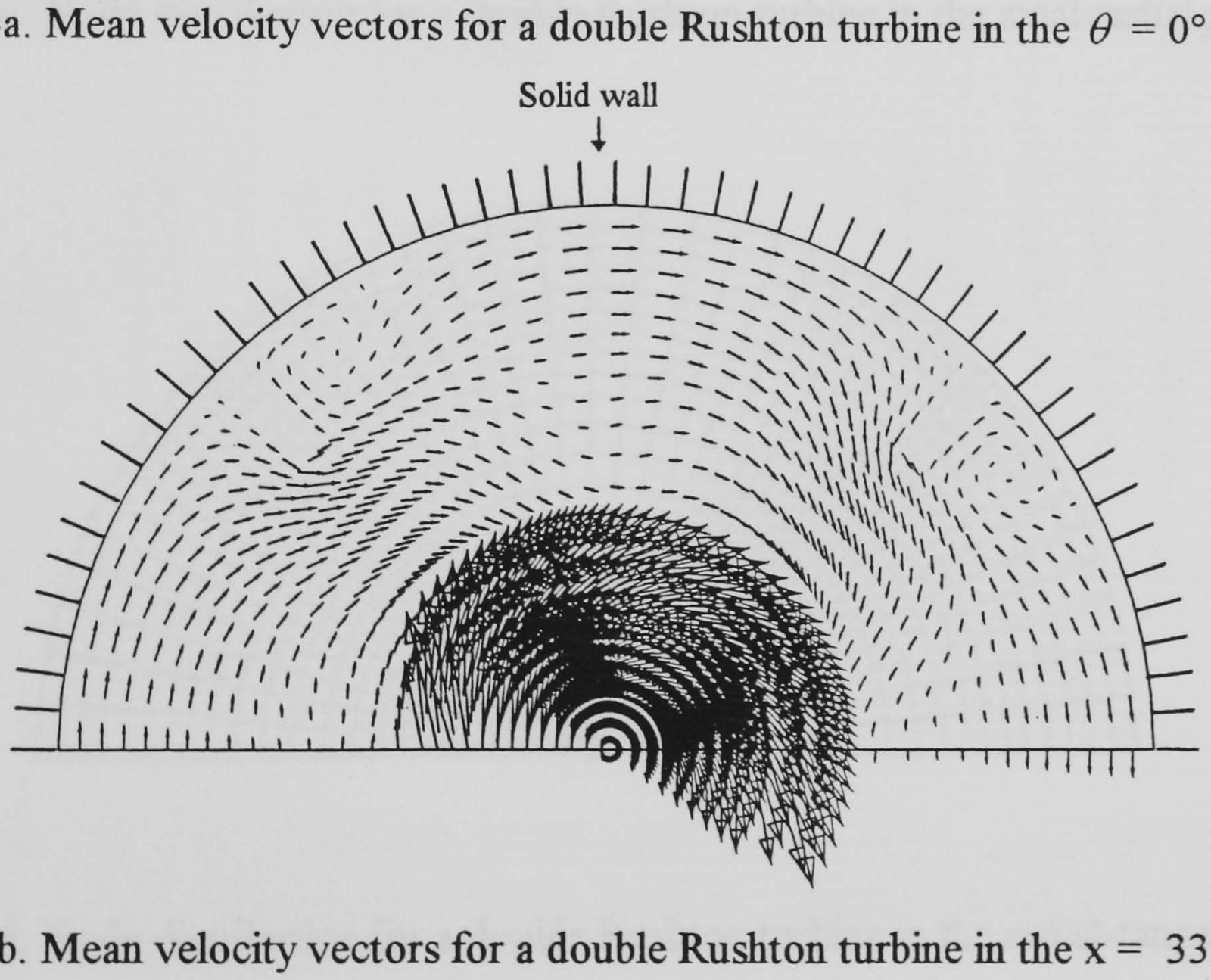



Figure.5.4b. Mean velocity vectors for a double Rushton turbine in the x = 33.1mm plane.

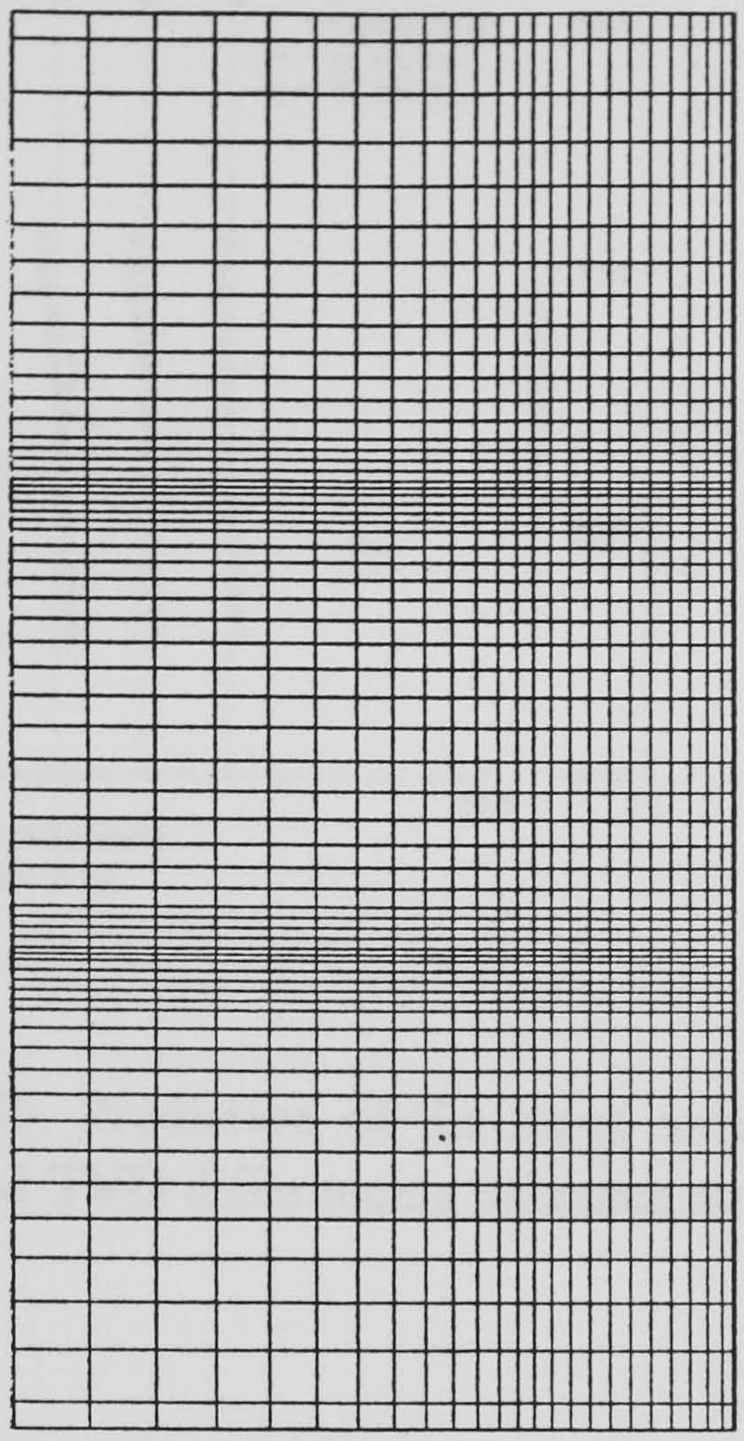


Figure.5.4c. Node distribution for a double Rushton turbine in the axial-radial plane.

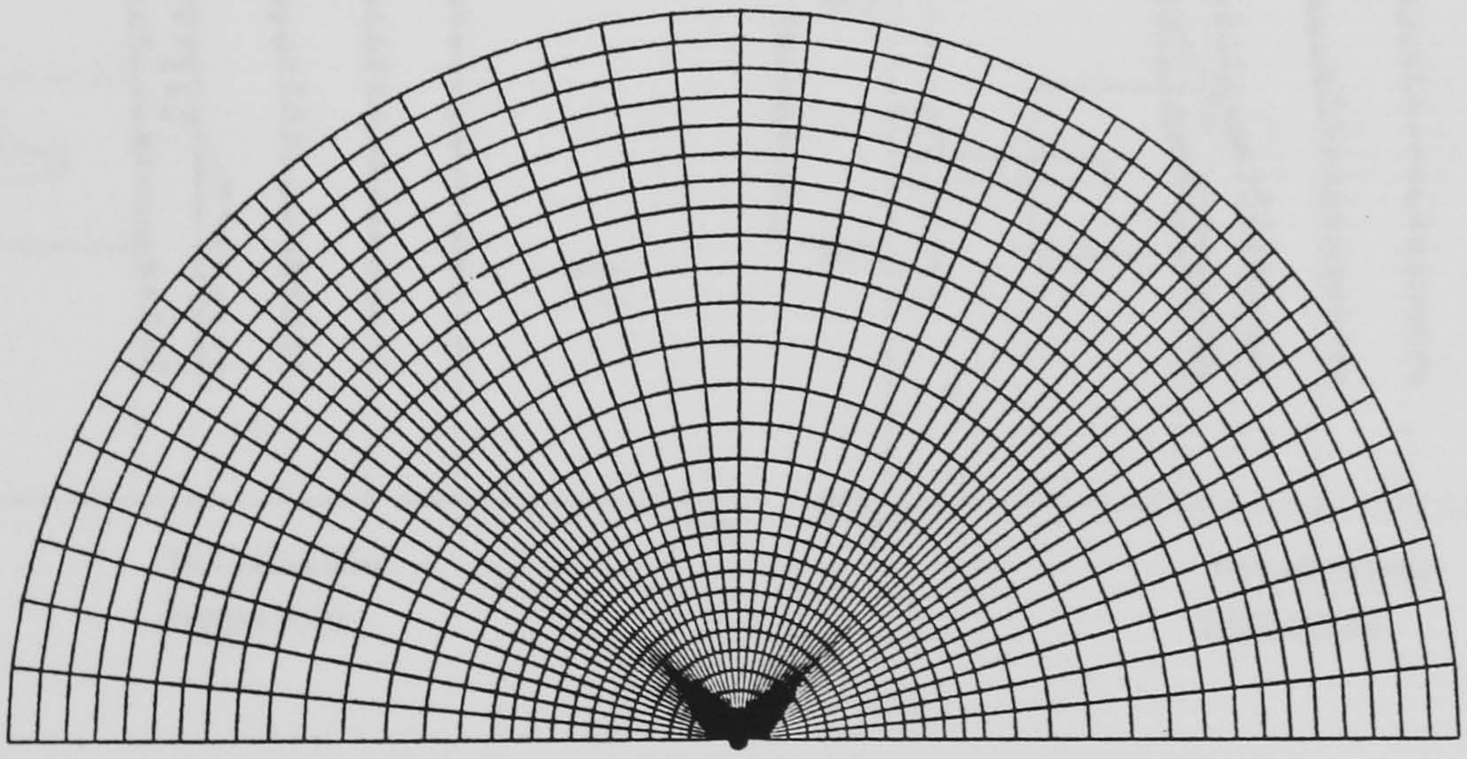


Figure.5.4d. Node distribution for a double Rushton turbine in the radial-tangential plane.

Figure.5.5a.




Figure.5.5b.

Figures 5.5a. and 5.5b. Prediction of the mean axial velocity using the Simple impeller model with Hybrid and TVD differencing schemes respectively in the plane $\theta = 0°$.

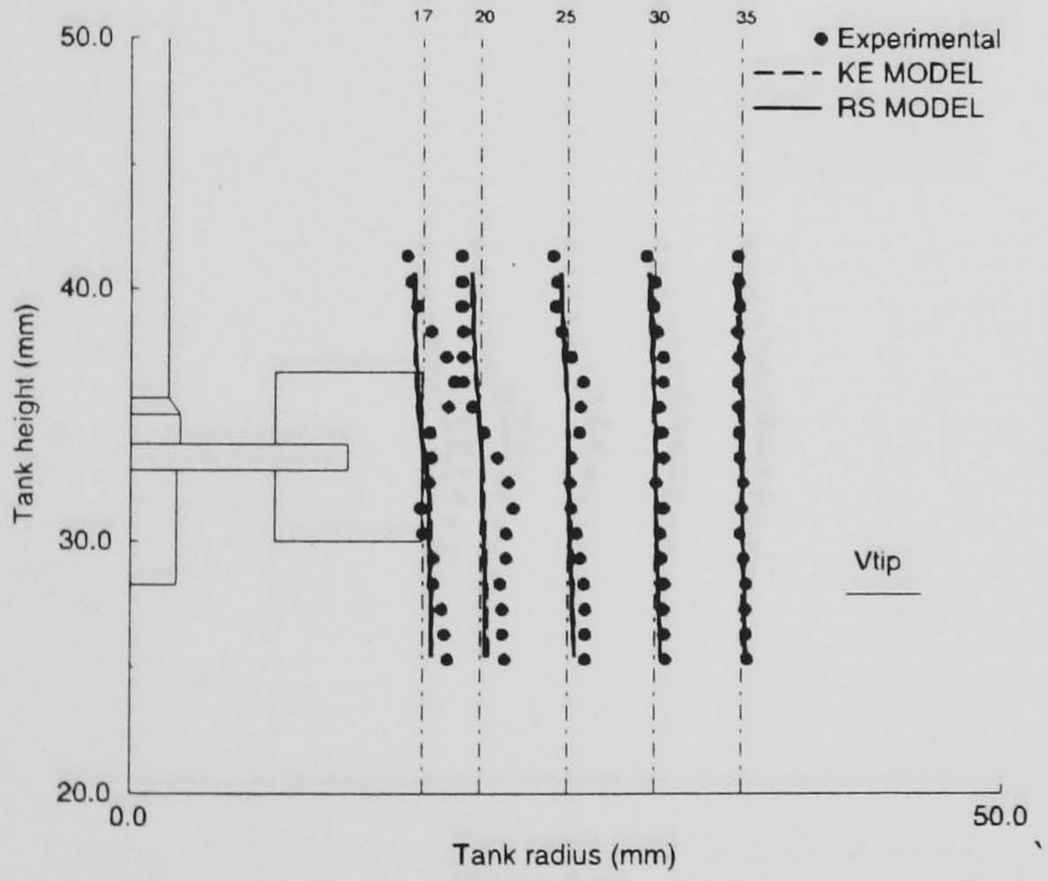



Figure.5.6a.

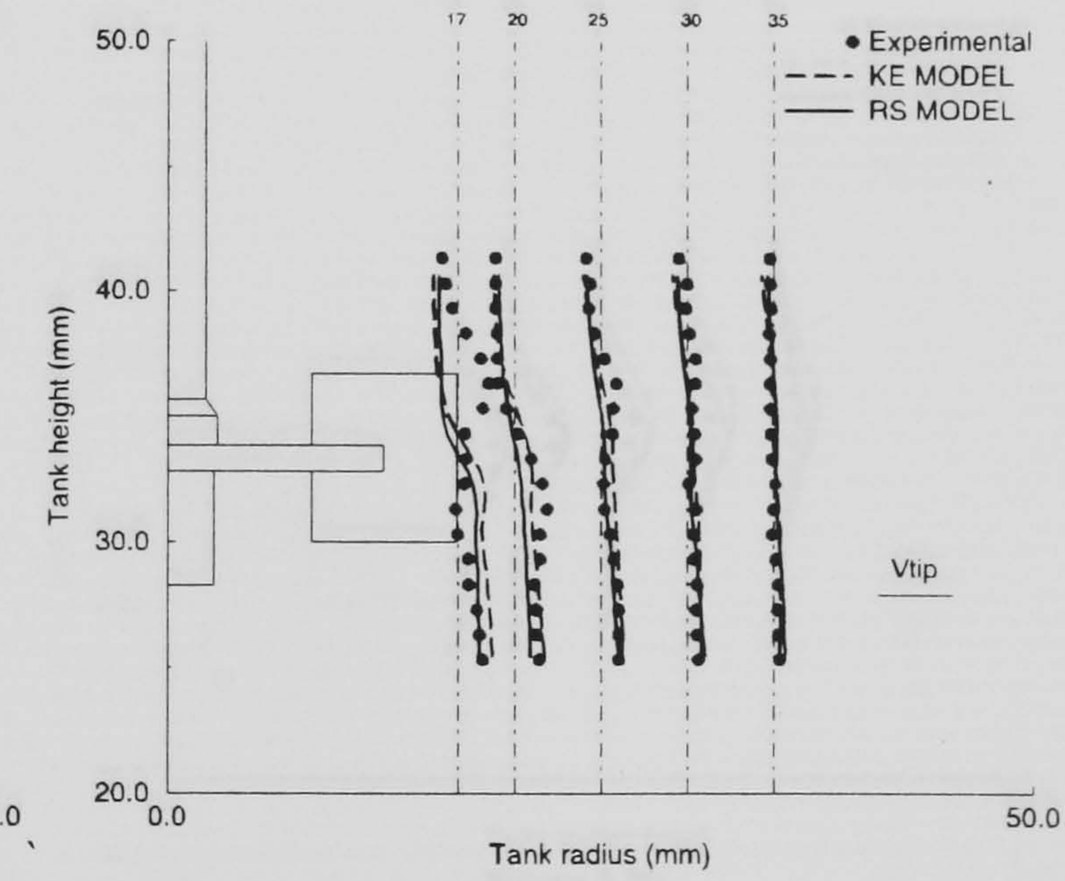



Figure.5.6b.

Figures 5.6a. and 5.6b. Prediction of the mean axial velocity using the Drag impeller model with Hybrid differencing and the Dynamic impeller model with TVD scheme respectively in the plane $\theta = 0°$.

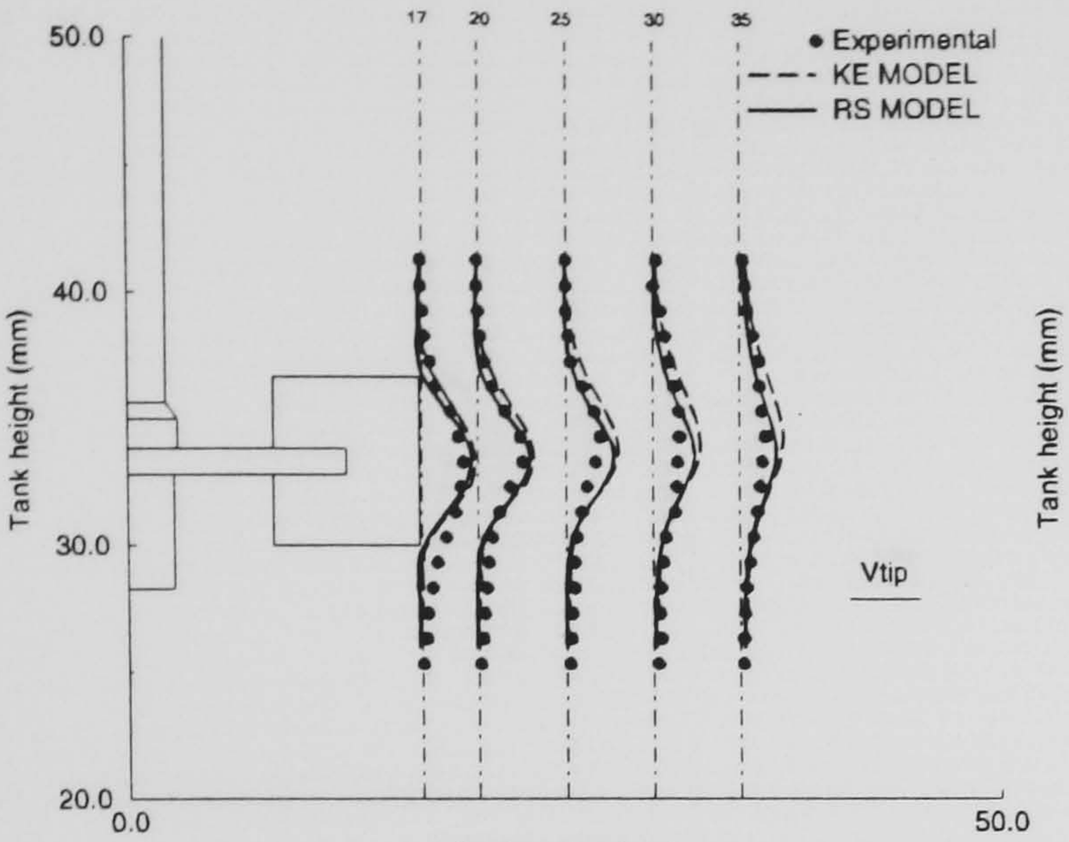


Figure.5.7a.

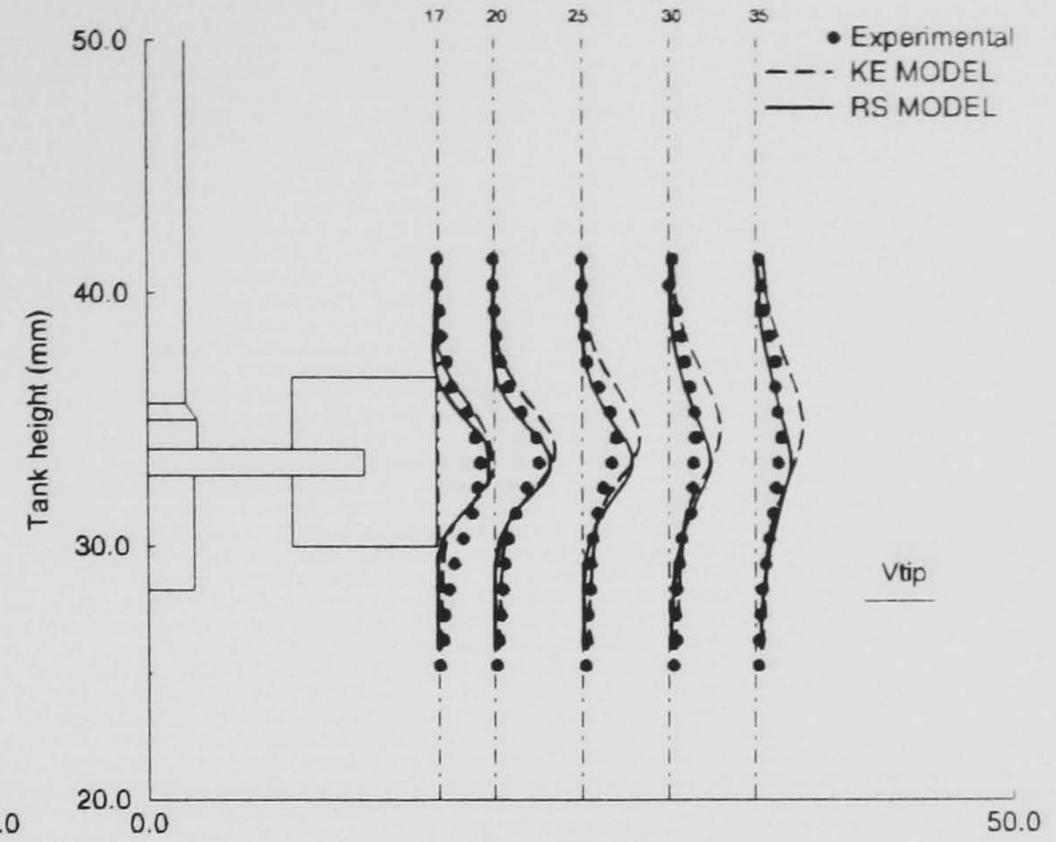


Figure.5.7b.

Figures 5.7a. and 5.7b. Prediction of the mean radial velocity using the Simple impeller model with Hybrid and TVD differencing schemes respectively in the plane $\theta = 0°$.

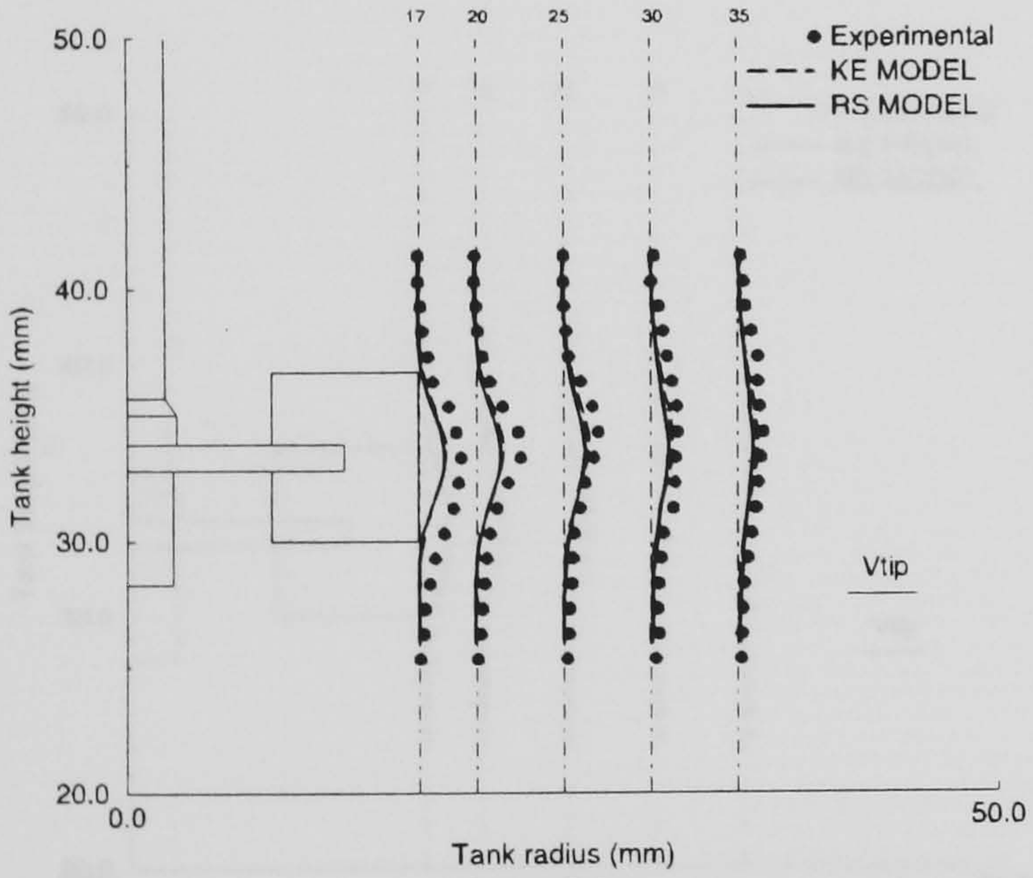


Figure.5.8a.

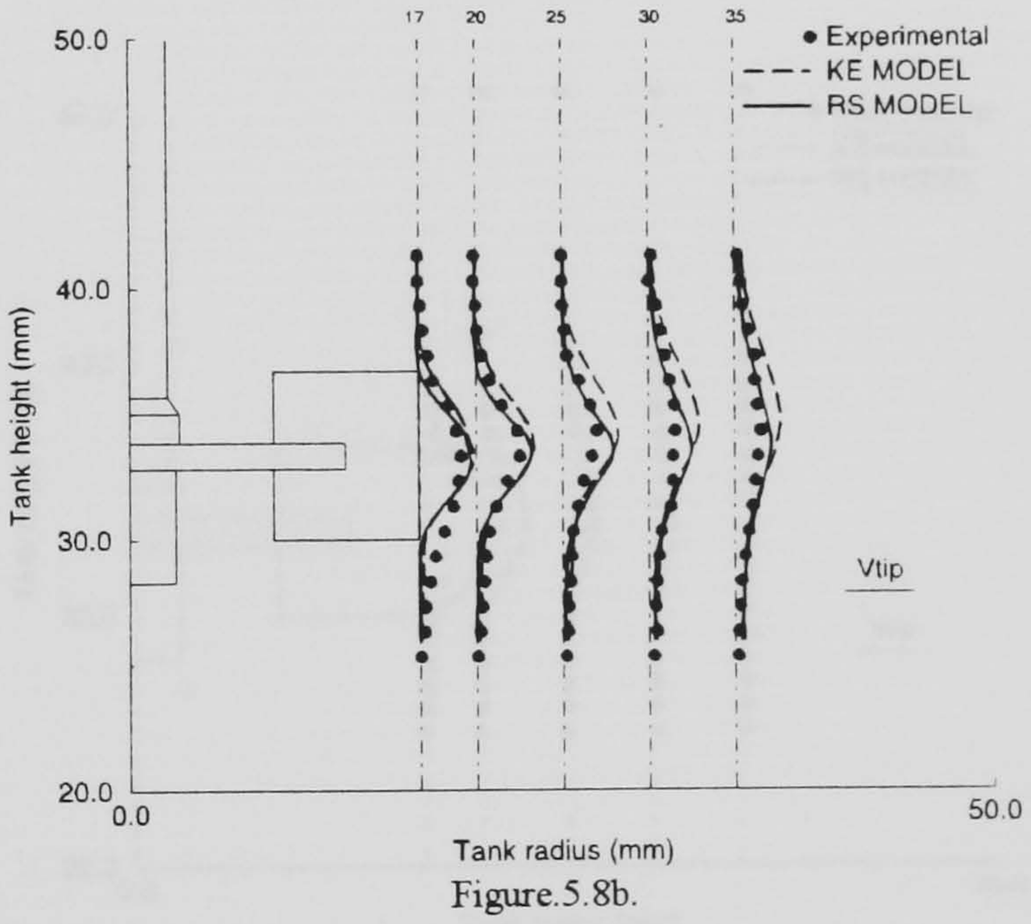


Figure.5.8b.

Figures 5.8a. and 5.8b. Prediction of the mean radial velocity using the Drag impeller model with Hybrid differencing and the Dynamic impeller model with TVD scheme respectively in the plane $\theta = 0°$.

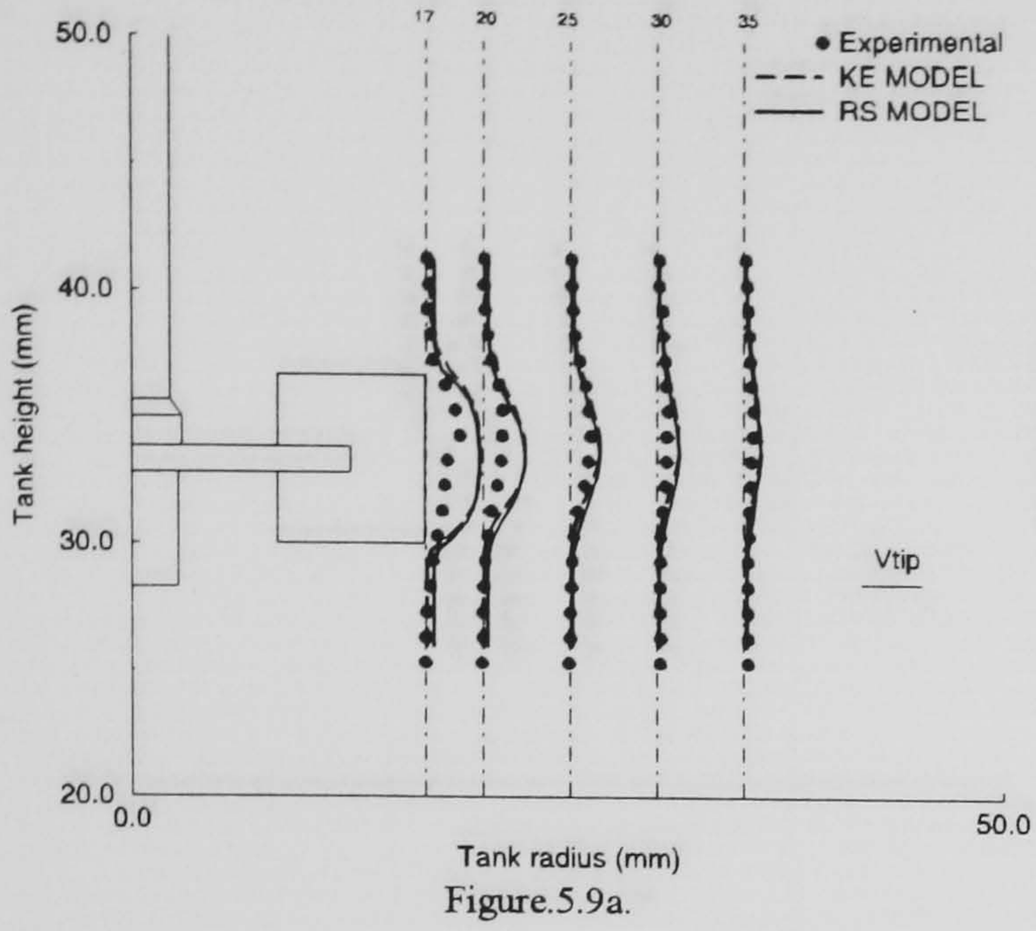


Figure.5.9a.

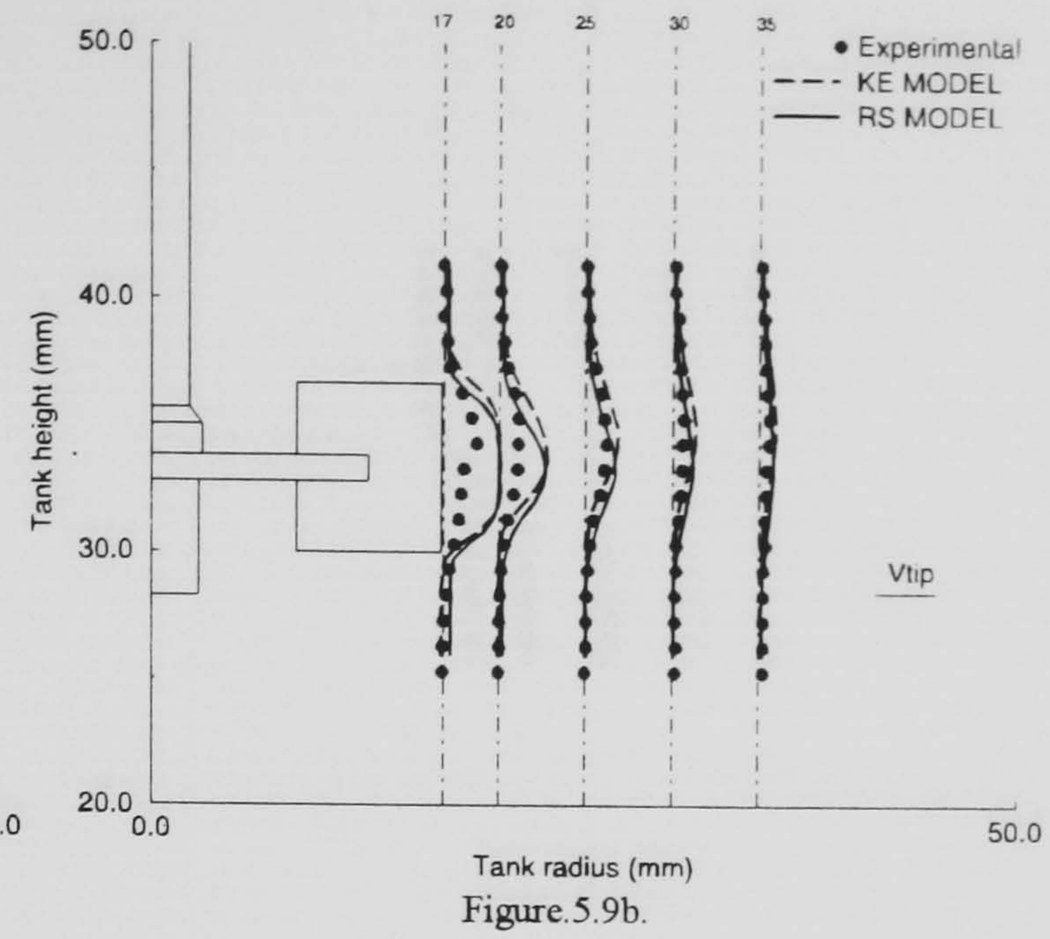


Figure.5.9b.

Figures 5.9a. and 5.9b. Prediction of the mean tangential velocity using the Simple impeller model with Hybrid and TVD differencing schemes respectively in the plane $\theta$ = 0°.

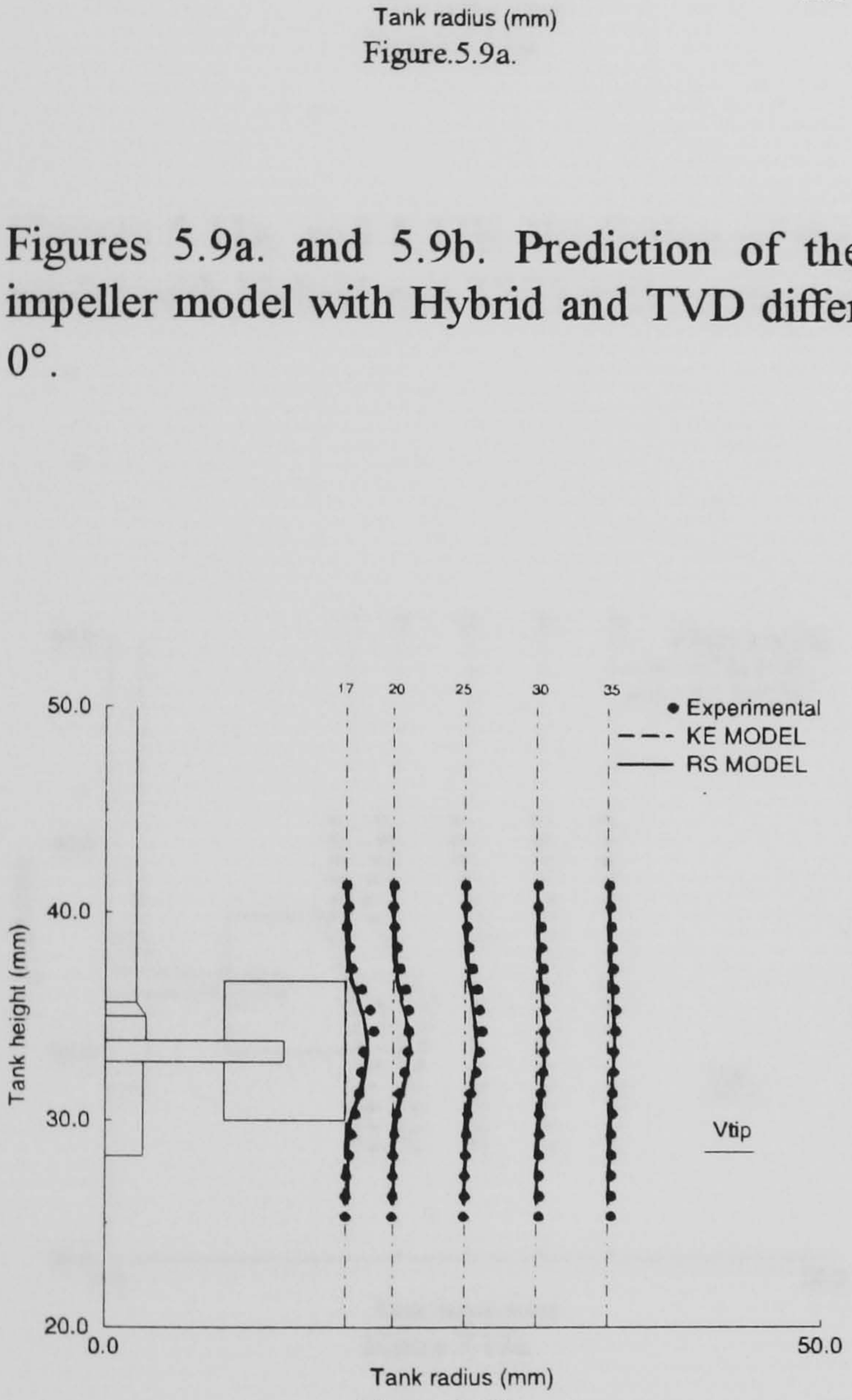


Figure.5.10a.

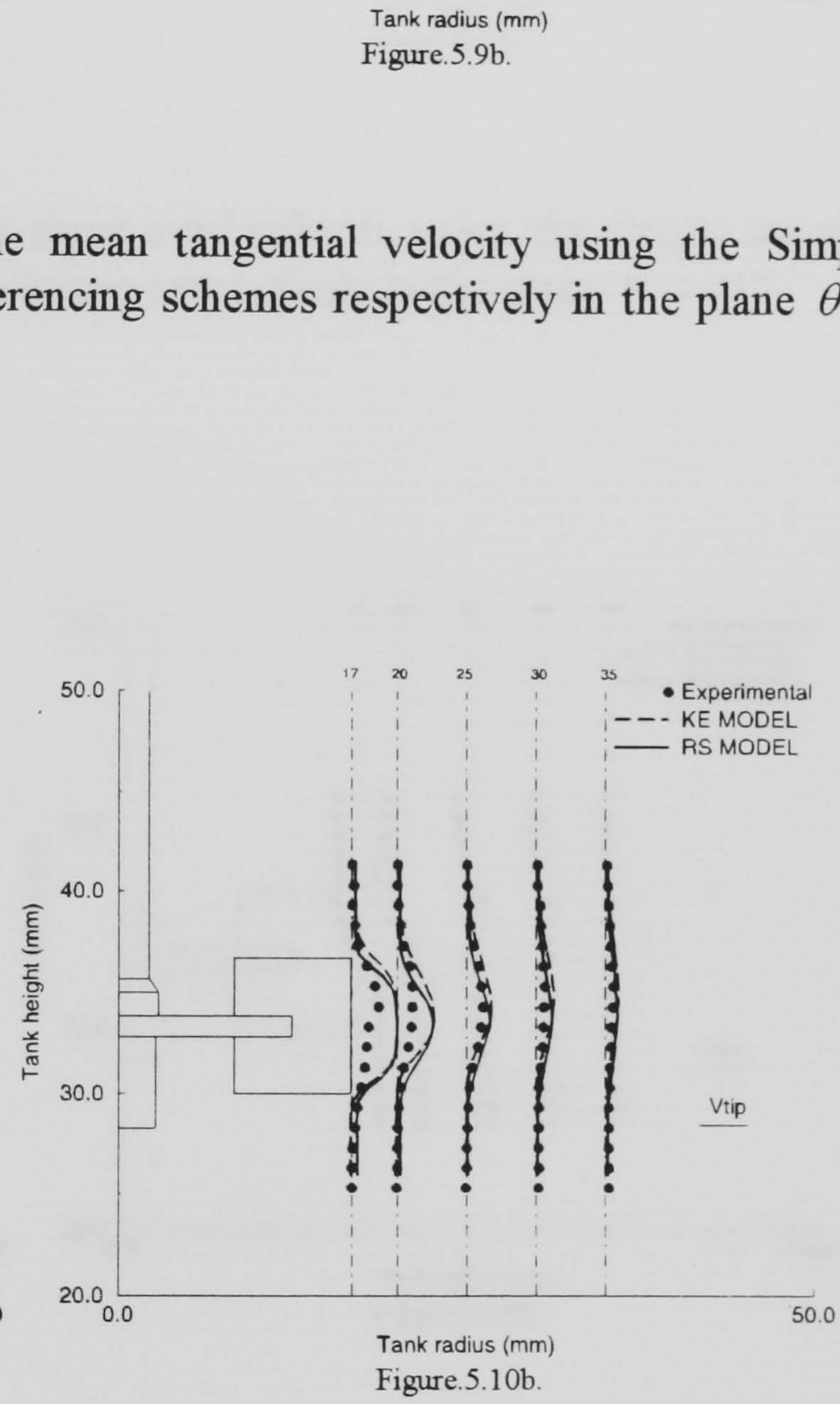


Figure.5.10b.

Figures 5.10a. and 5.10b. Prediction of the mean tangential velocity using the Drag impeller model with Hybrid differencing and the Dynamic impeller model with TVD scheme respectively in the plane $\theta = 0°$.

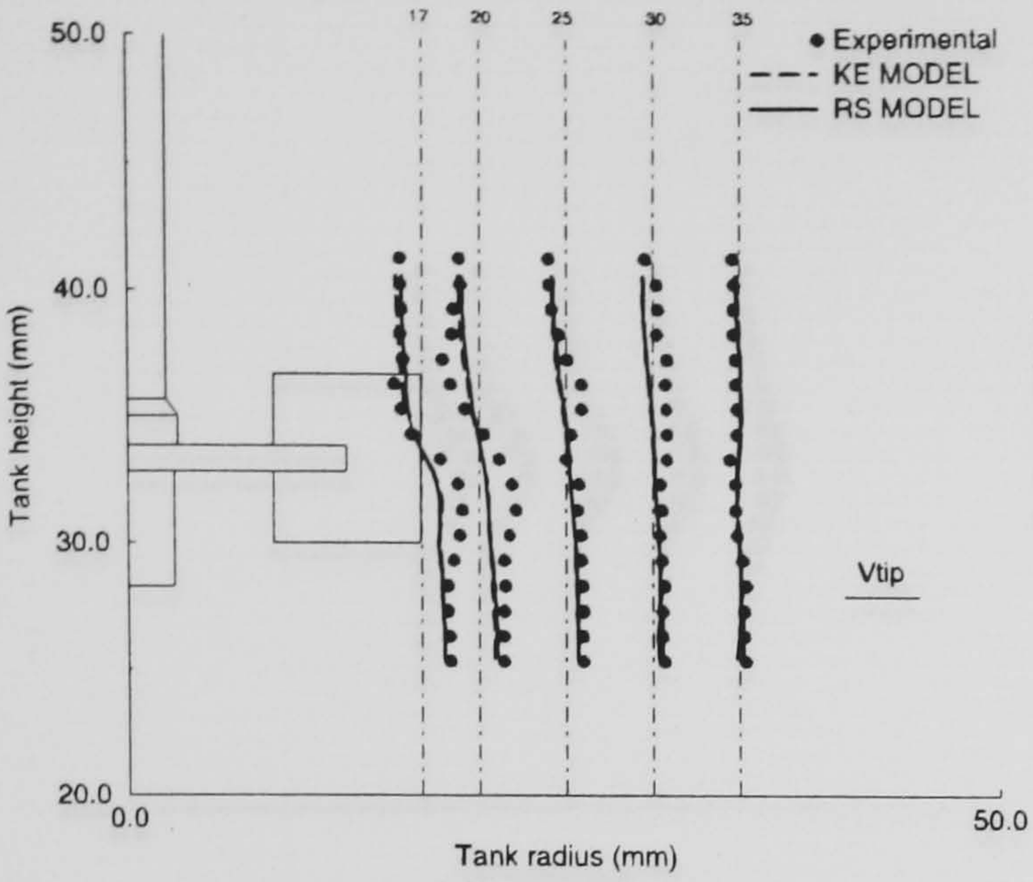


Figure.5.11a.

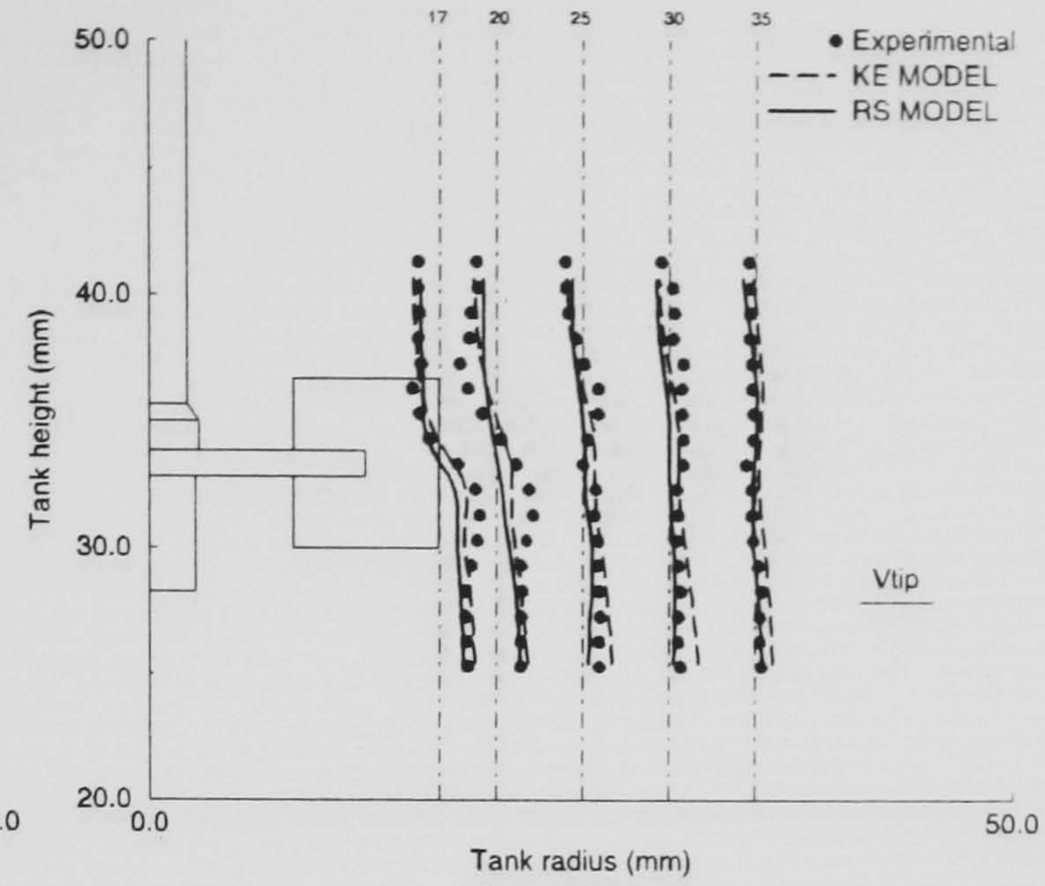


Figure.5.11b.

Figures 5.11a. and 5.11b. Prediction of the mean axial velocity using the Simple impeller model with Hybrid and TVD differencing schemes respectively in the plane $\theta = 45°$.

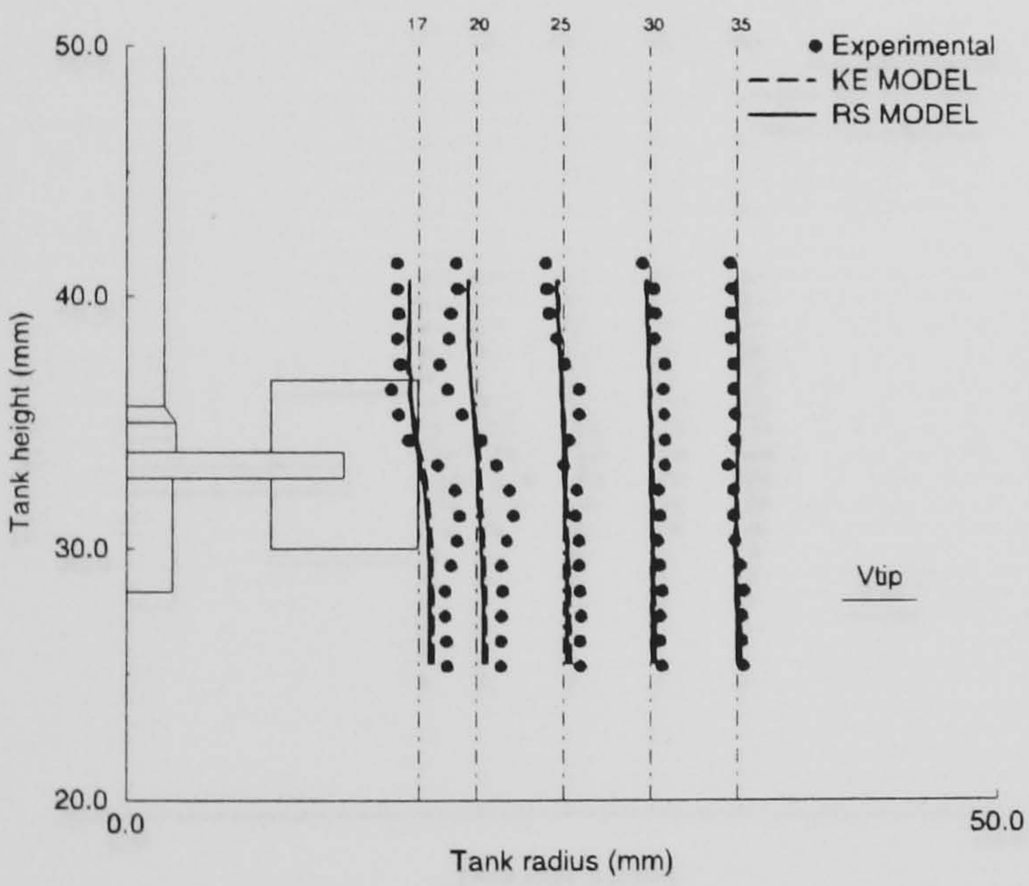


Figure.5.12a.

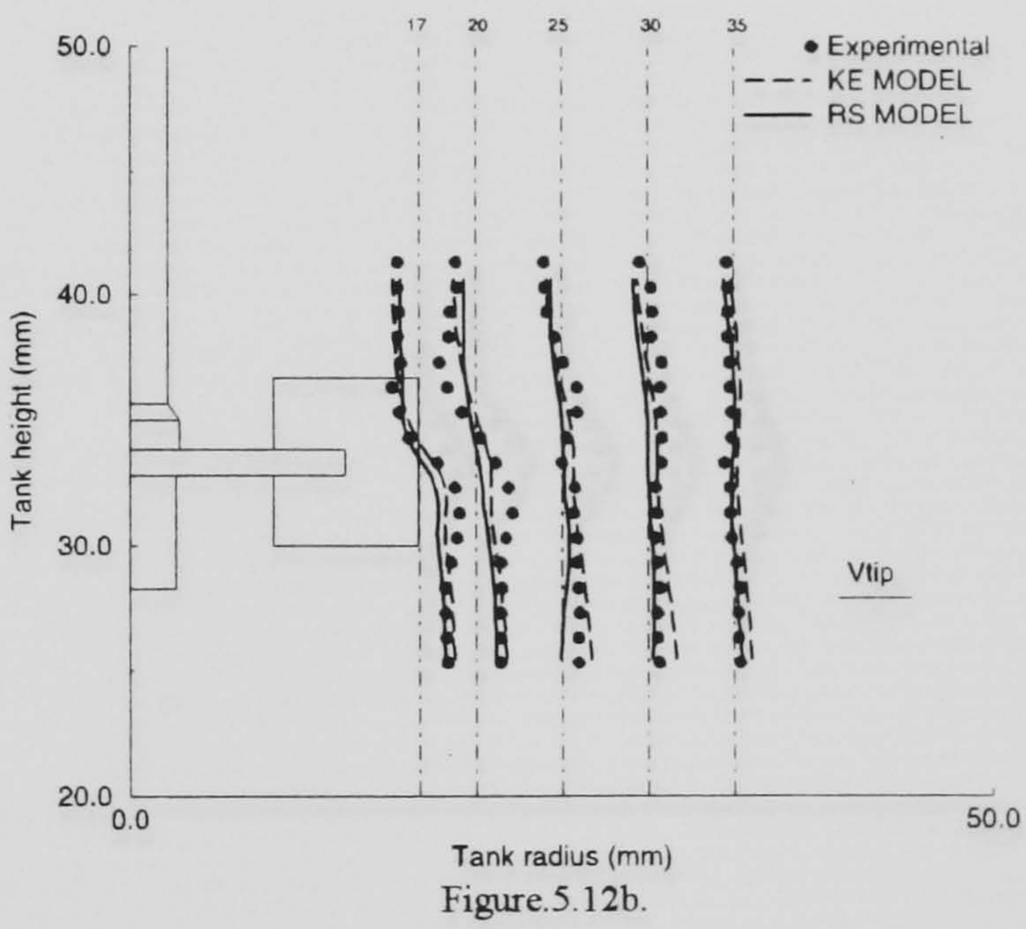


Figure.5.12b.

Figures 5.12a. and 5.12b. Prediction of the mean axial velocity using the Drag impeller model with Hybrid differencing and the Dynamic impeller model with TVD scheme respectively in the plane $\theta = 45°$.

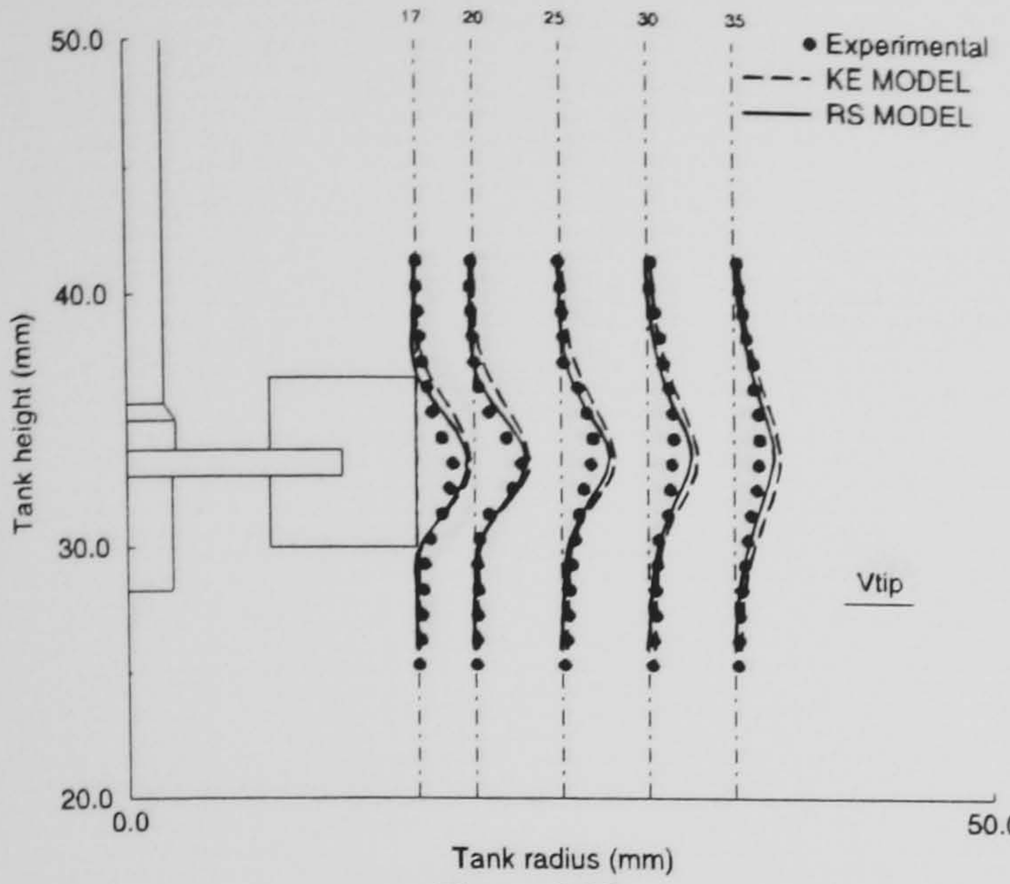



Figure.5.13a.

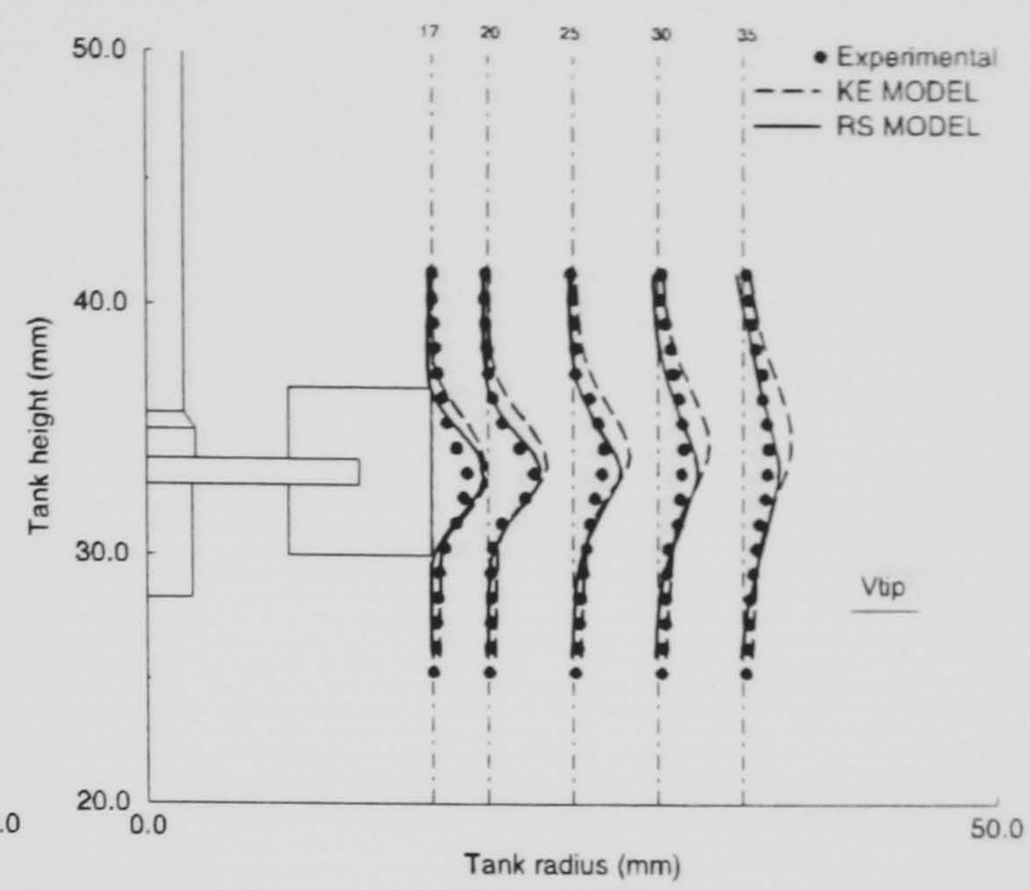



Figure.5.13b.

Figures 5.13a. and 5.13b. Prediction of the mean radial velocity using the Simple impeller model with Hybrid and TVD differencing schemes respectively in the plane $\theta = 45°$.

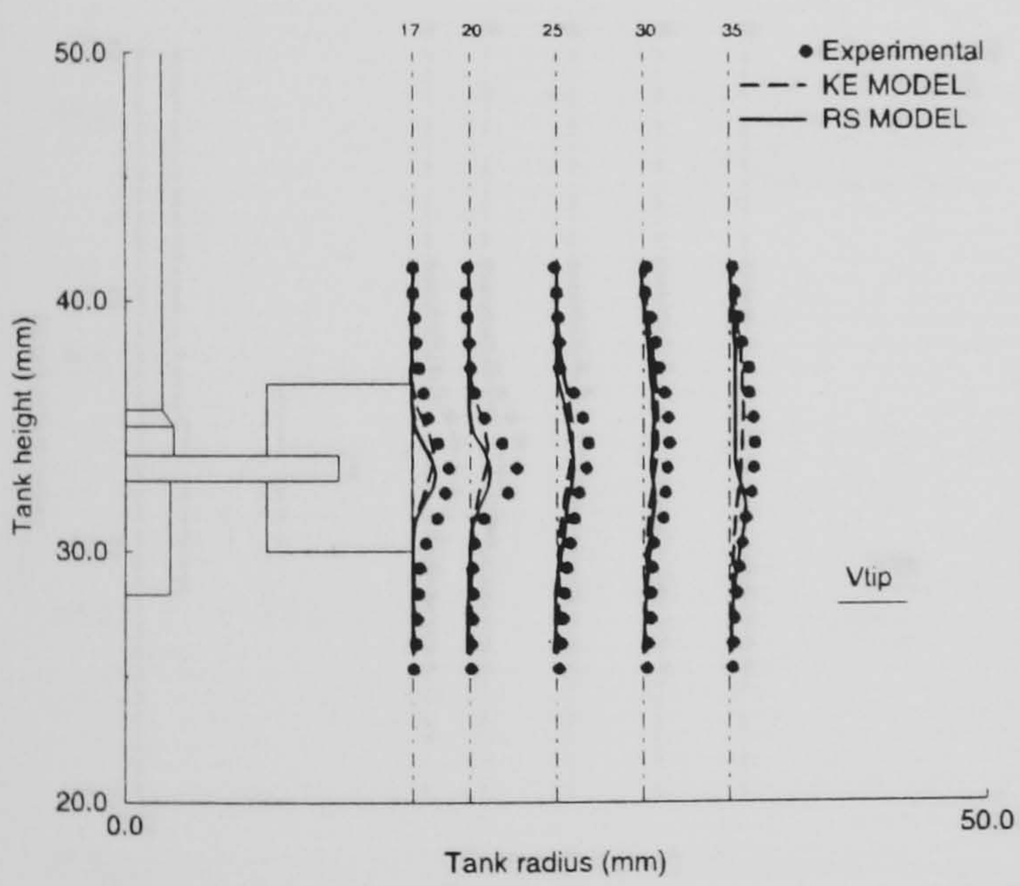



Figure.5.14a.

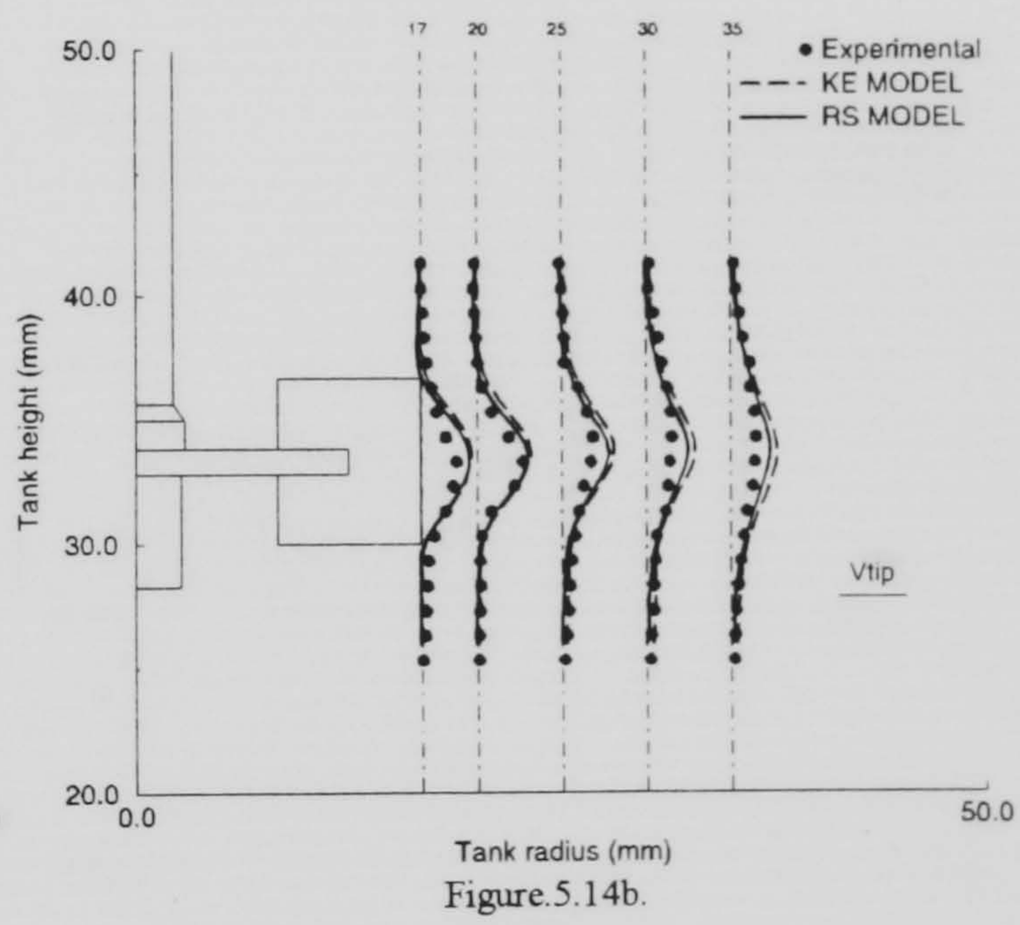



Figure.5.14b.

Figures 5.14a. and 5.14b. Prediction of the mean radial velocity using the Drag impeller model with TVD scheme and the Dynamic impeller model with Hybrid differencing respectively in the plane $\theta = 45°$.

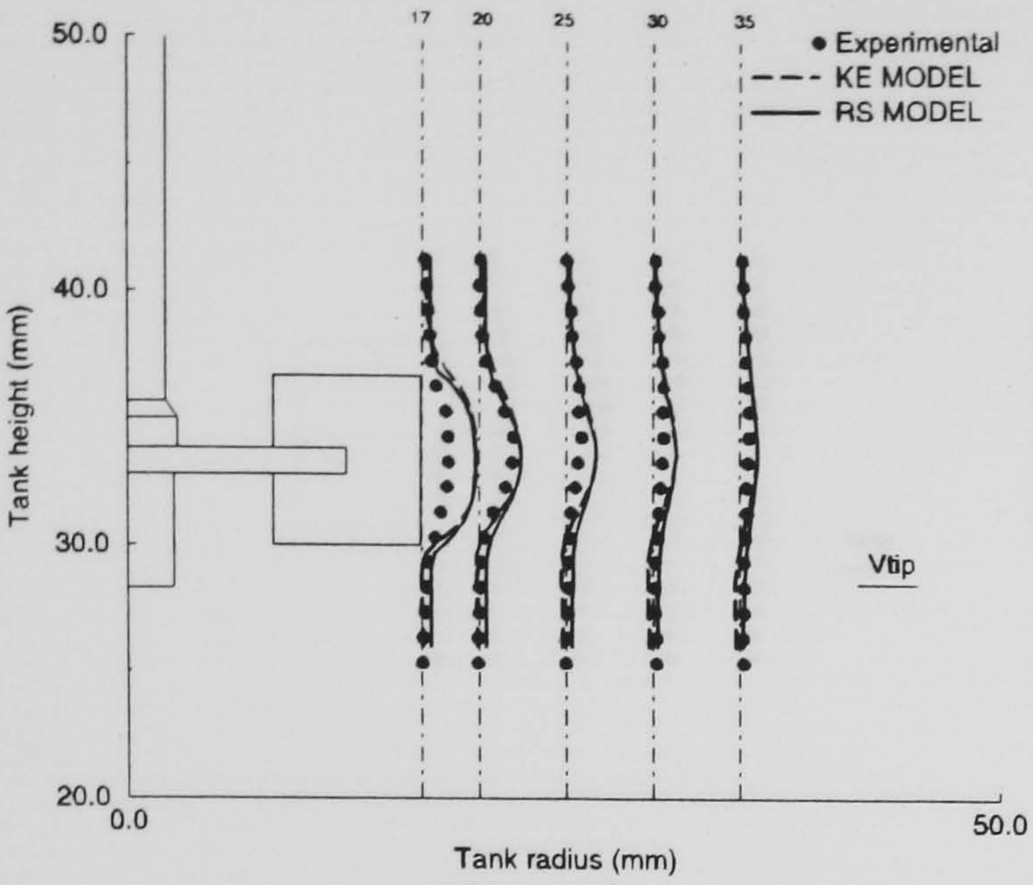


Figure.5.15a.

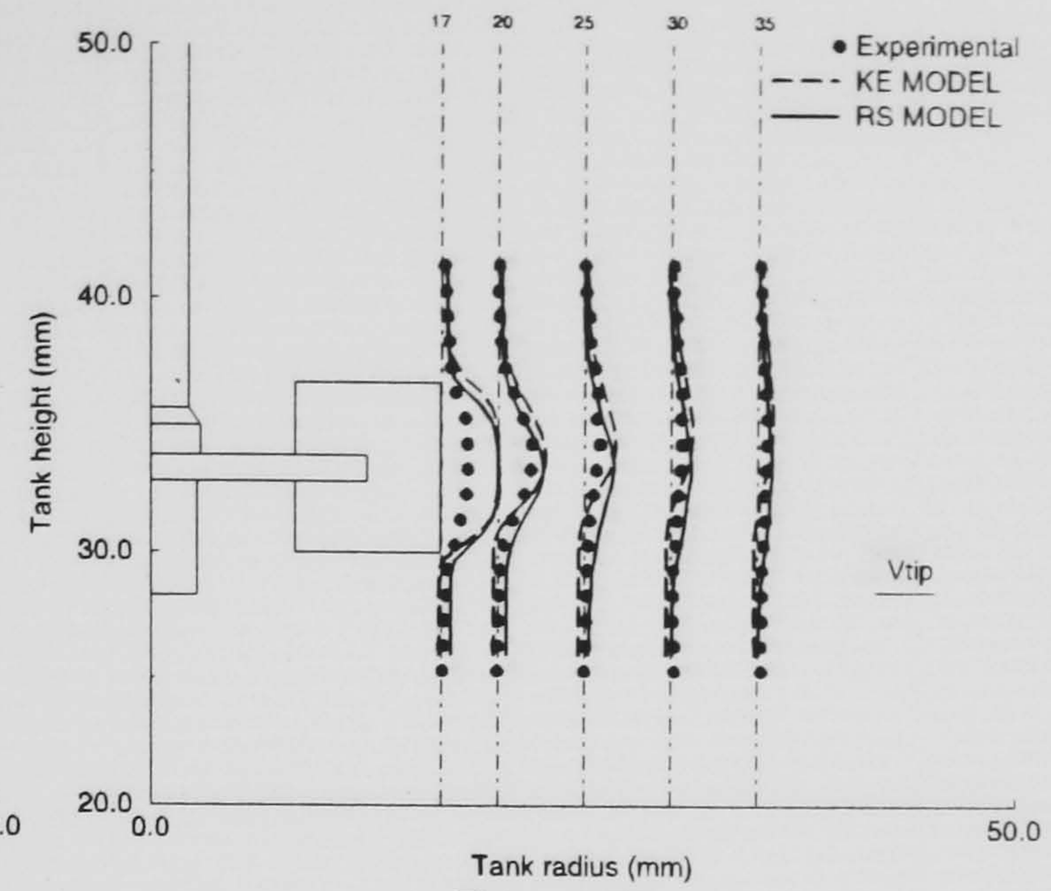


Figure.5.15b.

Figures 5.15a. and 5.15b. Prediction of the mean tangential velocity using the Simple impeller model with Hybrid and TVD differencing schemes respectively in the $\theta = 45°$.

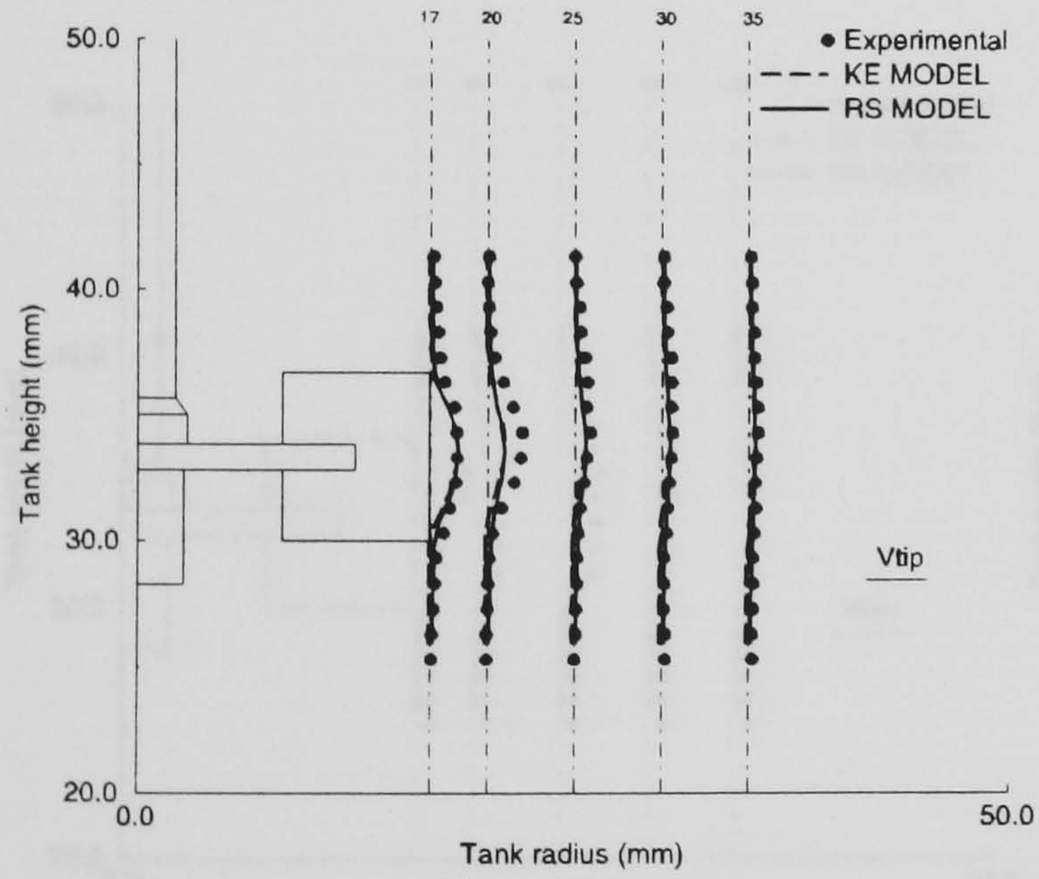


Figure.5.16a.

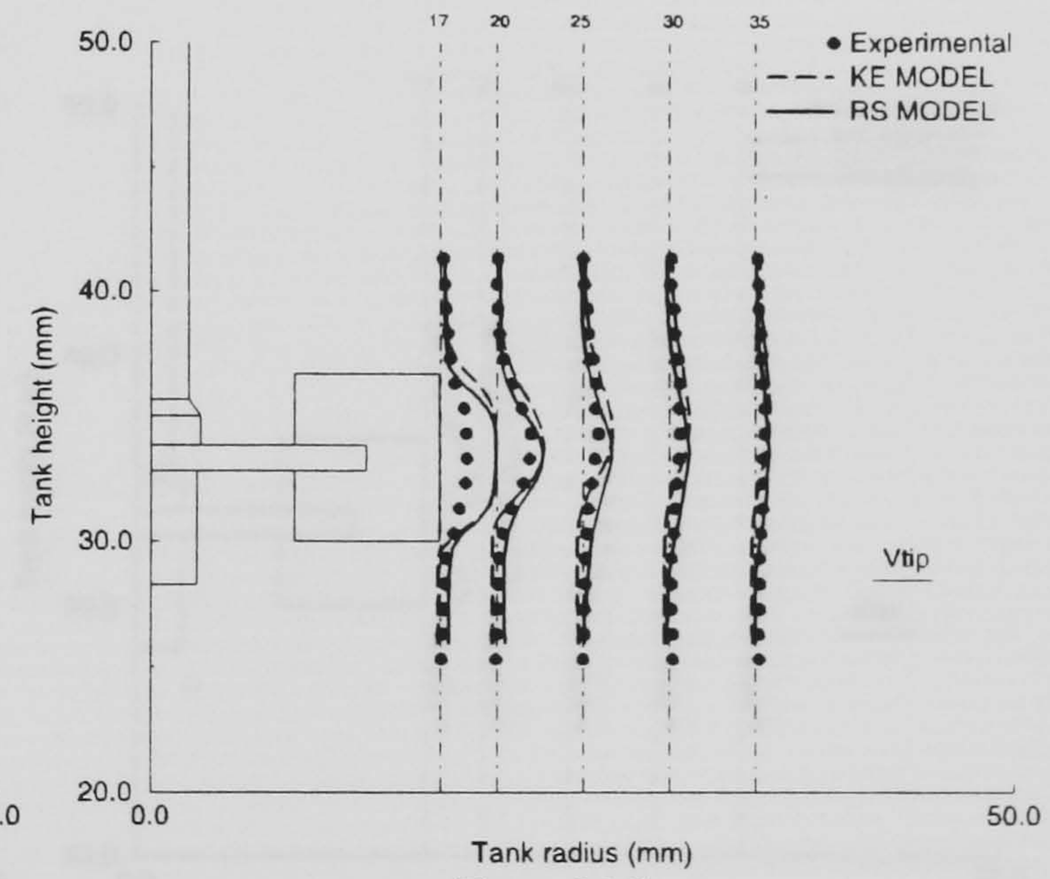


Figure.5.16b.

Figures 5.16a. and 5.16b. Prediction of the mean tangential velocity using the Drag impeller model with Hybrid differencing and the Dynamic impeller model with TVD scheme respectively in the plane $\theta = 45°$.

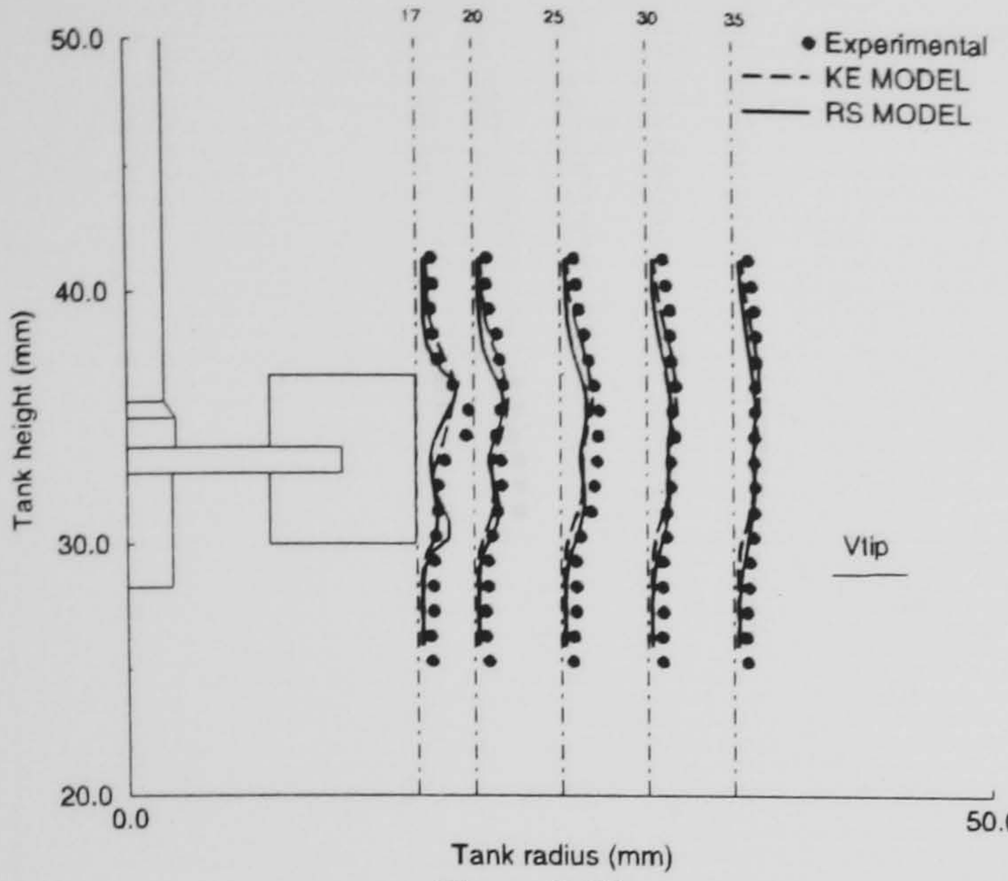


Figure.5.17a.

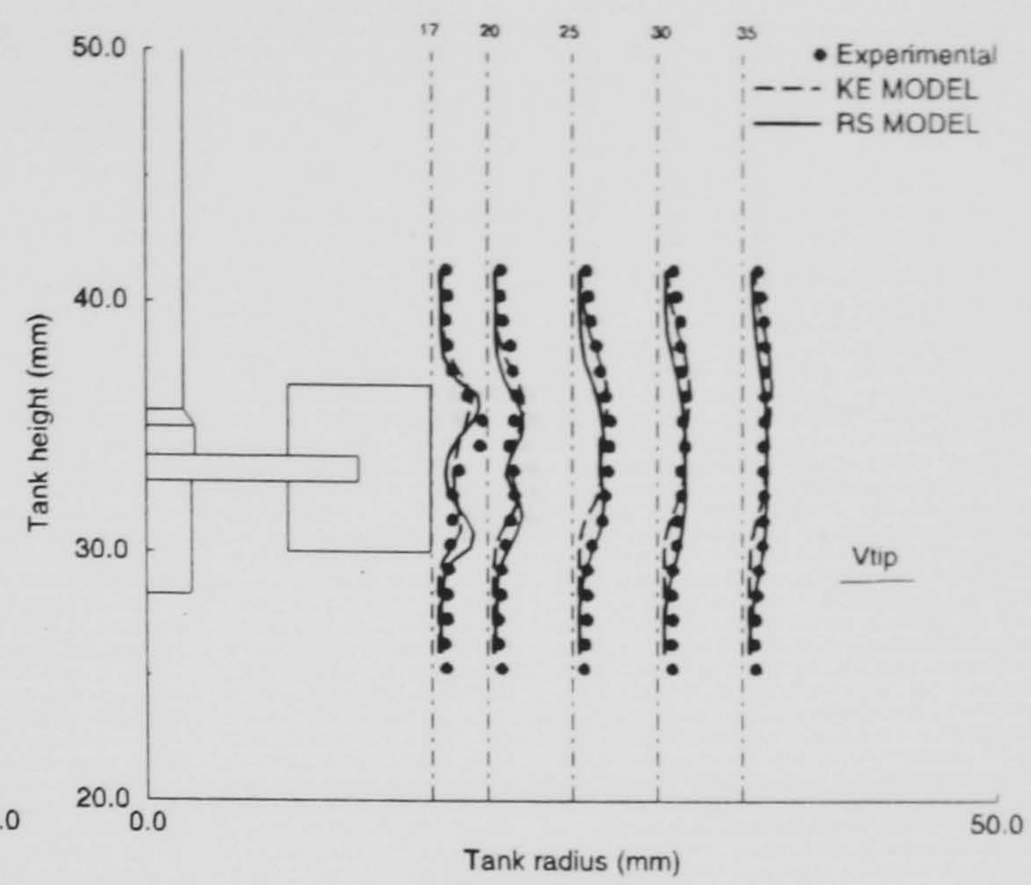


Figure.5.17b.

Figures 5.17a. and 5.17b. Prediction of the tangential fluctuating velocity using the Simple impeller model with Hybrid and TVD differencing schemes respectively in the plane $\theta$ = 0°.

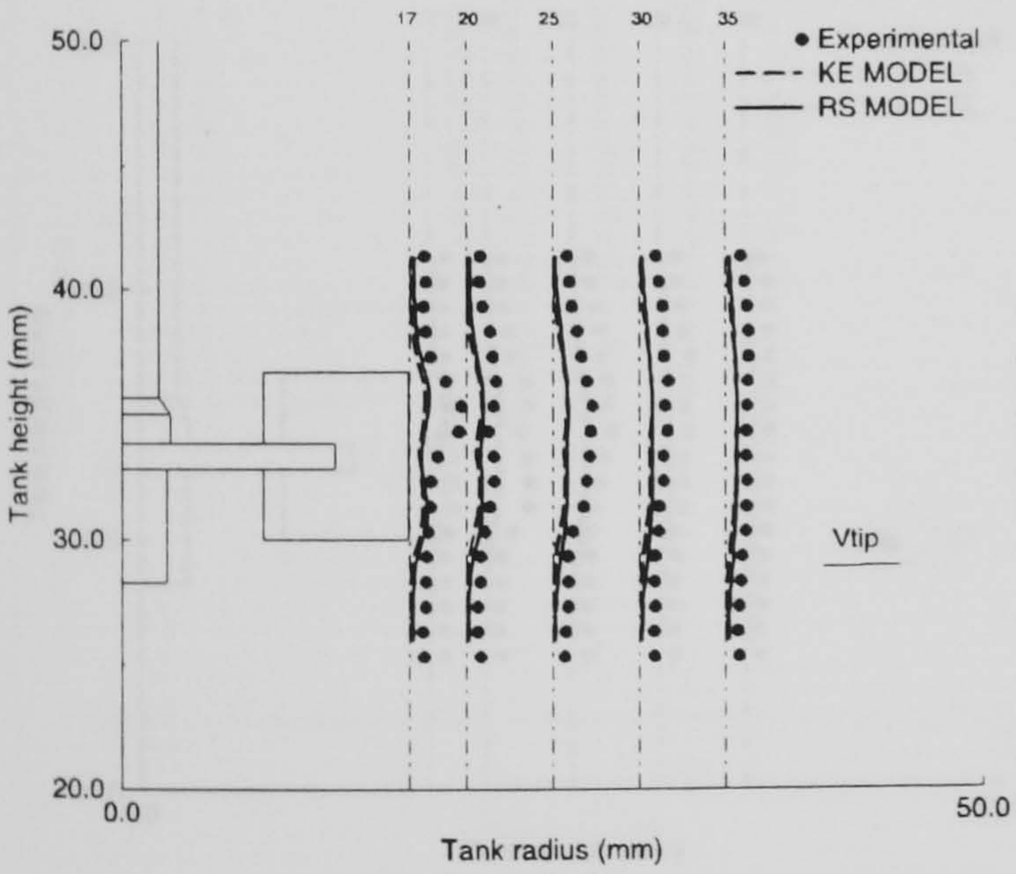


Figure.5.18a.

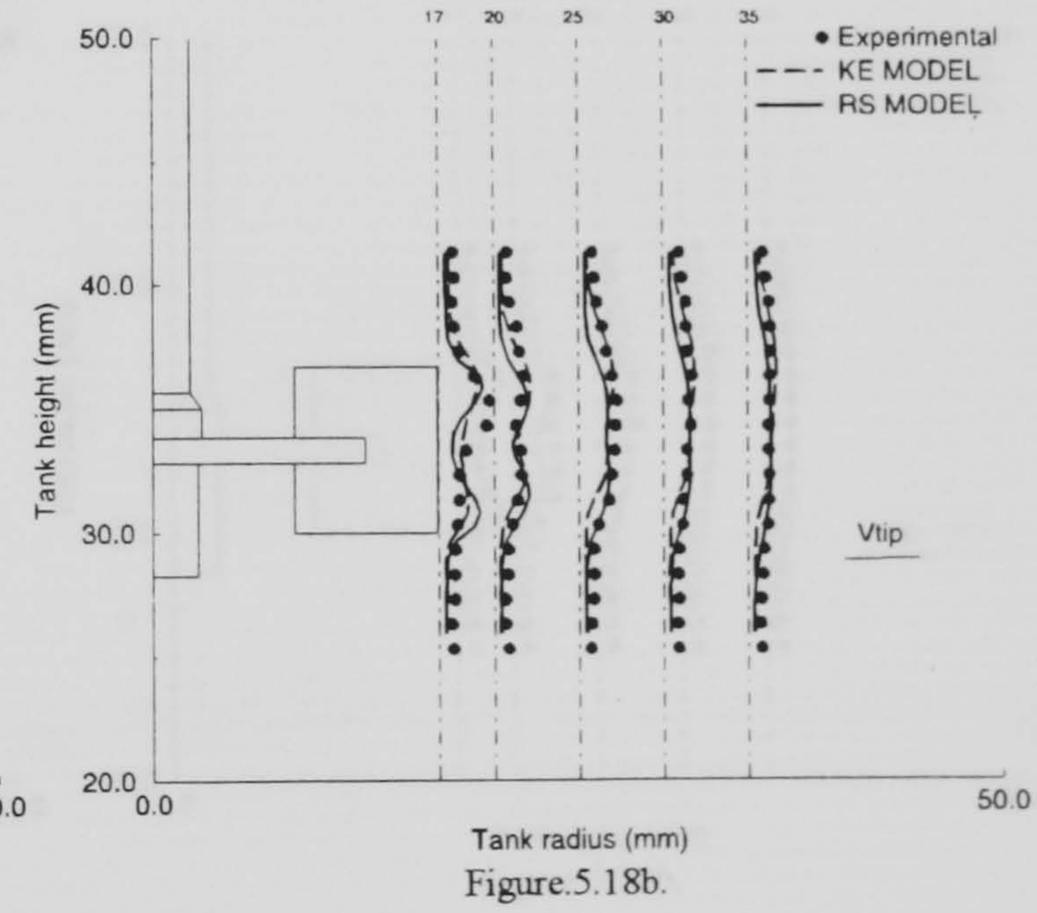


Figure.5.18b.

Figures 5.18a. and 5.18b. Prediction of the tangential fluctuating velocity using the Drag impeller model with Hybrid differencing and the Dynamic impeller model with TVD scheme respectively in the plane $\theta = 0°$.

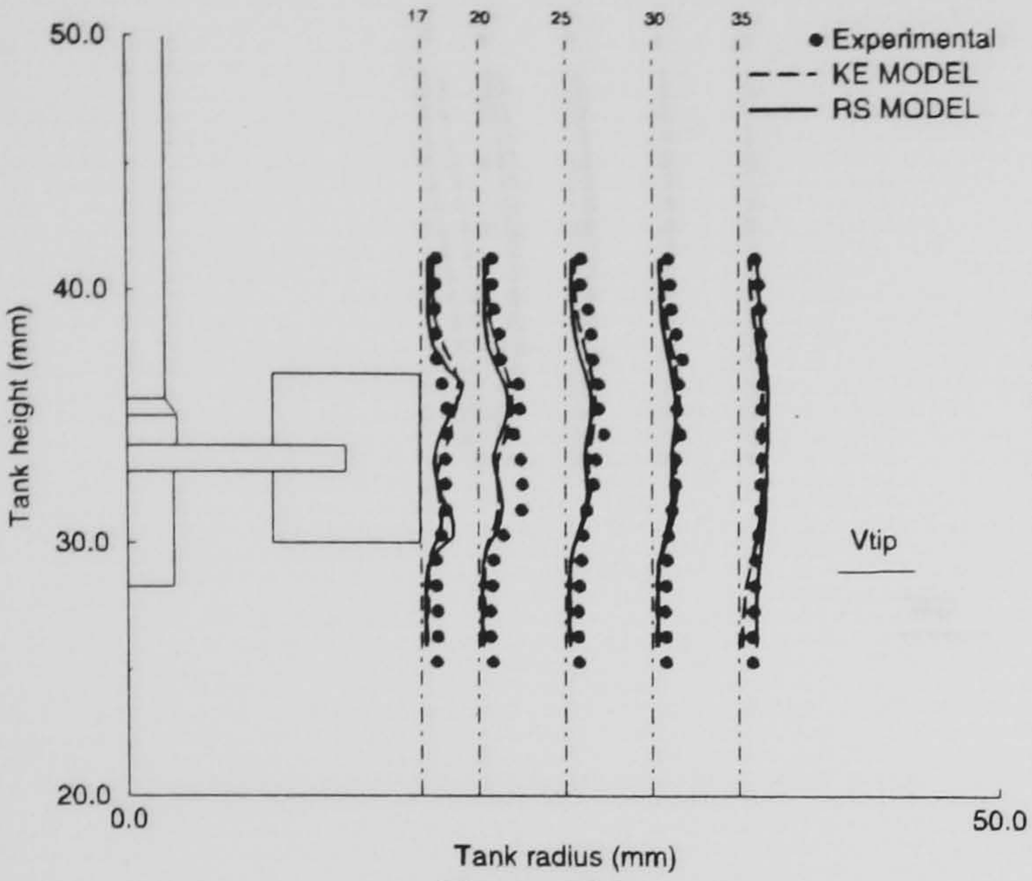


Figure.5.19a.

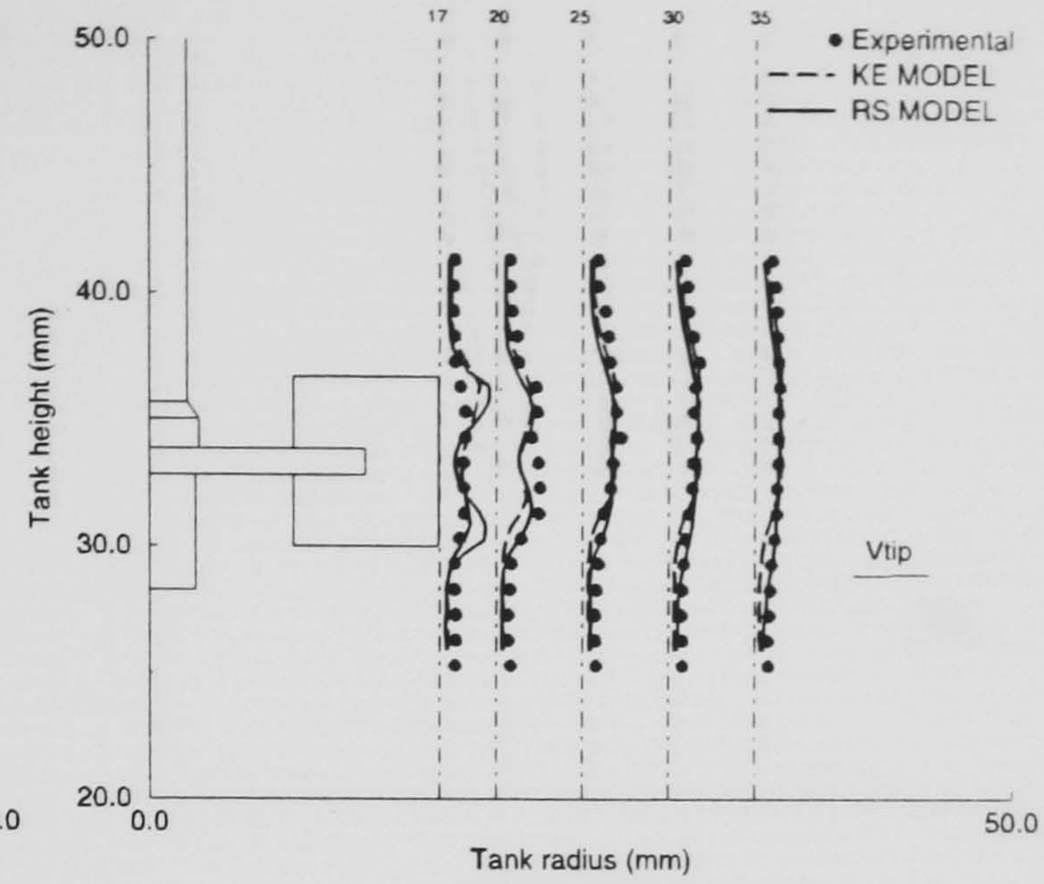


Figure.5.19b.

Figures 5.19a. and 5.19b. Prediction of the tangential fluctuating velocity using the Simple impeller model with Hybrid and TVD differencing schemes respectively in the plane $\theta$ = 45°.

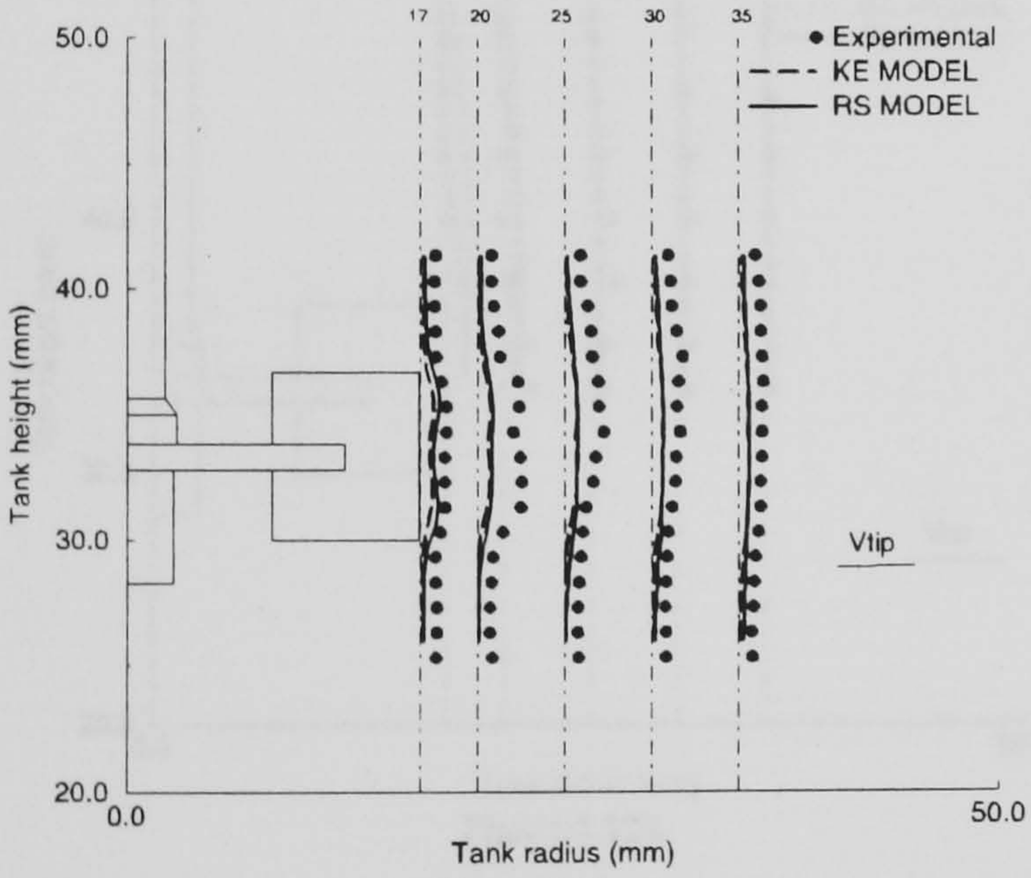


Figure.5.20a.

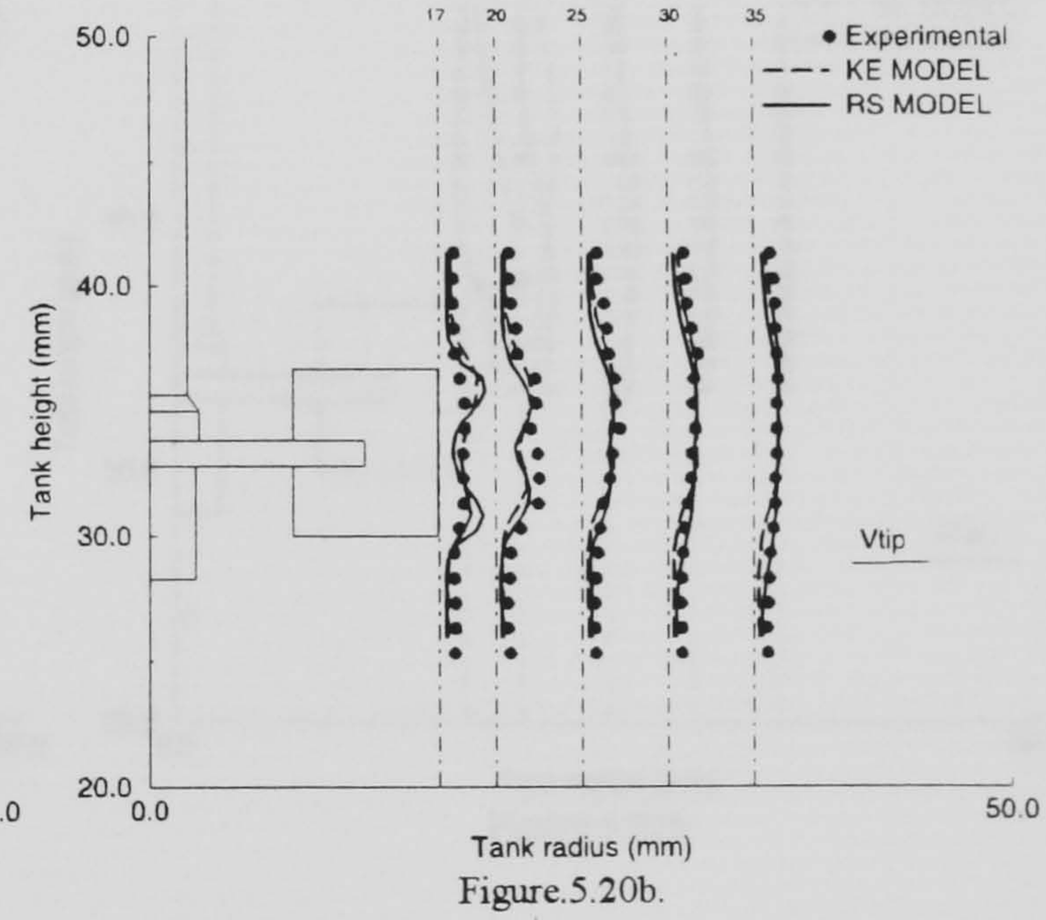


Figure.5.20b.

Figures 5.20a. and 5.20b. Prediction of the tangential fluctuating velocity using the Drag impeller model with Hybrid differencing and the Dynamic impeller model with TVD scheme respectively in the plane $\theta$ = 45°.

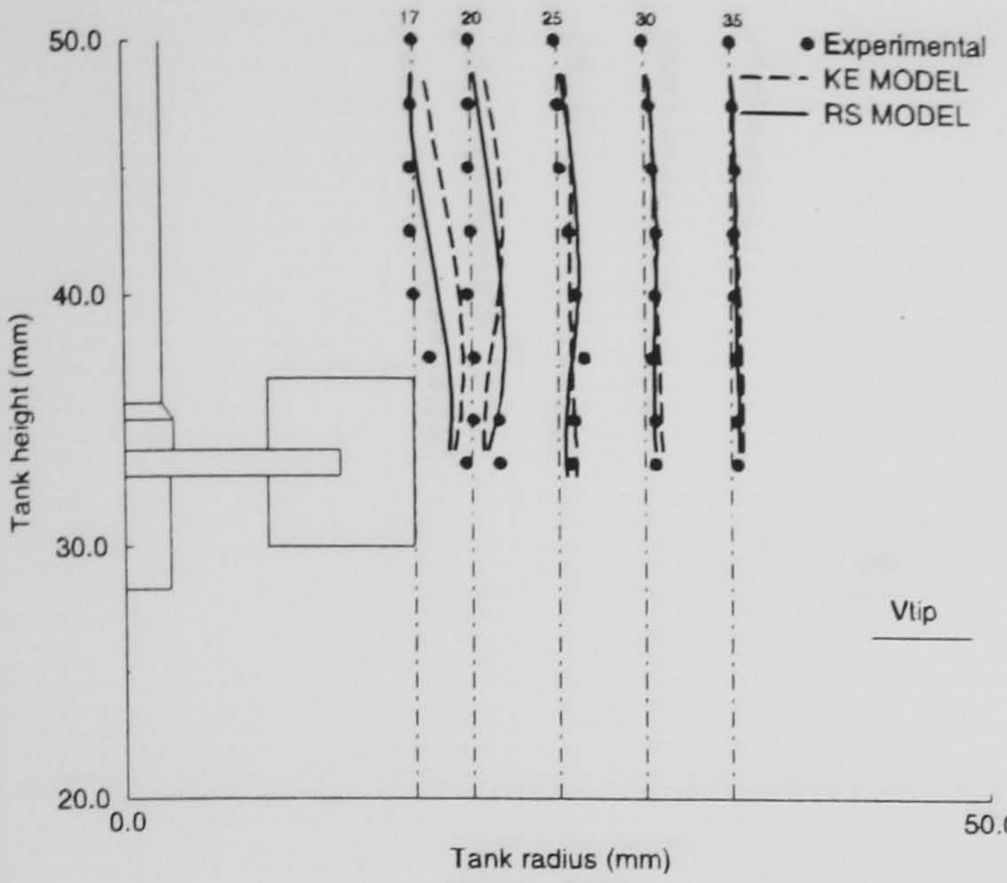


Figure.5.21a.

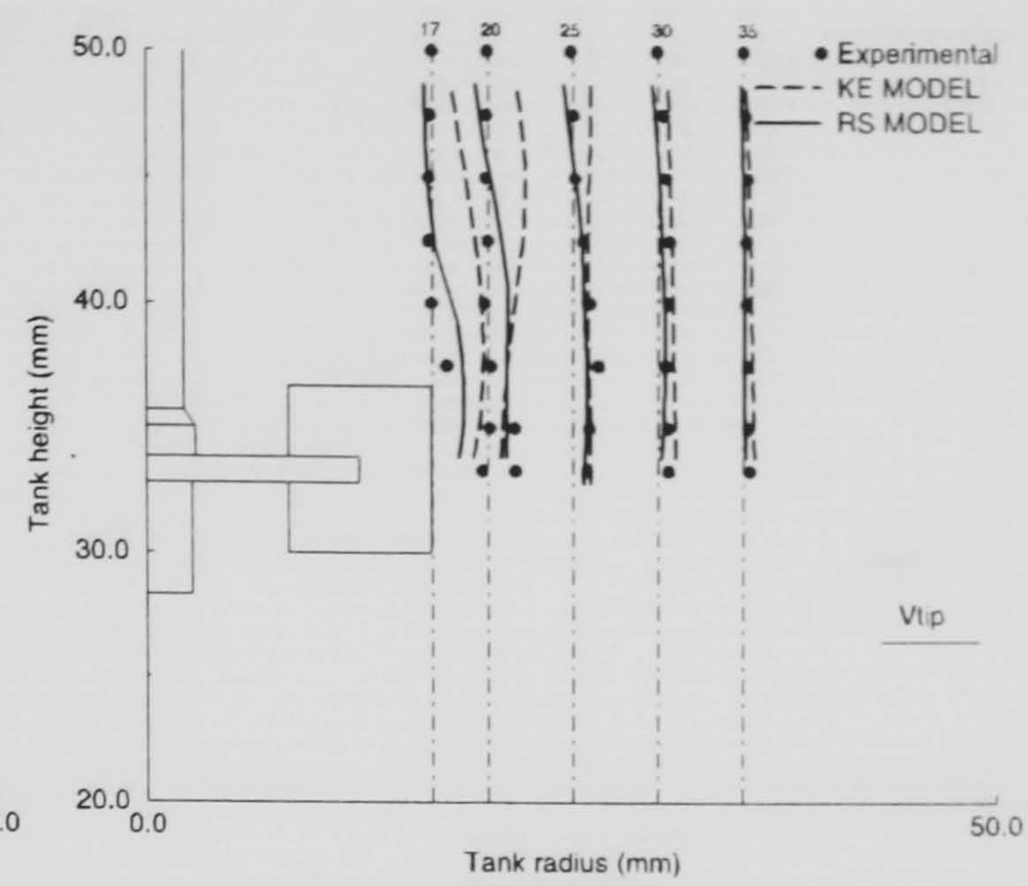


Figure.5.21b.

Figures 5.21a. and 5.21b. Prediction of the mean axial velocity using the Simple impeller model with Hybrid and TVD differencing schemes respectively in the plane $\theta = 0°$.

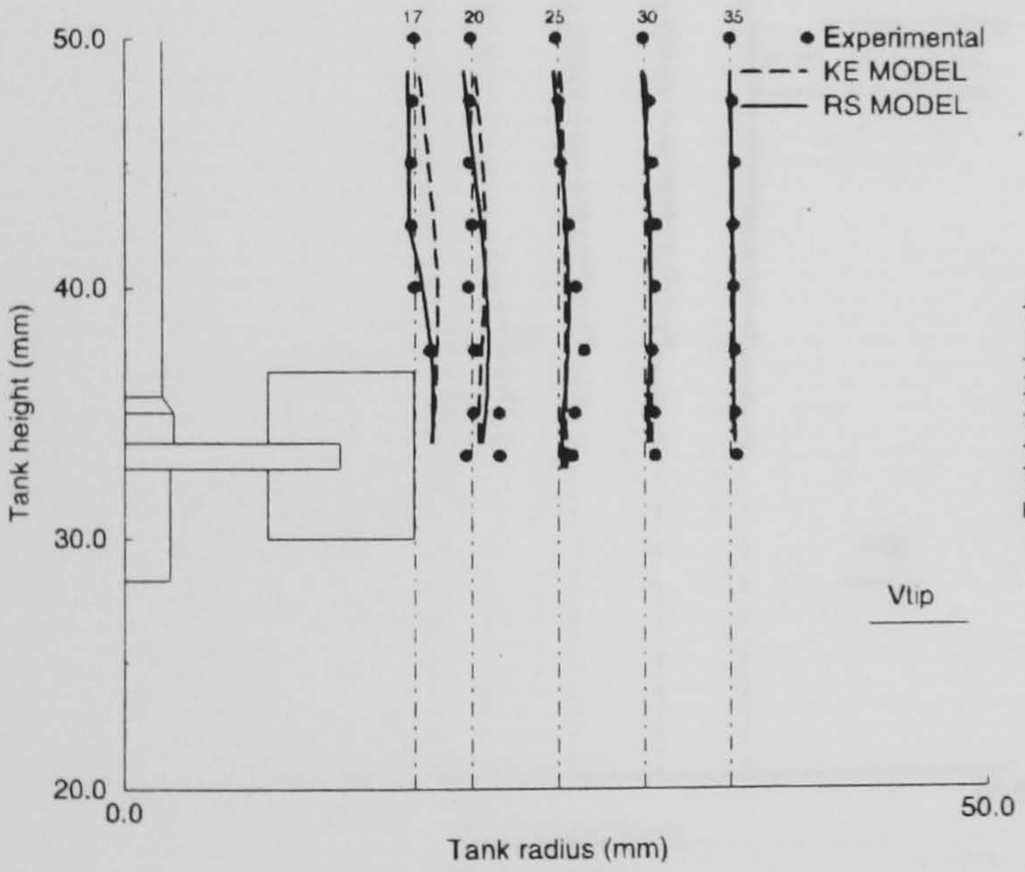


Figure.5.22a.

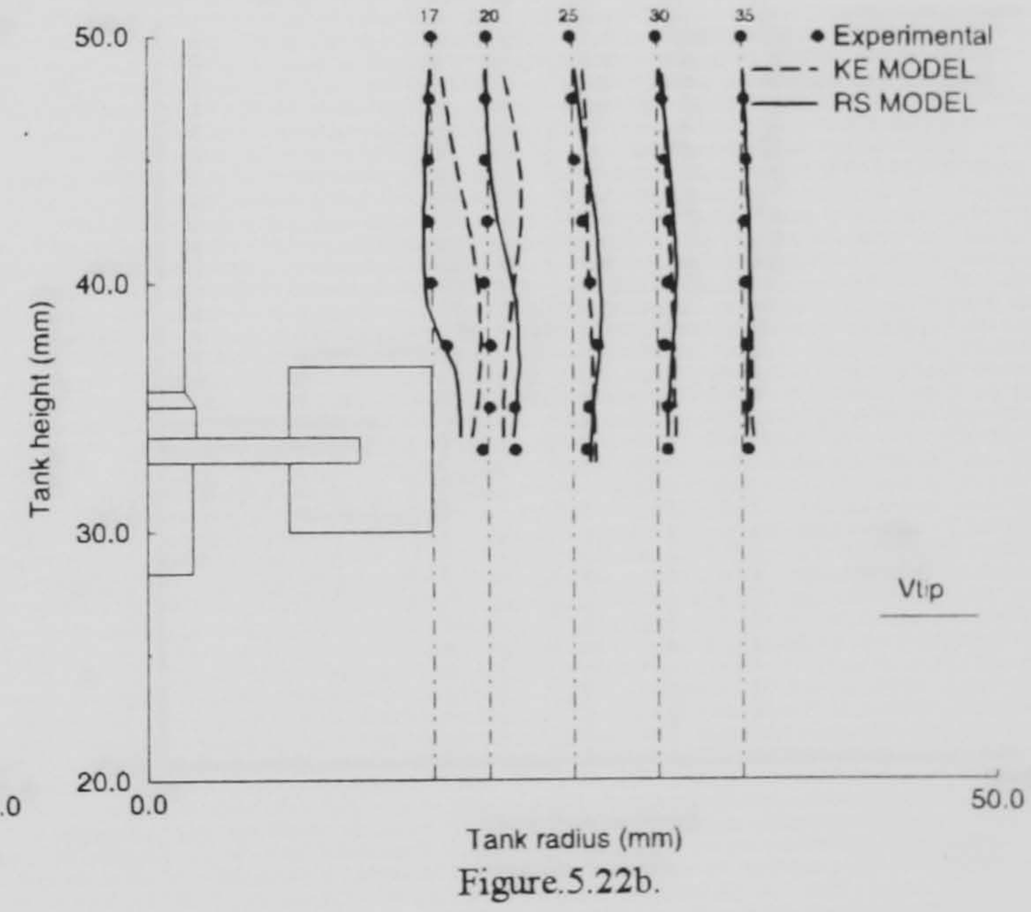


Figure.5.22b.

Figures 5.22a. and 5.22b. Prediction of the mean axial velocity using the Drag impeller model with Hybrid differencing and the Dynamic impeller model with TVD scheme respectively in the plane $\theta = 0°$.

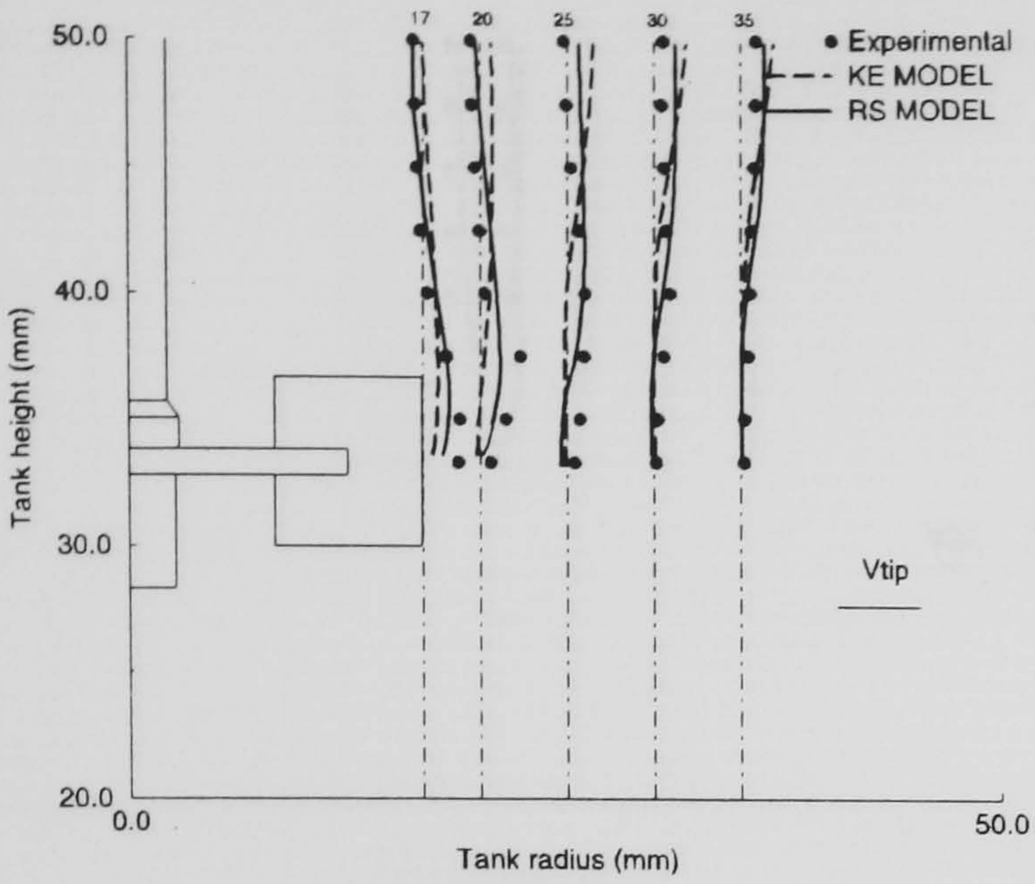



Figure.5.23a.

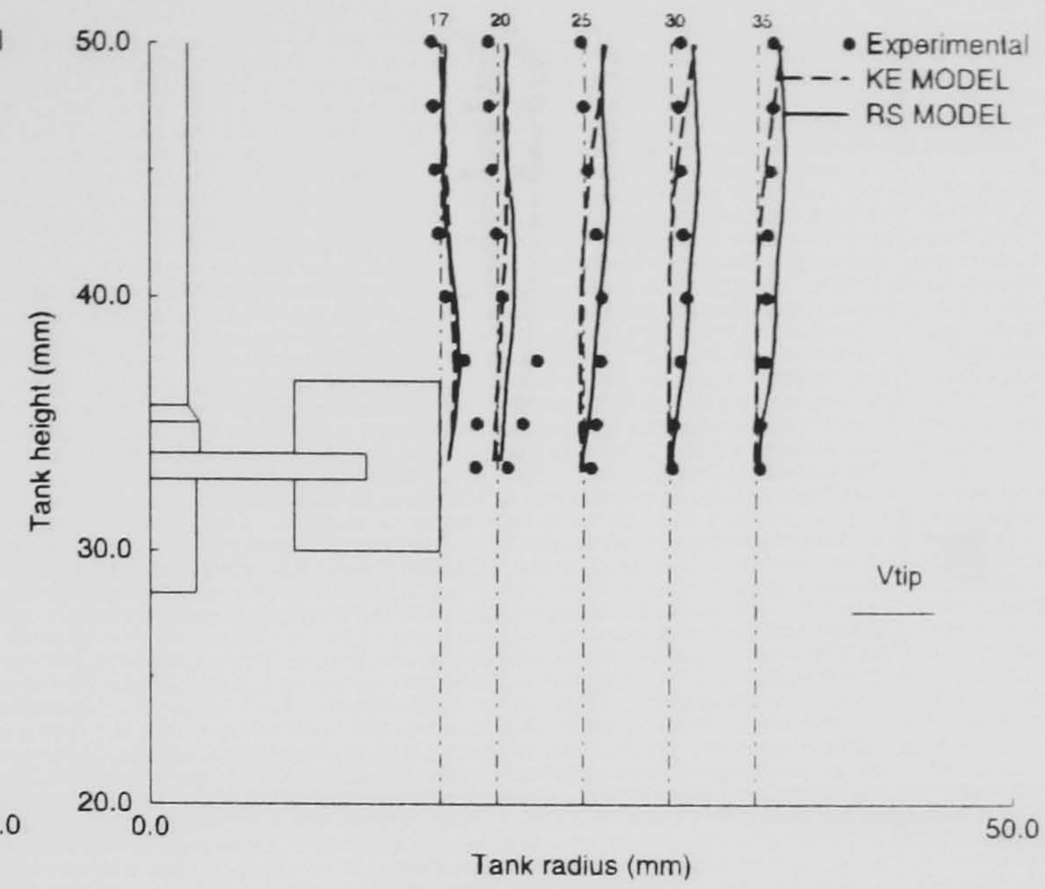



Figure.5.23b.

Figures 5.23a. and 5.23b. Prediction of the mean radial velocity using the Simple impeller model with Hybrid and TVD differencing schemes respectively in the plane $\theta = 0°$.

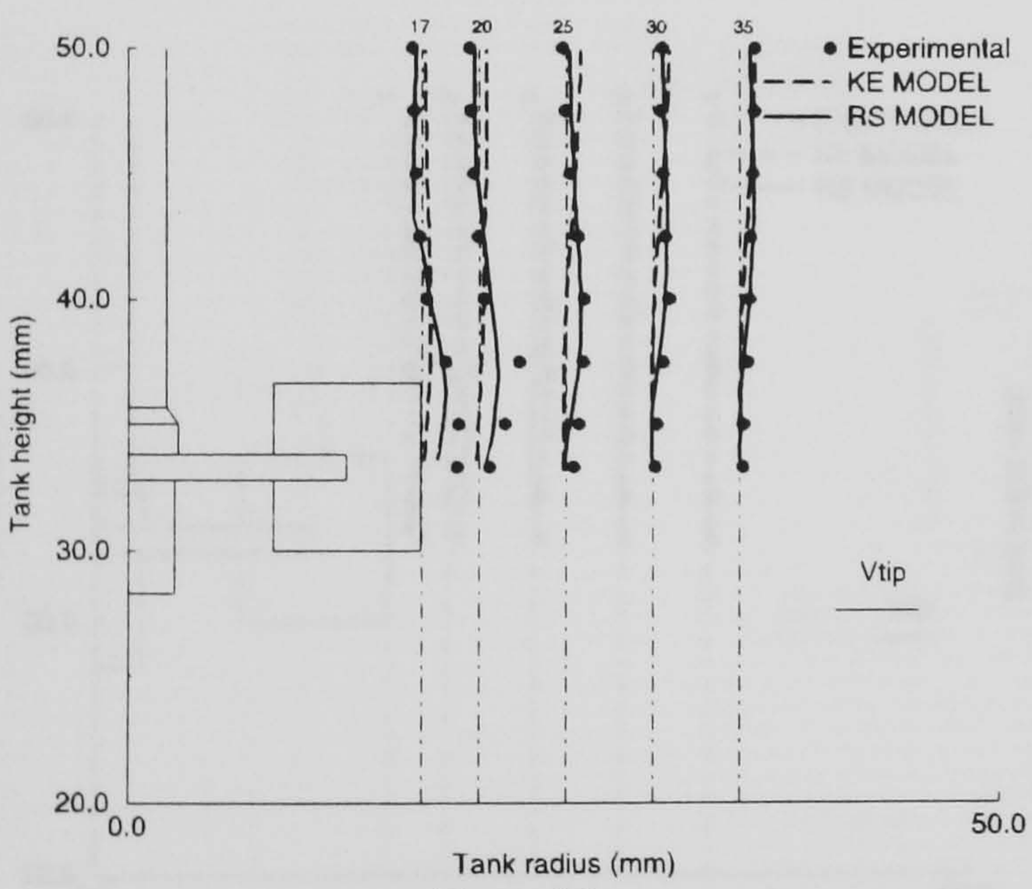



Figure.5.24a.

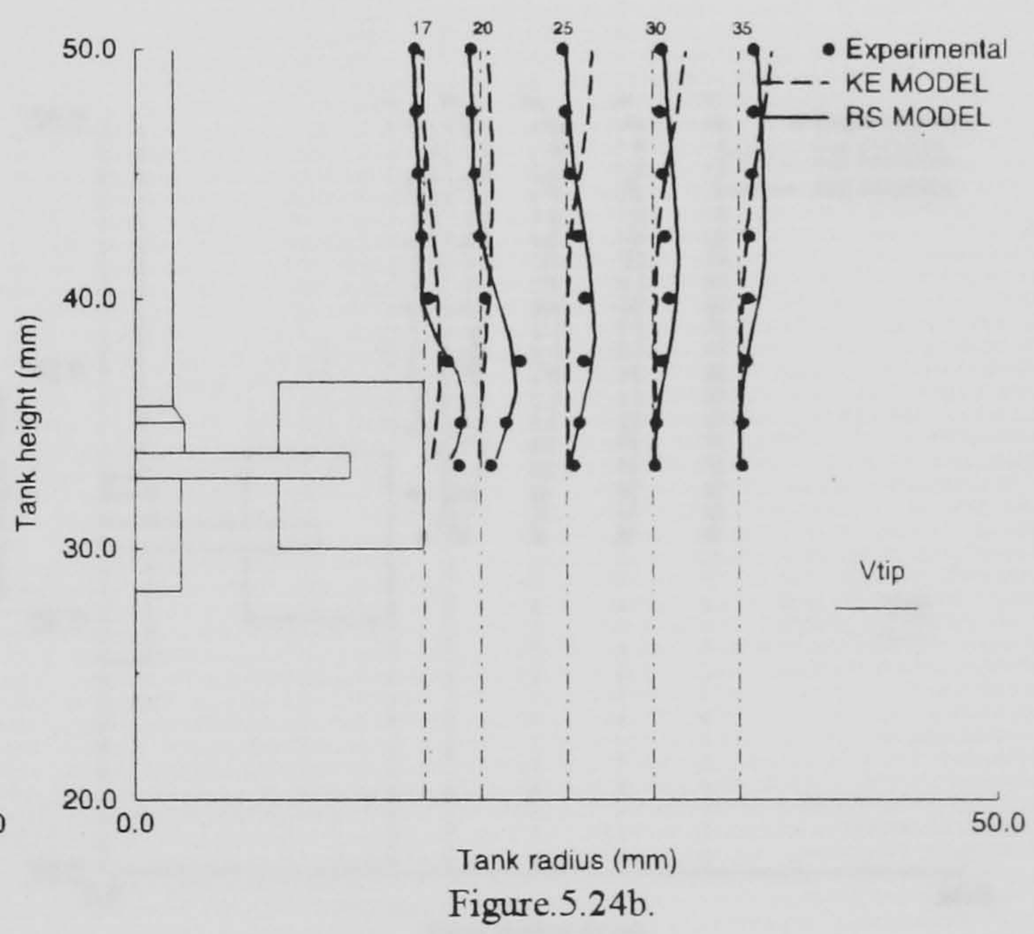



Figure.5.24b.

Figures 5.24a. and 5.24b. Prediction of the mean radial velocity using the Drag impeller model with Hybrid differencing and the Dynamic impeller model with TVD scheme respectively in the plane $\theta = 0°$.

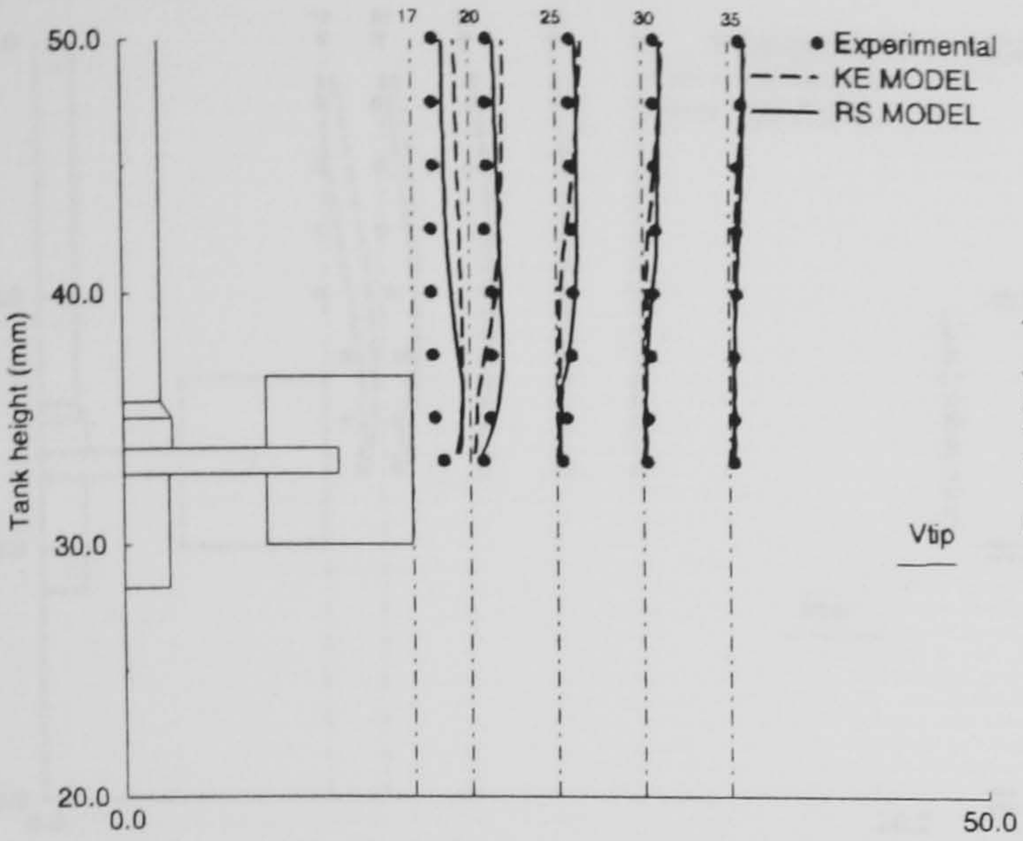



Figure.5.25a.

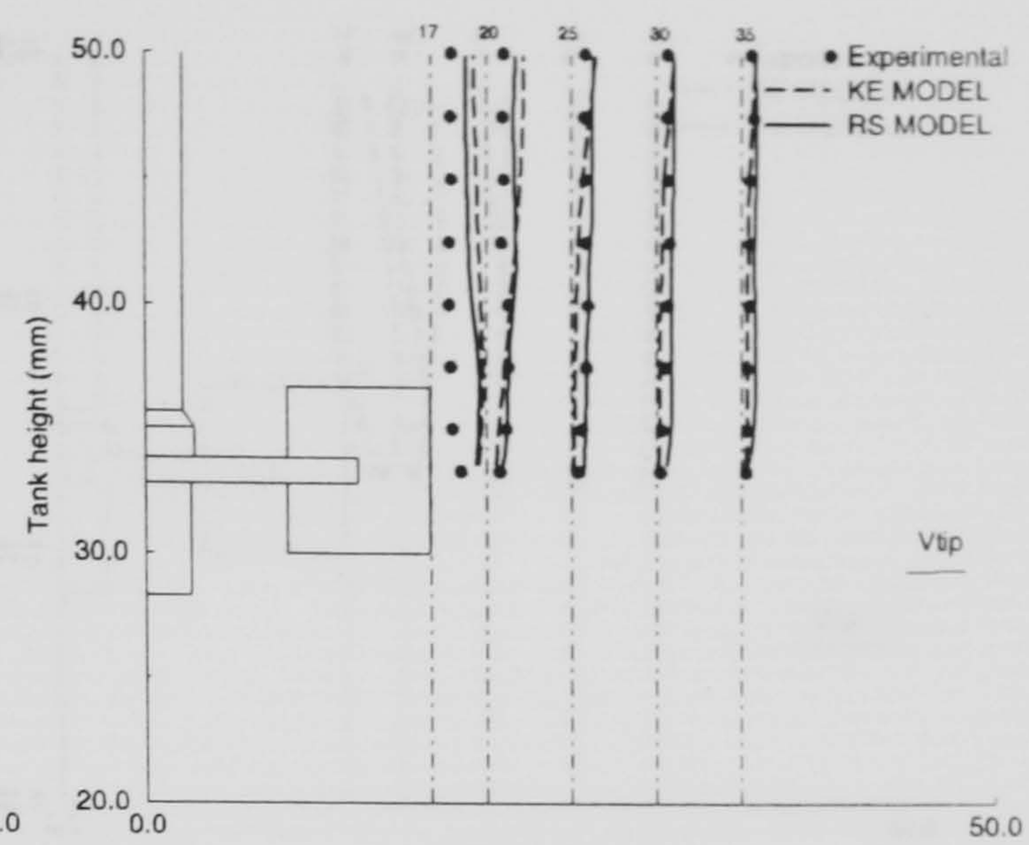



Figure.5.25b.

Figures 5.25a. and 5.25b. Prediction of the mean tangential velocity using the Simple impeller model with Hybrid and TVD differencing schemes respectively in the plane $\theta$ = 0°.

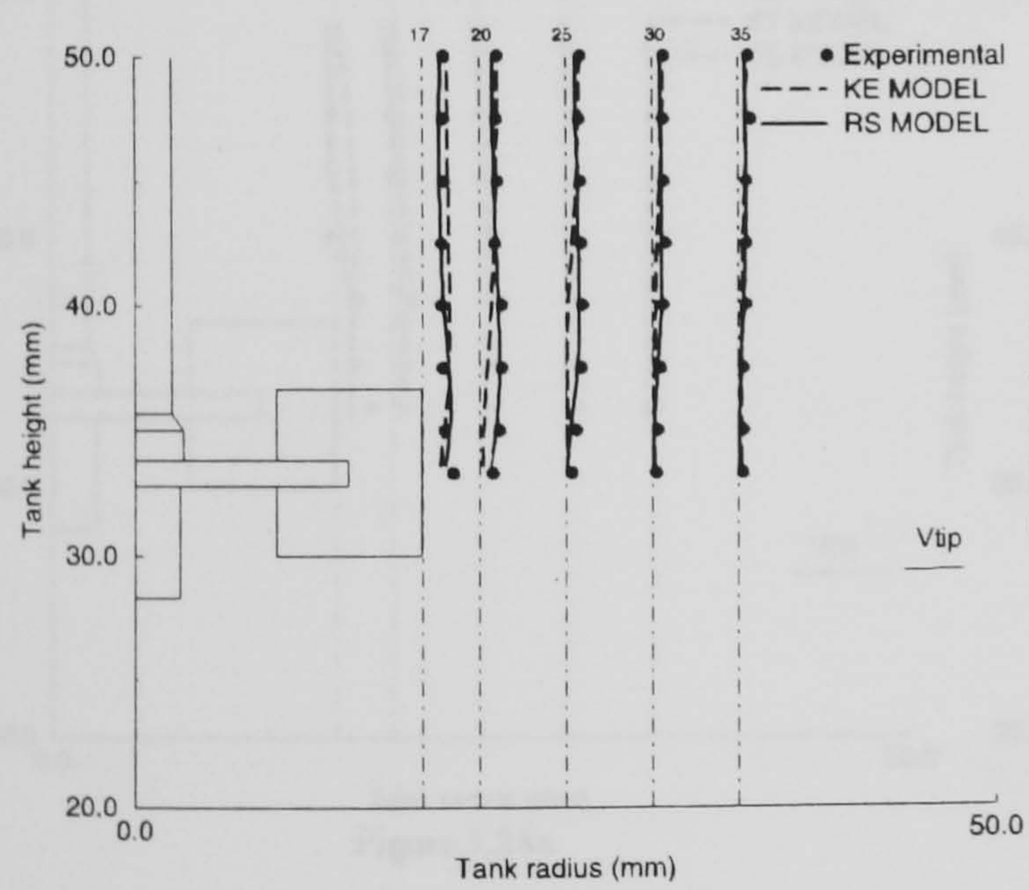



Figure.5.26a.

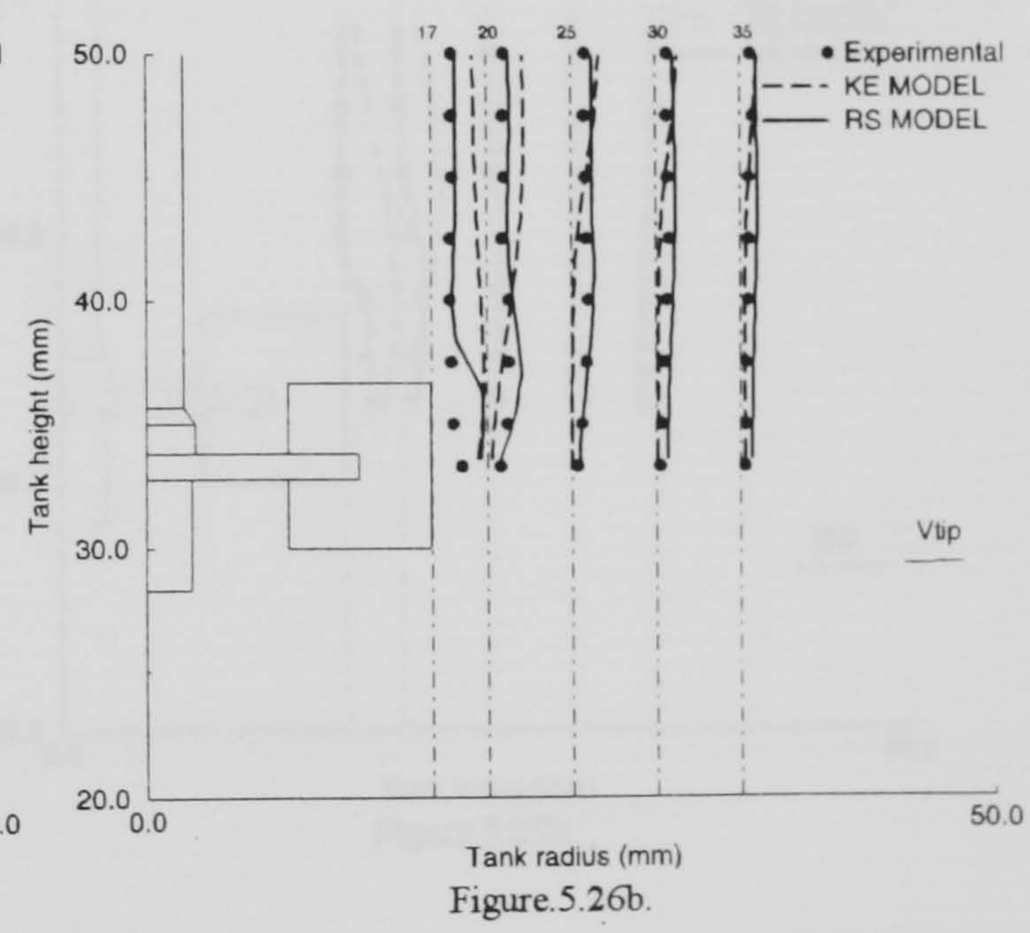



Figure.5.26b.

Figures 5.26a. and 5.26b. Prediction of the mean tangential velocity using the Drag impeller model with Hybrid differencing and the Dynamic impeller model with TVD scheme respectively in the plane $\theta$ = 0°.

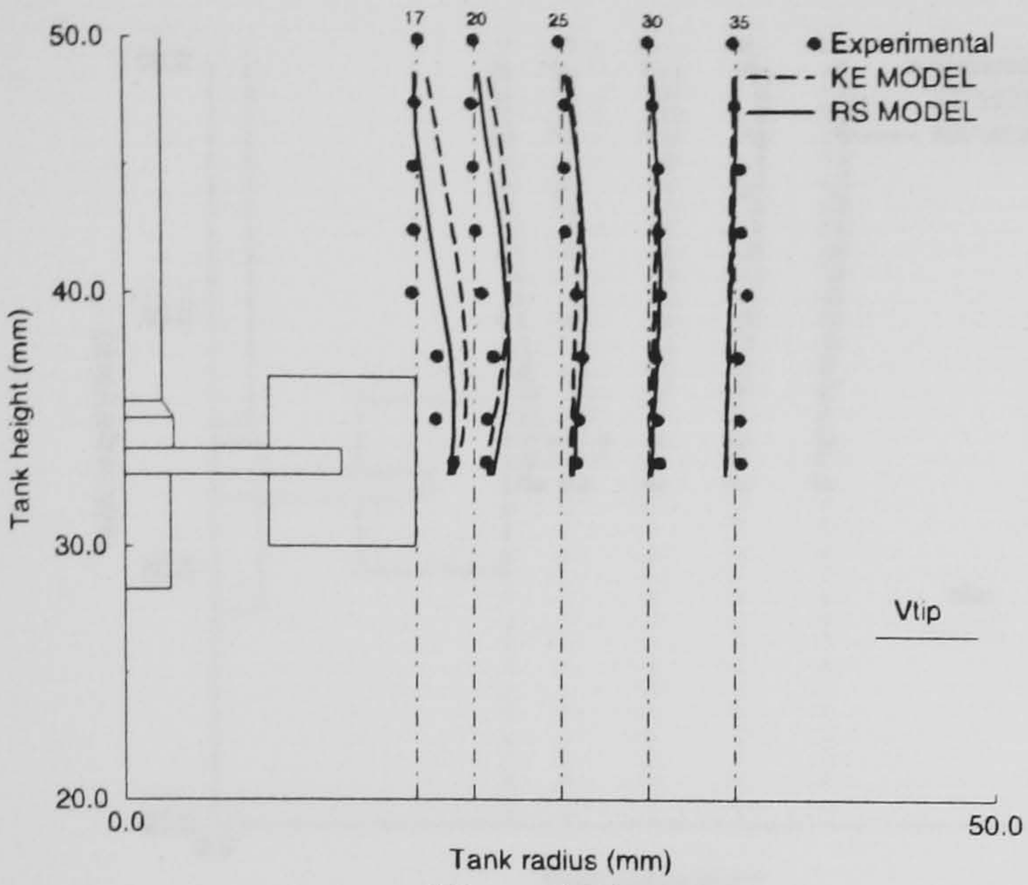



Figure.5.27a.

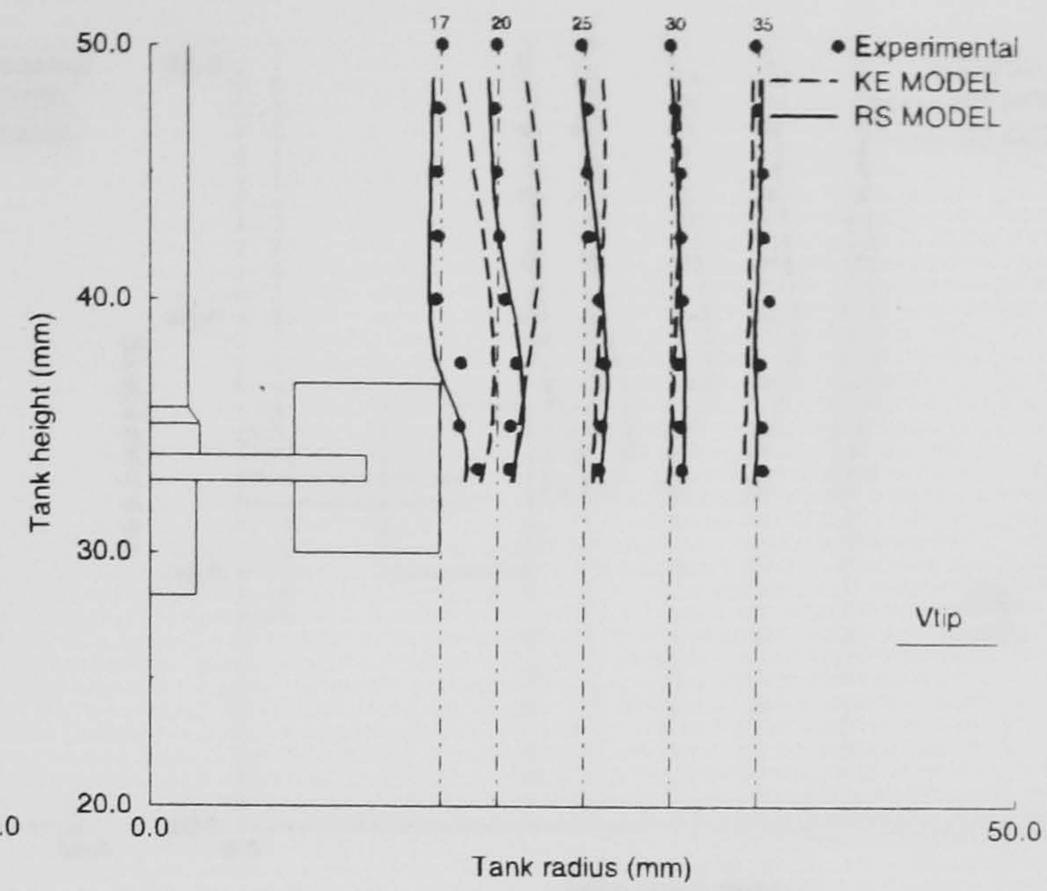



Figure.5.27b.

Figures 5.27a. and 5.27b. Prediction of the mean axial velocity using the Simple impeller model with Hybrid and TVD differencing schemes respectively in the plane $\theta = 45°$.

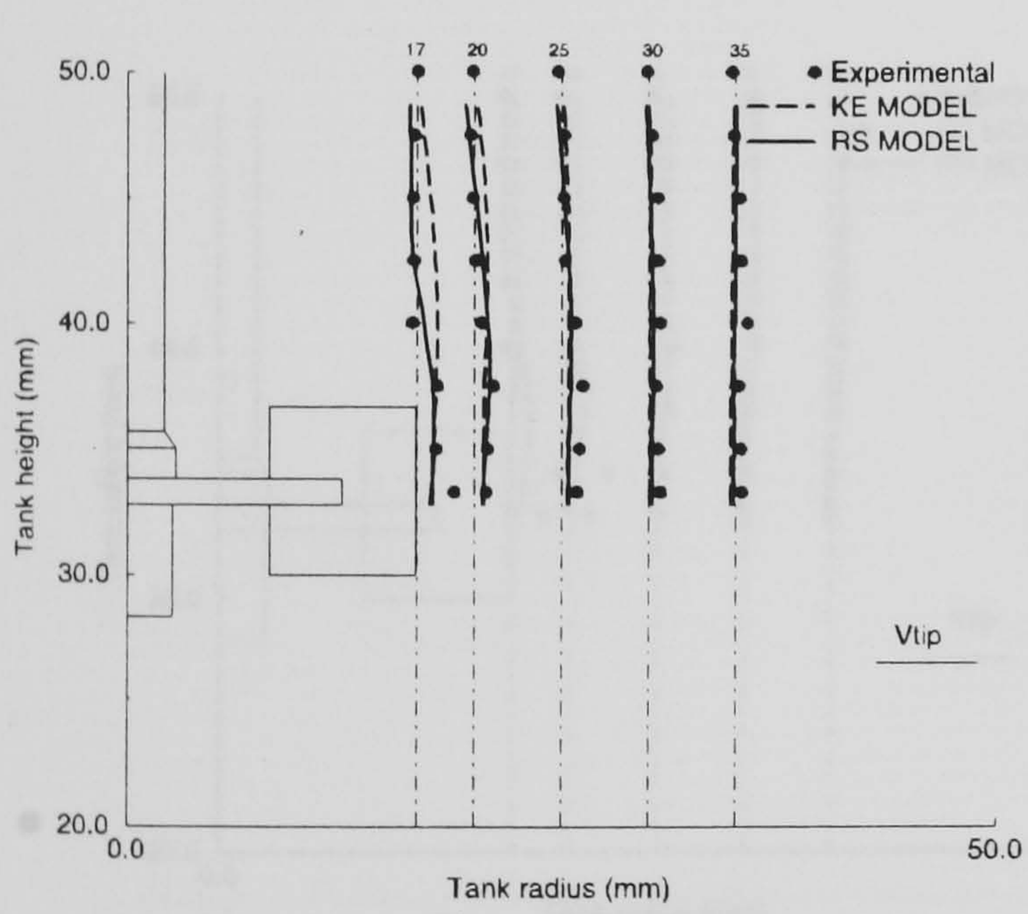



Figure.5.28a.

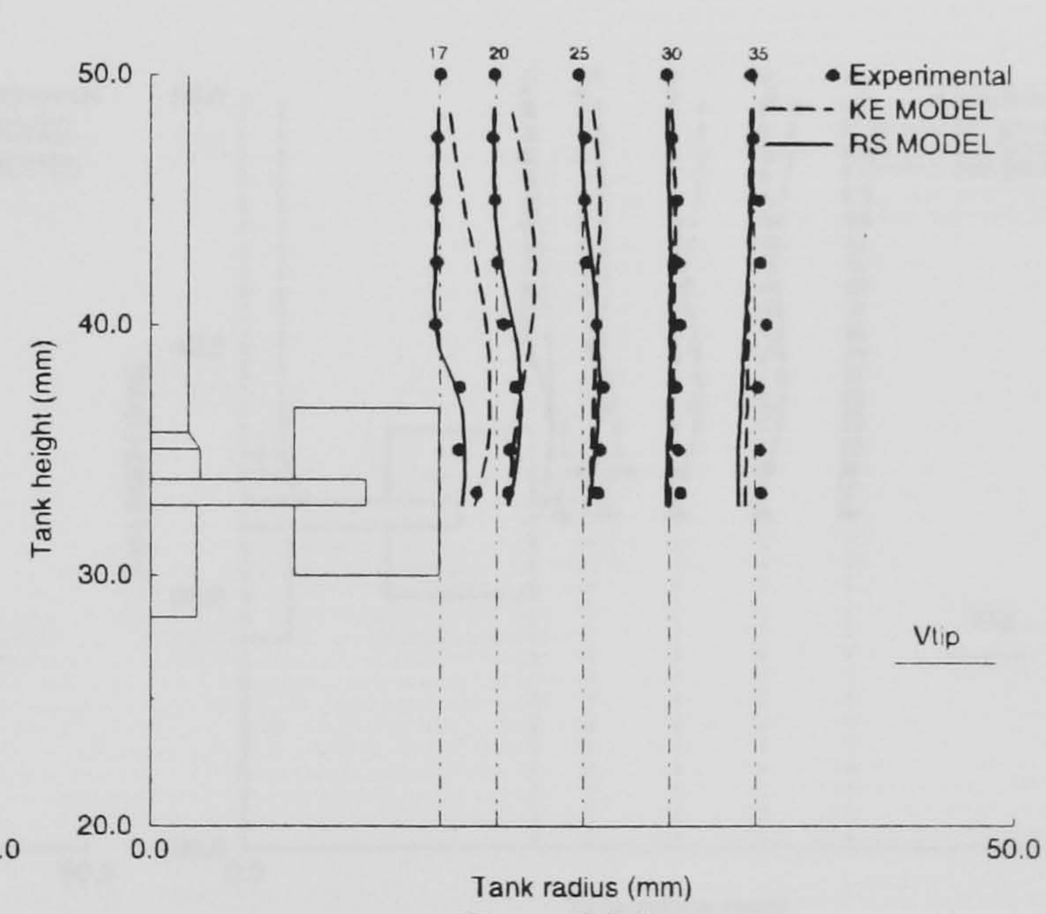



Figure.5.28b.

Figures 5.28a. and 5.28b. Prediction of the mean axial velocity using the Drag impeller model with Hybrid differencing and the Dynamic impeller model with TVD scheme respectively in the plane $\theta = 45°$.

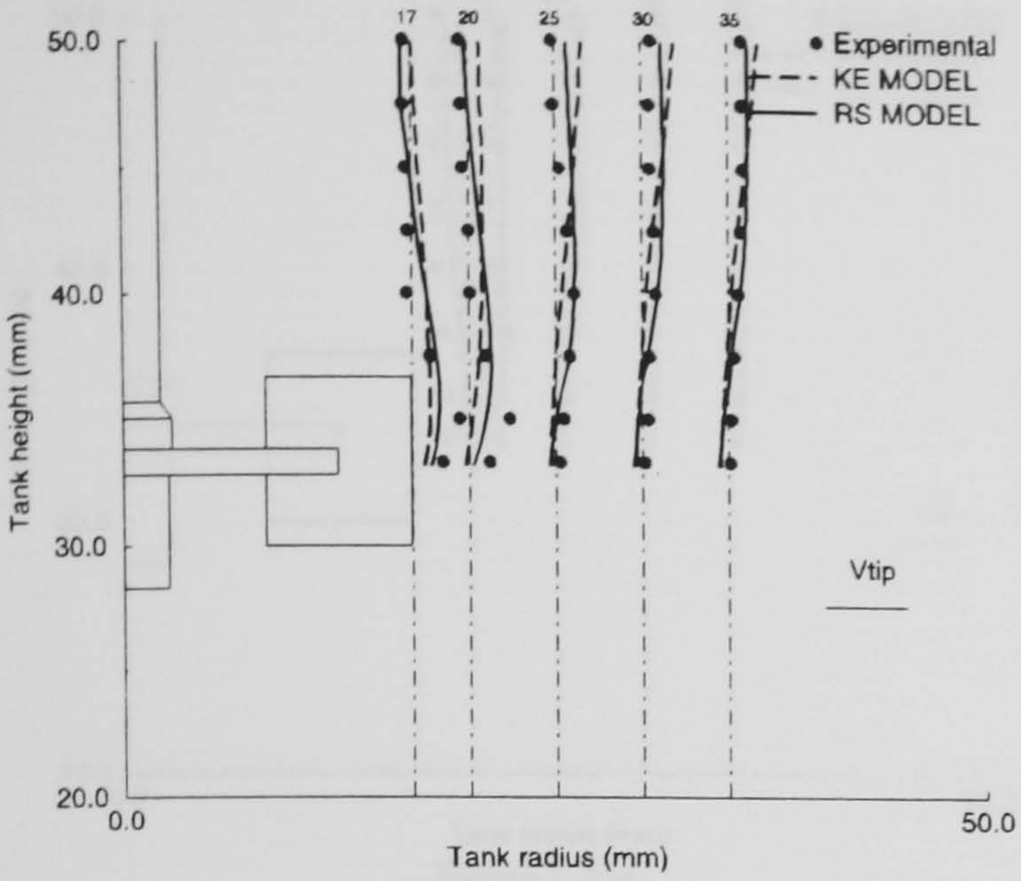



Figure.5.29a.

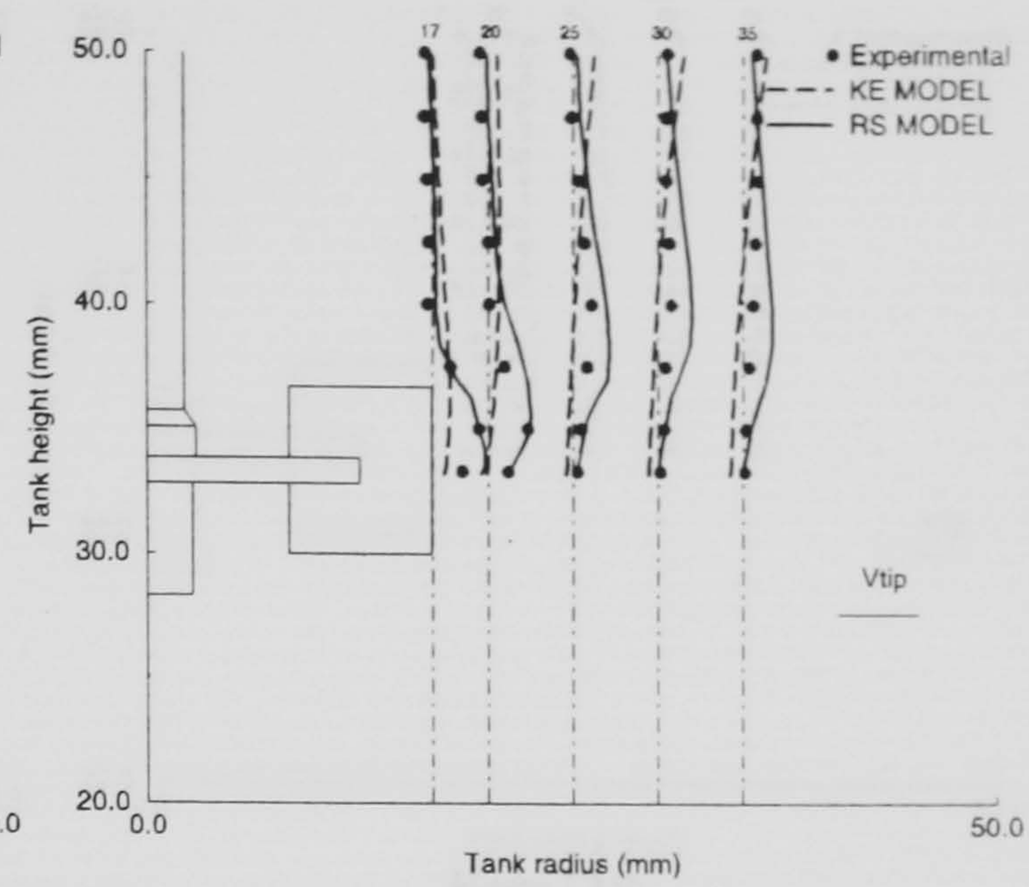



Figure.5.29b.

Figures 5.29a. and 5.29b. Prediction of the mean radial velocity using the Simple impeller model with Hybrid and TVD differencing schemes respectively in the plane $\theta = 45°$.

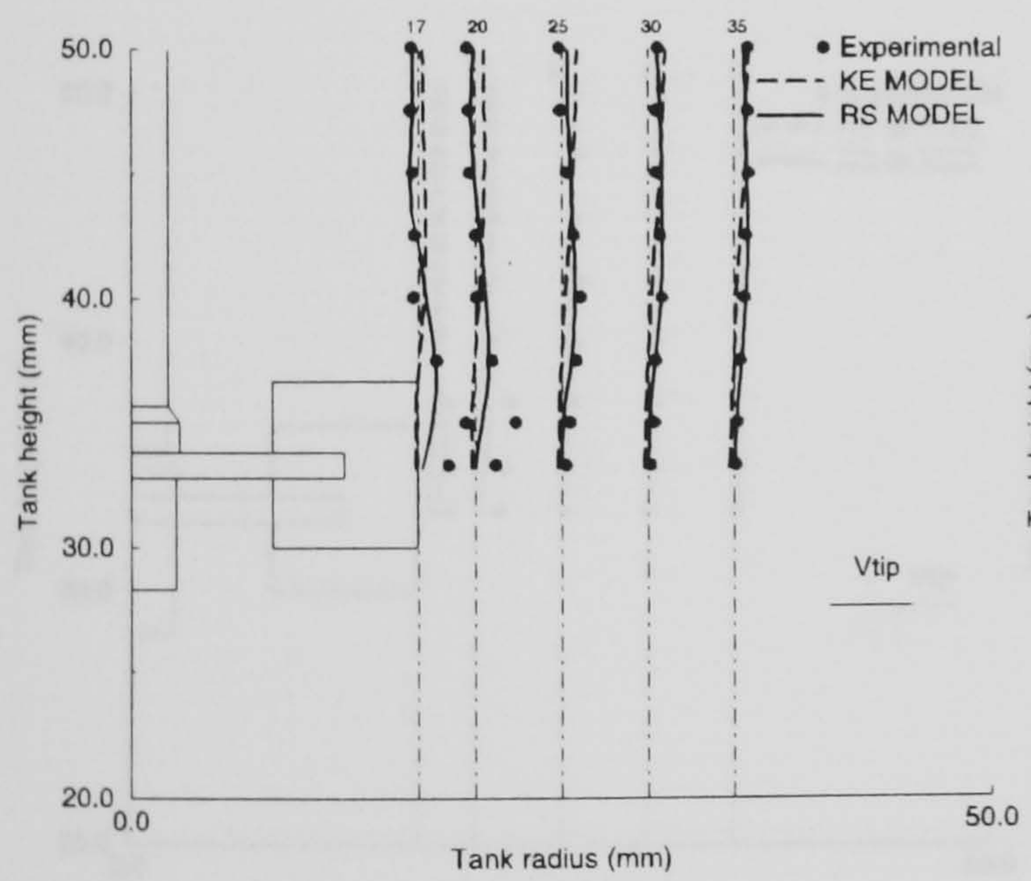



Figure.5.30a.

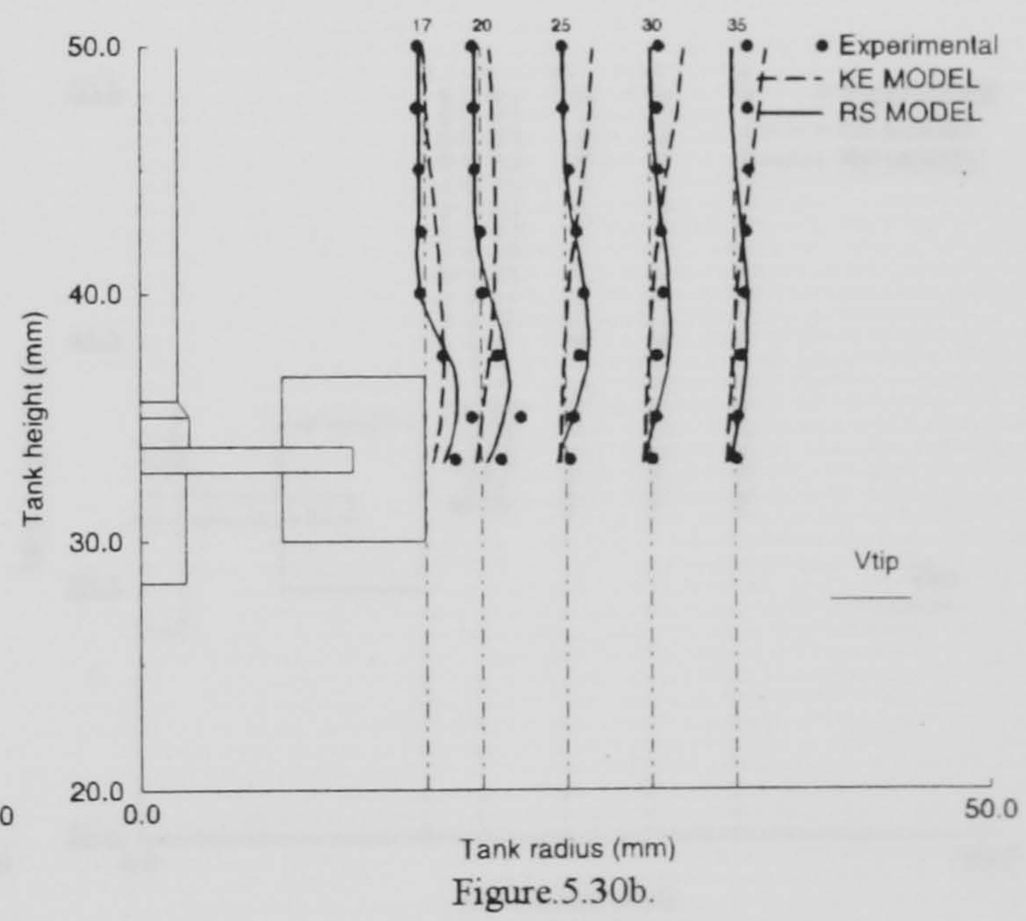



Figure.5.30b.

Figures 5.30a. and 5.30b. Prediction of the mean radial velocity using the Drag impeller model with Hybrid differencing and the Dynamic impeller model with TVD scheme respectively in the plane $\theta = 45°$.

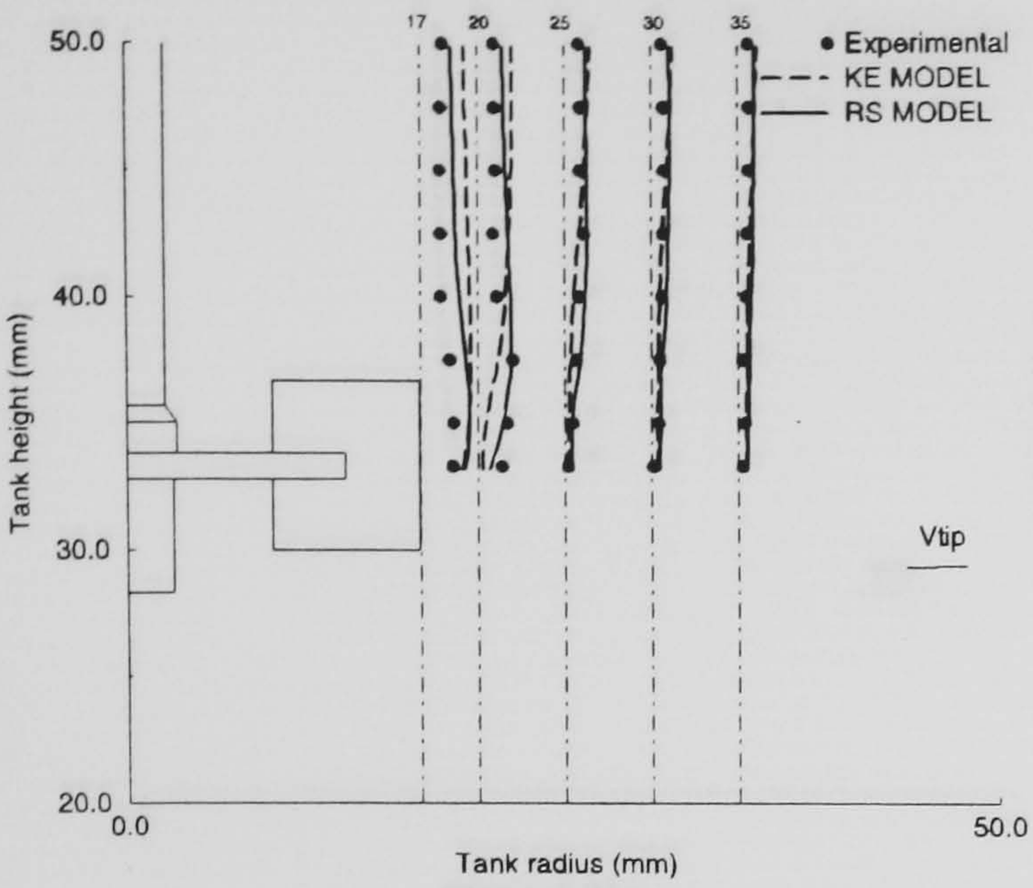



Figure.5.31a.

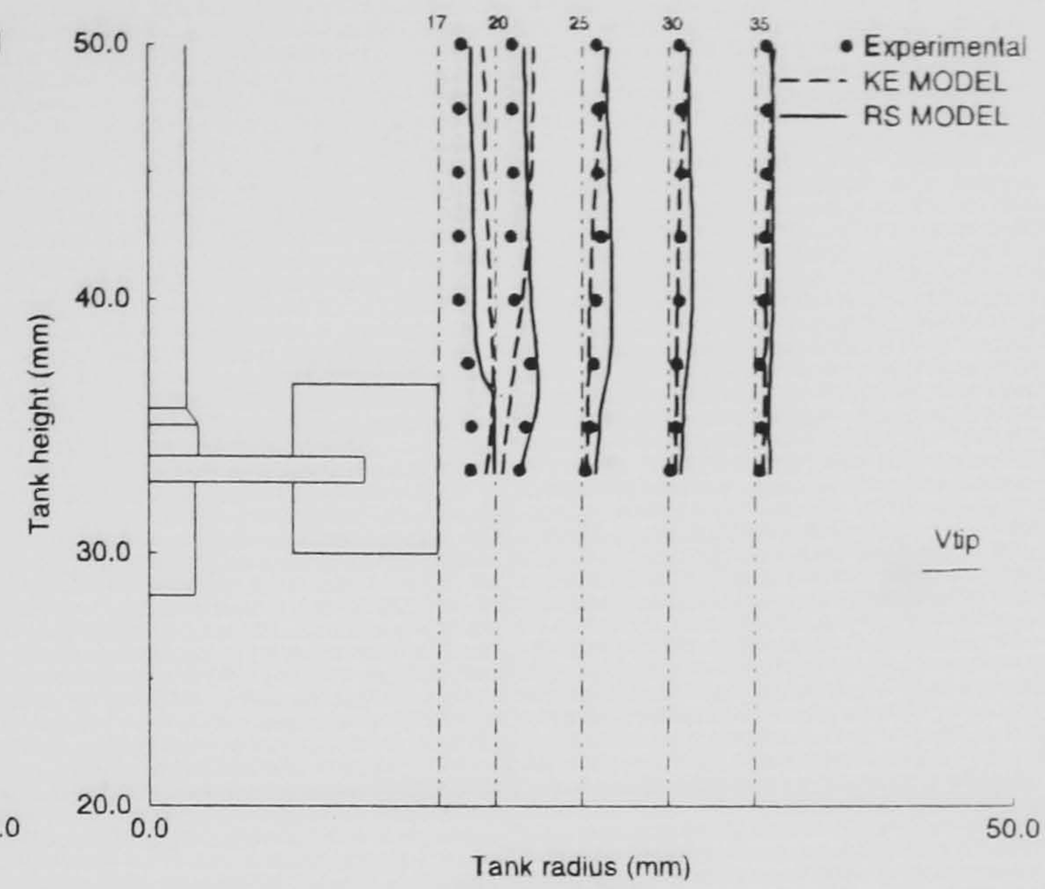



Figure.5.31b.

Figures 5.31a. and 5.31b. Prediction of the mean tangential velocity using the Simple impeller model with Hybrid and TVD differencing schemes respectively in the plane $\theta$ = 45°.

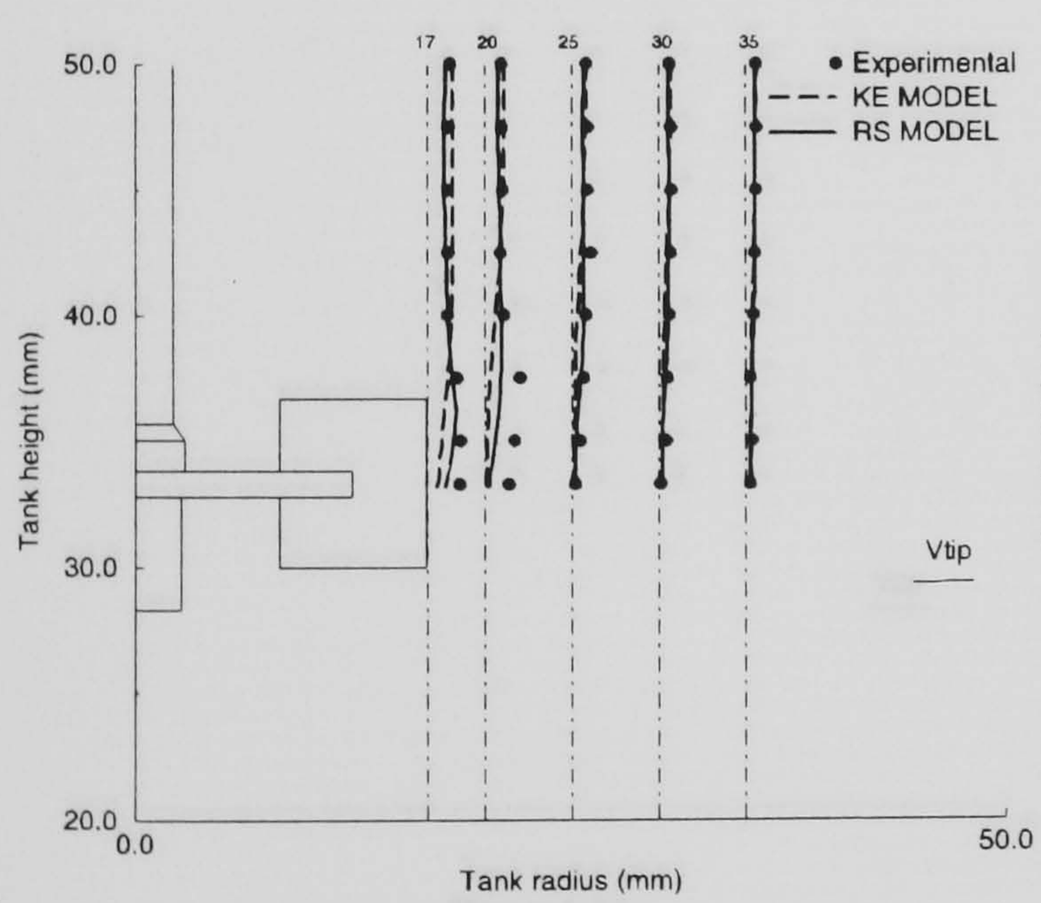



Figure.5.32a.

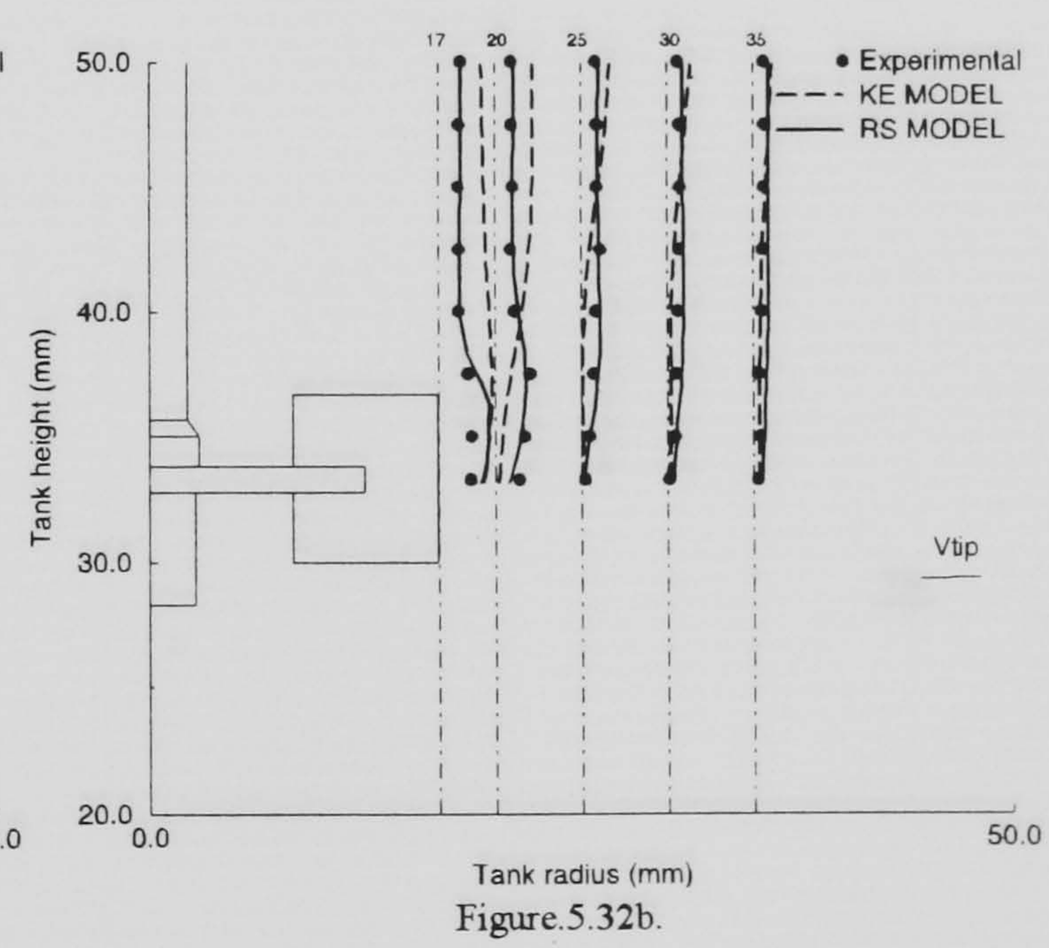



Figure.5.32b.

Figures 5.32a. and 5.32b. Prediction of the mean tangential velocity using the Drag impeller model with Hybrid differencing and the Dynamic impeller model with TVD scheme respectively in the plane $\theta$ = 45°.

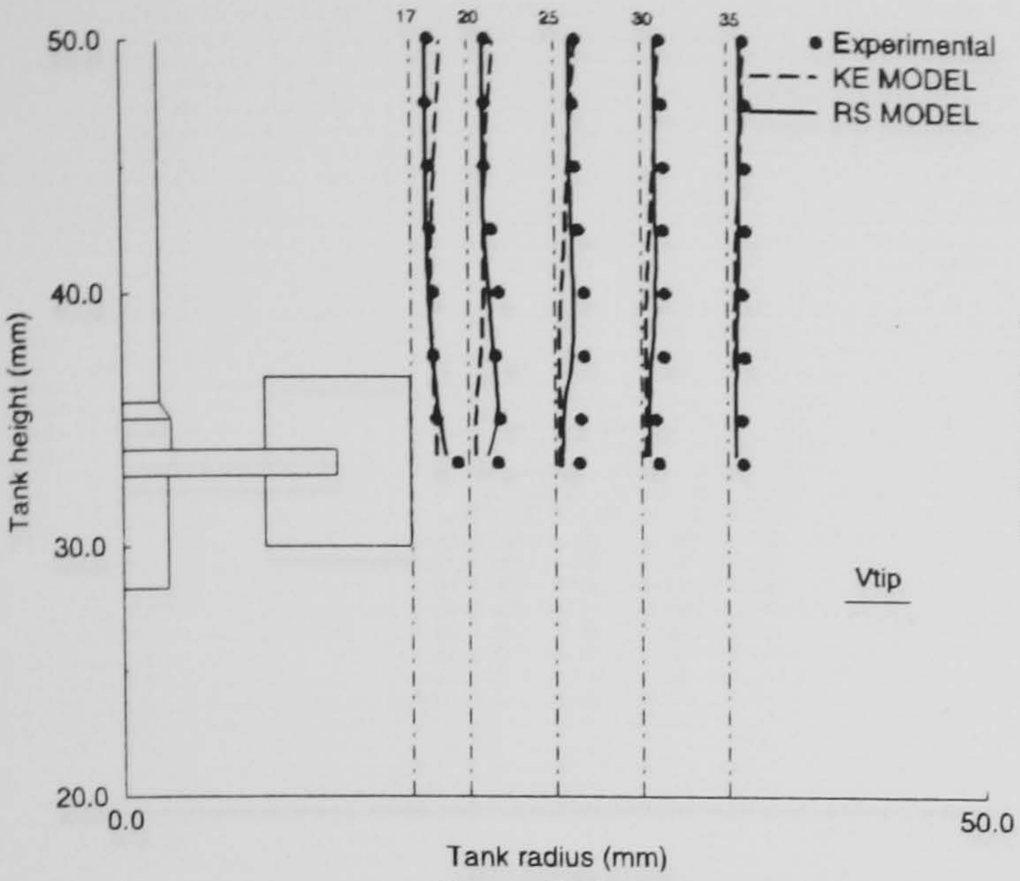



Figure.5.33a.

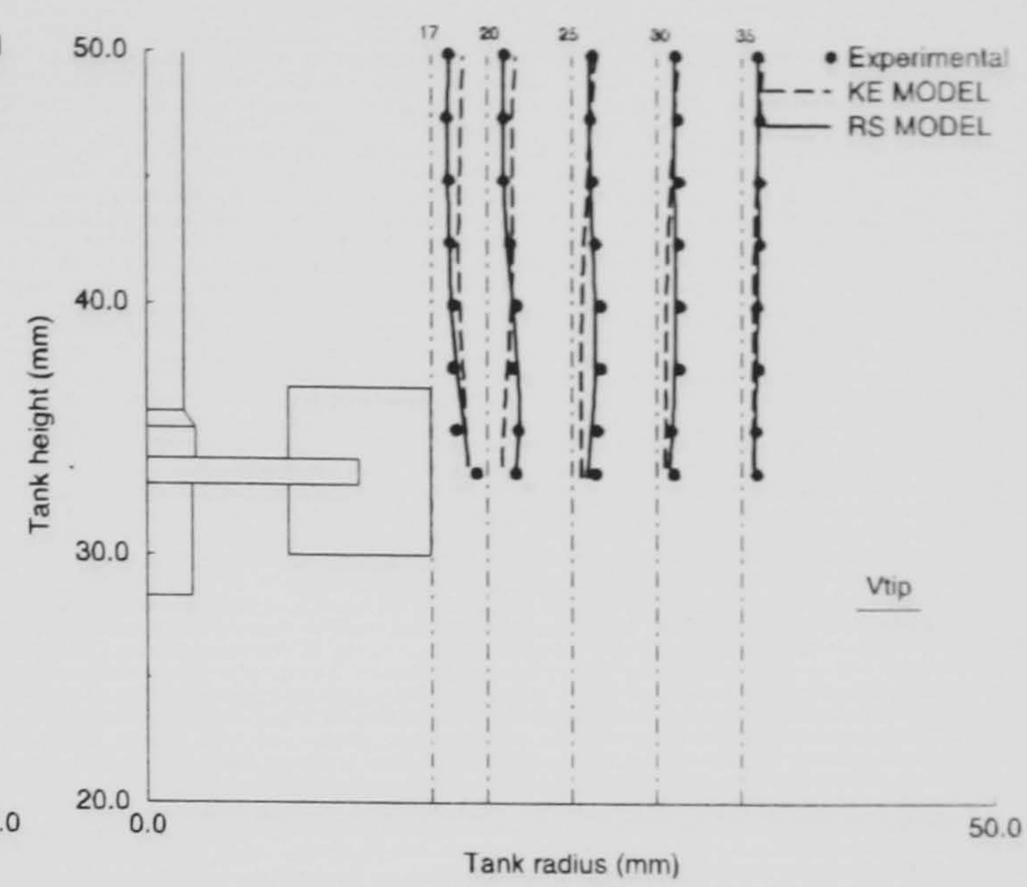



Figure.5.33b.

Figures 5.33a. and 5.33b. Prediction of the tangential fluctuating velocity using the Simple impeller model with Hybrid and TVD differencing schemes respectively in the plane $\theta$ = 0°.

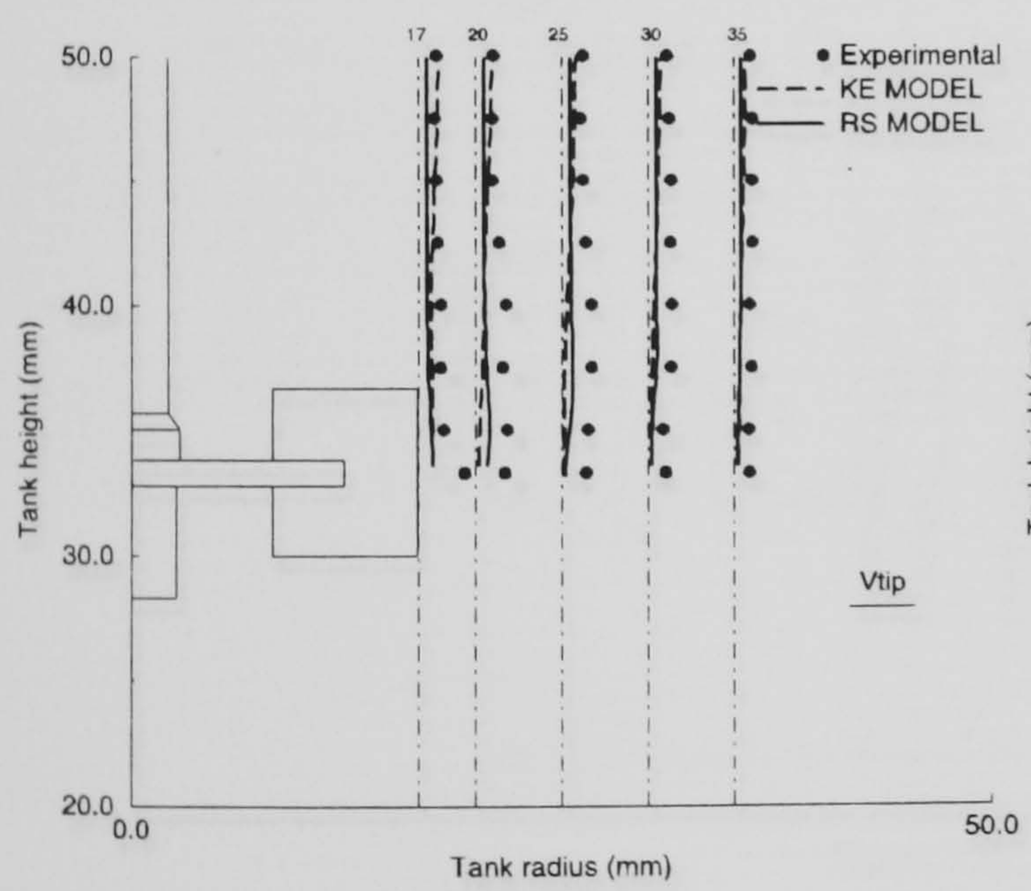



Figure.5.34a.

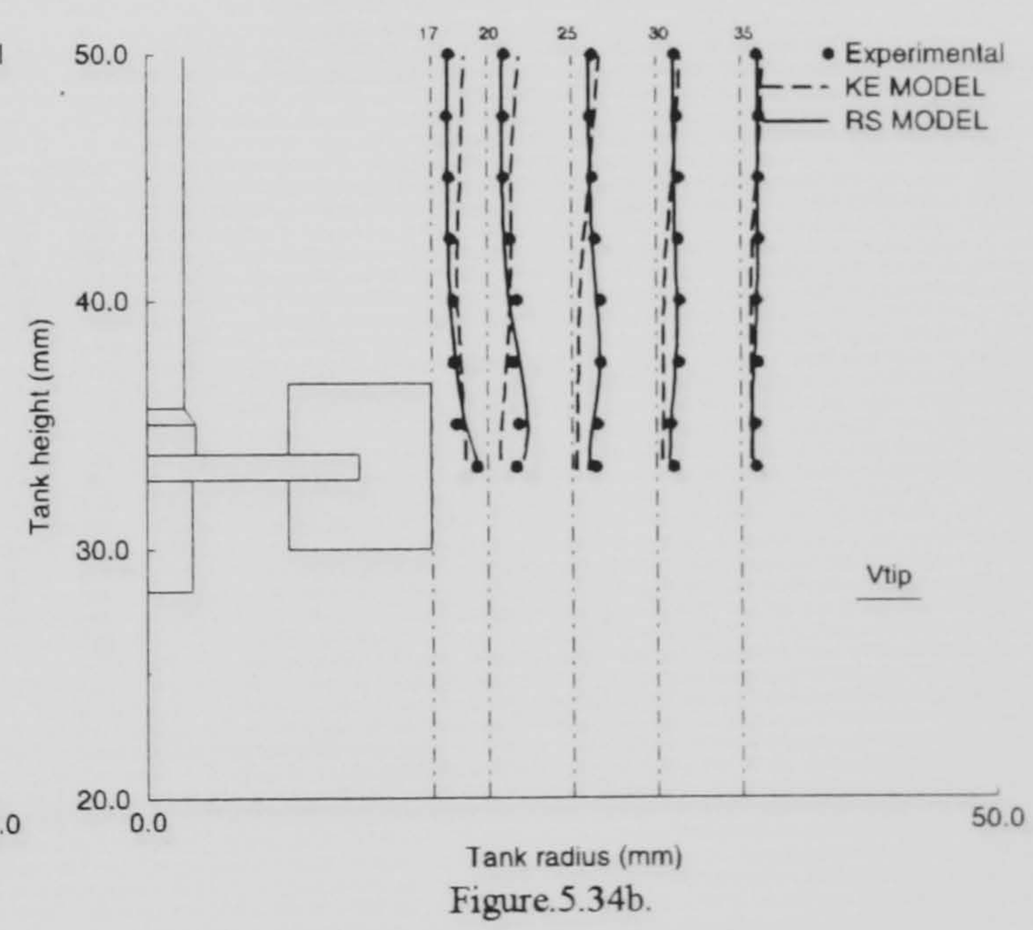



Figure.5.34b.

Figures 5.34a. and 5.34b. Prediction of the tangential fluctuating velocity using the Drag impeller model with Hybrid differencing and the Dynamic impeller model with TVD scheme respectively in the plane $\theta = 0°$.

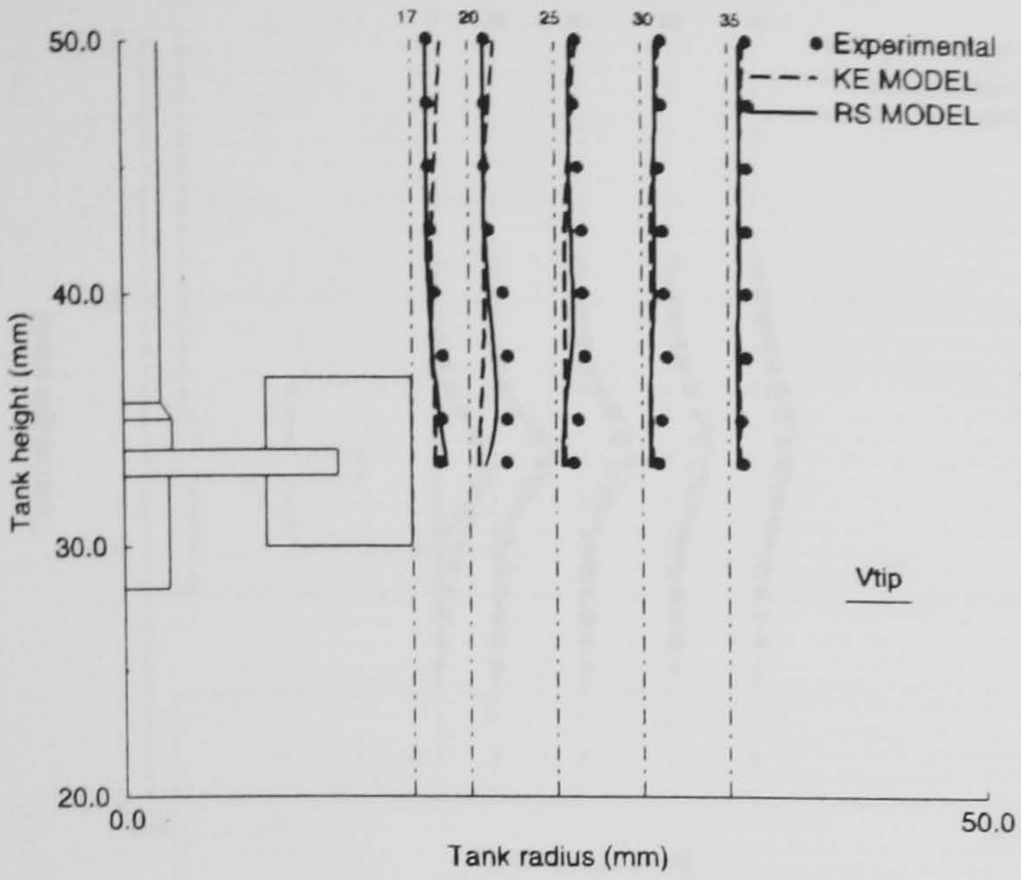



Figure.5.35a.

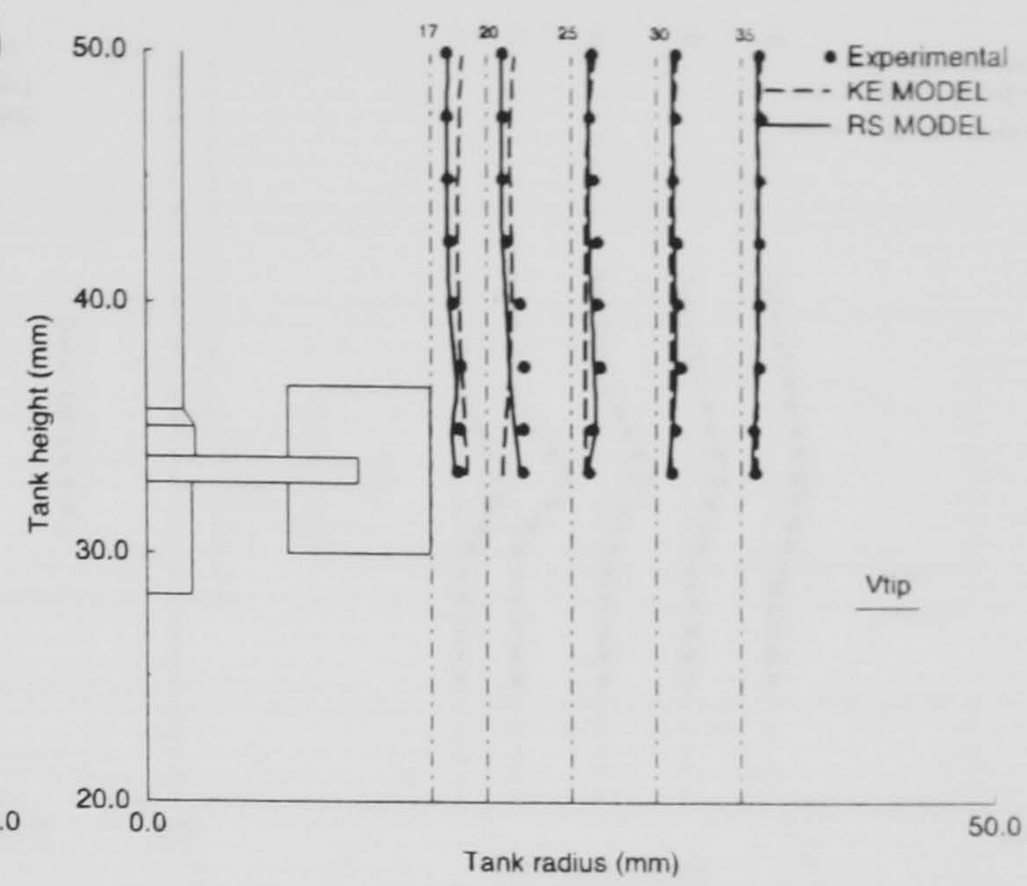



Figure.5.35b.

Figures 5.35a. and 5.35b. Prediction of the tangential fluctuating velocity using the Simple impeller model with Hybrid and TVD differencing schemes respectively in the plane $\theta$ = 45°.

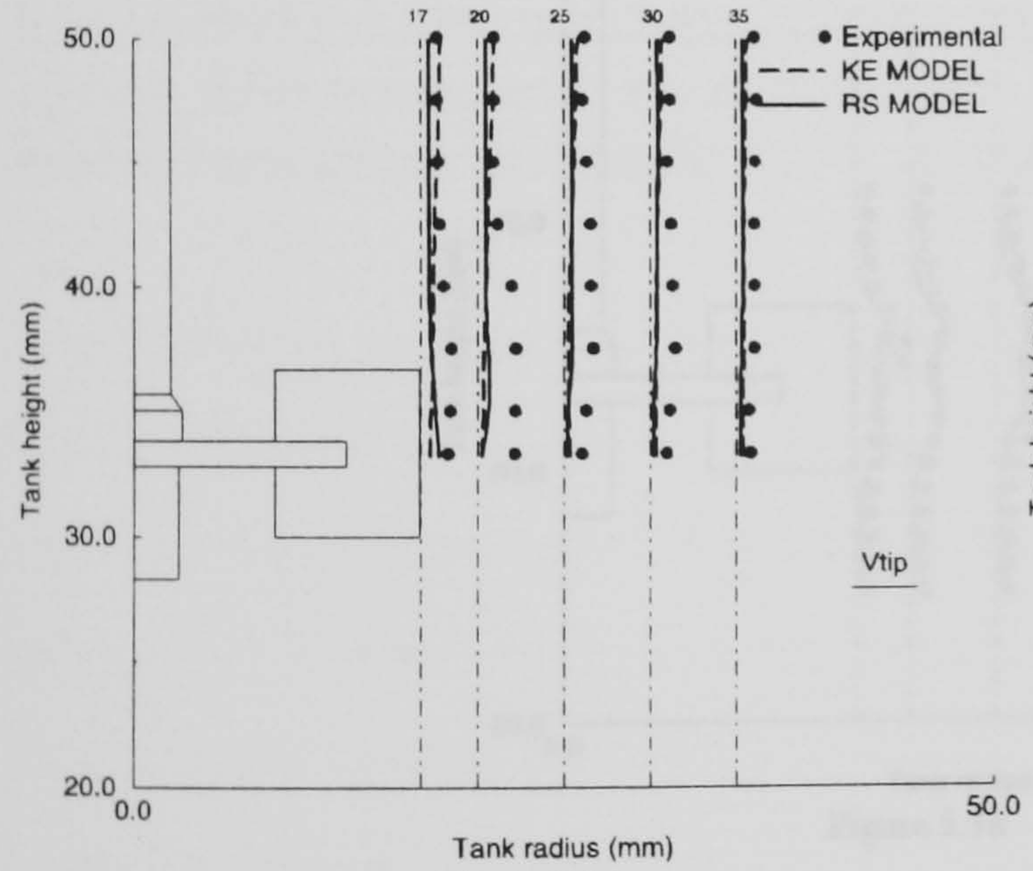



Figure.5.36a.

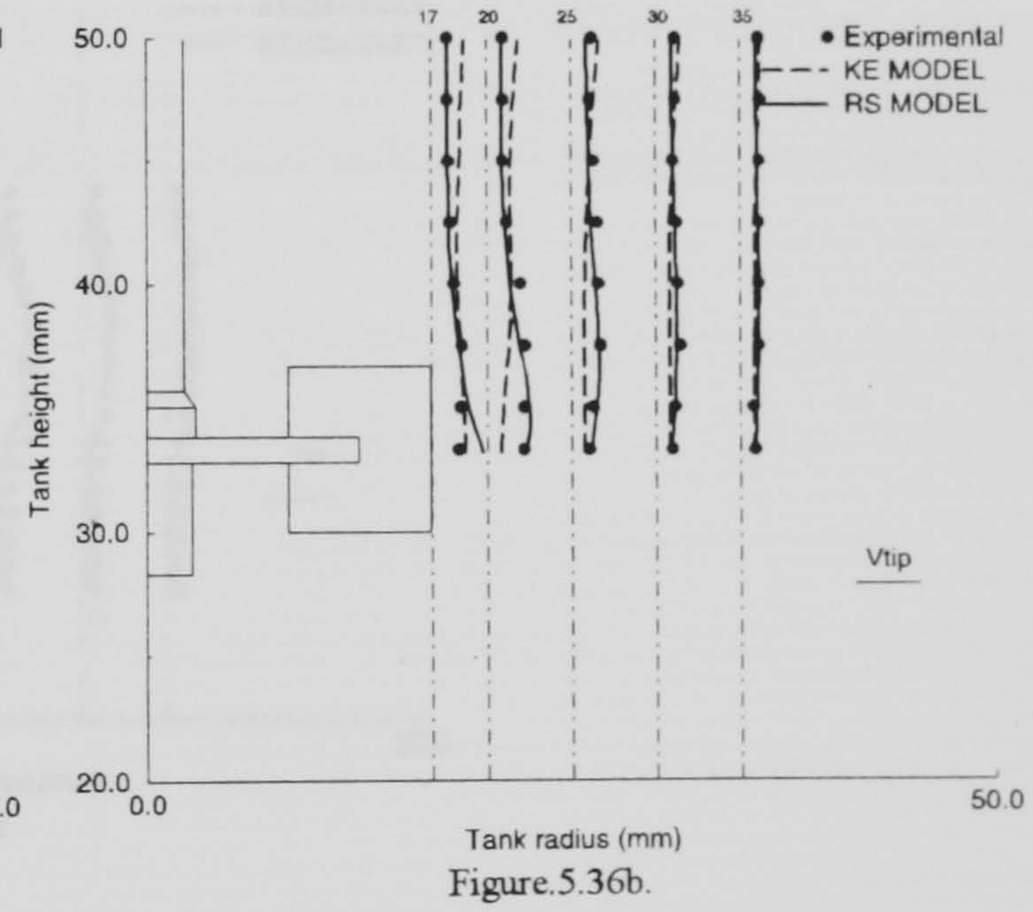



Figure.5.36b.

Figures 5.36a. and 5.36b. Prediction of the tangential fluctuating velocity using the Drag impeller model with Hybrid differencing and the Dynamic impeller model with TVD scheme respectively in the plane $\theta = 45°$.

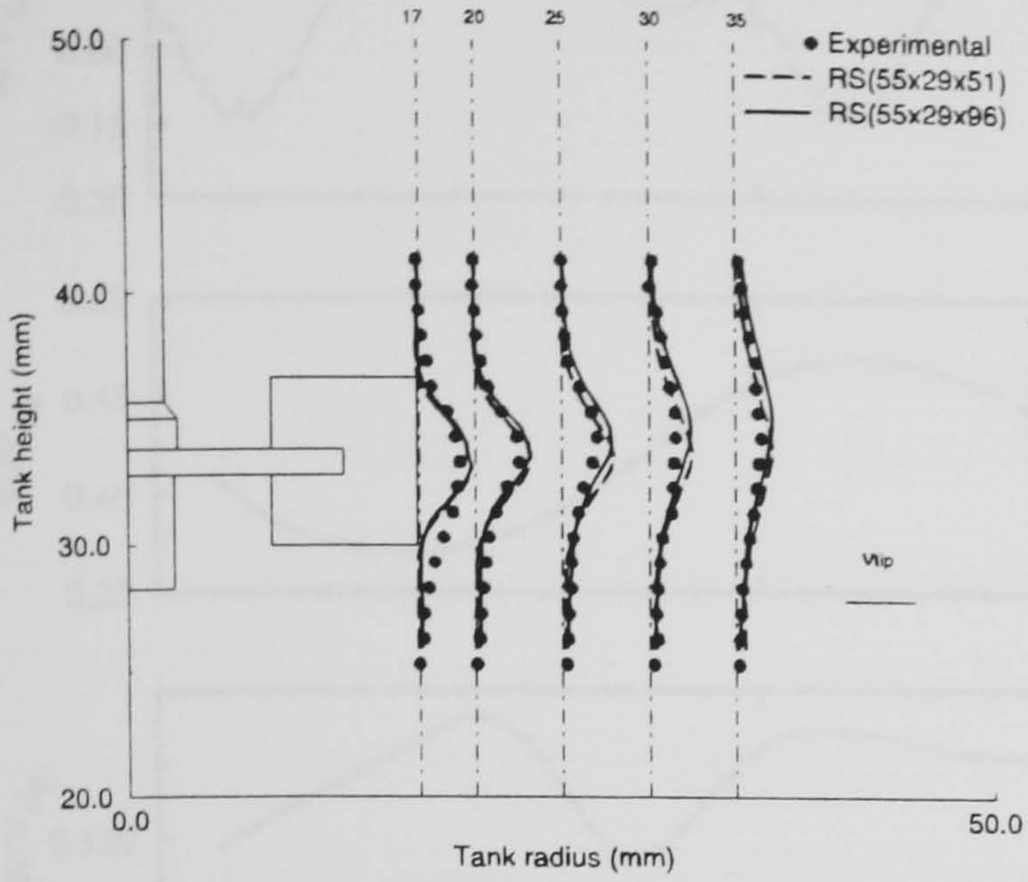


Figure.5.37a.

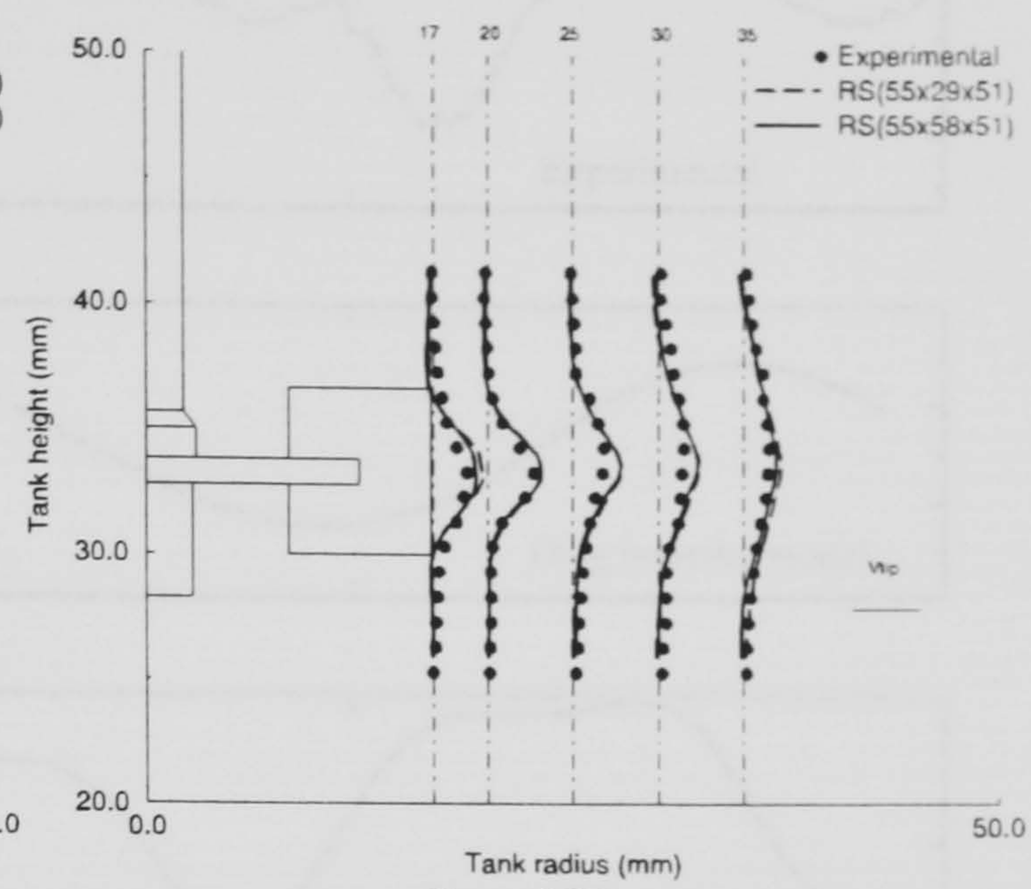


Figure.5.37b.

Figures 5.37a. and 5.37b. Prediction of the mean radial velocity using the Dynamic impeller model with TVD scheme in the planes $\theta = 0°$ and $\theta = 45°$ respectively.

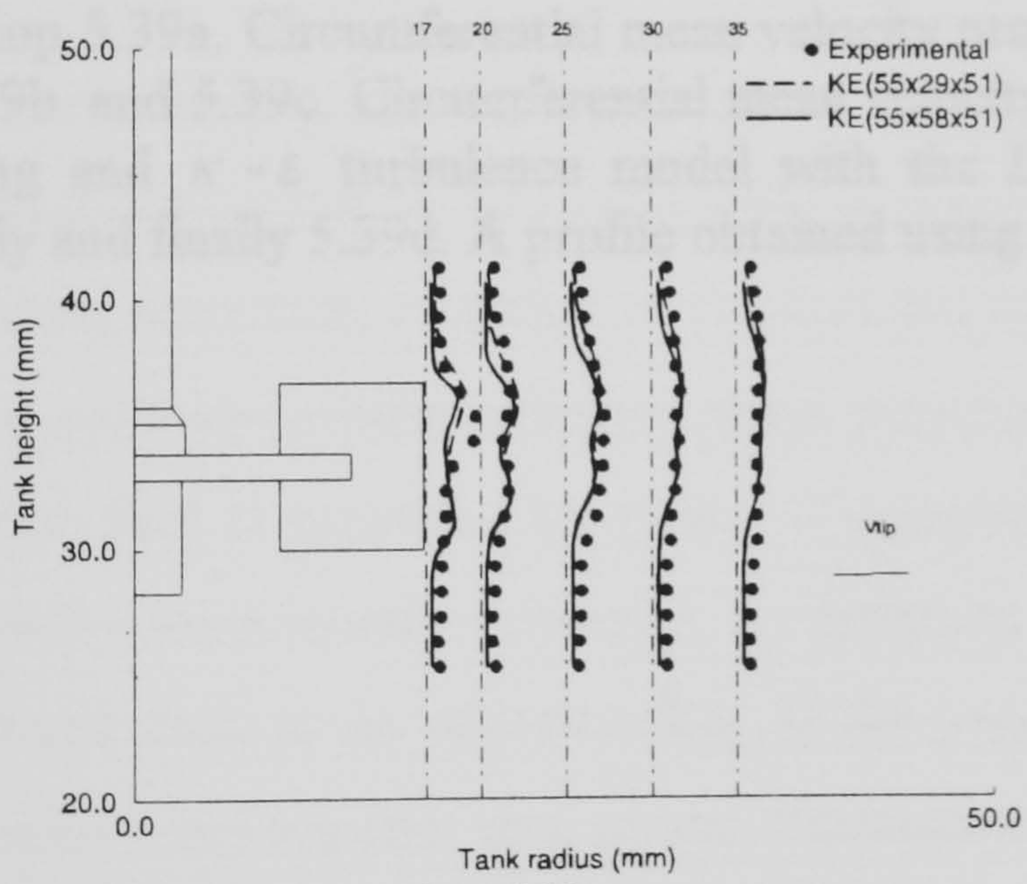
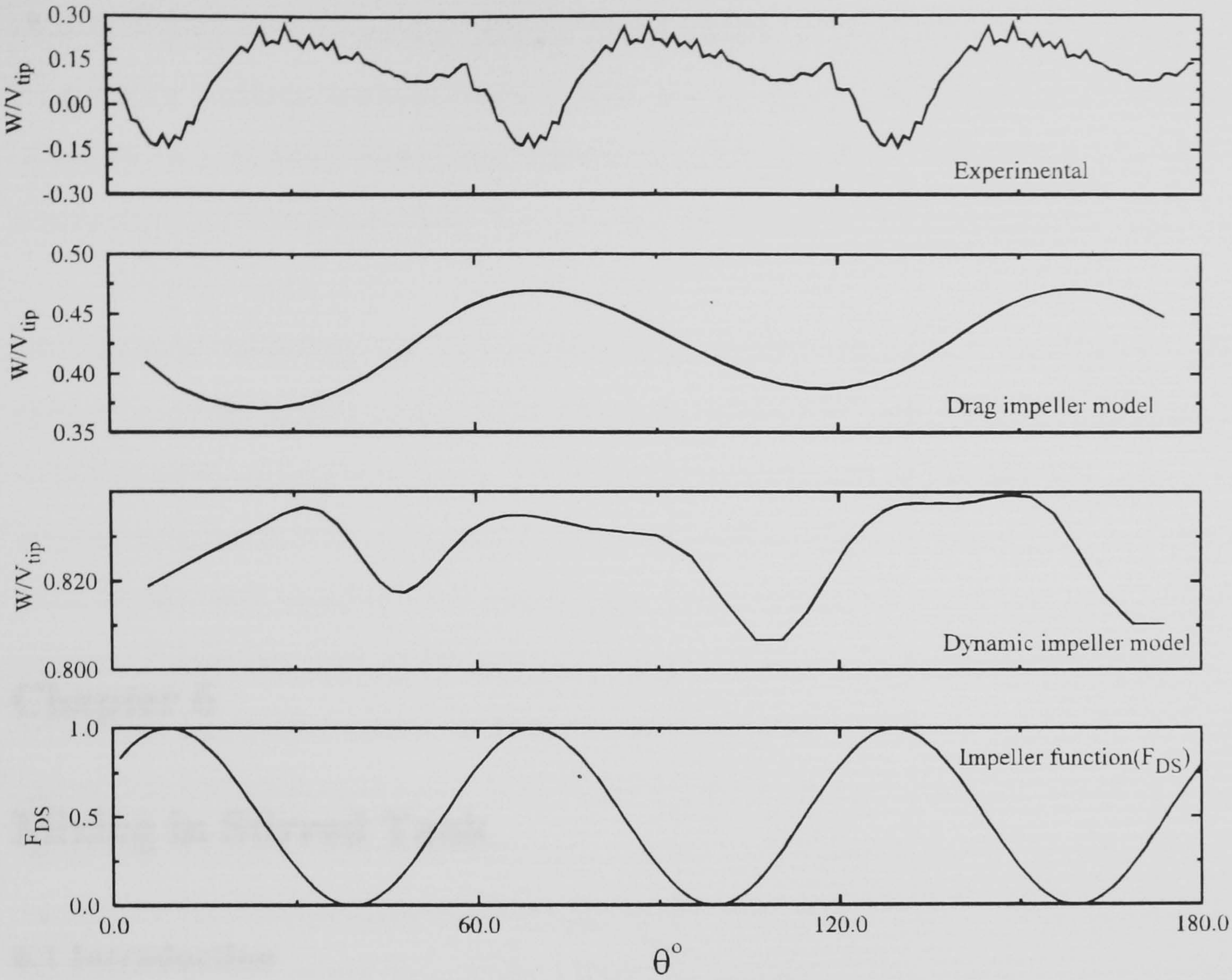


Figure.5.38

Figures 5.38. Prediction of the tangential fluctuating velocity using the Dynamic impeller model with Hybrid differencing in the plane $\theta = 0°$.




Figures from the top 5.39a. Circumferential mean velocity profile obtained experimentally by Lee(1995), 5.39b. and 5.39c. Circumferential mean velocity profiles obtained using the Hybrid differencing and $\kappa$ - $\varepsilon$ turbulence model with the Drag and Dynamic impeller models respectively and finally 5.39d. A profile obtained using the impeller function, $F_{DS}$.

# Chapter 6

# Mixing in Stirred Tank

## 6.1 Introduction

Mixing processes form a large part of the operation of the chemical, pharmaceutical, food processes, water treatment industries and are usually accomplished in mechanically stirred tanks. During a mixing operation, a number of physical and transport processes can occur simultaneously and agitation usually enhances these processes. In most stirred tanks a highly turbulent flow field is generated by means of agitation in order to accelerate the momentum, heat and/or mass transfer processes. To design an efficient mixer many factors have to be considered such as an understanding of the processes required, so that the optimum tank geometry and impeller size, power requirements and equipment have to be specified.

The design of mixing systems has for many years relied heavily on experiments and as a result the design process is labour intensive, time consuming and expensive. However, these experiments provided valuable information which have helped in understanding the

fluid flow generated by mixing vessels. For example, some of the recent work in vessels stirred by a Rushton impeller were carried out by Sano and Usui(1985), Yianneskis et al(1987), Nouri(1988), Nouri and Whitelaw(1990), Hockey(1990), Gaskey et al(1990), Yianneskis and Whitelaw(1993), Ruszkowski(1994), Lee(1995), Distelhoff et al(1996).

Mathematical modelling has been employed as another approach to optimise the mixing process in a fully baffled vessel and involves the solution of conservation equations subject to initial and boundary conditions. The boundary conditions of a baffled tank stirred by an impeller consists of a line of symmetry and solid walls which consists of top, bottom, outer wall, baffles and impeller disk and blades. These boundary conditions apart from the impeller blades are well established and many attempts of modelling the impeller were carried out by many workers as described in the previous chapter, section 5.1. The main aim of the computational work carried out by these workers was the calculation of the fluid flow field in a tank stirred by either single or double Rushton impellers. The main interest in this chapter is to compute the scalar concentration as a function of time in a cylindrical vessel stirred by a single Rushton impeller. Two earlier works on mixing computations in a tank stirred by a single Rushton impeller were those of Middleton et al(1986) and Ziman(1990).

Middleton et al(1986) used measurements of the product yield of a competitive-consecutive reaction system in three vessels, table 6.1, stirred by a single Rushton turbine to compare the applicability of three scale-up rules (power per unit volume, agitator tip speed and mixing time) and a prediction scheme based upon the Upwind differencing scheme and the $\kappa$ - $\varepsilon$ turbulence model to test scale-up. The authors concluded that, even with vessels which are geometrically similar, none of the above scale-up criteria can be successfully applied although thepredictions showed good agreement with the experimental data. No data, experimental or computational, was presented relating to the evolution of the product with respect to time or position in the tank and as such the study does not represent a good test case for computational methods.

Ziman(1990) also carried out mixing calculations in a fully baffled cylindrical tank stirred by a single Rushton turbine. The geometry of the tank is listed in table 6.1 and can be compared to that of Middleton et al. Ziman calculated the manner in which a salt solution mixes when added to a stirred tank initially containing water. The computations were performed on a mesh of 16,000 points in a 90° sector for the flow field and a 360° sector for the scalar mixing calculation. During the mixing calculation, the added scalar was set to unity at the cells near the injection point over the period of injection, 1 second. The mixing time was started at time, t = 0, when the value of the scalar was assumed to be zero at all points in the vessel. Ziman indicated that the agreement between the experimental data and predicted results is poor. In particular the initial concentration levels in the upper part of the tank are not predicted and in the lower part the concentration levels are too low and occurs too late when compared with the experimental data.

| | Ziman | Middleton | |
|---|---|---|---|
| Tank capacity(litres) | 4,390 | 30 | 600 |
| Diameter | 1.83m | 0.31m | 0.91m |
| Height | 1.67m | 0.42m | 0.91m |
| Clearance | 0.41m | 0.014m | 0.46m |
| Impeller Diameter | 0.90m | 0.15m | 0.3m |
| Disc Diameter | 0.65m | ------ | ------ |
| Blade Length | 0.23m | 0.038m | 0.076m |
| Blade Height | 0.18m | 0.03m | 0.06m |
| Baffle Width | 0.18m | 0.14m | 0.46m |

Table 6.1. Dimensions of stirred tank used by Middleton et al(1986) and Ziman(1990).

This chapter is concerned with scalar mixing calculations in a cylindrical tank stirred by a single Rushton impeller. Section 6.2, 6.3, 6.4, 6.5 and 6.6 present a detailed description of

the flow configuration, boundary conditions, discussion of the numerical results obtained for the scalar mixing computations, computational effort and summary respectively.

## 6.2 Flow Configuration

The flow configuration considered in this work is that studied experimentally by Distelhoff et al(1996)[1]. The cylindrical tank of diameter T = 147 mm and height H = 147 mm was fitted with four equally spaced baffles of width B = T/10 and thickness of T/100 mounted on the wall of the vessel. The working fluid used was water, which was stirred by a single Rushton impeller. The impeller, of overall diameter D = T/3, had six flat blades of height = D/5, width = D/4, and thickness of 1mm mounted on a disk also 1mm thick. The impeller was mounted on a hollow stainless steel shaft with a bottom clearance of C = T/3. During the mixing time calculations, the shaft was rotated with a rotational speed of 600 rpm which resulted in an impeller Reynolds number of 24,000. The dimensions of the tank and the impeller are summarised in figure 6.1. A batch of the working fluid containing the passive scalar was added to the vessel from a calibrated container mounted on top of the lid at the location shown in figures 6.1 and 6.2. The container was equipped with a plunger that sealed a hole with diameter of 7mm in the bottom of the container and by activating and raising the plunger for a prescribed period of time, 50ms, the fluid was allowed to flow under the action of gravity from the container into the stirred tank.

## 6.3 Boundary Conditions

The boundary conditions used for the numerical calculations of the mixing time of the tank stirred by single impeller are similar to the boundary conditions discussed in the previous chapter, section 5.3. The Simple, Drag and Dynamic impeller models were used to represent the impeller and are discussed in sections 5.4.1, 5.4.2 and 5.4.3 respectively.

Stirred vessels, including the impeller, exhibit rotational symmetry which can be exploited to make considerable savings. For example, in a vessel with four equally spaced baffles

[1] An LIF technique was used to obtain unobtrusive measurements of scalar concentration as a function of time and mixing time (99%) in a fully baffled stirred tank. The estimated error in the mixing time was 8%.

agitated with a 4-bladed impeller only a 90° sector of the tank needs to be carried out if a 6-bladed impeller is used a 180° sector is required. If mixing is taking place the symmetry of the vessel, with respect to the mixing field, may be broken although the symmetry of the velocity field may remain. In this study the flow field was calculated in a 180° sector using 55x29x51 nodes and the scalar mixing field in the full 360° using a mesh of 55x29x100 nodes. A time dependent mixing calculation was started, t = 0, from a converged velocity field by setting the value of the scalar at all points in the vessel to zero and then marching forward in time. The injection of the scalar into the tank was modelled by setting the value of the scalar to unity in the computational cell nearest to the addition point over the period of the injection time, 50ms. In cases where the Simple and Drag impeller models were used a "steady" velocity field was first precomputed and frozen for the duration of the mixing calculation. In the case of the Dynamic impeller model the velocity field was again precomputed, i.e. the calculation was repeated until a "cyclic" (with respect to time) flow field was reached and then the calculation of the velocity and the mixing were advanced through time during the mixing calculation.

## 6.4 Results and Discussion

### 6.4.1 Experimental Data

In the experimental carried out by Distelhoff et al(1996), the fluid was injected into the mixing vessel for a period of 50ms from a container located at the top of the tank in the $\theta$ = 0° plane as shown in figures 6.1 and 6.2 respectively. The concentration measurements were obtained at points along the circulation paths in vertical planes midway between the baffles located at $\theta$ = 0°, 90°, 180° and 270° from the location of injection. The measurement locations in each $\theta$ plane were selected according to the mean velocity field generated by the Rushton turbine, i.e. a radial jet stream and two ring vortices, and these locations are shown in figure 6.3.

Figures 6.4. and 6.5. present concentrations at a point as a function of time obtained experimentally by Distelhoff for the Rushton impeller at points A, B, C and D and at points G, H, I and J corresponding to planes above and below the impeller respectively. Referring to figures 6.4 and 6.5, the author indicated that the time needed to obtain a fully mixed concentration inside the mixing vessel is 5.7 seconds. This is the time required to mix the added scalar with the working fluid inside the vessel until uniformity was achieved all over the vessel. These figures show that in each plane, the variation between points A, B, C and D or G, H, I and J was small when compared to the variations between the planes. This is well illustrated in figure 6.5, the measurements at points G, H, I and J in the $\theta$ = 0° plane were more similar than the measurements at point G in the $\theta$ = 0°, 90°, 180° and 270° planes. It is noted that the level of concentration is highest in the 90° plane and decreased in the circumferential direction through the $\theta$ = 180°, 270° and 0° plane. It was also noted that the concentration gradient above and below the impeller was greater in the circumferential direction than the radial direction, indicating that the mixing in a vertical cross-section of a ring vortex was faster than the circumferential cross-section. This was also supported by Hockey(1990) who found that the axial and radial mean velocities were three times larger than the tangential mean velocity.

### 6.4.2 Results of Calculations

The results to be discussed were normalised with the fully mixed concentration, Cu, so that the normalised concentration, C, in the tank before the addition of the scalar was zero and unity in the fully mixed state after the addition of the scalar. The calculations were carried out using the Simple, Drag and Dynamic impeller models described in sections 5.4.1, 5.4.2 and 5.4.3 respectively with the following combinations of differencing scheme and turbulence model:

i) Hybrid scheme and $\kappa$ - $\varepsilon$ turbulence model.

ii) Hybrid scheme and Reynolds Stress/Scalar Flux turbulence model.

iii) TVD scheme and $\kappa$ - $\varepsilon$ turbulence model.

iv) TVD scheme and Reynolds Stress/Scalar Flux turbulence model.

Figures 6.6-6.15 present the predictions of the normalised fluid concentration, C/Cu, in the planes $\theta$ = 0°, 90°, 180° and 270° at points A, B, C and D above and points G, H, I and J below the impeller as a function of time. The different combinations of impeller model, differencing scheme and turbulence model presented in figures 6.6-6.15 are summarised in table 6.2.

| Figure number | Measurement points | Impeller model | Differencing scheme | Turbulence model |
|---|---|---|---|---|
| 6.6 | A B C D | Drag | Hybrid | $\kappa$ - $\varepsilon$ |
| 6.7 | G H I J | Drag | Hybrid | $\kappa$ - $\varepsilon$ |
| 6.8 | A B C D | Drag | TVD | $\kappa$ - $\varepsilon$ |
| 6.9 | G H I J | Drag | TVD | $\kappa$ - $\varepsilon$ |
| 6.10 | A B C D | Dynamic | TVD | $\kappa$ - $\varepsilon$ |
| 6.11 | G H I J | Dynamic | TVD | $\kappa$ - $\varepsilon$ |
| 6.12 | A B C D | Drag | Hybrid | RS/SF |
| 6.13 | G H I J | Drag | Hybrid | RS/SF |
| 6.14 | A B C D | Simple | TVD | RS/SF |
| 6.15 | G H I J | Simple | TVD | RS/SF |

Table 6.2. A summary of the different impeller model, differencing scheme and turbulence model combinations presented in figures 6.6-6.15.

Figures 6.6 and 6.7 present predictions of the concentration as a function of time in the upper and lower parts of the tank respectively using the Drag impeller model, Hybrid differencing and the $\kappa$ - $\varepsilon$ turbulence model. Comparing the predictions with the experimental data, figure 6.6 and 6.7, it is seen that the overall levels in the upper and lower parts of the tank are over and under predicted respectively, for example, at point A and B in the 0° plane the prediction show that the concentration is above 5 for 0.8 and 0.4 seconds respectively whereas in the measurement only point B exceeds 5 and only for less

than 0.2 seconds. In the lower part of the tank thepredictions show that at no time do the concentrations exceed 3.0 whilst the experimental data, particularly in the 90° plane, show significant excursions above 3.0. In addition to the general concentration errors large discrepancies between the predictions and the experimental data are noted for the time at which the scalar first arrives at the measurement point and final mixing time. Table 6.3 compares the predicted and measured first arrival times of concentration at the measurement points. This table show that at the lower part of the tank, the predicted first arrival time at all points in all planes are later than the measured first arrival time. For example, the predicted first arrival time at point, G, in the 0°, 90°, 180° and 270° planes are 1.0, 1.1, 1.2 and 1.2 whereas the measured values are 0.7, 0.7, 0.75 and 0.75 respectively. In the upper part of the tank, some of the predicted first arrival time are earlier than the measured values as shown at point A in the 0°, 180° and 270° planes, point B in the 0° and 270° planes and point C in the 0° plane.

| Planes | Points | | | | | | | |
|---|---|---|---|---|---|---|---|---|
| | A | | B | | C | | D | |
| | Predicted | Experimental | Predicted | Experimental | Predicted | Experimental | Predicted | Experimental |
| 0° | 0.1 | 0.2 | 0.15 | 0.2 | 0.4 | 0.45 | 0.75 | 0.45 |
| 90° | 0.35 | 0.25 | 0.75 | 0.7 | 1.2 | 0.3 | 0.75 | 0.45 |
| 180° | 0.4 | 0.5 | 0.9 | 0.6 | 1.25 | 0.6 | 0.9 | 0.5 |
| 270° | 0.25 | 0.7 | 0.42 | 0.85 | 0.9 | 0.85 | 1.0 | 0.7 |
| | G | | H | | I | | J | |
| 0° | 1.0 | 0.7 | 1.0 | 0.7 | 0.9 | 0.75 | 0.65 | 0.6 |
| 90° | 1.1 | 0.7 | 1.1 | 0.7 | 1.0 | 0.6 | 0.7 | 0.35 |
| 180° | 1.2 | 0.75 | 1.2 | 0.5 | 1.2 | 0.5 | 0.75 | 0.5 |
| 270° | 1.2 | 0.75 | 1.2 | 0.55 | 1.2 | 0.75 | 0.75 | 0.55 |

Table 6.3. Predicted and experimental concentration first arrival time (seconds) at measurement points above and below the impeller.

Figures 6.8 and 6.9 present predictions of the concentration as a function of time in the upper and lower parts of the tank respectively using the Drag impeller model, the TVD scheme and the $\kappa$ - $\varepsilon$ turbulence model. The principle difference between this set of predictions and those in figures 6.6 and 6.7 is the use of the TVD scheme as opposed for the Hybrid differencing. In the lower part of the tank, figure 6.9, the levels of concentration are considerably lower than those predicted using the Hybrid differencing, figure 6.7 for example at points G and I in the 0° plane, the concentration exceeds 2 for approximately one second whereas in figure 6.9 the concentration only exceeds 1 for approximately 0.5 seconds. In the upper part of the tank high values of concentration, > 5, are recorded at point A in all planes, as opposed to only in the 0° and 180° planes in figure 6.6.

Compared to the measured overall mixing time of 5.7 seconds, the predicted value of 10 seconds, figures 6.8 and 6.9, is considerably overpredicted. Table 6.4 presents the time at which the scalar is first detected at the measurement points and compared with table 6.3, it was noted that at the lower part of the tank the predicted arrival time in the 180° plane at points G, B and J were the same in both tables. In the 270° plane the predicted first arrival time presented in table 6.4 have started earlier at points G, B, I and J by 0.1, 0.1, 0.3 and 0.05 seconds respectively compared with table 6.3. In the upper part of the tank the predicted first arrival times have again started earlier, table 6.4, at points A, B and C in the 90°, 180° and 270° compared with predicted first arrival time shown in table 6.3. For example the predicted first arrival time obtained for points A, B and C in the 90° plane shown in table 6.4 are 0.2, 0.4 and 0.75 whereas in table 6.3 are 0.35, 0.75 and 1.2 respectively. At points A and B in the 0° plane the predicted first arrival time in both tables are the same.

| Planes | Points | | | | | | | |
|---|---|---|---|---|---|---|---|---|
| | A | B | C | D | G | H | I | J |
| 0° | 0.1 | 0.15 | 0.5 | 0.8 | 1.2 | 1.1 | 0.9 | 0.7 |
| 90° | 0.2 | 0.4 | 0.75 | 1.0 | 1.2 | 1.2 | 1.0 | 0.75 |
| 180° | 0.25 | 0.5 | 1.15 | 1.0 | 1.2 | 1.2 | 1.1 | 0.75 |
| 270° | 0.15 | 0.25 | 0.47 | 0.9 | 1.1 | 1.1 | 0.9 | 0.7 |

Table 6.4. Predicted concentration first arrival time (seconds) at measurement points above and below the impeller.

The overall mixing time predicted is larger than that predicted previously, 12 versus 10 seconds, and is twice that measured, 5.7 seconds.

Figures 6.10 and 6.11 present predictions of the concentration as a function of time in the upper and lower parts of the tank respectively using the Dynamic impeller model, the TVD scheme and the $\kappa$ - $\varepsilon$ turbulence model. Comparing figures 6.10 and 6.11 with 6.8 and 6.9 respectively it is seen that in the upper part of the tank the general level of concentration has been lowered and in the lower part similar levels are recorded. In addition in the upper part of the tank the peaks in the concentration have been "narrowed" and show better agreement with the experimental data; compared to figures 6.10 and 6.4. Table 6.5 presents the time at which the scalar is first detected at the measurement points. In the upper part of the tank the predicted first arrival times at all measurement points in all planes are shorter than shown in tables 6.3 and 6.4. For example in the 0° plane at A, B, C and D measurement points the first arrival time are 0.05, 0.05, 0.1 and 0.2 respectively whereas at tables 6.3 and 6.4 are 0.2, 0.2, 0.4 and 0.75 and 0.1, 0.15, 0.5 and 0.8 respectively. A similar behaviour was again noted in the lower part of the tank.

| Planes | Points | | | | | | | |
|---|---|---|---|---|---|---|---|---|
| | A | B | C | D | G | H | I | J |
| 0° | 0.05 | 0.05 | 0.1 | 0.2 | 0.45 | 0.45 | 0.45 | 0.3 |
| 90° | 0.05 | 0.1 | 0.2 | 0.3 | 0.45 | 0.45 | 0.45 | 0.3 |
| 180° | 0.1 | 0.2 | 0.41 | 0.4 | 0.45 | 0.45 | 0.45 | 0.3 |
| 270° | 0.1 | 0.2 | 0.44 | 0.4 | 0.48 | 0.48 | 0.48 | 0.3 |

Table 6.5. Predicted concentration first arrival time (seconds) at measurement points above and below the impeller.

The predictions have reached the fully mixed state after 4.5 seconds, which while it represents a considerable decrease compared to the previous predictions, it is now shorter than the experimentally measured value, 5.7 seconds.

Figures 6.12 and 6.13 present predictions of the concentration as a function of time in the upper and lower parts of the tank respectively using the Drag impeller model, Hybrid differencing and the Reynolds Stress/Scalar Flux model. In the lower part of the tank, figure 6.13, the predictions again show lower levels of concentration compared to figure 6.7 and later times of arrival of the scalar at the measurement points. Of particular note is the absence of large concentration fluctuations in the 90° plane at any of the measurement points, for example, in the upper part of the tank, figure 6.12, the concentration exceeds the fully mixed concentration, 1, for a much greater fraction of the mixing process than figure 6.6. Table 6.6 presents the time of arrival of the scalar at the measurement points. In the upper and lower parts of the tank, the predicted first arrival times are longer everywhere except in the upper part of the tank in the 90° plane at the measurement point A which is shorter in table 6.6 compared to table 6.3. The scalar at the G, H and I measurements points located in the 0°, 90° and 180° planes first arrival time is 1.8 seconds, whereas in the upper part of the tank the scalar at B and C measurement points located in the 90° and 180° planes first arrival time is 1.7 seconds.

| Planes | Points | | | | | | | |
|---|---|---|---|---|---|---|---|---|
| | A | B | C | D | G | H | I | J |
| 0° | 0.9 | 1.3 | 1.5 | 1.5 | 1.8 | 1.8 | 1.8 | 1.25 |
| 90° | 0.25 | 1.7 | 1.7 | 1.7 | 1.8 | 1.8 | 1.8 | 1.3 |
| 180° | 0.45 | 1.7 | 1.7 | 1.5 | 1.8 | 1.8 | 1.8 | 1.4 |
| 270° | 0.65 | 1.4 | 1.8 | 1.8 | 2.0 | 2.0 | 2.0 | 1.4 |

Table 6.6. Predicted concentration first arrival time (seconds) at measurement points above and below the impeller.

The final mixing time predicted is in excess of 10 seconds which overpredicts the experimental data, 5.7 seconds.

Figures 6.14 and 6.15 present predictions of the concentration as a function of time in the upper and lower parts of the tank respectively using the Simple impeller model, TVD scheme and the Reynolds Stress/Scalar Flux turbulence model. Comparing figures 6.14 and 6.15 with 6.12 and 6.13 respectively it is noted that in the upper part of the tank the general predicted levels of concentration has been lowered and the reverse applies in the lower part of the tank. In addition in the upper part of the tank, figure 6.14, the peaks in the concentration level have been "narrowed" and show better agreement with the experimental data compared to figures 6.12 and 6.4. Table 6.7 show the time at which the scalar is first detected at the measurements points. In the upper and lower parts of the tank the predicted first arrival times at all measurement points in all planes are shorter than those presented in table 6.6.

| Planes | Points | | | | | | | |
|---|---|---|---|---|---|---|---|---|
| | A | B | C | D | G | H | I | J |
| 0° | 0.2 | 0.48 | 0.25 | 0.25 | 0.5 | 0.7 | 0.55 | 0.55 |
| 90° | 0.15 | 0.2 | 0.45 | 0.6 | 0.5 | 0.6 | 0.5 | 0.55 |
| 180° | 0.3 | 0.45 | 0.46 | 0.5 | 0.5 | 0.7 | 0.6 | 0.6 |
| 270° | 0.1 | 0.4 | 0.4 | 0.6 | 0.5 | 0.7 | 0.7 | 0.5 |

Table 6.7. Predicted concentration first arrival time (seconds) at measurement points above and below the impeller.

Comparing figures 6.14 and 6.15 with 6.10 and 6.11 respectively it is noted that in the upper part of the tank the concentration levels at point B in the 0° and 90° planes, figure 6.10, are higher and show better agreement with the experimental data compared to figure 6.14. Point A in the 90° plane, figure 6.10, again show better agreement with the experimental data compared with figure 6.14. In the lower part of the tank the concentration level at point J, figure 6.11, is higher and agree better with the experimental data in the 90°, 180° and 270° planes compared with figure 6.15. The predicted first arrival times, figures 6.14 and 6.15, at all measurement points in all planes are longer and agree better with the experimental data first arrival times than those of figures 6.10 and 6.11.

The fully mixed time, figures 6.14 and 6.15, is in excess of 6.2 seconds which exceeds the experimental data by 0.5 seconds and that in figures 6.12 and 6.13 by 4.3 seconds. However, the fully mixed concentration time, figures 6.10 and 6.11, is in excess of 4.5 seconds which is shorter than the measured data by 1.2 seconds.

## 6.5 Computational Effort

The computations carried out for the different combinations shown in table 6.2 and discussed above were computed on a DEC Alpha workstation. Table 6.8 presents the scalar CPU time per iteration, in seconds, of the predictions shown in figures 6.6-6.15.

| Impeller model | Differencing scheme | Turbulence model | CPU time/iteration (seconds) |
|---|---|---|---|
| Drag | Hybrid | $\kappa$ - $\varepsilon$ | 9.5 |
| | | RS/SF | 92.8 |
| | TVD | $\kappa$ - $\varepsilon$ | 12.5 |
| Dynamic | TVD | $\kappa$ - $\varepsilon$ | 154.7 |
| Simple | TVD | RS/SF | 122.1 |

Table 6.8. Scalar CPU time required to complete one iteration (refer to footnote on page 69).

| Impeller models | Turbulence models | Velocity variables | Scalar variables | No of transport equations |
|---|---|---|---|---|
| Drag | $\kappa$ - $\varepsilon$ | ---------- | $\Phi$, $\overline{\phi^2}$ | 2 |
| | RS/SF | ---------- | $\Phi$, $\overline{\phi^2}$, $\overline{u\phi}$, $\overline{v\phi}$, $\overline{w\phi}$ | 5 |
| Dynamic | $\kappa$ - $\varepsilon$ | U, V, W, $\delta$P, $\kappa$, $\varepsilon$ | $\Phi$, $\overline{\phi^2}$ | 8 |
| Simple | RS/SF | ---------- | $\Phi$, $\overline{\phi^2}$, $\overline{u\phi}$, $\overline{v\phi}$, $\overline{w\phi}$ | 5 |

Table 6.9. Scalar transport equations solved.

Table 6.8 shows that using the Reynolds Stress/Scalar Flux turbulence model takes longer CPU time to complete one iteration than the $\kappa$ - $\varepsilon$ turbulence model. For example, it took 92.8 seconds of CPU time to complete one iteration when using the Drag impeller model,

Hybrid differencing and the Reynolds Stress/Scalar Flux turbulence model. whereas it only took 9.5 seconds of CPU time when using the same impeller model and differencing scheme but with the $\kappa$ - $\varepsilon$ turbulence model. The increase in CPU time is expected due to the additional 3 equations being solved by the Reynolds Stress/Scalar Flux transport equations, table 6.9, and to the increase complexity of the Reynolds Stress/Scalar Flux transport equations compared with the $\kappa$ - $\varepsilon$ turbulence model.

Table 6.8 shows that the TVD scheme uses 24 percent more CPU time to complete one iteration than the Hybrid differencing due to the additional contributions to the convection terms containing flux limiters which were added to the source term. For example, the TVD scheme with the Drag impeller model and $\kappa$ - $\varepsilon$ turbulence model took 3.0 seconds more CPU time than the Hybrid differencing with the same impeller model and turbulence model. The ratio of CPU time between the TVD and Hybrid differencing schemes is constant at 1.316.

The Dynamic impeller model with TVD scheme and $\kappa$ - $\varepsilon$ turbulence model used 21 percent more CPU time per iteration than the Simple impeller model with TVD scheme and Reynolds Stress/Scalar Flux turbulence model, table 6.8, because the Dynamic impeller model uses an additional 3 equations as indicated by table 6.9 compared with the Simple impeller model.

Finally the Dynamic impeller model with TVD scheme and $\kappa$ - $\varepsilon$ turbulence model took 154.7 seconds of CPU time per one iteration, whereas the Drag impeller model with again the TVD scheme and $\kappa$ - $\varepsilon$ turbulence model only took 12.5 seconds of CPU time. This great CPU time difference between the Dynamic and Drag impeller models is due to the additional 6 equations which were used by the Dynamic impeller model.

## 6.6 Summary

The Rushton impeller, described in chapter 5, generates a radial jet stream and two ring vortices, one above and one below the impeller. During mixing, the dye added to the top of the tank will be transported by the upper ring vortex to the impeller region and after discharge in the radial direction part of the dye will be transported by the upper and lower ring vortex to the top and bottom of the tank a number of times respectively until a fully mixed concentration is reached. The flow through the impeller and discharge stream limits the transport of the scalar between the upper and lower regions of the tank. This indicates the importance of modelling the impeller region in any mixing process taking place in a stirred tank which in turn effects the accuracy of the flow field, mixing concentration levels and mixing time.

In this chapter the calculations of the scalar mixing in a cylindrical tank stirred by a single Rushton impeller were carried out using the Simple, Drag and Dynamic impeller models described in sections 5.4.1, 5.4.2 and 5.4.3 respectively with the following combinations of differencing scheme and turbulence model:

i) Hybrid scheme and $\kappa$ - $\varepsilon$ turbulence model.
ii) Hybrid scheme and Reynolds Stress/Scalar Flux turbulence model.
iii) TVD scheme and $\kappa$ - $\varepsilon$ turbulence model.
iv) TVD scheme and Reynolds Stress/Scalar Flux turbulence model.

The flow field was calculated in a 180° sector using 55x29x51 nodes and the scalar mixing field in the full 360° using a mesh of 55x29x100 nodes. A time dependent calculation was started at time, t = 0, by setting the value of the scalar at all points in the tank to zero and then marching forward in time. The injection of the scalar into the vessel was modelled by setting the scalar value to unity in the computational cell nearest to the addition point over the period of the injection time, 50ms. The predictions of the concentration as a function of time were then compared with experimental data obtained by Distelhoff et al(1996).

The use of TVD scheme, figures 6.8 and 6.9, has improved the performance of the predictions obtained in the upper and lower parts of the tank respectively bringing a closer agreement with the experimental data compared with the Hybrid differencing, figures 6.6 and 6.7. For example, in the upper part of the tank, the TVD scheme has increased the concentration levels, > 5, recorded at point A in all planes as opposed to only in the 0° and 180° planes when the Hybrid differencing is used. However, the TVD scheme has increased the overall mixing time by 2 seconds compared with the Hybrid differencing, 10 seconds, bringing a greater disagreement with the experimental measurement, 5.7 seconds.

The effects of the Dynamic impeller model are revealed when figures 6.10 and 6.11 are compared with figures 6.8 and 6.9 respectively. The Dynamic impeller model, figure 6.10, has decreased the levels of concentration and "narrowed" the peaks and shows better agreement with the experimental data shown in figure 6.4. The first arrival times at all measurement points in all planes are sooner and more in line with the experimental data than those of figures 6.8 and 6.9. The predictions using the Dynamic impeller model have reached the fully mixed state after only 4.5 seconds, as opposed to 12 seconds obtained using the Drag impeller model.

The use of the Simple impeller model with TVD scheme and Reynolds Stress/Scalar Flux turbulence model, figures 6.14 and 6.15, has narrowed the peaks in the upper part of the tank and shows better agreement with the experimental data compared with the predictions obtained in the upper part of the tank using the Drag impeller model, Hybrid differencing and Reynolds Stress/Scalar Flux turbulence model, figure 6.12. In addition the first arrival time in the upper and lower parts of the tank at all measurement points in all planes, figures 6.14 and 6.15, are sooner and agree more closely with the experimental data than those of figures 6.12 and 6.13. The fully mixed concentration time, figures 6.14 and 6.15, exceeds the experimental data by only 0.5 seconds, whereas the fully mixed time shown in figures 6.12 and 6.13 exceeds the experimental data by 4.3 seconds.

To summarise, the first arrival time and the fully mixed concentration time were better represented by the Simple impeller model with the TVD scheme and Reynolds Stress/Scalar Flux turbulence model, whereas the peaks levels were better represented by the Dynamic impeller model with TVD scheme and $\kappa$ - $\varepsilon$ turbulence model.

The sources of the differences between the predictions and the measurements can be identified as numerical and modelling errors. Numerical errors arise from inaccurate representation of the geometry, the impeller and discretisation errors (both in time and space). Modelling errors arise in both the modelling of the turbulent flow and mixing processes. The prediction of scalar mixing is made more complex because of the dependence of the scalar mixing processes on the flow field so that errors in the velocity field "feed" through to the scalar mixing calculation. It is fortunate that in the stirred tanks considered here the flow field is not dependent on the scalar field.

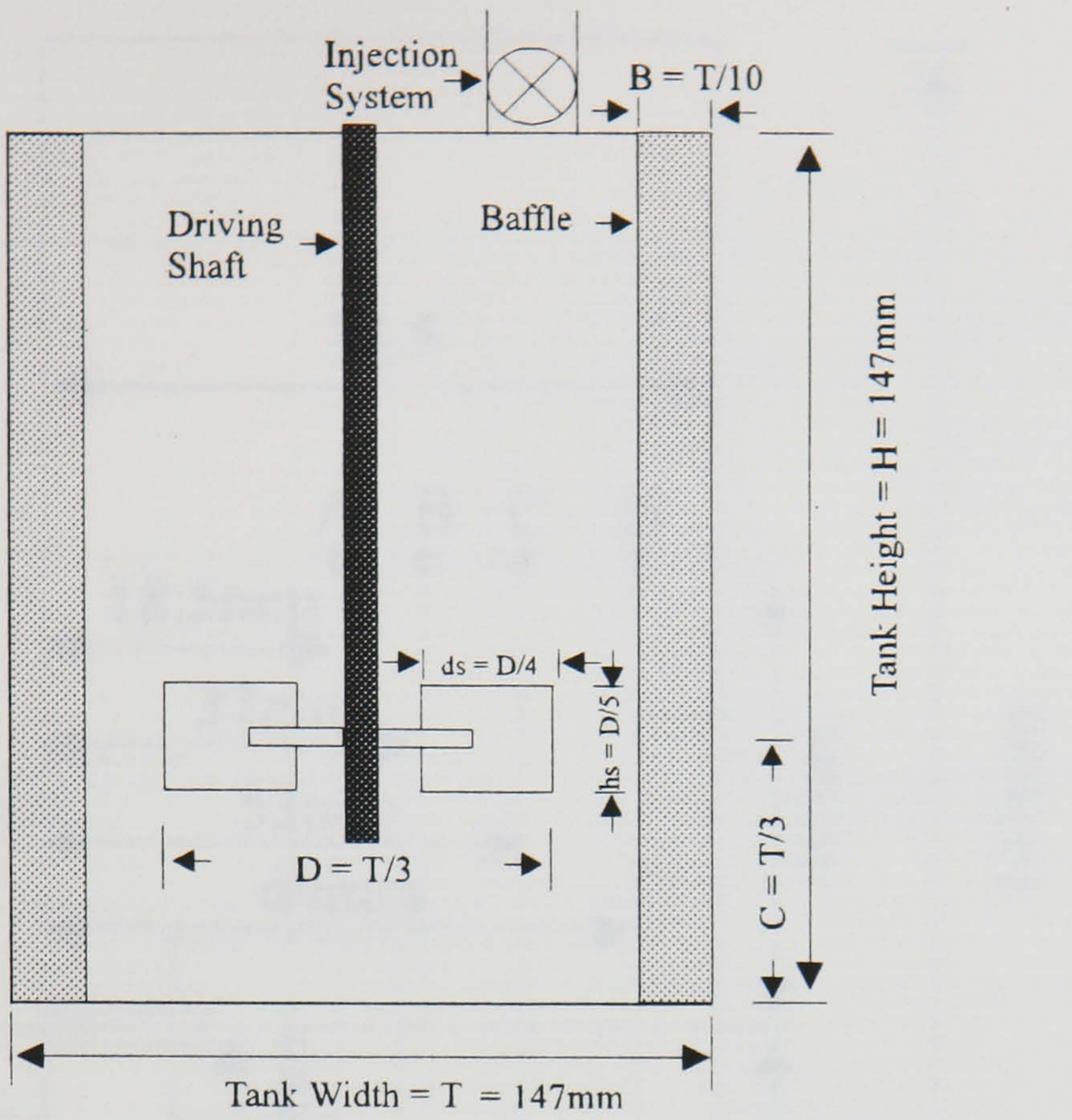



Figure.6.1. Cylindrical tank with single Rushton turbine impeller and injection system.

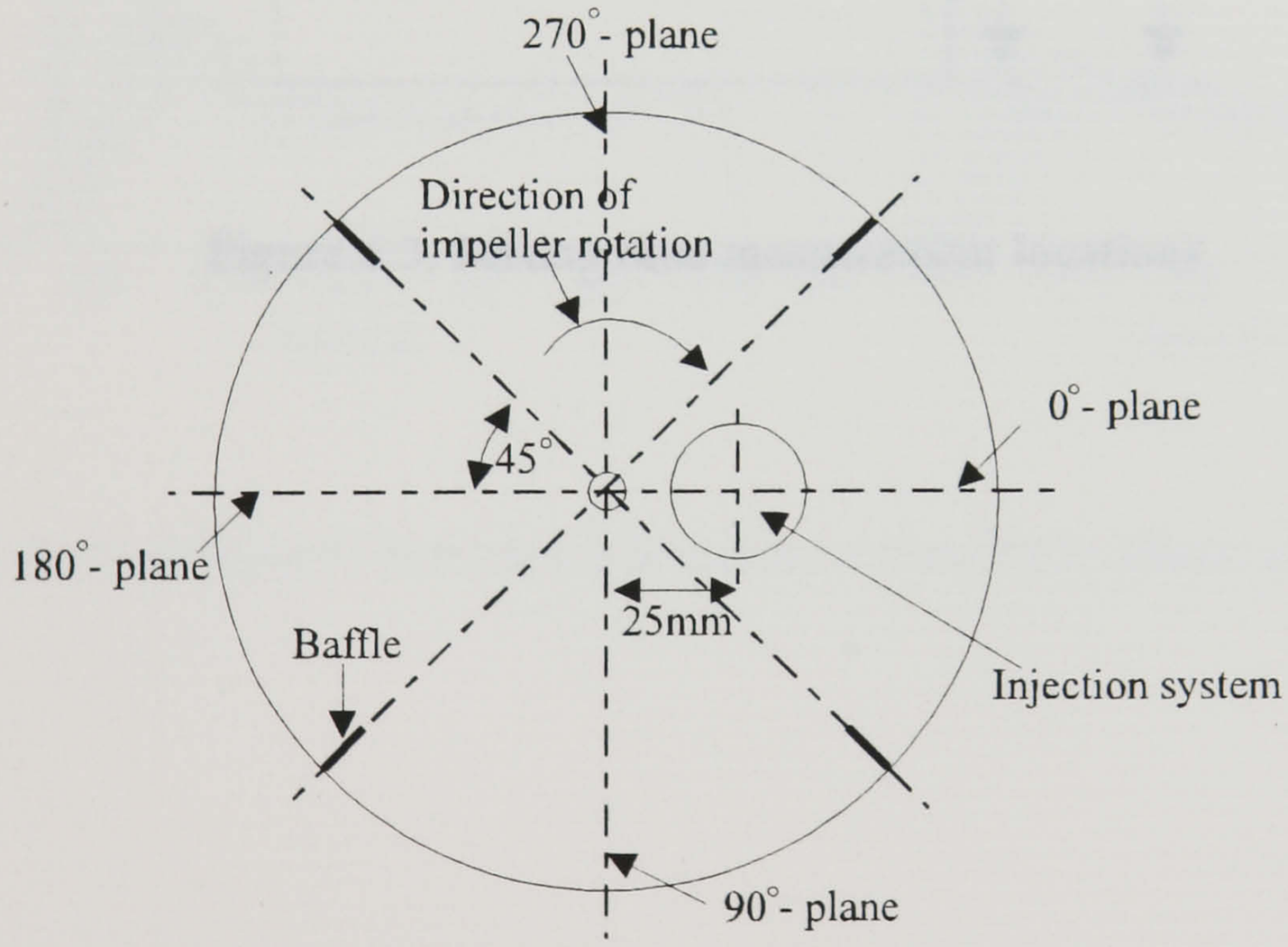



Figure.6.2. Top view of cylindrical tank with injection system.

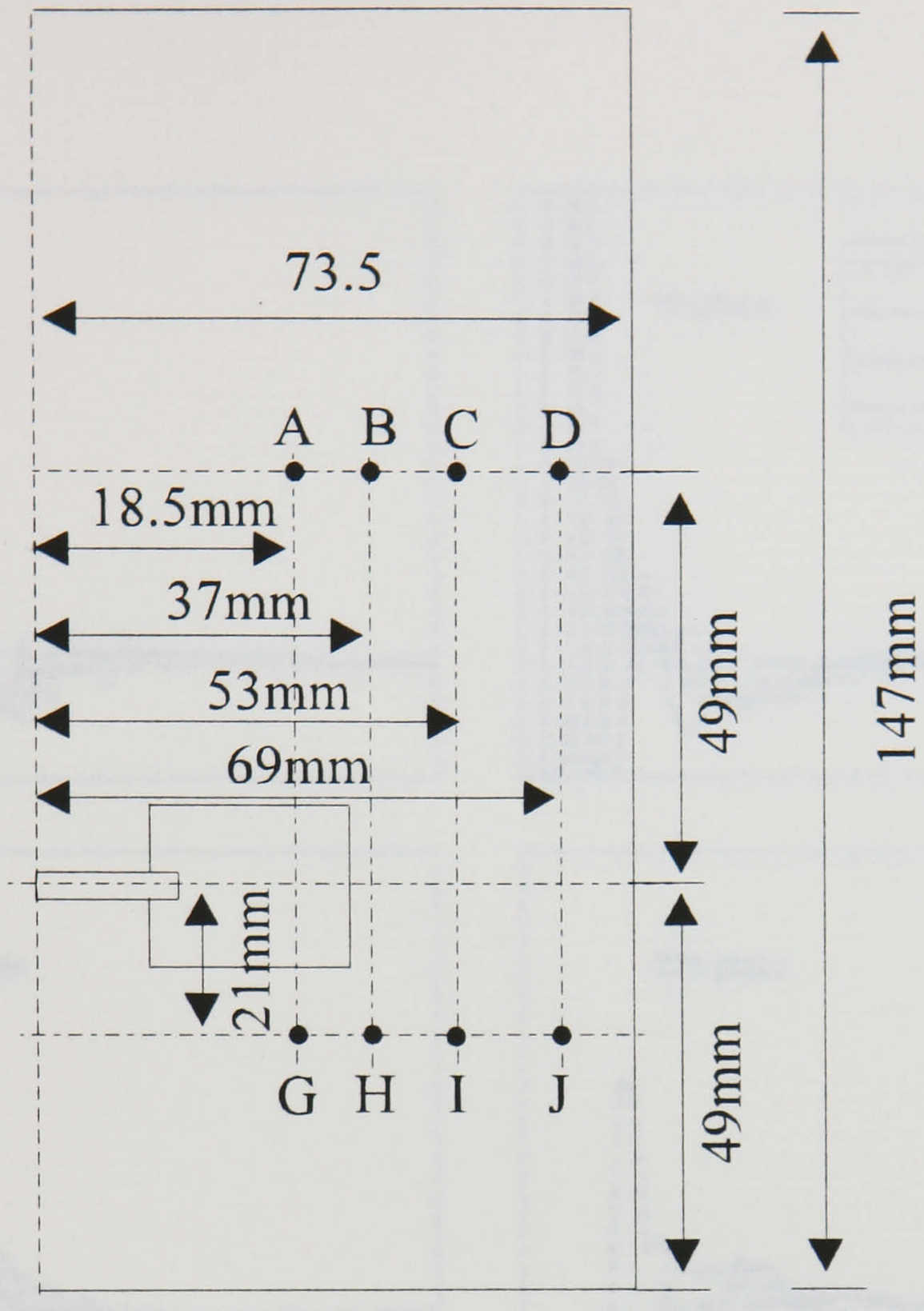
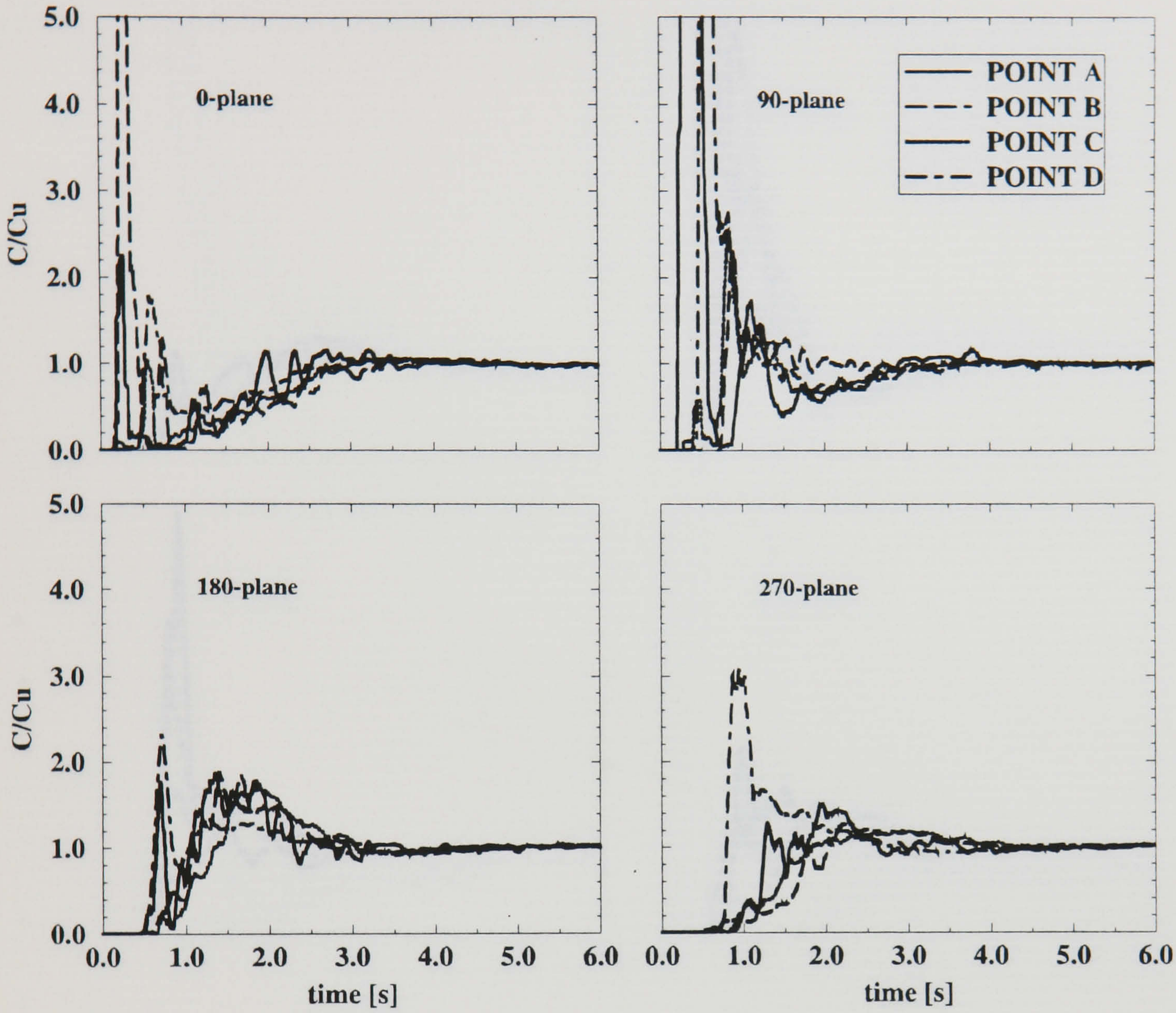



Figure.6.3. Mixing time measurement locations.




Figiure.6.4. Experimental data for the Rushton turbine for locations above the impeller.

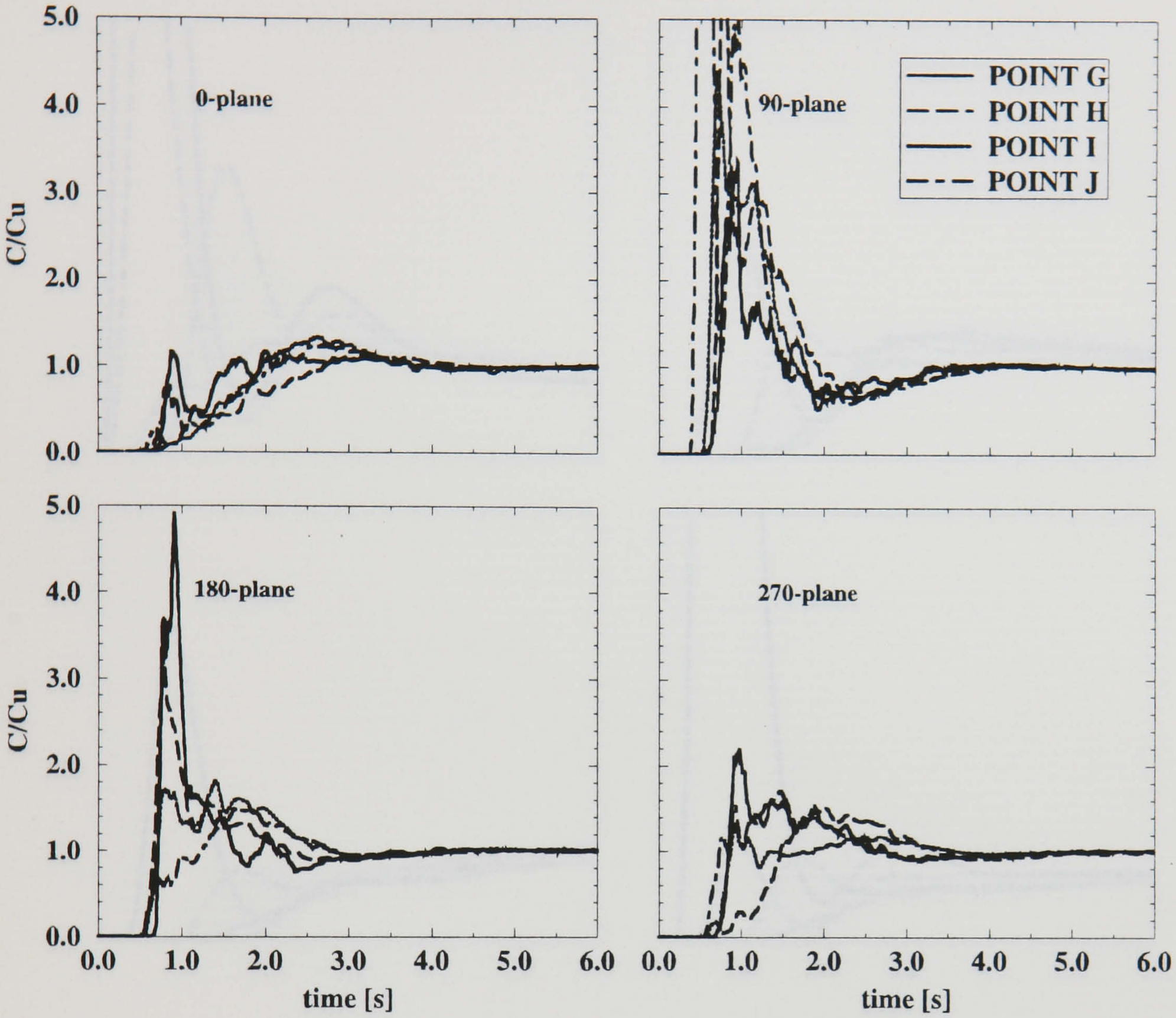



Figure.6.5. Experimental data for the Rushton turbine for locations below the impeller.

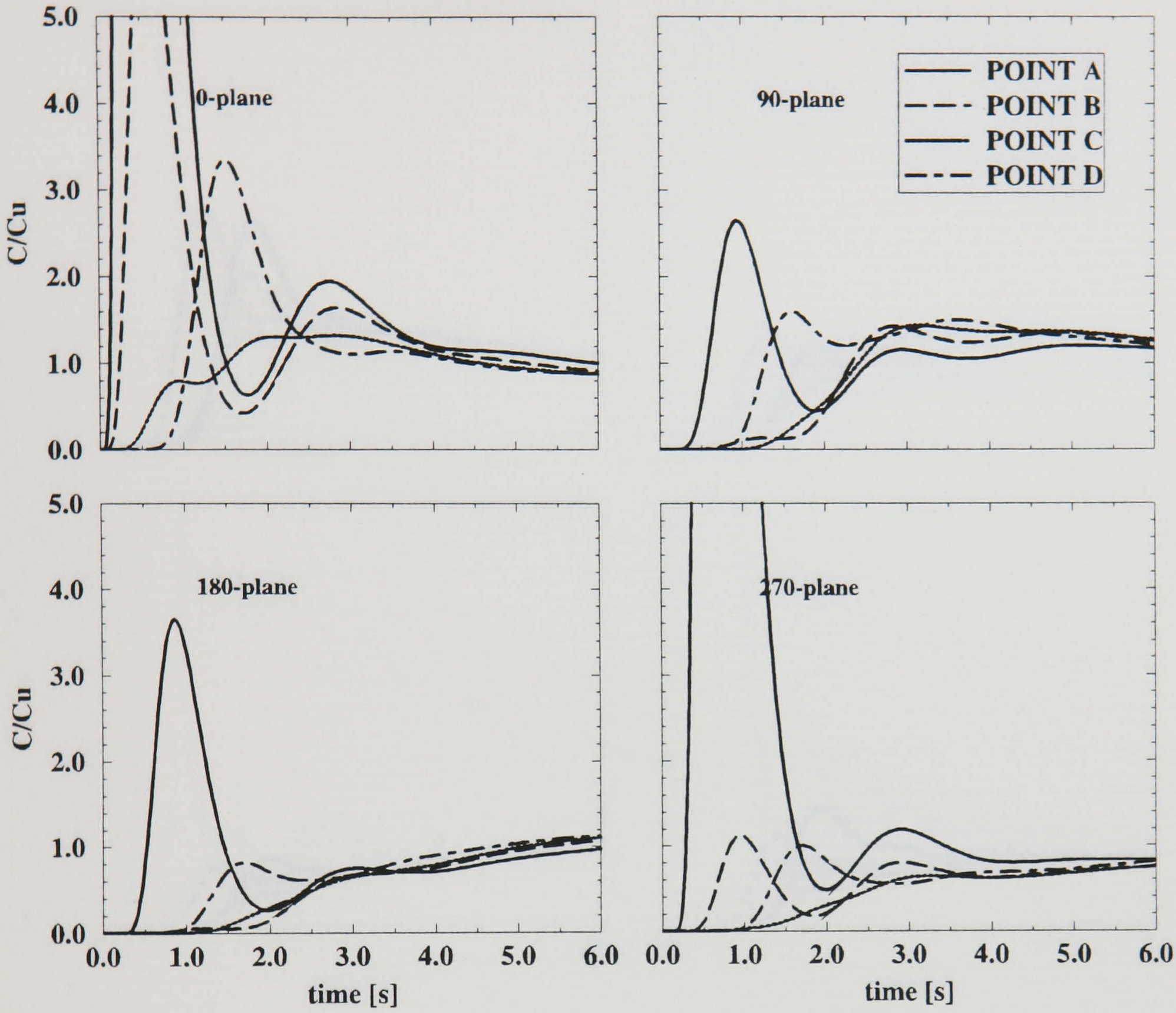



Figure.6.6. Predictions for the Rushton turbine for locations above the impeller obtained using the Drag impeller model with Hybrid scheme and $\kappa$ - $\varepsilon$ turbulence model.

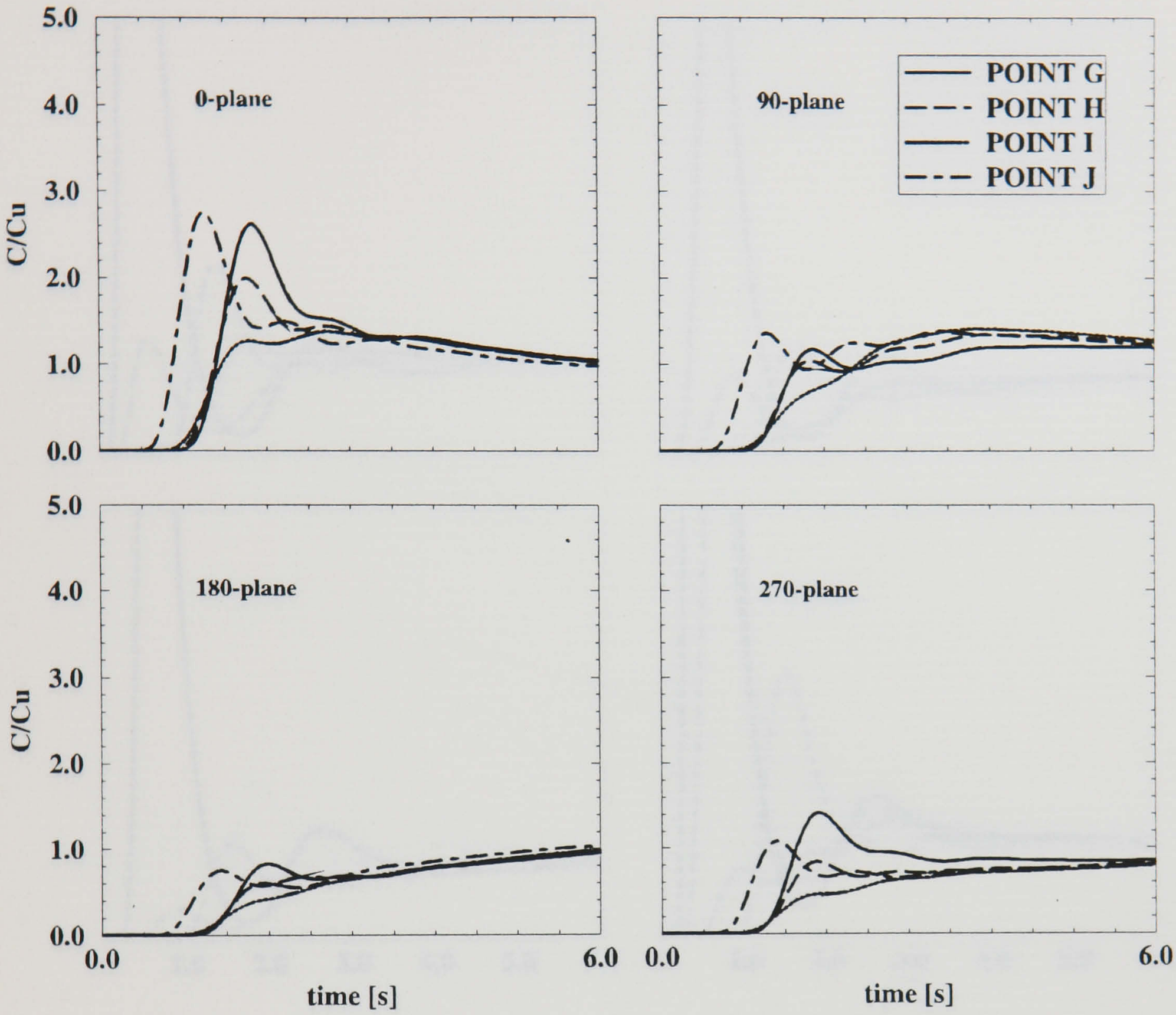



Figure.6.7. Predictions for the Rushton turbine for locations below the impeller obtained using the Drag impeller model with Hybrid scheme and $\kappa$ - $\varepsilon$ turbulence model.

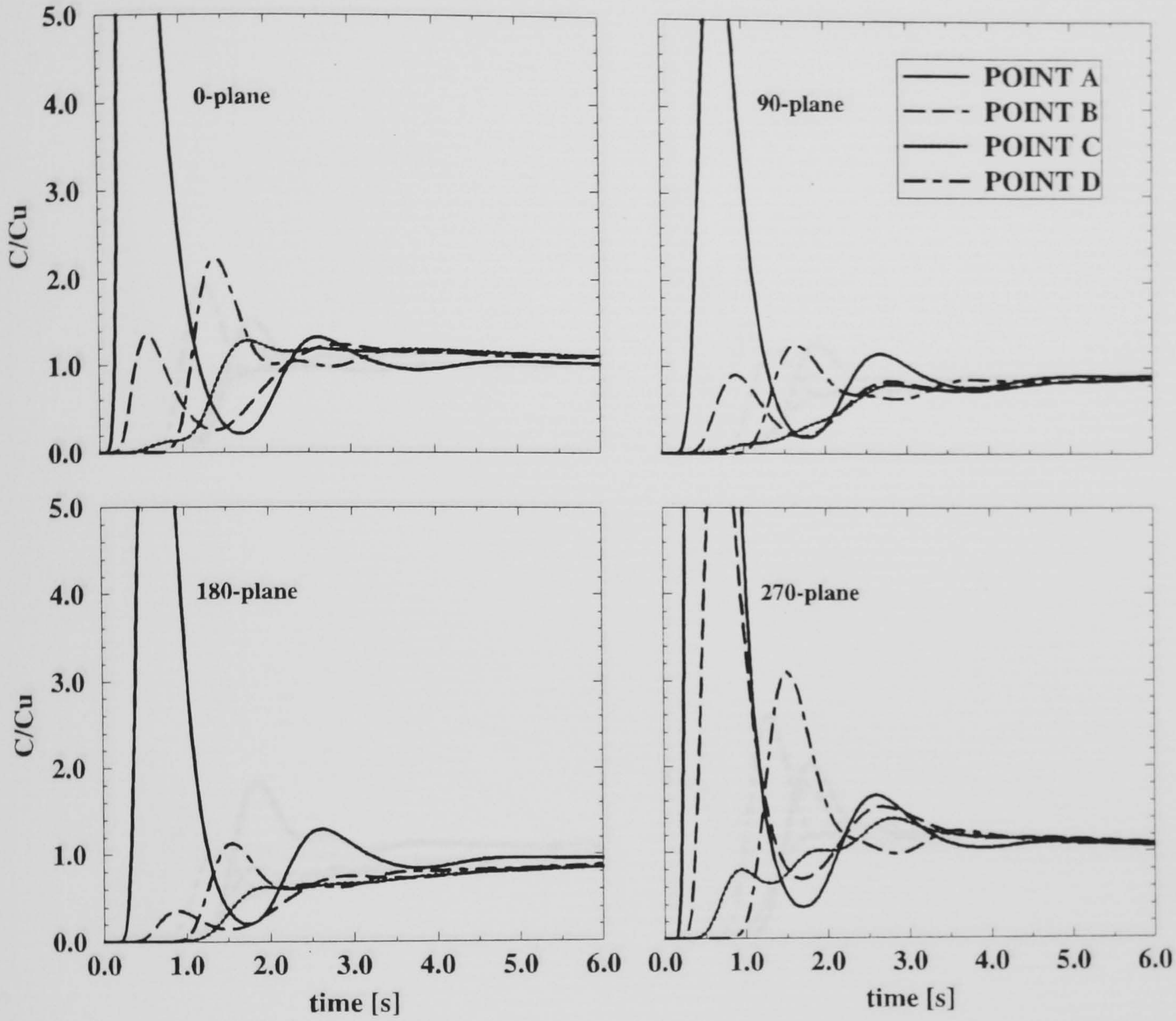



Figure.6.8. Predictions for the Rushton turbine for locations above the impeller obtained using the Drag impeller model with TVD scheme and $\kappa$ - $\varepsilon$ turbulence model.

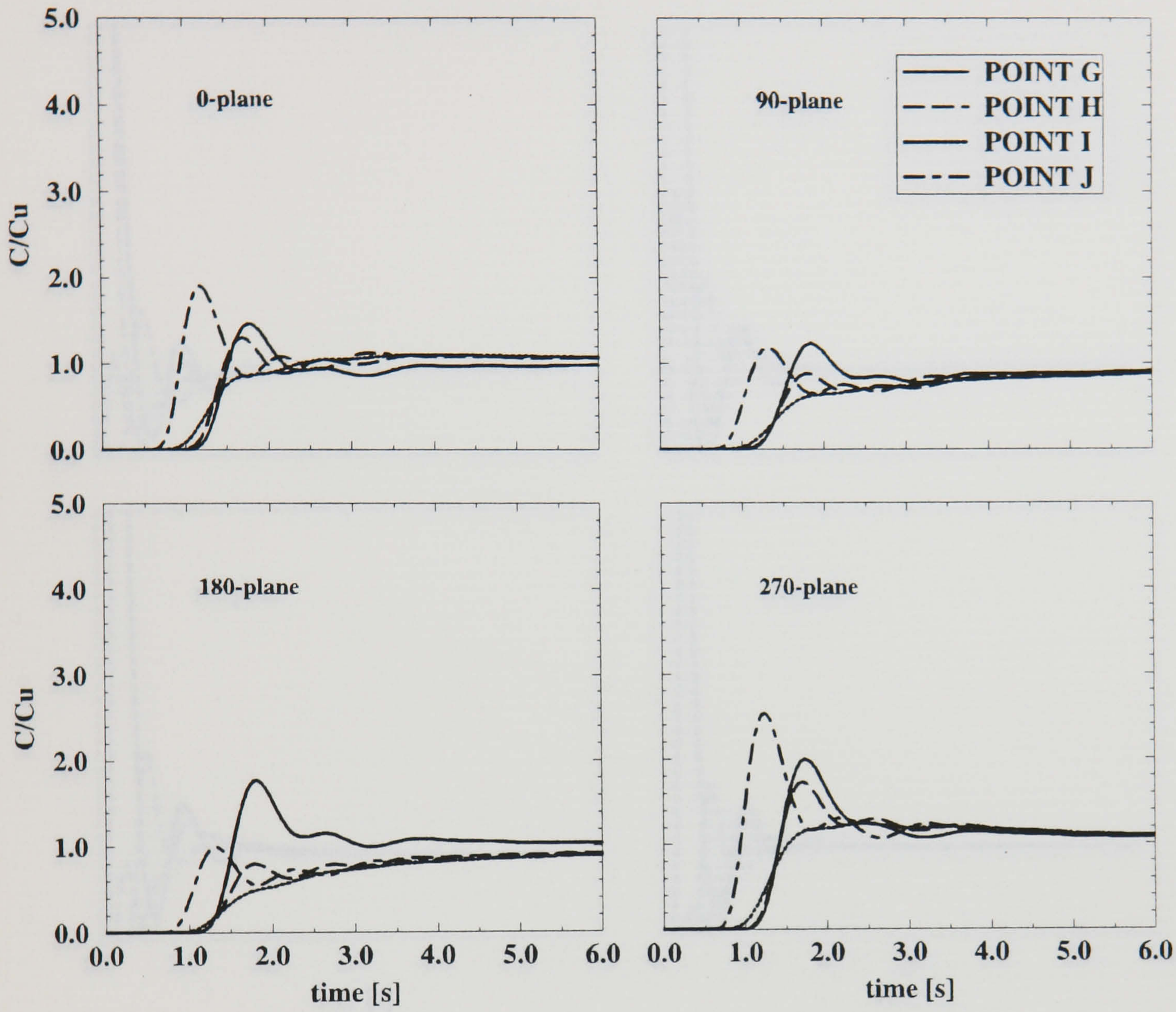



Figure.6.9. Predictions for the Rushton turbine for locations below the impeller obtained using the Drag impeller model with TVD scheme and $\kappa$ - $\varepsilon$ turbulence model.

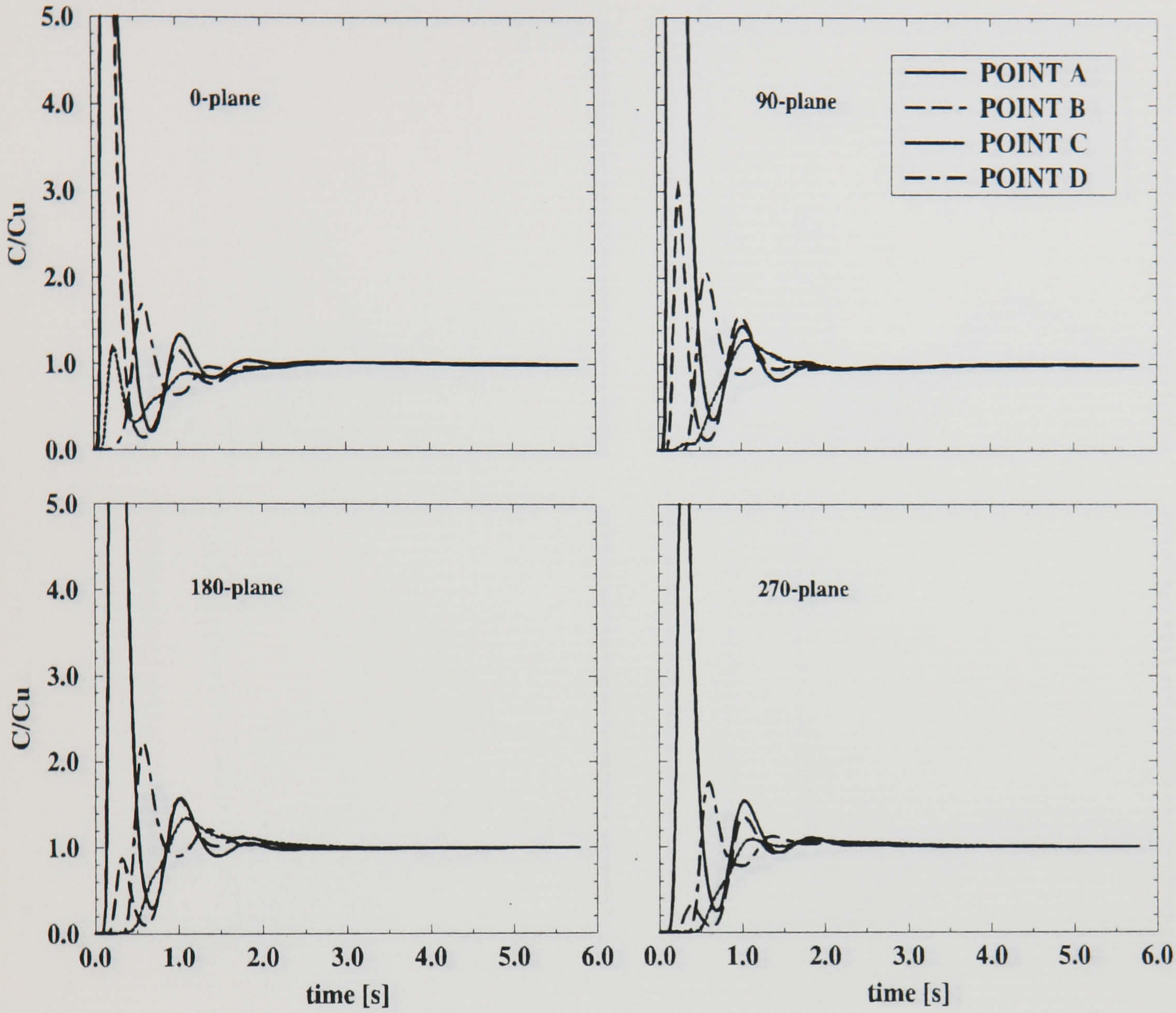



Figure.6.10. Predictions for the Rushton turbine for locations above the impeller obtained using the Dynamic impeller model with TVD scheme and $\kappa$ - $\varepsilon$ turbulence model.

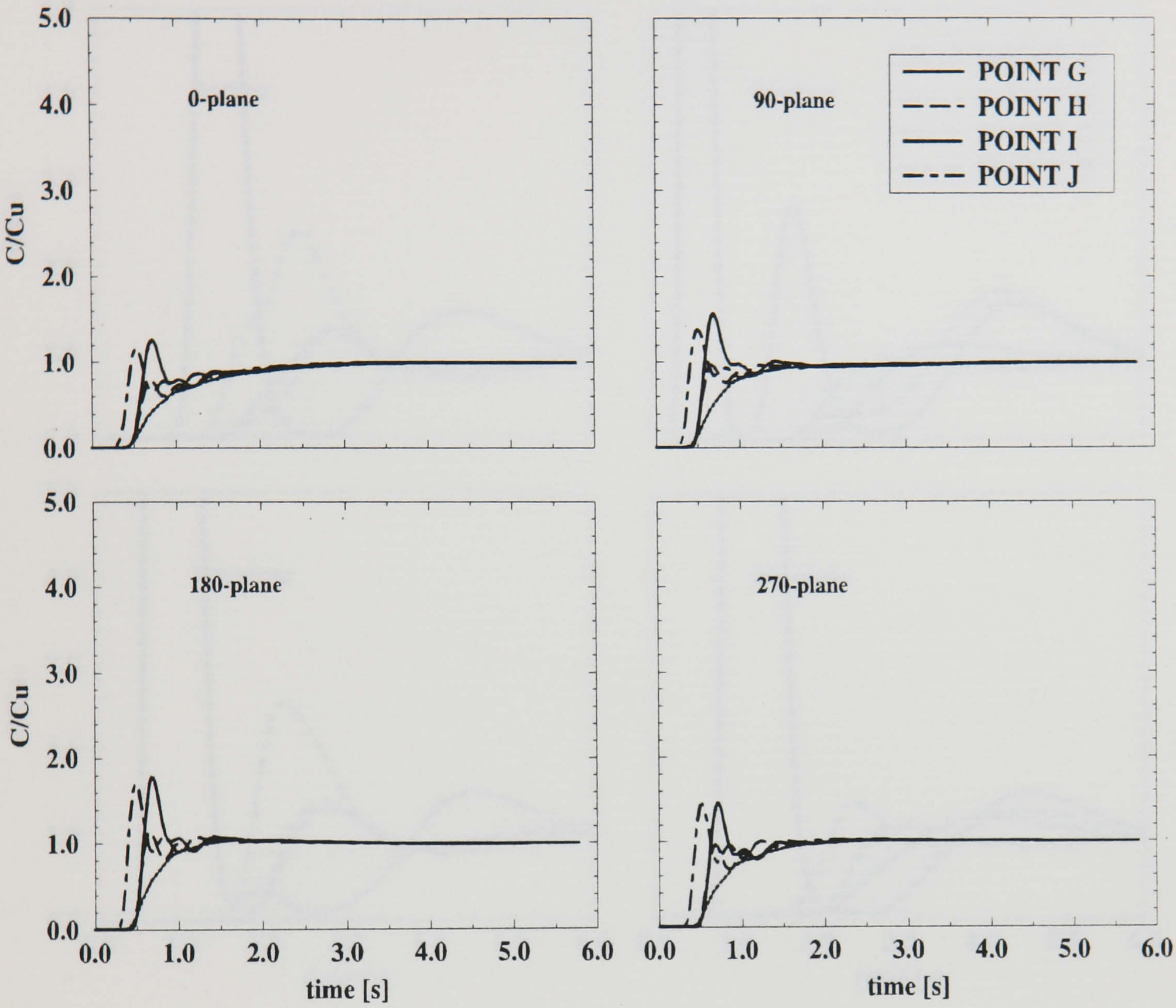



Figure.6.11. Predictions for the Rushton turbine for locations below the impeller obtained using the Dynamic impeller model with TVD scheme and $\kappa$ - $\varepsilon$ turbulence model.

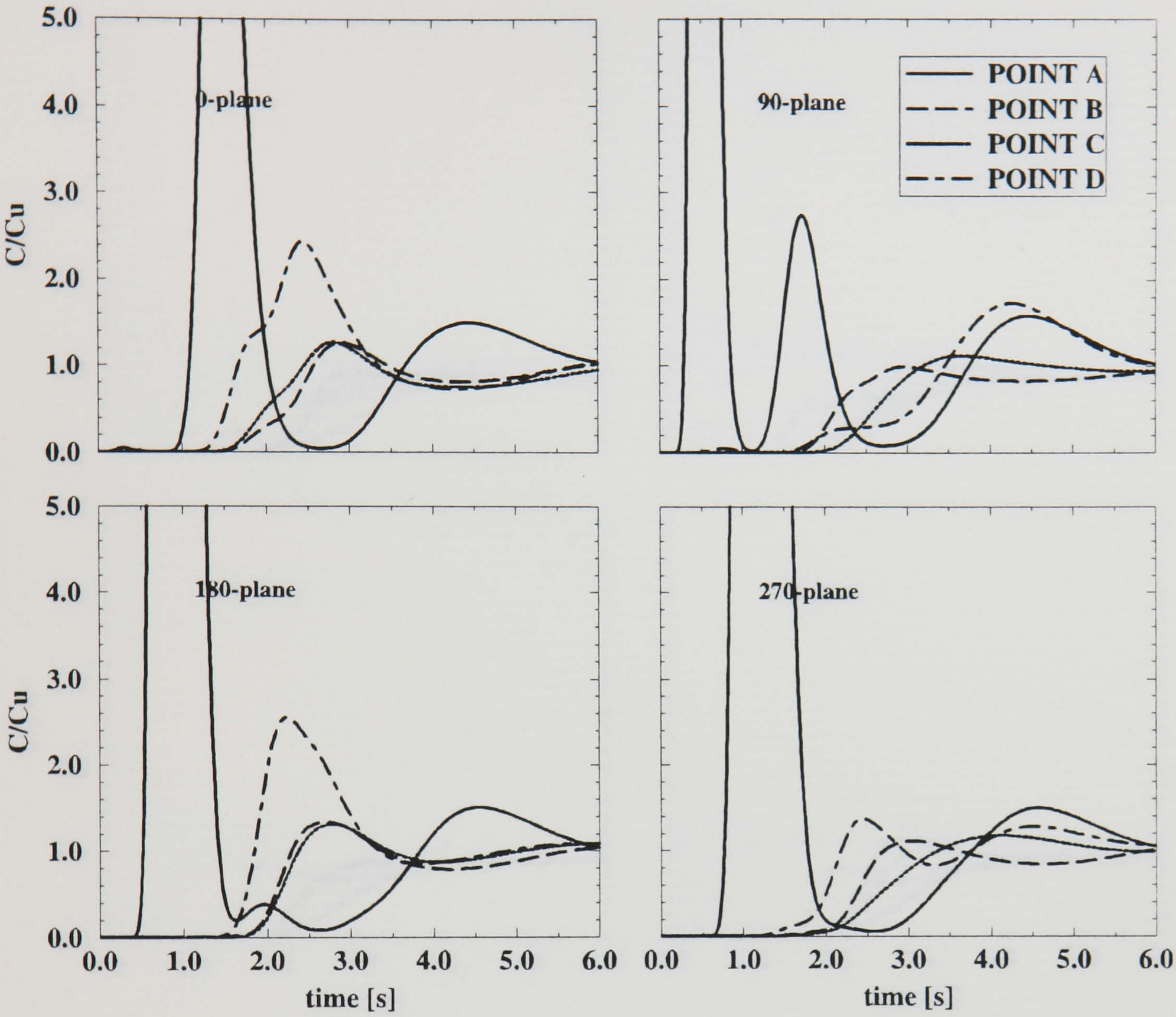



Figure.6.12. Predictions for the Rushton turbine for locations above the impeller obtained using the Drag impeller model with Hybrid differencing and Reynolds Stress/Scalar Flux turbulence model.

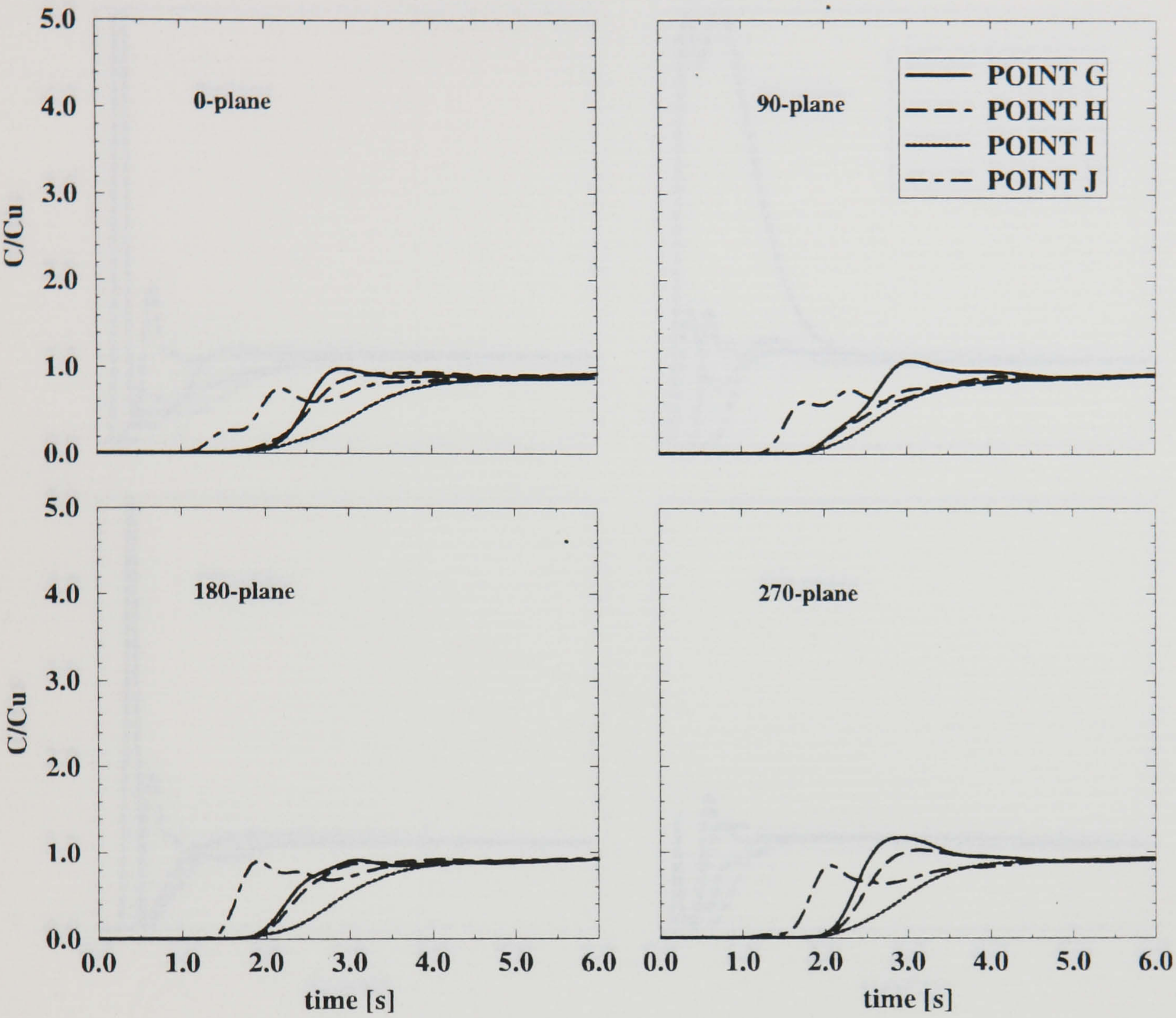



Figure.6.13. Predictions for the Rushton turbine for locations below the impeller obtained using the Drag impeller model with Hybrid scheme and Reynolds Stress/Scalar Flux turbulence model.

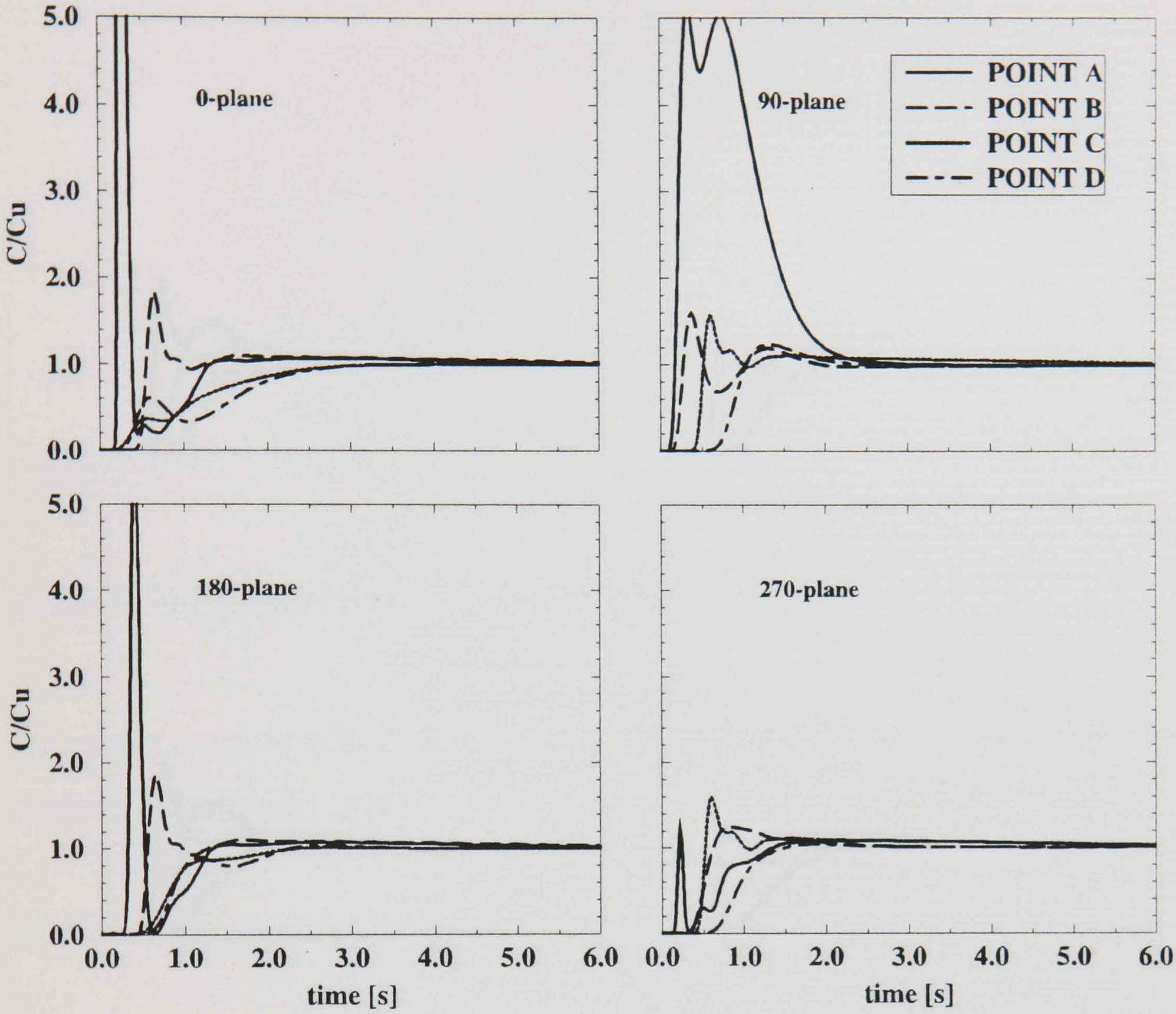



Figure.6.14. Predictions for the Rushton turbine for locations above the impeller obtained using the Simple impeller model with TVD scheme and Reynolds Stress/Scalar Flux turbulence model.

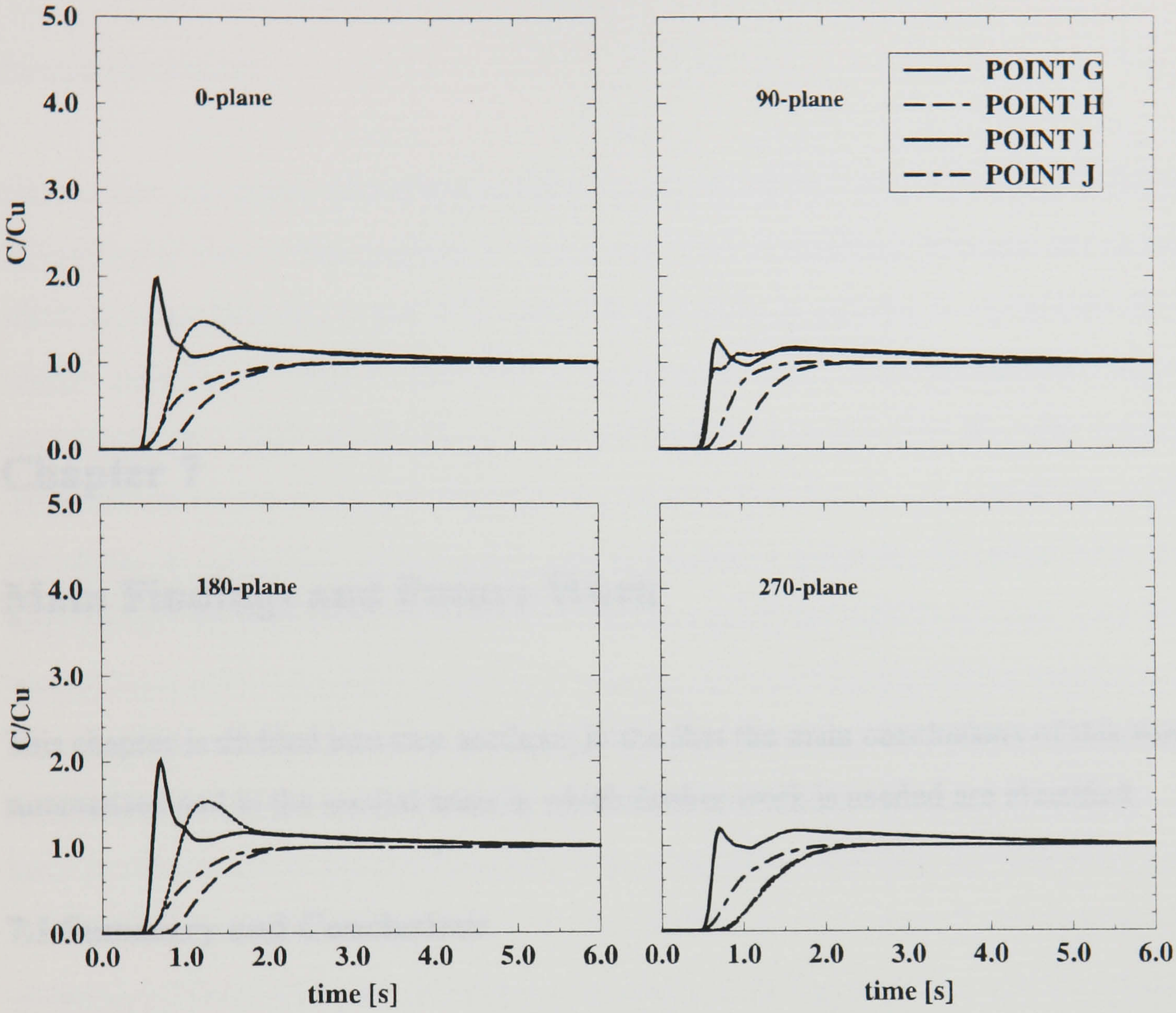



Figure.6.15. Predictions for the Rushton turbine for locations below the impeller obtained using the Simple impeller model with TVD scheme and Reynolds Stress/Scalar Flux turbulence model.

# Chapter 7

# Main Findings and Future Work

This chapter is divided into two sections; in the first the main conclusions of this work are summarised and in the second areas in which further work is needed are identified.

## 7.1 Summary and Conclusions

The aim of this work was to predict the flow and mixing processes in a stirred tank and the method selected was the finite difference solution of the Navier-Stokes and associated equations with particular emphasis placed on using accurate discretisation schemes and turbulence models.

*Discretisation Schemes*

Hybrid, Linear Upwind and Total Variation Diminishing (TVD) differencing schemes were tested for their accuracy and boundedness using simple two-dimensional convection-diffusion problems. The numerical results showed that the Linear Upwind and TVD

differencing schemes were more accurate than the Hybrid differencing scheme but that the Linear Upwind exhibited boundedness problems and as a result the TVD scheme was selected for further work.

*Turbulence Models*

The sudden expansion of swirling coaxial water jets studied experimentally by Roback et al(1983) provided a test problem to carry out a full comparison between the predictions obtained using the Hybrid and TVD differencing schemes and the $\kappa$ - $\varepsilon$ and the Reynolds Stress turbulence models and the experimental data. The predictions were also investigated for grid independency. The predictions showed that the grid independent solutions obtained using either differencing scheme and the $\kappa$ - $\varepsilon$ turbulence model are the same, as expected, whereas the grid independent solutions obtained with the two differencing schemes and the Reynolds Stress turbulence model are not, and this was unexpected, and it is possible, although unlikely, that a grid independent solution was not reached. The results also showed that the Reynolds Stress turbulence model was able to improve the physical behaviour of the predictions and in particular both turbulence models have predicted the experimental anisotropic turbulence, although the literature indicates that the $\kappa$ - $\varepsilon$ turbulence model is not always able to correctly predict anisotropic turbulence. The predictions of the mean velocities, axial normal stress and $\overline{uw}$ obtained by the Reynolds Stress turbulence model (using the TVD scheme) are better predicted than those obtained by the $\kappa$ - $\varepsilon$ turbulence model, whereas the predictions of the radial and angular normal stresses and $\overline{uv}$ were better predicted by the $\kappa$ - $\varepsilon$ turbulence model indicating that the balance of the predictions is in favour of the Reynolds Stress turbulence model. Finally, the predictions showed that the TVD scheme improved the numerical accuracy of the calculations and enabled grid independent solutions to be obtained on smaller computational meshes leading to less CPU time.

Three-dimensional fluid flow simulations were carried out for a cylindrical fully baffled tank stirred by one or two Rushton impellers to compare the accuracy of three impeller models (Simple, Drag and Dynamic), two differencing schemes (Hybrid and TVD) and two turbulence model closures ($\kappa$ - $\varepsilon$ and Reynolds Stress). Comparisons were made with the experimental data of Lee(1995) and the effect of refining the mesh was studied.

To investigate the grid independency of the solutions, the grid was refined in each direction separately. Comparisons between the refined and unrefined predictions showed very small differences and it is possible therefore that a grid independent solution has been reached which ideally should be confirmed by repeating the calculations on a mesh refined in all three directions simultaneously.

The differences between the predictions of the single impeller obtained using the Simple and Dynamic impeller models were small irrespective of the differencing scheme or turbulence model used and generally agreed more with the experimental data than the predictions obtained using the Drag impeller model; except very close to the impeller, where the predictions of the mean tangential velocity obtained using the Drag impeller model were the closest to the experimental data. The experimental data of Lee shows large variations in the circumferential direction especially in the mean axial velocity adjacent to the upper region of the impeller, whereas the predictions do not show any variation. As a result of this, while the predictions obtained in the plane of the baffles agreed well with the experimental data, especially those of the Simple and Dynamic impeller models, those obtained mid-way between the baffles do not agree well with the experimental data.

The major differences between the predictions of the double impeller were in general located adjacent to the impellers and where the two impeller streams merged. Close to the impellers the choice of the impeller model again largely influenced the behaviour of the

predictions, as was the case for the single impeller. The use of the Dynamic impeller model results in the best agreement with the experimental data except in the plane between the baffles where the mean tangential velocity were best predicted by the Drag impeller model. In the region where the impeller streams merge large levels of both circumferential velocity and turbulence are produced. As a result the predictions based on the Reynolds Stress turbulence model and the TVD scheme produced the best agreement with the experimental data. Overall, therefore, it is seen that the combination of the Dynamic impeller model and TVD scheme with the Reynolds Stress turbulence model in general produces better agreement between the predictions and the experimental data.

Finally, in case of the single impeller, the predictions were effected mainly by the impeller model which is expected because the influence of the impeller determines the whole flow field. The predictions obtained using the Simple and Dynamic impeller models in most cases were closer to the experimental data compared with the Drag impeller model. The choice of differencing scheme and turbulence model made little, compared to the choice of impeller model, impact in the agreement between the experimental data and the predictions. In the double impeller case, the flow field is determined by not only the impeller but the interaction of the impeller streams which combine to generate large circumferential velocities and high levels of turbulence. Around the impeller, as in the single impeller case the impeller model is important, whereas mid-way between the impellers the choice of differencing scheme and turbulence model is more important. As a result the predictions obtained using the Dynamic impeller model with the TVD scheme and Reynolds Stress turbulence closure agree the most with the experimental data.

*Mixing*

Three-dimensional calculation of mixing in a batch operated fully baffled cylindrical tank stirred by single Rushton impeller was carried out using again three impeller models (Simple, Drag and Dynamic), two differencing schemes (Hybrid and TVD) and two turbulence model closures ($\kappa$ - $\varepsilon$ and Reynolds stress/Scalar Flux). The predictions of the

flow fields were influenced by the choice of the impeller model while the scalar mixing calculations depended on the choice of turbulence model and differencing scheme. As a result, the predictions obtained using the following two combinations were closest to the experimental data of Distelhoff et al(1996): first, the Simple impeller model with TVD scheme and Reynolds Stress/Scalar Flux turbulence model, and second, the Dynamic impeller model with TVD scheme and $\kappa$ - $\varepsilon$ turbulence model. The first combination was better at reproducing the first arrival time of the dye at a point and the final mixing time, whereas, the second combination predicted the peak values more accurately. However, it should be pointed out that the general agreement between the predictions and the experimental data is poor.

## 7.2 Suggestions for Future Work

The differences between the predictions and measurements of the fluid flow and mixing in the stirred tank can be attributed to numerical and modelling errors. Numerical errors result from discretisation errors (in both time and space) and the impeller model. Modelling errors occur during the modelling of the turbulence processes in both the velocity and scalar fields. As a result three areas for further work are suggested, namely, grid refinement, impeller modelling and the modelling of scalar mixing in a continuously stirred tank.

First, refining the grid in each direction separately in the stirred tank calculations showed very small differences between the refined and unrefined predictions and it is possible that a grid independent solution has been reached, but this should be confirmed by repeating the calculations on a mesh refined in all three directions simultaneously. This approach is probably unrealistic because this will greatly increase the computational effort (in terms of both storage space and CPU time). An unstructured mesh approach would allow the grid points to be placed in areas where grid refinement is most desirable, for example in areas of steep gradients. This approach would reduce overall the number of computational cells required for a grid independent solution and reduce the computer storage and running

time. This approach should also be applied to the 2D problem of chapter 4 to establish a grid independent solution.

Second, improving the modelling of the flow field generated by the impeller model will greatly improve overall of both the velocity and the scalar fields. A suitable starting point may be found in the works of Luo et al(1993) and Tabor et al(1996). The authors have used a sliding-shearing mesh technique in the impeller region in the numerical solution of a fully baffled tank stirred by a Rushton impeller. In this approach the flow field in the tank is divided into two parts in which the part of the mesh that surrounds the impeller is allowed to rotate with it, whilst the other part of the mesh that overlays the tank and remains stationary. At the interface between the two domains the mesh is allowed to shear and/or slide to accommodate the relative motion. The $\kappa$ - $\varepsilon$ turbulence model has been used by both authors and a self-filtering second order scheme used by Luo et al, while the central differencing is used by Tabor et al. In both works the authors indicated that the numerical data obtained captured the characteristic flow features correctly. To take full advantage of the sliding-shearing technique, the fluid flow and mixing computations carried out in this work should be repeated using this technique in an attempt to obtain more accurate velocity fields in and around the impeller region resulting in more accurate mixing calculations.

Finally, the current fluid flow and scalar mixing calculation are complicated by the need to resolve the dynamics of both the velocity and the scalar fields. The modelling of a continuously stirred tank, whilst still exhibiting some cyclic behaviour, will ease this problem. In addition the collection of experimental data in such a flow is much easier and, see for example Distelhoff(1997), more complete sets of data exist than for the batch mixing configuration used here.

# References


Abid,R., Speziale,C.G. and Thangams,S. (1991), "Application of a new $\kappa$ - $\tau$ model to near-wall turbulent flows", AIAA- 91- 0614.

Aggarwal,S.K. (1987), "Numerical study of convection-diffusion-reaction equations for large Damkohler and cell Reynolds Numbers", Num. Heat Transfer., Vol.11, pp143-164.

Alvarez,J.E. (1994), "Calculation of the velocity and temperature fields in a jet in cross-flow", Ph.D. Thesis, University of London.

Amano,R.S. (1984), "Development of a turbulence near-wall model and its application to separated and reattached flows", Num. Heat Transfer., Vol.7, p59.

Anderson,J.D.(1995), "Computational Fluid Dynamics", The Basics with Applications, Pub. McGraw-Hill, New York., p137.

Atias,M., Wolfshtein,M. and Israeli,M. (1977), "Efficiency of Navier-Stokes solvers", J. AIAA, Vol.15, p263.

Bertrand,J., Couderc,J.C. and Angelino,H. (1980), "Power consumption, pumping capacity and turbulence intensity in baffled stirred tanks; comparison between several turbines", Chem. Eng. Sci., Vol.35, pp2157-2163.

Boussinesq,J. (1877), "Theorie de l' ecoulement tourbillant", Mem. Pre. Par div. Sav., Vol. 23, Paris.

Bradshaw,P. (1976), "Introduction of Topics in Applied Physics", Vol.12,Turbulence, Springer-Verlag.

Brucato,A., Ciofalo,M., Grisafi,F. and Micale,G. (1994), "Complete numerical simulation of flow fields in baffled stirred vessels: the inner-outer approach", 8th European Conference on Mixing, IChemE Vol.136, pp155-162.

Calabrese,R. and Stoots,C.M. (1989), "Flow in the impeller region of a stirred tank", Chem. Eng. Prog., pp43-50.

Castro,I.P. and Jones,J.M. (1987), "Studies in numerical computations of recirculating flows", Int. J. Num. Methods Fluids., Vol.7, pp793-823.

Champagne,F.H., Harris,V.B. and Corrsin,S. (1970), "experiments on nearly homogeneous turbulent shear flow", J. Fluid Mechs. Vol.41, p81.

Chou,P.Y. (1945), "On velocity correlation's and the solution of the equations of turbulent fluctuation", Quart. J. Appl., Vol.3 pt.1, pp38-54.

Claus,R.W., Neely,G.M. and Syed,S.A. (1985), "Reducing numerical diffusion for incompressible flow calculations", NASA Tech Memo 83621.

Courant,R., Isaacson,E. and Rees,M. (1952), "On the solution of non-linear hyperbolic equations by finite differences", Comm. Pure Appld. Math., Vol.5, pp243-255.

Crozier,D.B.A. (1989), "A detailed study of the flow characteristics in a tall stirred tank", Proc 3rd Int Conf on Laser Anemometry - Advances and Applications, Wales, pp16.1-16.10.

Daly,B.J. and Harlow,F.H. (1970), "Transport equations in turbulence", Physics of Fluids., Vol.13, pp2634-2649.

Davidov,B.I. (1961), "On the statistical dynamics of an incompressible turbulent fluid". Dokl. AN SSSR.,Vol.136, pp47-50.

Dekeyser,I. (1985) "Numerical predictions of an axisymmetrical heated plane jet with a second moment turbulence closure", Int. J. Heat and Mass Transfer., Vol.28 No.3, pp653-662.

Dianat,M., Fairweather,M. and Jones,W.P. (1991), "Predictions of a turbulent jet impacting a flat surface", Proc. 8th Turbulent Shear Flows Symp., Munich, Germany.

Distelhoff,M.F.W., Marquis,A.J., Nouri,J.M. and Whitelaw,J.H. (1996), "Scalar mixing measurements in batch operated stirred tanks", To appear in Can. J. Chem. Eng.

Distelhoff,M.F.W., "Scalar mixing in stirred tanks", Ph.D. Thesis, University of London (to be submitted in 1997).

Fairweather,M., Jones,W.P. and Marquis,A. (1988), "Predictions of the concentration field of a turbulent jet in a crossflow", Combustion, Science and Technology. Vol.62, p 61.

Ferziger,J.H. and Peric,M. (1996), "Computational Methods for Fluid Dynamics", Pub. Springer-Verlag, Berlin Heidelberg , pp157-159.

Gaskey,S., Vacus,P., David,R., Villermaux,J. and Andre,J.C. (1990), "A method for the study of turbulent mixing using fluorescense spectroscopy", Experiments in Fluids 9, pp 137-147.

Gunkel,A.A. and Weber, M.E. (1975), "Flow phenomena in stirred tanks", AICHE J., Vol.21, p 931.

Hah,C. (1983), "Calculation of various diffuser flows with inlet swirl and inlet distortion effects", AIAA J., Vol.21, pp1127-1133.

Hanjalic,K. and Launder,B.E. (1972), "A Reynolds Stress model of turbulence and its application to thin shear flows", J. Fluid Mech., Vol.52, pp609-638.

Hanjalic,K., Launder,B.E. and Schiestel,R. (1980), "Turbulent shear flows", Vol.II, Eds. Bradbury,L.J.S., F.Durst, B.E., Launder,F.W. and Schmidt and J.H.Whitelaw, (Springer Verlag, New York).

Harlow,F.H. and Welsh,J.E. (1965), "Numerical calculation of time dependent viscous incompressible flow of fluid with free surface", Physics of Fluid. Vol.8. No.12, pp2182-2189.

Harlow,F.H. and Nakayama,P.L. (1967), "Turbulent transport equations", The Physics of Fluids, Vol.10, p2323.

Harvey,P.S. and Greaves,M., (1982), "Turbulent flow in an agitated vessel", Part I, Trans. IChemE, Vol.60, pp195-200.

Hassan,Y.A. and Kim,J.H. (1985a), "A Navier-Stokes analysis of three dimensional negatively buoyant jet injected into a hot cross flow", Nucl. Science and Eng., Vol.89, pp70-78.

Hinze,J.O. (1959), "Turbulence, an introduction to its mechanism and theory", McGraw-Hill, New York.

Hockey,R.M. (1990), "Turbulent Newtonian and non-Newtonian flows in a stirred reactor", Ph.D. Thesis, University of London.

Houghton and Brock. (1970), "Aerodynamics for engineering students", ARNOLD, London.

Jayathi,Y.M., Sanjay,R.M. and Dipankar,C. (1994), "CFD simulation of flows in stirred tank reactors using a sliding mesh technique", 8th European Conference on Mixing. IChemE Vol.136, pp341-345.

Jones,W.P. (1971), "Laminarisation in strongly accelerated boundary layers", Ph.D. Thesis, University of London.

Jones,W.P. and Launder,B.E. (1972), "The prediction of laminarisation with a two equation model of turbulence", Int. J. Heat and Mass Transfer, Vol.15, p301.

Jones,W.P. (1980), "Models for turbulent flows with variable density and combustion", Prediction methods for turbulent flows edited by W. Kollmann, Hemisphere Pub. Co., New York.

Johnson, B.V. and Bennett,J.C. (1981), "Mass and momentum turbulent transport experiments with confined coaxial jets", NASA Contractor Report NASA-CR-165574, UTRC Report R81-915540-9.

Joseph,M. (1983), "Finite difference representations of vorticity transport", Comp. Methods. Appld. Mech. Eng., Vol.39, pp107-116.

Keller,L. and Friedmann,A. (1924), "Differentialgleichungen fur die turbulente bewegung einer kompressiblen flussigkeit", Congress Appl. Mech., delft, pp395-405.

Kolmogorov,A.N. (1942), "Equations of turbulent motion of an incompressible fluid". Izv. Akad. Nauk. Ssr, Seria Fizicheska Vi., No.1-2, pp56-58. (English translation: Imperial College, Mech. Eng. Dept. Report. ON/6).

Launder,B.E. (1978), "Heat and mass transport in turbulence", In topics in Applied Physics, Vol.12(edited by P. Bradshaw), Springer Berlin.

Launder,B.E. and Dekeyser,I. (1983), "A comparison of triple-moment temperature-velocity correlations in the axisymmetric heated jet with alternative closure models", 4th. Symposium on Turbulent Shear Flows, Sept 12-14, Karlsruhe, Germany.

Launder,B.E. and Spalding,D.B. (1972), "Mathematical models of turbulence", Acad. Press, London and N.Y.

Launder,B.E. and Spalding,D.B. (1974), "The numerical computation of turbulent flows", Comp. Meth. Appl. Mech. Eng., Vol.3, pp 269-289.

Launder,B.E., Reece,G.J. and Rodi,W. (1975), "Progress in the development of a Reynolds-Stress turbulence closure", J. Fluid. Mech.Vol.68, p537.

Lee,K.C. (1995), "An experimental investigation of the trailing vortex structure and mixing characteristics of stirred vessels", PhD. Thesis, University of London.

Lee,K.C. and Yianneskis.M. (1994), "The extent of periodicity of the flow in vessels stirred by Rushton impellers", In Industrial Mixing Technology: Chemeical and Biological Applications, ed. G. Tatterson, A. IChemE.

Leschziner,M.A. (1980), "Practical evaluation of three finite difference schemes for the computation of steady-state recirculating flows", Comp. Methods. Appld. Mech. Eng.. Vol.23, pp293-312.

Lumely,J.L. and Khajeh-Nouri,B. (1974), "Computational modelling of turbulent transport", Adv. Geophys. 18, p169.

Luo,J.Y., Gosman,A.D., Issa,R.I., Middleton,J.C. and Fitzgerald,M.K. (1993), "Full flow field computation of mixing in baffled stirred vessels", Trans. IChemE, Vol.71, pp342-344.

Mahmoudi,S.M. and Yianneskis,M. (1991), "The variation of flow pattern with impeller spacing in stirred vessels with two Rushton impellers", Proc 7th Europ Conf Mixing, Brugges, pp18-20.

Mahmoudi,S.M. and Yianneskis,M. (1992), "The effect of impeller spacing on the mean flow and turbulence in stirred vessels with two Rushton impellers", Proc IChemE Research Event, Manchester, pp380-382.

Mahmoudi,S.M. (1994), "Velocity and mixing characteristics of stirred vessels with two impellers", Ph.D. Thesis, University of London.

Marquis,A.J. (1986), "The application of high order convection approximations and second order turbulence closures to recirculating flows", Ph.D. Thesis, University of London.

Middleton,J.C., Pierce,F. and Lynch,P.M. (1986), "Computations of flow fields and complex reaction yield in turbulent stirred reactors, and comparison with experimental", Chem. Eng. Res. Des., Vol. 64, pp18-22.

Mujumdar,A.S., Huang,B., Wolf,D., Weber,M.E. and Douglas,W.J.M. (1970). "Turbulence parameters in stirred tank", Can. J. Chem. Eng., Vol.48, p475.

Mujumdar,A.S. (1988), Num. Heat Transf., Vol.13, pp125-132.

Musonge,P. (1983), "The prediction of free turbulent flows.", PhD Thesis University of London.

Nouri,J.M. (1988), "Single and two-phase flows in ducts and stirred reactors", Ph.D. Thesis, University of London.

Nouri,J.M. and Whitelaw (1990), "Effects of size and confinement on the flow characteristics in stirred reactors", Proceedings of the 5th International Symposium on Applications of Laser Techniques to Fluid Mechanics, Paper 23.2, Lisbon 9-12 July.

Patel,M.K. and Markatos,N.C. (1986), "An evaluation of eight discretisation schemes for two-dimensional convection-diffusion equations", Int. J. Num. Methods Fluids., Vol.6, pp129-154.

Patankar,S.V. and Spalding,D.B. (1972), "A calculation procedure for heat, mass and momentum transfer in three-dimensional parabolic flows", Int. J. Heat and Mass Transfer, Vol.15, p1787.

Patankar,S.V. (1980), "Numerical Heat Transf. and Fluid Flow", McGraw Hill New York.

Pericleous,K.A. and Patel,M.K. (1987), "The source-sink approach in the modelling of stirred reactors", Phys. Chem. Hydrodynam., Vol.9, p279.

Placek,J.and Tavlarides,L.L. (1985), "Turbulent flow in stirred tanks. Part I: Turbulent flow in turbine impeller region", AIChE J., Vol.31, p1113.

Placek,J., Tavlarides,L.L., Smith,G.W. and Fort,I. (1986), "Turbulent flow in stirred tanks. Part II: A two-scale turbulent model", AIChE J., Vol.32, p1771.

Prandtl,L. (1945), "Uber ein neues formelsystem fur die ausgebildeten turbulenz". Nachr.Akad. Wiss., Gottingen, Math.-Phys. Klasse, p6.

Prandtl,L. (1925), "Bericht uber untersuchungen zur ausgebildeten turbulenz", ZAMM, Vol.5, p136.

Price,H.S., Varga,R.S. and Warren,J.E. (1966), "Application of oscillation matrices to diffusion-convection equations", J. Maths Physics., Vol.45, pp301-311.

Ranade,V.V., Joshi,J.B. and Marathe,A.G. (1989), "Flow generated by pitched blade turbines II: Simulation using $\kappa$ - $\varepsilon$ model", Chem. Eng. Commun., Vol.81, pp225-248.

Ranade,V.V. and Joshi,J.B. (1990), "Flow generated by a disk turbine: Part I. Experimental", Trans. IChemE, Vol.68A, pp19-33.

Ranade,V.V. and Joshi,J.B. (1990), "Flow generated by a disk turbine: Part II. Mathematical modelling and comparison with experimental data", Trans. IChemE, Vol.68A, pp34-50.

Reed,X.B., Princz,M. and Hartland,S. (1977), "Laser-Doppler measurements of turbulence in a standard stirred tank", 2nd European Conference on Mixing, Cambridge. (BHRA-Cranfield), p B1.1.

Reynolds,O. (1883), "An experimental investigation of circumstances which determine whether the motion of water shall be direct or sinuous, and of the law of resistance in parallel channels", Phil. Trans., Vol.174, pp935-982.

Reynolds,O. (1894), "On the dynamical theory of incompressible viscous fluids and the determination of the criterion", Phil. Trans. Roy. Soc., Vol.186A, pp123-164.

Rhie,C.M. and Chow,W.L. (1983), "Numerical study of the turbulent flow past an airfoil with trailing edge separation", AIAA J., Vol.21 (No.11.), pp1525-1532.

Roback,R. (1983), "Mass and momentum turbulent transport experiments with confined swirling coaxial jets", NASA Contractor Report NASA-CR-168252.

Roache,P.J. (1972), "Computational Fluid Dynamics", Pub. Hermosa Publishers, Albuquerque, N. Mexico, revised edition, pp1-8.

Rosten,H.I. and Spalding,D.B. (1985), "PHOENICS - beginners guide and users manual", CHAM TR/100.

Rotta,J.C. (1951), "Statistische theorie nichthomogener turbulenze", Zeitsch f. Physik, Bd.129, pp547-572, and Bd.131, pp51-77. (English Translation:Imperial College, Dept. Mech. Eng., Reports TWF/TN/38, 39.)

Rotta,J.C. (1968), "Uber eine methode zur berechnung turbulenter scherstrom ungen", Aerodynamische Versuchsanstalt Gottington Report 69 A 14.

Ruszkowski,S. (1994), "A rational method for measuring blending performance and comprison of different impeller types", 8ht European Conference on Mixing, IChemE, Mixing 8, 136, pp283-292.

Saffman,P.G. (1970), "A model for inhomogeneous turbulent flow". Proc. R. Soc. Lond. A317.

Samaraweera,D.S.A. (1978), "Turbulent heat transport in two and three dimensional temperature fields", PhD. Thesis,University of London.

Sano,Y. and Usui,H. (1985), "Interrelations among mixing time, power number and discharge flow rate number in baffled mixing vessels", Journal of Chemical Engineering of Japan, 18, p47.

Shyy,W. (1983), "Study of finite difference schemes approximations to steady-state convection-dominated flow problems", General Electric Technical Information Series Report 83CRD189.

Shyy,W. (1984), "A note on assessing finite difference procedures for large Peclet/Reynolds number flow calculation", 3rd Int Conf on Boundary and Interior Layers: Computational and Asymptotic Methods.

Shyy,W. and Correa,S.M. (1985), "A systematic comparison of several numerical schemes for complex flow calculations", AIAA 23rd Aerospace Sciences Meeting, Reno, Nevada. AIAA-85-0440.

Smith,R.M. and Hutton,A.G. (1982), "The numerical treatment of advection: a performance comparison of current methods", Num. Heat Transfer., Vol.5, pp439-461.

Smith,G.W., Tavlarides,L.L. and Placek,J. (1990), "Turbulent flow in stirred tanks: scale-up computations for vessel hydrodynamics", Chem. Eng. Comm., Vol.93, pp49-73.

Spalding,D.B. (1971), "Concentration fluctuations in a round turbulent free jet". Chem. Eng. Sci., 26, pp95-107.

Spalding,D.B. (1972), "A novel finite difference formulation for differential expressions involving both first and second derivatives", Int. J. Num. Meth. Eng., Vol.4. pp551-559.

Tabor,G., Gosman,A.D. and Issa,R.I. (1996), "Numerical simulation of the flow in a mixing vessel stirred by a Rushton turbine", IChemE, Ch.30, No.140, pp25-34.

Taylor (1937), "The mechanical properties of fluids", Blackie, London.

Tennekes,H. and Lumley,J.L. (1992), "A First Cource in Turbulence", 8th Edition, MIT press, Cambridge, Massachusetts, and London.

Thom,A. (1933), "The flow past cylinders at low speed", Proc. Roy. Soc. of London, Vol.A141, p651.

Timin,T. and Esmail,N. (1983), "A comparative study of central and upwind difference schemes using the primitive variables", Int. J. Num. Methods Fluids., Vol.3, pp295-305.

van Leer,B. (1974), "Towards the ultimate conservative difference scheme", Monotonicity and conservation combined in a second order scheme, J. Comp. Phys., Vol.14, pp361-370.

van der Molen,K. and Van Maanen,H.R.E. (1978), "Laser-Doppler measurements of turbulent flow in stirred vessels to establish scaling rules", Chem. Eng. Sci., Vol.33, p1161.

van't Riet,K. and Smith,J.M. (1973), "The behaviour of gas-liquid mixtures near Rushton turbine blades", Chem. Eng. Sci., Vol.28, p1031.

van't Riet,K. and Smith,J.M. (1975), "The trailing vortex system produced by Rushton turbine agitators", Chem. Eng. Sci., Vol.30, p1093.

van't Riet,K., Bruijn,W. and Smith,J.M. (1976), "Real and pseudo-turbulence in the discharge stream from a Rushton turbine", Chem. Eng. Sci., Vol.31, p407.

Vanka,S.P. (1987), "Second order upwind differencing in recirculating flow", AIAA J., Vol.25, pp1435-1441.

Von Karman,T.H. (1930), "Mechanische ahnlichkeit und turbulenz", Proc. 3rd Int. Congress Appl. Mech.,Stockholm, Pt. 1, p85.

Wendt,J.F., Anderson,J.D., Degrez,G., Dick,E. and Grundmann,R. (1991), "Computational Fluid Dynamics", Pub.Spring-Verlag, New York., pp5-13.

Wilkes,N.S. and Thompson,C.P. (1983), "An evaluation of higher-order upwind differencing for elliptic flow problems", AERE report CSS 137.

Yianneskis,M., Popiolek,Z. and Whitelaw,J.H. (1987), "Steady and unsteady flow characteristics of stirred reactors", J. Fluid Mechanics., Vol.175, pp537-555.

Yianneskis,M. and Whitelaw,J.H. (1993), "On the structure of the trailing vortices around Rushton turbine blades", Trans. IChemE., Vol.71A, pp543-550.

Ziman,H.J. (1990), "A computer prediction of chemically reacting flows in stirred tanks", PhD. Thesis,University of London.